

MULTISCALE MODELLING OF METABOLISM AND TRANSPORT PHENOMENA IN LIVING TISSUES

THÈSE N° 3803 (2007)

PRÉSENTÉE LE 24 MAI 2007

À LA FACULTÉ DES SCIENCES DE BASE
Chaire de modélisation et calcul scientifique
SECTION DE MATHÉMATIQUES

ÉCOLE POLYTECHNIQUE FÉDÉRALE DE LAUSANNE

POUR L'OBTENTION DU GRADE DE DOCTEUR ÈS SCIENCES

PAR

Carlo D'ANGELO

dottore in ingegneria elettronica, Politecnico di Milano, Italie
et de nationalité italienne

acceptée sur proposition du jury:

Prof. J. P. Buser, président du jury
Prof. A. Quarteroni, directeur de thèse
Prof. L. Formaggia, rapporteur
Prof. J. Rappaz, rapporteur
Dr M. Weiser, rapporteur



ÉCOLE POLYTECHNIQUE
FÉDÉRALE DE LAUSANNE

Suisse
2007

A papà

Abstract

The range of applications of mathematical modelling in biosciences has recently expanded to encompass problems posed by *biomedicine* and *sport sciences*. Topics of interest are for instance the prediction of the response of an athlete to exercise, the pharmacokinetics of a chemical compound, or the detection of illicit drugs.

In this work, we consider some of these problems, related to metabolism, circulation and mass transport in tissues. First, we address the quantitative analysis of the biochemical reactions that are responsible of energy production in muscle cells. These reactions are strictly dependent on chemical exchanges between blood and tissues, by several physiological auto-regulation mechanisms. For this reason, we consider coupled problems in which the reaction phenomena are influenced by transport in blood. In particular, the problem of local blood perfusion and supply of substrates to tissues is studied in detail.

The processes underlying the interaction between metabolism and circulation feature a multiscale nature: for instance, although metabolism takes place in cells, it modifies the hemodynamics of peripheral (capillaries) and central (heart) circulation. Therefore, we will set up a hierarchy of models, corresponding to these different scales.

At first, we adopt an integrative approach, based on a compartmental model of the whole-body response to exercise, or more generally to variations in skeletal muscle metabolism. This model is the higher level of the hierarchy, describing the interactions between organs. Then, we increase the level of detail and focus on isolated tissues and vessels, considering more accurate one-dimensional models for blood flow and mass transport, as well as coupled 1D-3D models of tissue perfusion. In the latter models, the microvascular matrix is represented as a three-dimensional homogeneous medium, where larger vessels are described as 1D networks: circulation, transport and reaction of biochemical species are modelled at both the scales.

The models considered in this work may provide a multi-scale analysis of metabolic processes, such as those induced by exercise, that often begin at cellular level, progressively propagate up through the hierarchy of scales, until adaptation of the whole body is reached.

Examples of simulations, dealing with exercise protocols or clinical study cases, are provided to support the range of applications.

Keywords: mathematical models, metabolism, exercise, blood perfusion, multiscale models.

Résumé

La modélisation mathématique a récemment élargi son domaine d'applications à la *médecine* et aux *sciences du sport*. Quelques sujets d'intérêt sont par exemple la prédiction de la réponse corporelle d'un athlète lors de l'exercice, la pharmacocinétique et le métabolisme d'un médicament, la détection de substances illégales.

Dans cette thèse, on considère quelques-uns de ces problèmes, concernant le métabolisme, la circulation sanguine, et le transport de masse dans les tissus. Premièrement, on aborde l'analyse quantitative des réactions bio-chimiques qui soutiennent la production d'énergie mécanique dans les cellules musculaires. Ces réactions dépendent fortement des échanges chimiques entre le sang et les tissus par le biais des plusieurs systèmes physiologiques d'autorégulation. Nous étudions donc l'influence entre le métabolisme, l'hémodynamique et le transport de masse. Deuxièmement, nous considérons en détail le problème de la perfusion sanguine et de la distribution des substrats dans les tissus.

Le métabolisme et la circulation sanguine reposent sur des processus qui ont lieu à différentes échelles. D'une part, le métabolisme interagit au niveau cellulaire. D'autre part, il influence l'hémodynamique de la circulation périphérique (capillaires) et centrale (cœur). Par conséquent, nous introduisons une hiérarchie des modèles correspondants à ces différentes échelles.

À un premier niveau, on considère une approche globale basée sur un système d'équations différentielles qui modélise la réponse corporelle à l'exercice. Ce modèle représente le sommet de la hiérarchie, qui correspond aux interactions entre les organes. À un deuxième niveau, on améliore la précision en considérant des modèles unidimensionnels de flux sanguin, ainsi que des modèles couplés 1D-3D de perfusion de tissus. Dans ces derniers, le réseau des capillaires est décrit comme un milieu poreux 3D, tandis que les vaisseaux majeurs sont représentés par des objets 1D.

Les modèles considérés dans ce travail peuvent contribuer à l'analyse multi-échelle des processus métaboliques qui naissent au niveau cellulaire, se propagent le long de la hiérarchie d'échelles, jusqu'à ce que l'ensemble du corps se soit adapté.

Finalement, on présente quelques exemples de simulations, concernant cas pratiques en médecine et physiologie du sport, afin de présenter un éventail des applications possibles.

Mots-clés : modèles mathématiques, métabolisme, exercice, perfusion des tissus, modèles multi-échelle.

Acknowledgments

At first, I would like to thank Prof. Alfio Quarteroni, who has given me the great opportunity of working in his research group. During these years, he has continuously stimulated my research towards new directions, always providing new suggestions and ideas.

I am very grateful to Prof. Sandro Salsa for his precious advice on a number of mathematical issues I encountered in my work. I am also indebted with Prof. Gianni Gilardi for his hints and guidelines.

I am grateful to all the colleagues of the big CMCS family (Chair of Modelling and Scientific Computing). In particular, I thank my office mates Gianluigi and Christian for their invaluable help. Special thanks to Klaus, who has been a colleague and a true friend!

I would like to thank all the members of the jury: Prof. Jacques Rappaz and Prof. Luca Formaggia for the many observations and stimulating remarks, Prof. Peter Buser for presiding the jury, and Martin Weiser, for the interesting discussions about multiscale approaches.

I acknowledge the SRE (Sport and Rehabilitation Engineering) programme, that supported my research. I also thank Prof. Pierre-Étienne Bourban, who has coordinated the groups involved in this transdisciplinary initiative of the EPFL, and Prof. Yves Papelier, for his many suggestions about mathematical models in sport physiology.

I would like to say thank you to my mother and my brother for the support and encouragement, and to all friends from Italy and Switzerland for the many adventures, trips and dinners over those years.

This thesis is dedicated to my father, for everything he did for me and our family.

Lausanne, May 2007

Contents

Introduction	1
1 Interaction between circulation and tissue metabolism	5
1.1 Introduction	5
1.1.1 Cardiovascular parameters and auto-regulation	5
1.1.2 Gas exchange and ventilation	8
1.1.3 Metabolism	9
1.2 Cardiovascular Model (CVM)	11
1.3 Tissue Metabolism Model (TMM)	15
1.3.1 Arterial and venous concentrations	15
1.3.2 One-chemical model	15
1.3.3 General multi-chemical model	16
1.4 Coupling between CVM and TMM: parameter estimation	19
1.4.1 Identification methods	21
1.5 Simulations of coupled CVM and TMM	27
1.5.1 One-chemical model	27
1.5.2 Multi-chemical model	29
1.6 Conclusions	30
2 Reduced one-dimensional models for transport of chemicals in blood vessels	33
2.1 Introduction	33
2.2 A reduced model for chemical transport	34
2.2.1 The transport diffusion equation	34
2.2.2 Axisymmetric transport diffusion equation (TDE) in cylindrical coordinates	35
2.2.3 The reduced non-dimensional equation	36
2.2.4 The averaged equations	36
2.2.5 The reduced averaged equations in dimensional form	37
2.2.6 Closure of system (2.11)	37
2.3 Characteristics	39
2.4 Analysis of the system for <i>flat profile</i>	41
2.5 Taylor-Galerkin numerical approximation of the solution	46
3 Introducing coupled 1D-3D diffusion-reaction models	53
3.1 Introduction	53
3.2 The problem and model equations	54
3.2.1 Geometry	54

3.2.2	Diffusion-advection-reaction equations	56
4	Analysis of 1D-3D coupled problems	65
4.1	Dirichlet problem with source term on a line	66
4.1.1	Analysis in weighted Sobolev spaces	68
4.2	Neumann-Robin problem with exchange term on a line	74
4.3	1D-3D coupled problems with exchange term on a line	78
5	Finite element approximation of 1D-3D coupled problems	81
5.1	FEM discretization of the coupled 1D-3D problem	84
5.2	Convergence tests	89
5.2.1	2D-axisymmetric discretization.	90
5.2.2	Full 3D-1D discretization : the error introduced by the lumped approximation.	91
6	Modelling blood flow and mass transport in vascularized tissues	95
6.1	Introduction	95
6.2	Macroscale: 1D and $\frac{1}{2}$ D models for blood flow and transport	98
6.2.1	The linearized 1D model for blood flow	99
6.2.2	Quasistatic approximation: the $\frac{1}{2}$ D model	100
6.2.3	The 1D transport model	101
6.3	Microscale: 3D models for blood flow and transport	102
6.3.1	Hierarchical perfusion model for blood flow in the tissue	102
6.3.2	Multi-pressure models (hierarchical discretization)	104
6.3.3	The transport model in the tissue	107
6.4	Some examples of blood perfusion simulations	109
6.4.1	A three-hierarchies perfusion model for the tissue	109
6.4.2	From retinal imaging to retinal perfusion simulation	114
6.4.3	Brain Angiography	114
6.5	1D-3D coupling between blood vessels and surrounding tissue	119
6.6	Algorithmic and numerical aspects	122
6.6.1	1D diffusion-advection equations on trees	122
6.6.2	3D-1D simulations of blood flow and mass transport	136
6.6.3	An example of numerical simulation	142
6.6.4	An application to the study of brain perfusion	148
A	Weighted Sobolev Spaces	157
A.1	Spaces $L^2_\alpha(\Omega)$	157
A.2	Spaces $W^{1,p}(\Omega, \mu)$: fundamental properties	158
A.3	Spaces $H^1_\alpha(\Omega)$	159
A.4	Nečas theorem	161

Introduction

The increasing interest in biomathematics has recently led to new applications of scientific computing in domains that were previously exclusive of medicine: starting with metabolism and other phenomena taking place at cellular level, up to the description of tissues and organs and their regulatory mechanisms, mathematical modelling may help to understand the behavior of whole-body processes.

As an example, the body's response to heavy exercise begins in skeletal muscles, but rapidly induces adaptations of peripheral and central circulation. In order to correctly describe this response, one has to take into account at the same time blood flow, transport of chemicals (oxygen, carbon dioxide, lactate, . . .) in blood, and biochemical reactions in tissues [12], [91], [59]. Similar problems are encountered in the pharmacokinetics of specific drugs. All these problems have an intrinsic interest in medicine: in particular, the quantitative prediction of the distribution of a chemical compound in living tissues may provide important contributions to the development of new treatments or products.

Mass transport in tissues is led by blood *perfusion*, that is the blood volume flow exchange through a given volume of tissue. Perfusion is a valuable indicator of the physiological condition of the tissue. For example, it is known that changes in blood perfusion correlate with several pathological processes, such as those found with the development of tumors. Detecting changes in local perfusion may help finding, identifying, and determining the extent of tumors or lesions. In general, the evaluation of the microcirculation in a variety of tissues (e.g. myocardial, renal, intestinal, cerebral, and spinal) is a valuable information in a number of cases, from surgical intervention to the design of biomedical devices. Of course, modelling and simulating tissue perfusion may provide a better understanding of the inherent mechanisms and improve diagnosis. The benefits of using computer models are even more pronounced when dealing with the transport of oxygen and other chemicals. Just to cite a few examples, in [82, 87] accurate methods are employed to study the transfer of oxygen and other chemicals to the arterial walls; in [63, 19], models of circulation and mass transport are used to predict the effects of pathologies or devise different shapes of prostheses for the treatment of heart diseases; computer simulation of biological transport phenomena has been applied in sport medicine as well [106, 62], since the study of the physiological processes from oxygen uptake to local biochemical pathways [69, 26, 41] has a remarkable interest.

From this picture, it is clear that mathematical models of blood perfusion and transport of chemicals in tissues are important tools for diagnosis and research in medicine. However, the description of blood flow from large vessels down to the network of hundreds of thousands of capillaries per square centimeter supplying a tissue, is a very complex matter. The more precise the models, the more expensive the corresponding computations: thus, a three-dimensional simulation of blood flow and transport is unaffordable for the whole human cardiovascular system. Only local results are available in this regard (see for example to [82]). If on one hand a need for global predictive models exists, on the other hand the complex multiscale nature of circulation and metabolism makes their simulation a difficult task. To our knowledge the only mathematical models allowing both the simulation of mass transport

at the macroscopic scale of the whole cardiovascular loop and the prediction of substrate delivery to a specific organ or location, are purely *lumped* models (obtained by compartmental analysis, see for instance [15]), in which any geometrical information about flow or distribution of chemicals is lost: works adopting this approach are for instance [12], [58]. Nevertheless, alternative approaches exist, consisting in using reduced models preserving some geometrical informations. For instance, three-dimensional models of blood flow can be reduced to one-dimensional [84, 86, 29, 104, 31]: thanks to the computational saving, they allow simulating the behavior of complex vascular networks.

The purpose of this thesis is to develop numerical methods for the simulation of transport-reaction phenomena in living tissues. We follow a multiscale approach, in which a hierarchy of models, having different levels of detail, is employed. Models belonging to different scales interact to represent the mutual influence of the corresponding “subsystems” of the body, with the aim of describing complex processes such as exercise (see fig. 1). As instances of interacting scales we will consider: organs and circulatory system; fast flow in large vessels and slow flow in the capillary bed; the transport of a chemical in a vessel and the metabolism of the same chemical in the tissue supplied by the vessel.

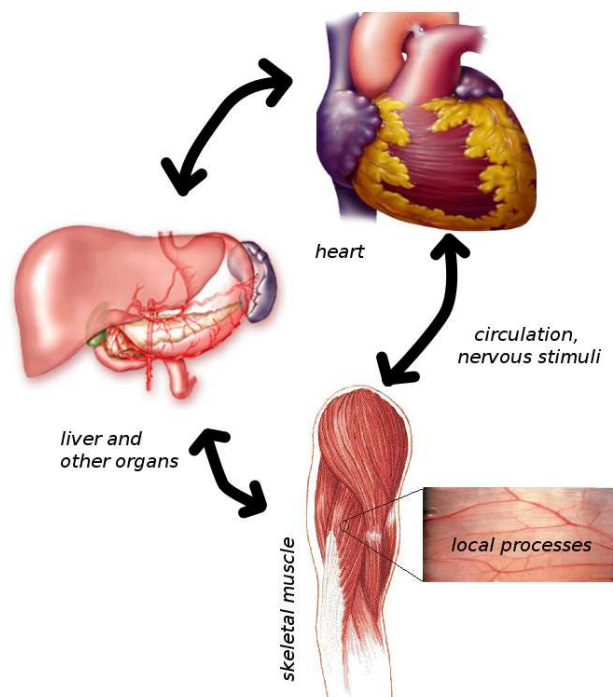


Figure 1: Macroscales and microscales interacting in the human body: local processes taking place at cellular level affect the behavior of whole organs. For instance, if local metabolism is altered in skeletal muscle because of exercise, this results in local changes in tissue concentration of oxygen, carbon dioxide, lactate and several other substrates. The peripheral circulation responds by increasing the cross-sectional area of the vessels supplying the tissue. This fall in peripheral resistance is partially responsible of adaptation of heart beat. On the other hand, liver and other organs are involved in the process as regulators of arterial concentrations of some substrates (i.e. glucose).

The outline of this dissertation is as follows (see also the thesis organization in fig 2).

In *chapter 1*, we investigate the use of mathematical models for describing the response of circulation and metabolism to extreme conditions at high power output by a *compartmental* approach. A special attention is paid to the modelling of biochemical pathways at cellular level. We include in our analysis the baroreflex and chemoreflex feed-back systems, which are responsible of the mutual influence of circulation and metabolism (see [101], [59]). The results of simulations of typical exercise protocols are discussed, emphasizing the changes in blood concentrations of relevant chemicals such as oxygen, carbon dioxide, lactate, glucose.

There is a number of works dealing separately with cardiovascular or metabolic modelling; however, the interaction between these processes due to physiological feedback systems is often poorly described, even if integrative models have been proposed as well (see for instance [12]). In this chapter we give a more detailed analysis of the interplay between circulation and biochemistry during effort conditions, for instance considering the key role of the tissue vasomotor tone adaptations, and the modified baroreflex regulatory effect during exercise.

Moreover, we treat in detail the problem of parameter identification, which is a central topic when dealing with a large number of equations modelling biochemical reactions, since usually only partial informations are available *in vivo*. Several approaches (gradient algorithms, genetic algorithms, hybrid algorithms) are compared and discussed.

In *chapter 2*, we introduce reduced models for the simulation of the mass transport in vessels. We extend an already existing one-dimensional model of blood flow to treat for instance oxygen transport and, in general, the transport of any chemical. By an asymptotic analysis, we derive the 1D mass transport equations in the vessel and give an accurate analysis of the special case of *flat profiles* for both velocity and mass. In the latter case, we show the global existence of regular solutions under suitable hypotheses, basing our arguments on [13]; in particular we treat the finite vessel case. Moreover we perform an accurate characteristics analysis of the coupled system (blood flow and mass transport) in order to assign suitable boundary conditions. We provide numerical results including an example of coupling between the 1D model and a dynamical system representing a perfused tissue.

In *chapters 3 and 4*, we propose a mathematical framework that will be the basis of our multiscale approach to tissue perfusion. Namely, we study the coupling between two diffusion-reaction problems, one defined on a 3D domain, the other on a 1D manifold embedded in the 3D domain. The motivation is to apply such models to capture the influence of the *geometry* of a vessel network on the perfusion of the surrounding tissue. The coupled 3D-1D problems have a high dimensional gap: the 3D solutions are singular near the 1D manifold, so that a special analysis is needed. We introduce *ad-hoc* functional spaces and prove the well-posedness in cases of interest.

To our knowledge, this is the first attempt to employ such kind of multiscale models for blood flow and transport phenomena in living tissues. A similar approach is often adopted in geomechanics, for example when modelling groundwater flows in fractured porous media. Nevertheless, the dimensional gap of the 1D-3D coupling between fractures and porous matrix is not standard: its analysis is the main contribution of this chapter.

In *chapter 5* finite element approximation schemes for the problems introduced in chapters 3 and 4 are considered and discussed. We introduce several numerical techniques that allow for accurate solutions despite the presence of the singularity. We consider the case in which the 1D mesh is built as an *edge path* in the 3D computational grid; a specific algorithm to extract such edge path from medical data is presented in the next chapter.

In *chapter 6*, we introduce specific models for tissue perfusion and mass transport in tissues. We take advantage of the theory presented in chapters 3 and 4, and use a *multiscale approach*: the 3D microvascular matrix is represented as an homogeneous medium, where larger vessels, described as 1D manifolds and possibly arranged in network structures, are supplying blood to the lower vascular hierarchies in the tissue. The major advantage of this approach is the reduced computational cost of simulations, at least with respect to a full 3D model of the vessel network. The low cost is also due to the fact that time scales split as well: typically blood flow is *fast* in the network of major vessels and *slow* in the microvascular matrix. Consequently, we can consider different time resolutions (*multirate schemes*) for the two scales, assigning a larger time step to the 3D part of the coupled model.

We discuss computational techniques, we propose algorithms to automatically extract the mesh of the 1D vessel network from the 3D tissue mesh and available data provided by medical imaging, and show applications in some cases of clinical interest dealing with blood perfusion and oxygen delivery to tissues (for instance the brain).

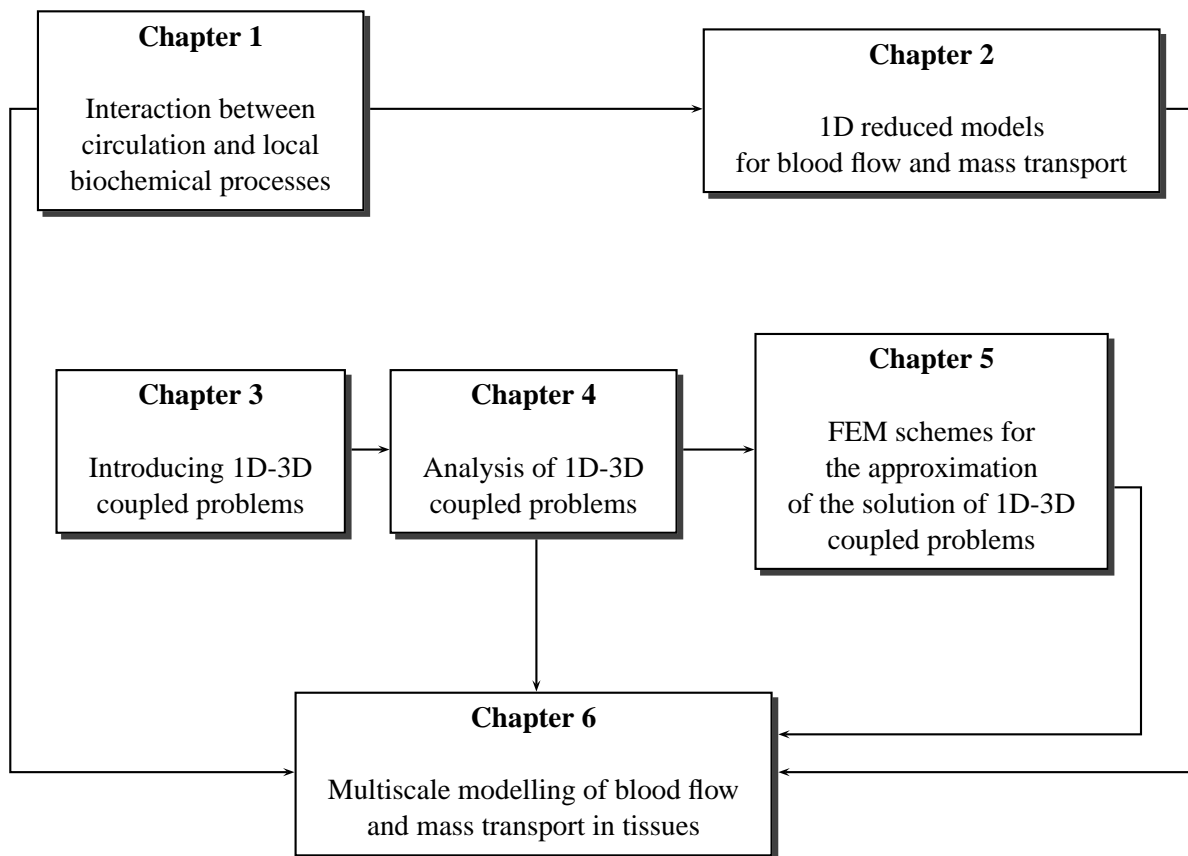


Figure 2: Thesis organization.

Chapter 1

Modelling the interaction between cardiovascular system and skeletal muscle metabolism

1.1 Introduction

The analysis of the physiological response of the human body to local variations in metabolism is a very complex subject. Despite a certain number of biochemical data, only a few mathematical models are available to provide quantitative descriptions of the coupling between hemodynamics and metabolism. Beyond doubt, the following aspects have important roles in the physiological adaptations:

- a) the biochemical processes in skeletal muscle;
- b) the substrate (oxygen, glucose, lactate, . . .) transfer between blood and tissues;
- c) the cardiovascular feedback with respect to arterial pressure and substrate concentrations (i.e. baroreflex and chemoreflex effect).

In this chapter¹ we consider the mathematical modelling of the interplay between blood flow and local biochemical reactions, especially under effort conditions. Very often the existing studies either focus on the cardiovascular part (as in [59]) or investigate the biochemical processes (see [52], [49], [53]); an integrative approach is developed in [12], however the topic of the autoregulation of the cardiovascular system is neglected. In the next sections, we first introduce the physiological framework of the problem and discuss the standard variables of interest, considering for instance an individual running on a treadmill or riding a cycloergometer; then we present the model, and finally we discuss the results of numerical simulations, comparing them with available data.

1.1.1 Cardiovascular parameters and auto-regulation

In a standard treadmill test, sport physicians usually measure some typical parameters related to *gas exchange*, like the *oxygen uptake* \dot{V}_{O_2} and the *carbon dioxide production* \dot{V}_{CO_2} . Both \dot{V}_{O_2} and \dot{V}_{CO_2} are mass transfer rates (they are expressed for instance in [$l \text{ min}^{-1}$]); their values are obtained by a

¹Part of this chapter has been published in the proceedings of CEMRACS 2004 [21].

digital system that samples the expired air, and measures chemical concentrations by mass spectrometry².

Among the other variables measured in such a test, there is *heart rate* HR , whose units are beats per minute $[\text{bpm}] = [\text{min}^{-1}]$. The heart rate is related to the *cardiac output* Q and the *stroke volume* V_{stroke} by the simple relation

$$Q = HRV_{\text{stroke}},$$

where Q (usually expressed in $[\text{l min}^{-1}]$) is the total volume of blood pumped by the heart through the circulatory system per unit time, and V_{stroke} is the volume of blood ejected at each heart contraction.

A normal value for cardiac output at rest is close to $5\text{-}6 \text{ l min}^{-1}$. This increases to approximately $15\text{-}25 \text{ l min}^{-1}$ in healthy adults at maximal exercise. Stroke volume ranges from approximately 80 ml during upright rest up to 130 ml during exercise. In elite endurance athletes however, stroke volumes can be as high as $180\text{-}200 \text{ ml}$. During dynamic exercise heart rate increases with respect to the workload and oxygen consumption [10]. Typically, heart rate ranges from $50\text{-}70 \text{ bpm}$ at rest up to $180\text{-}200 \text{ bpm}$ at maximal effort.

The measurement of substrate concentrations in blood is a more complex procedure: it is generally performed via catheter sampling. We denote the chemical concentrations by $[O_2]$, $[CO_2]$, and so on: an important role in exercise physiology is played by the blood concentration of O_2 in arteries, $[O_2]_a$, and in veins, $[O_2]_v$. The arterial-venous O_2 difference

$$\Delta_v^a[O_2] = [O_2]_a - [O_2]_v$$

is an index of the oxygen consumption by tissues (especially skeletal muscle). Chemical concentrations in blood are generally expressed in terms of molar values $[\text{mmol/l}]$ or fractional values $[\text{ml/l}]$. The arterial-venous oxygen difference is related to \dot{V}_{O_2} and Q by the following relationship

$$\dot{V}_{O_2} = Q\Delta_v^a[O_2],$$

which expresses the balance between oxygen intake and consumption.

We point out that it is possible to measure chemical concentrations *in tissues* as well, after a local biopsy; however, this is a rather complex procedure, so that *in vivo* data for human metabolism under effort conditions are difficult to obtain. Recently, MRI is becoming a powerful tool for non-invasive measurement of local metabolic demand [90]. Often the units associated to the concentration in a tissue are $[\text{mmol/kgdw}]$, where $[\text{kgdw}]$ means kg of dry weight of tissue.

In dynamic exercise the whole body arteriovenous oxygen difference $\Delta_v^a[O_2]$ increases with exercise intensity and oxygen consumption. Typically, $\Delta_v^a[O_2]$ ranges from $50 \text{ ml}(O_2)/\text{l}(\text{blood})$ at rest to approximately 150 ml/l during maximal exercise. Arterial oxygen content of approximately $200 \text{ ml}(O_2)/\text{ml}(\text{blood})$ does not change substantially with increasing exercise intensity but venous content falls considerably until approximately 85% of the oxygen is extracted at maximal effort. Moreover, at rest only a small percentage of the total capillaries in a given tissue are open, while during dynamic exercise the reduced oxygen concentration causes the arterioles and capillaries to dilate, and the opening of closed capillaries. This effect, called *chemoreflex*, provide more blood (and

²Generally one measures the fractional concentrations F_e of expired gases; this provides the pulmonary gas exchange rates, since the fractional concentrations of inspired gases F_i are known. For example,

$$\dot{V}_{O_2} = \dot{V}_e \left(F_{i,O_2} \frac{1 - F_{e,O_2} - F_{e,CO_2}}{F_{i,N_2}} - F_{e,O_2} \right),$$

where \dot{V}_e is the ventilation.

then more oxygen) to the tissues. It is a biochemical effect that involves the cardiovascular system, because it results in a dramatic fall in *hydrodynamic resistance*³ of the tissues fed by the circulatory system.

This high variability in the peripheral resistance of the small vessels influences the cardiac activity via the *baroreflex* effect, which is a physiological regulation system that maintains the arterial pressure in the large arteries close to a reference mean value (typically 90 – 100 mmHg). It consists of stretch receptors in most of the large arteries of the thorax and neck (especially the aortic arch and carotid sinus), which respond to changes and rate of change in pressure between 60 and 180 mmHg for the carotid and 90 and 210 mmHg in the aorta. The receptors act on the heart rate and on the heart contractility: for example, if the arterial pressure decreases, the *firing rate* (that is the nerve activity, expressed in impulses/second) of the aortic arch and carotid sinus increases, and this causes a rise in *HR* and in heart contractility (that is, as we will see, in V_{stroke}). The baroreflex effector controls also the peripheral resistance of the arterioles and capillaries, but during exercise the main effect is on the heart. The baroreflex is a very important feedback system because the arterial pressure is a vital parameter (if the blood pressure does fall, the oxygen partial pressure does; conversely, high pressures are related to cardiovascular diseases).

Typically, the oxygen fall in exercising tissues causes (via chemoreflex) a reduction in their hydrodynamic resistance and then in the overall systemic resistance; in turn, the baroreflex acts immediately to compensate the arterial pressure decrease. Hence, the mean arterial pressure does not change significantly (generally an increase up to 125 – 130 mmHg is observed), while the cardiac output does (see tab. 1.1). The functional structure of these interactions is represented in fig. 1.1.

Parameter	Rest	Exercise	$\Delta\%$
Cardiac output Q [$l \text{ min}^{-1}$]	6	21	+250%
Arterial Pressure P [mmHg]	90	105	+16.7%
Systemic resistance R [mmHg min l^{-1}]	15	5	-66.7%

Table 1.1: Differences in Q , P and $R = P/Q$ between rest and strenuous dynamic exercise.

To sustain physical activity for more than a few seconds requires dramatic circulatory adjustments to ensure adequate perfusion of the exercising skeletal muscle as well as of vital organs such as the heart and brain [35]: in fact, the demand of blood flow in a large volume of exercising muscle can approximate the maximal cardiac output [92]. Thus, the cardiovascular system has to control the delicate balance between pressure regulation and oxygen delivery, being the *redistribution* of the blood flow to each tissue affected by the local state of vessel dilatation and number of open capillaries (as reported in tab. 1.2). The exact mechanisms involved in this integrated process are not entirely known. It is established that hemodynamic adaptations to exercise are mediated by a decrease in parasympathetic and an increase in sympathetic activity controlled both by feed-forward stimuli from increased central drive (due to the voluntary muscle contraction) and by feedback arising from mechanically and metabolically sensitive afferent nerve endings in the large arteries and contracting skeletal muscles.

³We recall the Poiseuille's law for a cylindrical tube. If a pressure jump ΔP is applied between the inlet and the outlet, the flow rate is given by

$$Q = \frac{\Delta P}{R}, \quad R = \frac{8\eta l}{\pi r^4},$$

where l is the tube length, r the section radius, and η the blood viscosity. R is called haemodynamic resistance, as if the tube were an electrical resistance (in which Q is a current and ΔP a voltage).

Organ i	Q_i (ml min ⁻¹), rest	Q_i/Q %	Q_i (ml min ⁻¹), exercise	Q_i/Q %
Brain	650	13	750	4
Heart	215	4	750	4
Skeletal Muscle	1030	20	12500	73
Skin	430	9	1900	11
Kidney	950	20	600	3
Splanchnic Organs	1200	24	600	3
Others	545	10	400	2
Total	5000	100	17500	100

Table 1.2: Flow rates at rest and at strenuous dynamic exercise [34] .

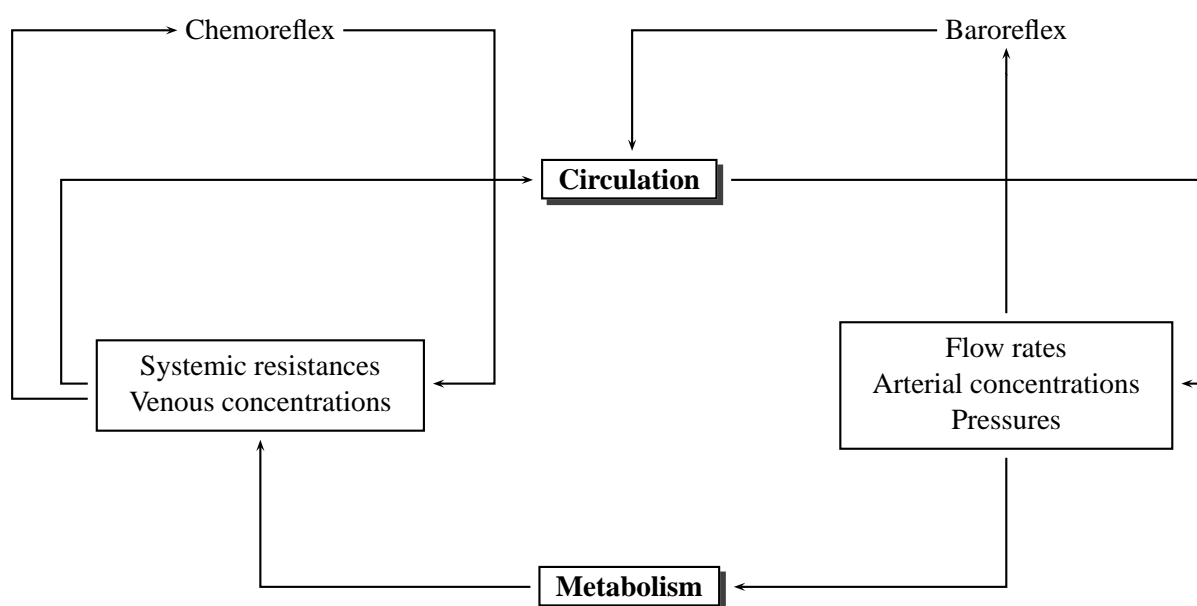


Figure 1.1: Functional representation of the interaction between circulation and metabolism.

1.1.2 Gas exchange and ventilation

If $\dot{V}_{O_2} = \dot{V}_{O_2}(t)$ is measured during an exercise consisting of an increasing workload, the time course shows a maximal oxygen uptake $\dot{V}_{O_{2max}}$ that cannot be exceeded. For young subjects, this plateau is usually 10-20 times the basal \dot{V}_{O_2} uptake and it can be increased by appropriate training in high-fit up to 20-22 times the basal \dot{V}_{O_2} .

This maximal oxygen uptake is an useful (even if somehow imperfect) predictor of the ability to perform prolonged dynamic external work or, more specifically, of endurance athletic performance, because in this case the energy currency of muscles is the aerobic one. In principle, as there are several physiological mechanisms controlling the ventilation, we should consider a model of gas exchange; nevertheless, for healthy people the limiting factor to aerobic performances is determined not by lungs (as the concentration gradient between the alveolar oxygen and the venous one is often high enough to saturate the arterial blood, even at a very high cardiac output), but rather by the cardiovascular system. In fact, as described in tab. 1.3, we can observe that the arterial partial pressures P_{O_2} and P_{CO_2} are

Exercise intensity	\dot{V}_e (l min ⁻¹)	P_{O_2} (mmHg)	P_{CO_2} (mmHg)	Blood pH
Rest	5	103	36	7.40
Walking	20	103	36	7.40
Jogging	45	106	44	7.40
Running fast	75 - 44	110	44	7.32

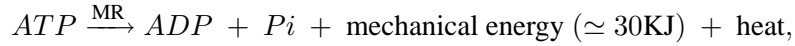
Table 1.3: Acute respiratory response to graded dynamic exercise in a 30-year-old untrained woman.

almost the same at rest and under effort conditions. Hence, in this chapter we do not consider a ventilation model and we suppose that $[O_2]_a$ and $[CO_2]_a$ are constant.

In tab. 1.3 a decrease in blood pH (acidosis) with respect to exercise intensity is observed. From the midway point between $\dot{V}_{O_2\text{rest}}$ and $\dot{V}_{O_2\text{max}}$, lactic acid begins to accumulate in blood. This point, which depends on the type of work involved and on the level of fitness of the subject, is called *lactate threshold*. Lactate concentration gradually rises with work intensity, as more and more muscle fibers must rely on anaerobic metabolism: this causes metabolic acidosis, which is partially responsible for muscle fatigue.

1.1.3 Metabolism

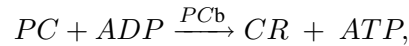
Several chemicals are involved in muscle contraction: a large number of reactions take place in each fiber in order to transform the chemical energy of certain molecular bounds to mechanical work. In particular, this is obtained from *ATP* (adenosine triphosphate) breakdown as follows:



where *Pi* is an inorganic phosphate group, and *ADP* is the molecule of adenosine diphosphate. We denote by MR the *metabolic rate*, that is the rate at which *ATP* is converted to *ADP* in the skeletal muscle tissue (expressed in [mmol/ s]). As muscle contractions rely completely on the former reaction, MR is related to the power output during exercise. Actually, the amount of the mechanical energy available for muscular work obtained from *ATP* breakdown is not always equal to 30KJ: it depends on the exercise level [50], so that the relationship between MR and power output is generally nonlinear.

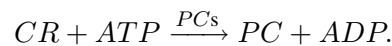
Several reactions act to sustain the energy production in cells by restoring *ATP* (see [37]): following [11], we will assume the metabolic pathways described below.

1. **Phosphocreatine breakdown:** this is the most important pathway for short-term *ATP* production. The reaction is

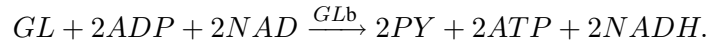


where creatine (*CR*) and *ATP* are produced from phosphocreatine (*PC*) and *ADP*. We denote by *PCb* this reaction. As a source of *ATP*, the phosphagen system can only supply a cell for 8 to 10 seconds during the most strenuous exercise; then the *PC* concentration becomes too small for sustaining the reaction.

2. **Phosphocreatine synthesis (*PCs*):** this is the inverse pathway of *PCb*, and allows to restore the *PC* stores using *ATP*:

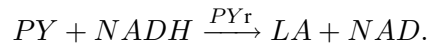


3. **Anaerobic glycolysis** (GLb). The overall stoichiometry of glycolysis is the following one (we denote it by GLb , or glucose breakdown):



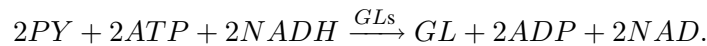
Like most chemical reactions, glycolysis slows down as its products, pyruvic acid PY and the reduced coenzyme $NADH$, build up.

4. **Pyruvate reduction** (PYr). In order to speed up the glycolysis, pyruvate can be reduced and converted to lactate:



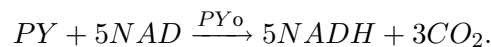
Lactic acid itself eventually builds up, slowing metabolism and contributing to muscle fatigue.

5. **Gluconeogenesis** (GLs) In splanchnic organs (namely in the liver) pyruvate can be converted back to glucose:

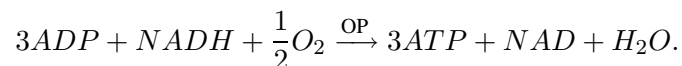


This pathway is not observed in skeletal muscle.

6. **Pyruvate oxidation** (PYo). This pathway allows to metabolize the pyruvic acid aerobically. Pyruvic acid is converted to a molecule called acetyl group and put into the *Krebs cycle*, from which high energy electrons are released to NAD :

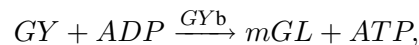


7. **Oxidative phosphorylation**. The high energy electrons obtained by the oxidation of PY are sent to a process within the mitochondria known as the *electron transport chain* which produces ATP , the waste products being CO_2 and H_2O :

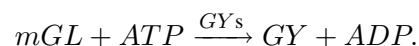


This reaction will be denoted by OP (oxidative phosphorylation). In this process, O_2 is one of the reactants: this reaction is responsible for the high oxygen demand of tissues during exercise.

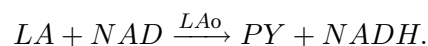
8. **Glycogen synthesis and breakdown** (GYs , GYb): skeletal muscle and liver contain a certain store of glycogen (GY), a big molecule that is a sort of gathering of several glucose molecules. Glycogen can provide glucose by the following reaction:



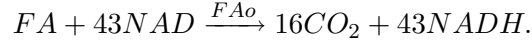
where m is the number of GL molecules in one GY molecule. However, GY can be restored from GL via the following pathway



9. **Lactate oxidation** (LAo): this is the inverse reaction of PYr . Pyruvate can be produced starting from lactate:



10. **Free Fatty Acid oxidation (FAo):** cells can oxidize free fatty acids (FA) to provide *NADH* to the electron transport chain. The stoichiometry of this reaction is the following one:



The main biochemical pathways we consider are depicted in fig. 1.2. We remark that there are some

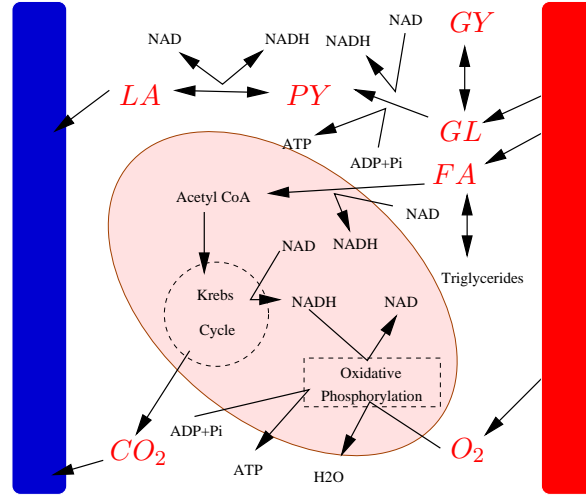


Figure 1.2: Sketch of the main metabolic pathways.

chemicals that are *transported* by the blood, and other chemicals that are not. We assume that *PC*, *CR*, *ADP*, *ATP*, *NAD*, *NADH* and *GY* are not transported; they are produced and consumed within the tissue.

1.2 Cardiovascular Model (CVM)

A cardiovascular model (CVM) is needed to compute the blood flow and the substrate flux delivered to the different organs/tissues. In this chapter, we adopt a *compartmental* description of the processes of interest: our CVM will be a simple system of ordinary differential equations. We will take into account the systemic circulation, but not the pulmonary one. The model scheme is depicted in fig. 1.3: the block RH/L/LH represents the right heart, the pulmonary circulation with the lungs, and the left heart. The left ventricle pumps the blood in the main arteries with a flow rate Q_a (corresponding to the cardiac output Q). The main arteries are represented by a compliance C_a ⁴ and a resistance R_a , that is the arterial pressure P_a obeys the equation

$$C_a \frac{dP_a}{dt} = Q_a - \frac{P_a - P_s}{R_a}, \quad (1.1)$$

being P_s the mean blood pressure between the main arteries and the capillary bed of tissues (systemic pressure). The tissues include a global systemic compliance C_s and a resistance. In the sequel we will consider three compartments with different metabolic activities:

⁴We refer to [46] for the description of vessel compliance: basically, we linearize the mechanical behaviour of the vessels and introduce a constant C such that the volume variations of blood in the considered compartment are proportional to the pressure, that is $V = V_u + CP$, where V_u is the unstressed volume (constant).

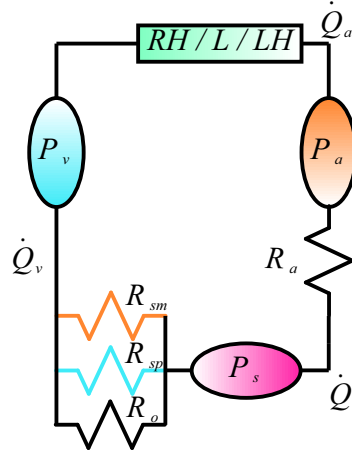


Figure 1.3: Scheme of a reduced circulatory system.

1. the *skeletal muscle* compartment, with resistance R_{sm} and blood flow rate Q_{sm} ;
2. the *splanchnic* compartment, with resistance R_{sp} and blood flow rate Q_{sp} ;
3. a compartment representing *other organs*, with resistance R_o and blood flow rate Q_o .

Introducing the venous pressure P_v and the venous compliance C_v , we are able to express the flow rate in each compartment as

$$Q_i = \frac{P_s - P_v}{R_i}, \quad i \in \{sm, sp, o\}. \quad (1.2)$$

Moreover, we have the following equation for the systemic pressure:

$$C_s \frac{dP_s}{dt} = \frac{P_a - P_s}{R_a} - \frac{P_s - P_v}{R_s}, \quad (1.3)$$

being R_s the total systemic resistance:

$$R_s = \left(\frac{1}{R_{sm}} + \frac{1}{R_{sp}} + \frac{1}{R_o} \right)^{-1}. \quad (1.4)$$

By the conservation of the total mass of blood, the venous pressure P_v is linearly dependent on P_a and P_s : if V_0 and V_u is the total and unstressed volume of blood, we have

$$C_v P_v = V_0 - V_u - C_a P_a - C_s P_s. \quad (1.5)$$

Equations (1.1, ..., 1.5) can be recast in a set of two first-order linear ordinary differential equations, once the cardiac output $Q_a(t)$ is given. As we know from the previous section, Q_a is related to heart rate and stroke volume by

$$Q_a = HR V_{\text{stroke}}, \quad (1.6)$$

and both HR and V_{stroke} are under the control of the sympathetic and parasympathetic activities. We assume

$$V_{\text{stroke}} = V_{e, \text{dia}}(P_v) - V_{u, \text{vent}} - \frac{P_a}{E}, \quad (1.7)$$

where $V_{e,dia}$ is the end-diastolic ventricular volume (which is a known function of the venous pressure, [107]), $V_{u,vent}$ is the unstressed ventricular volume, and E is the ventricular *elastance*. Defining the heart period $T = 1/HR$, we follow [101] and assume

$$\tau_T \frac{dT}{dt} = T_0 - T - \sigma_{T,s}(f_{es}) + \sigma_{T,v}(f_{ev}), \quad (1.8)$$

$$\tau_E \frac{dE}{dt} = E_0 - E - \sigma_E(f_{es}), \quad (1.9)$$

$$f_{es} = f_{es,\infty} + (f_{es,0} - f_{es,\infty})e^{-k_{es}f_{cs}}, \quad (1.10)$$

$$f_{ev} = \frac{f_{ev,0} + f_{ev,\infty} \exp((f_{cs} - f_{cs,0})/k_{ev})}{1 + \exp((f_{cs} - f_{cs,0})/k_{ev})}, \quad (1.11)$$

$$f_{cs} = \frac{f_{min} + f_{max} \exp((\tilde{P}_a - P_n)/k_a)}{1 + \exp((\tilde{P}_a - P_n)/k_a)}, \quad (1.12)$$

where $\sigma_{T,s}$, $\sigma_{T,v}$ and σ_E are monotonically increasing functions, P_n is the *reference pressure* value (for example 100 mmHg), \tilde{P}_a is a zero-pole filtering of the arterial pressure,

$$\tau_p \frac{d\tilde{P}_a}{dt} = P_a - \tilde{P}_a + \tau_z \frac{dP_a}{dt}, \quad (1.13)$$

and f_{es} , f_{ev} , f_{cs} are respectively the *efferent sympathetic* activity, *efferent vagal* activity and the *carotid sinus firing rate*. In this way the baroreflex control on the heart rate and elastance is taken into account: if we consider a low-frequency regime, we have $\tilde{P}_a \simeq P_a$, and f_{cs} increases with respect to the arterial pressure. Thus, equations (1.8,1.9) represent a feedback system that acts on the arterial pressure P_a to get it close to the reference value P_n . For example, if P_a is small, then $dT/dt < 0$ and $dE/dt < 0$, and the cardiac output increases; this in turn causes the rise of P_a toward the equilibrium point P_n .

If the hydrodynamic resistances of tissues were known, equations (1.1,...,1.13) would form a closed linear dynamical system with 5 state variables $P_a, P_s, T, E, \tilde{P}_a$. However, the vagal activity and chemoreflex effect do influence the tissue resistances, so that we have to consider more state variables. We model the chemoreflex as in [101], that is we define for $i \in \{sm, sp, o\}$:

$$\tau_{\tilde{R}_i} \frac{d\tilde{R}_i}{dt} = \tilde{R}_{i,0} - \tilde{R}_i + \sigma_{\tilde{R}_i}(f_{es}), \quad (1.14)$$

and then we follow an approach similar to [102], considering

$$\begin{aligned} R_{sm} &= \frac{\tilde{R}_{sm}}{1 + x_{sm}}, \\ R_{sp} &= \tilde{R}_{sp}(1 + x_{sp}), \\ R_o &= \frac{\tilde{R}_o}{1 + x_o}, \end{aligned} \quad (1.15)$$

where x_i , $i \in \{sm, sp, o\}$, are new variables, that are supposed to be affected by the chemoreflex activity f_{cm} :

$$\tau_{x_i} \frac{dx_i}{dt} = x_{i,0} - x_i + G_{x_i} f_{cm}, \quad i \in \{sm, sp, o\}, \quad (1.16)$$

where G_{x_i} are positive constants. The chemoreflex effector $f_{cm} = f_{cm}([O_2]_{sm})$ is a non-increasing function of the oxygen concentration in the skeletal muscle tissue; by (1.16) and (1.15), the lower the

Compliances and unstressed blood volumes:		
$C_a = 0.3 \text{ ml/mmHg}$	$C_s = 3 \text{ ml/mmHg}$	$C_v = 61.11 \text{ ml/mmHg}$
$V_0 = 5300 \text{ ml}$	$V_u = 4700 \text{ ml}$	$V_{u,vent} = 16.77 \text{ ml}$
Vagal and sympathetic activity parameters in eq. (1.9-1.12): as in [101], where for $\theta \in \{T_s, E, \tilde{R}_{sm}, \tilde{R}_{sp}, \tilde{R}_o\}$:		
$\sigma_\theta(f_{es}) = \begin{cases} G_\theta \ln(f_{es} - f_{es,min} + 1) & \text{if } f_{es} > f_{es,min} \\ 0 & \text{otherwise} \end{cases}$, and:		
$\sigma_{T,v}(f_{ev}) = G_{T,v} f_{ev}$.		
$T_0 = 0.02 \text{ s}$	$\tau_T = 2 \text{ s}$	$G_{T,s} = 0.52 \text{ s}^2$
		$G_{T,v} = 0.26 \text{ s}^2$
$E_0 = 1.69 \text{ mmHg/ml}$	$\tau_E = 2 \text{ s}$	$G_E = 0.2 \text{ s} \cdot \text{mmHg/ml}$
$\tilde{R}_{sm,0} = 0.6 \text{ mmHg} \cdot \text{s/ml}$	$\tau_{\tilde{R}_{sm}} = 10 \text{ s}$	$G_{\tilde{R}_{sm}} = 5.5 \text{ mmHg} \cdot \text{s}^2/\text{ml}$
$\tilde{R}_{sp,0} = 1 \text{ mmHg} \cdot \text{s/ml}$	$\tau_{\tilde{R}_{sp}} = 10 \text{ s}$	$G_{\tilde{R}_{sp}} = 3.5 \text{ mmHg} \cdot \text{s}^2/\text{ml}$
$\tilde{R}_{o,0} = 0.6 \text{ mmHg} \cdot \text{s/ml}$	$\tau_{\tilde{R}_o} = 10 \text{ s}$	$G_{\tilde{R}_o} = 1.5 \text{ mmHg} \cdot \text{s}^2/\text{ml}$
$x_{sm,0} = 1$	$\tau_{x_{sm}} = 1 \text{ s}$	$G_{x_{sm}} = 6 \text{ s}$
$x_{sp,0} = 1$	$\tau_{x_{sp}} = 1 \text{ s}$	$G_{x_{sp}} = 0.04 \text{ s}$
$x_{o,0} = 1$	$\tau_{x_o} = 1 \text{ s}$	$G_{x_o} = 1 \text{ s}$
Chemoreflex activity and P_n shifting:		
$k_{cm} = 0.25 \text{ kgdw}^2/\text{mmol}^2/\text{s}$	$[O_2]_{sm}^0 = 6 \text{ mmol/kgdw}$	
$P_{n,0} = 92 \text{ mmHg}$	$\tau_{P_n} = 10 \text{ s}$	$G_{P_n} = 10 \text{ s} \cdot \text{mmHg}$

Table 1.4: Cardiovascular model parameters.

oxygen concentration in exercising tissues, the lower their resistance and the higher the splanchnic resistance. In particular, we found a good agreement with standard data (i.e. those of tab. 1.2) with a quadratic dependence of f_{cm} on the oxygen concentration (which is a compromise between the linear [102] and the exponential [58] case):

$$f_{cm} = \begin{cases} 0 & \text{if } [O_2]_{sm} > [O_2]_{sm}^0 \\ k_{cm}([O_2]_{sm}^0 - [O_2]_{sm})^2 & \text{otherwise} \end{cases}, \quad (1.17)$$

where $[O_2]_{sm}^0$ is a fixed threshold value for the oxygen concentration.

As pointed out in [71], [72], the response of baroreflex effector to the increased metabolic rate can be described by a *shifting* of the reference value P_n of the sigmoid curve $f_{cs} = f_{cs}(\tilde{P}_a)$ defined by (1.12). We included this effect in our model considering P_n as a state variable affected by the chemoreflex:

$$\tau_{P_n} \frac{dP_n}{dt} = P_{n,0} - P_n + G_{P_n} f_{cm}. \quad (1.18)$$

Equations (1.1,...,1.18) form our final global cardiovascular model. We point out that in these equations $[O_2]_{sm}$ is an *input variable*; in other words we need a *tissue metabolism model* (TMM) in order to provide this variable to the cardiovascular model (CVM). The CVM and TMM shall be coupled via the oxygen concentrations (TMM \rightarrow CVM) and the flow rates (CVM \rightarrow TMM). In tab. 1.2 the parameters for “standard” healthy individuals (rest heart rate 60 bpm, rest cardiac output 5 l min^{-1} , ...) are reported (being the undefined values as in [101]); however, they have to be slightly adjusted when simulations are carried out for different subjects (we will present an example in the section devoted to the numerical results).

1.3 Tissue Metabolism Model (TMM)

We will deal with two kinds of metabolism models. The former is very simple as the only chemical considered is oxygen. The second one is more detailed and describes several chemical pathways (see section 1.1.3) that allows to account for the dynamic of a number of metabolites, such as *PC*, *GL*, *LA* and so on.

1.3.1 Arterial and venous concentrations

The concentration of any chemical in the venous blood is strongly related to the concentration of that chemical in the upstream tissue. As in [11], [12], we will assume a linear relation between venous and tissue concentration, that is, for each metabolite C we assume

$$[C]_{v,i} = \sigma_i^C [C]_i, \quad (1.19)$$

being $[C]_{v,i}$ the venous concentration downstream the i -th tissue, $[C]_i$ the concentration in the tissue, and σ_i^C the *partition coefficient* of the chemical C . The mean venous concentration $[C]_v$ in blood is obtained imposing the mass conservation, that is:

$$[C]_v = \sum_{i \in \{sm, sp, o\}} \frac{Q_i}{Q_a} [C]_{v,i}. \quad (1.20)$$

As previously discussed, we assume that the only chemical species affected by the pulmonary circulation are O_2 and CO_2 ; according to tab. 1.3, their arterial concentrations are constant. For the remaining chemicals, we assume no mass exchange in the pulmonary circulation. In short:

$$\begin{aligned} [C]_a &= [C]_v, & C \notin \{O_2, CO_2\}; \\ [C]_a &= [C]_a^0, & \text{otherwise.} \end{aligned} \quad (1.21)$$

1.3.2 One-chemical model

A simple metabolism model is the one in which only oxygen is taken into account. If the rate of oxygen consumption in a certain tissue is known, we can assume the following balance equation for the oxygen concentration:

$$V_i \frac{d[O_2]_i}{dt} = -OP_i(t) + Q_i(t)([O_2]_{a,i} - \sigma_i^{O_2} [O_2]_i), \quad (1.22)$$

where V_i is the “volume⁵” or mass of the tissue (depending on the units used for concentrations), $[O_2]_i$ is the O_2 concentration in compartment i , OP_i is the oxygen consumption rate (the oxygen consumed by the oxidative phosphorylation per unit time), Q_i is the blood flow rate, $[O_2]_{a,i}$ is the arterial concentration of O_2 , and $\sigma_i^{O_2}$ is the oxygen partition coefficient. The resting metabolic rate OP_i^0 is usually known, as well as the resting arterial and tissue concentrations $[O_2]_{a,i}^0$ and $[O_2]_i^0$, and the mean resting flow rate Q_i^0 . Thus, $\sigma_i^{O_2}$ can be estimated by the following balance equation at rest:

$$\sigma_i^{O_2} = \frac{[O_2]_{a,i}^0 - OP_i^0 / Q_i^0}{[O_2]_i^0}.$$

⁵Very often, being the available physiological data for $[O_2]_i$ expressed in mmol kg^{-1} or mmol kgdw^{-1} (where kgdw means “kg of dry tissue”) V_i is not a volume; it is rather a weight (or a dry weight).

Another way to estimate the partition coefficient is to set directly

$$\sigma_i^{O_2} = [O_2]_{v,i}^0 / [O_2]_i^0,$$

where $[O_2]_{v,i}^0$ is the resting venous oxygen concentration: the two approaches have to give about the same results.

1.3.3 General multi-chemical model

In order to take into account the interaction between several chemicals and substrates in tissues, and to obtain a more detailed description of the skeletal muscle bioenergetics, we have to consider more complex multi-chemical metabolism models based on the main pathways described in section 1.1.3. In metabolic control analysis (see [39],[89]), pathways are represented by associating a *reaction rate* ψ_R to each reaction R . A reaction rate is a function of the chemical concentrations (and of time) which represents the molar consumption of a reference substrate in R per unit time (mmol sec^{-1}). To each reaction R presented in sec. 1.1.3, we associate a reference reactant (tab. 1.5), and we define ψ_R as the molar consumption rate of that chemical by that reaction.

Reaction	Reactant	Reaction	Reactant	Reaction	Reactant
PCb	PC	PCs	CR	GLb	GL
PYr	PY	GLs	PY	PYo	PY
OP	O_2	GYs	GL	GLs	GY
LAo	LA	FAo	FA		

Table 1.5: Reactions and associated reactant.

For each compartment i , we define a *state vector* \mathbf{c}_i consisting of the chemical concentrations of metabolites we are interested in, and a *reaction rate vector* $\boldsymbol{\psi}_i$ whose components are the reaction rates of all the reactions.

The explicit expression of $\boldsymbol{\psi}_i$ may be given in a different way for each compartment i , and state vectors referring to distinct compartments may include distinct metabolites.

The stoichiometry of the chemical reactions is taken into account by means of a *stoichiometric matrix* \mathbf{A}_i (an example is shown in tab. 1.7 for $i = sm$) such that the element $(\mathbf{A}_i)_{hk}$ is the (signed) number of produced molecules of the h^{th} metabolite when one molecule of the reactant associated to the k^{th} reaction is consumed. For example, if ψ_{PYo} is the rate at which PY is consumed by pyruvate oxidation, we have that -1 and 5 are the corresponding stoichiometric coefficients for respectively PY and $NADH$ (because for each consumed molecule of the associate reactant PY , -1 molecules of PY and 5 molecules of $NADH$ are *produced*).

In this manner, the conservation of the mass of each chemical reads as the following system of (nonlinear) differential equations:

$$V_i \frac{d\mathbf{c}_i}{dt} = \mathbf{A}_i \boldsymbol{\psi}_i(\mathbf{c}_i, t) + \mathbf{b}_i(\mathbf{c}_i, \mathbf{c}_a, Q_i, t), \quad (1.23)$$

where V_i is the tissue mass of the i -th compartment, \mathbf{c}_a is the vector of the *arterial concentrations* of chemicals transported by blood flow, and $\mathbf{b}_i(\mathbf{c}_i, \mathbf{c}_a, Q_i, t)$ is the *transport term*. This term is given by $Q_i(\mathbf{c}_a - \mathbf{c}_v)$, where \mathbf{c}_v is the vector of *venous concentrations*, expressed as a function of \mathbf{c}_a and \mathbf{c}_i . This is a quite general paradigm for a metabolism model, where the *state variables* are the chemical

concentrations in the tissue, and the arterial concentrations and the flow rate play the role of *input variables*. For instance, it is possible [11] to define $\mathbf{c}_v = \boldsymbol{\sigma}_i \cdot \mathbf{c}_i$, where the dot means componentwise vector product, and $\boldsymbol{\sigma}_i = (\sigma_i^{PC}, \dots, \sigma_i^{CO_2})^T$ is the vector of the partition coefficients. Therefore, the transport term reads

$$\mathbf{b}_i(\mathbf{c}_i, \mathbf{c}_a, Q_i, t) = Q_i(\mathbf{c}_a - \boldsymbol{\sigma}_i \cdot \mathbf{c}_i), \quad (1.24)$$

Depending on each compartment i , the concentration of metabolites which are transported by blood might not appear as a state variable in \mathbf{c}_i . In that case, the metabolite venous concentration downstream the tissue has to be defined *a priori*.

The most general form of system (1.23) is presented in tab. 1.6, where all the metabolites are considered, and b_{PC}, \dots, b_{CO_2} denote the components of \mathbf{b}_i . Being particularly interested in skeletal muscle bioenergetics, for the sm compartment we will adopt the full set of equations of tab. 1.6, while for other compartments a reduced set of chemicals (and, correspondingly, of equations) will be considered.

$$\begin{aligned} V d[PC]/dt &= PCs - PCb + b_{PC}, \\ V d[GL]/dt &= GLs - GLb - GYs + mGYb + b_{GL}, \\ V d[PY]/dt &= 2GLb - 2GLs - PYr - PYo + LAo + b_{PY}, \\ V d[GY]/dt &= \frac{1}{m}GYs - GYb + b_{GY}, \\ V d[LA]/dt &= PYr - LAo + b_{LA}, \\ V d[FA]/dt &= -FAo + b_{FA}, \\ V d[ADP]/dt &= PCs - PCb - 2GLb + 2GLs - 6OP + \frac{1}{m}GYs - GYb + MR + b_{ADP}, \\ V d[NADH]/dt &= 2GLb - 2GLs - PYr + 5PYo + LAo - 2OP + 43FAo + b_{NADH}, \\ V d[O_2]/dt &= -OP + b_{O_2}, \\ V d[CO_2]/dt &= 3PYo + 16FAo + b_{CO_2}, \\ &\text{and} \\ [CR](t) &= [CR](0) + [PC](0) - [PC](t), \\ [ATP](t) &= [ATP](0) + [ADP](0) - [ADP](t), \\ [NAD](t) &= [NAD](0) + [NADH](0) - [NADH](t). \end{aligned}$$

Table 1.6: Metabolism kinetics (we omitted the subscripts). Concentrations $[CR]$, $[ATP]$ and $[NAD]$ do not belong to the vector state because each of the sums $[CR] + [PC]$, $[ATP] + [ADP]$ and $[NAD] + [NADH]$ is constant.

Skeletal muscle compartment

As in [11] we assume that in skeletal muscle ($i = sm$) Michaelis-Menten laws hold for the reaction rates. These reaction rates are controlled by the *phosphorylation state* PS and the *redox state* RS , where

$$PS = \frac{[ADP]_{sm}}{[ATP]_{sm}}, \quad RS = \frac{[NADH]_{sm}}{[NAD]_{sm}}.$$

It is known [11] that the higher PS , the higher the reaction rate of the ATP producing pathways; analogously, the higher RS , the higher the reaction rate of the NAD producing pathways. We con-

sider in the state equation the full set of metabolites: tab. 1.7 shows the related state vector, reaction rate vector, stoichiometric matrix and transport vector. We remark that a few chemicals are not transported (namely PC , GY , ADP , $NADH$) and, accordingly, their arterial concentration and partition coefficient are both zero. The complete set of reaction rates is presented in tab. 1.8: moreover we assume $GLs_{sm} = 0$ as discussed in section 1.1.3.

In the Michaelis-Menten laws there are parameters which are not provided by experiments. In fact, in each reaction R we have a *maximal rate* coefficient ϕ_R and one or more characteristic constants k_R : these coefficients are not known *a priori*, except in a few cases. Therefore, *parameter identification* is mandatory in order to find the coefficients that reproduce the dynamic of the metabolic pathways fitting the available physiological data, and this will be the subject of the last part of this chapter.

$$\begin{aligned}
 \mathbf{c}_{sm} &= [[PC]_{sm}, [GL]_{sm}, [PY]_{sm}, [LA]_{sm}, [GY]_{sm}, [FA]_{sm}, [ADP]_{sm}, [NADH]_{sm}, [O_2]_{sm}, [CO_2]_{sm}]^T, \\
 \psi_{sm} &= [PCb_{sm}, PCs_{sm}, GLb_{sm}, GLs_{sm}, GYs_{sm}, GYb_{sm}, PYr_{sm}, LAo_{sm}, PYo_{sm}, OP_{sm}, FAo_{sm}, MR_{sm}]^T, \\
 \mathbf{A}_{sm} &= \begin{bmatrix} -1 & 1 & 0 & 0 & 0 & 0 & 0 & 0 & 0 & 0 & 0 \\ 0 & 0 & -1 & 1 & -1 & 10 & 0 & 0 & 0 & 0 & 0 \\ 0 & 0 & 2 & -2 & 0 & 0 & -1 & 1 & -1 & 0 & 0 \\ 0 & 0 & 0 & 0 & 0 & 0 & 1 & -1 & 0 & 0 & 0 \\ 0 & 0 & 0 & 0 & 1/m & -1 & 0 & 0 & 0 & 0 & 0 \\ 0 & 0 & 0 & 0 & 0 & 0 & 0 & 0 & 0 & 0 & -1 \\ -1 & 1 & -2 & 2 & 1/m & -1 & 0 & 0 & 0 & -6 & 0 \\ 0 & 0 & 2 & 2 & 0 & 0 & -1 & 1 & 5 & -2 & 43 \\ 0 & 0 & 0 & 0 & 0 & 0 & 0 & 0 & 0 & -1 & 0 \\ 0 & 0 & 0 & 0 & 0 & 0 & 0 & 0 & 0 & 3 & 0 & 16 \end{bmatrix}, \quad \mathbf{b}_{sm} = Q_{sm} \begin{bmatrix} 0 \\ [GL]_a - \sigma_{sm}^{GL} [GL]_{sm} \\ [PY]_a - \sigma_{sm}^{PY} [PY]_{sm} \\ [LA]_a - \sigma_{sm}^{LA} [LA]_{sm} \\ 0 \\ [FA]_a - \sigma_{sm}^{FA} [FA]_{sm} \\ 0 \\ 0 \\ [O_2]_a - \sigma_{sm}^{O_2} [O_2]_{sm} \\ [CO_2]_a - \sigma_{sm}^{CO_2} [CO_2]_{sm} \end{bmatrix}
 \end{aligned}$$

Table 1.7: State vector \mathbf{c}_{sm} , reaction rate vector ψ_{sm} , stoichiometric matrix \mathbf{A}_{sm} and transport vector \mathbf{b}_{sm} in eq. (1.23) for $i = sm$. Notice the zero terms in \mathbf{b}_{sm} corresponding to chemicals for which we neglect the transport by blood.

Splanchnic compartment

Splanchnic organs, as liver, provide glucose and free fatty acids when the body needs them. They may also convert pyruvate in glucose ($GLs_{sp} \neq 0$). As splanchnic organs metabolism is not strongly affected by PC , ADP and $NADH$ as the skeletal muscle metabolism is, we consider as state variables only the concentrations of GL , GY , PY , LA , FA , O_2 and CO_2 . Moreover, we don't have to specify their venous concentrations, since we assume that PC , ADP and $NADH$ are not transported by blood.

Finally, we assume *linear reaction rates*: the corresponding expressions are listed in tab. 1.9. As for the skeletal muscle tissue, the coefficients of these expressions have to be (at least partially) estimated by means of parameter identification techniques.

Reaction	Stoichiometry	Rate
PC_s	$CR + ATP \longrightarrow PC + ADP$	$\phi_{PC_s} \frac{1}{PS/k_{PC_s} + 1} [CR]$
PC_b	$PC + ADP \longrightarrow CR + ATP$	$\phi_{PC_b} \frac{PS}{PS + k_{PC_b}} [PC]$
GL_b	$GL + 2ADP + 2NAD \longrightarrow 2PY + 2ATP + 2NADH$	$\phi_{GL_b} \frac{PS}{PS + k_{GL_b}^{PS}} \frac{1}{RS/k_{GL_b}^{RS} + 1} [GL]$
GY_s	$mGL + ATP \longrightarrow GY + ADP$	$\phi_{GY_s} \frac{1}{PS/k_{GY_s} + 1} [GL]$
GY_b	$GY + ADP \longrightarrow mGL + ATP$	$\phi_{GY_b} \frac{PS}{PS + k_{GY_b}} [GY]$
PY_r	$PY + NADH \longrightarrow LA + NAD$	$\phi_{PY_r} \frac{RS}{RS/k_{PY_r} + 1} [PY]$
LA_o	$LA + NAD \longrightarrow PY + NADH$	$\phi_{LA_o} \frac{1}{RS/k_{LA_o} + 1} [LA]$
PY_o	$PY + 5NAD \longrightarrow 5NADH + 3CO_2$	$\phi_{PY_o} \frac{1}{RS/k_{PY_o} + 1} [PY]$
OP	$3ADP + NADH + \frac{1}{2}O_2 \longrightarrow 3ATP + NAD + H_2O$	$V_{O_2}^{\max} \frac{RS}{RS + k_{OP}} \frac{1}{1 + \left(\frac{K_{ADP}}{[ADP]}\right)^n} [O_2]$
FA_o	$FA + 43NAD \longrightarrow 16CO_2 + 43NADH$	$\phi_{FA_o} \frac{1}{RS/k_{FA_o} + 1} [FA]$
MR	$ATP \longrightarrow ADP + \text{energy}$	$MR(t)$

Phosphorylation state: $PS = [ADP]/[ATP]$
Redox state: $RS = [NADH]/[NAD]$

Table 1.8: Reaction rates for the skeletal muscles (the subscript $i = sm$ is omitted).

Other organs

In the third compartment $i = o$, that represents the remaining tissues, we assume that metabolite concentrations are known. Consequently, the venous content downstream the compartment is assigned: for the sake of simplicity, the venous concentration of each transported chemical is set to the corresponding constant basal value.

1.4 Coupling between CVM and TMM: parameter estimation

The models introduced in the previous sections can be coupled to describe the mutual interaction between hemodynamics and bioenergetics (see fig. 1.4).

The coupling is due to the dependence (1.15,1.16,1.17) of hydraulic resistance R_i , $i \in \{sm, sp, o\}$, on the oxygen concentration $[O_2]_{sm}$ in the sm tissue compartment, which is the simplest case of

Reaction	Stoichiometry	Rate
GLb	$GL \longrightarrow 2PY$	$\phi_{GLb}[GL]$
GLs	$2PY \longrightarrow GL$	$\phi_{GLb}[PY]$
GYs	$mGL \longrightarrow GY$	$\phi_{GYs}[GL]$
GYb	$GY \longrightarrow mGL$	$\phi_{GYb}[GY]$
PYr	$PY \longrightarrow LA$	$\phi_{PYr}[PY]$
LAo	$LA \longrightarrow PY$	$\phi_{LAo}[LA]$
PYo	$PY \longrightarrow 3CO_2$	$\phi_{PYo}[PY]$
FAo	$FA \longrightarrow 16CO_2$	$\phi_{FAo}[FA]$

Table 1.9: Reaction rates for the splanchnic organs (the subscript $i = sp$ is omitted).

chemoreflex effect. More generally, we could assume a dependence on other chemicals. The global model is intended to give a prediction of the cardiovascular and metabolic behaviour under effort conditions; the main *input variable* is the *skeletal muscle metabolic rate* $MR(t)$, that is the rate of *ATP* breakdown, which is related to exercise workload. As *output variables*, we obtain the cardiac output, heart rates, local blood flow and concentration of several substrates in the blood.

However, as we pointed out previously, we have to estimate the unknown Michaelis-Menten parameters in the reaction rate expressions. Parameter identification is a major issue in mathematical biology (for instance see [16]): we will introduce some tools to fit a set of known data, and discuss the applications to our specific case. Let us denote by \mathbf{p} the vector of the unknown parameters: the idea is to minimize a cost functional $J = J(\mathbf{p})$ which measures the “distance” between a set of known *objective variables* $\mathbf{y}_{ob} = \mathbf{y}_{ob}(t)$ (for instance, the tissue concentrations) and the corresponding quantities \mathbf{y} predicted by the model. Formally, we can set

$$J(\mathbf{p}) = \sum_j \omega_j \frac{\|y_j(\mathbf{p}, t) - y_{ob,j}(t)\|^2}{\|y_{ob,j}(t)\|^2}, \quad (1.25)$$

where $\|\cdot\|$ is a suitable norm, as the 2-norm $\|f\|_2 = \sqrt{\int_t f^2(t) dt}$ or the ∞ -norm $\|f\|_\infty = \max_t |f(t)|$, the weights ω_j are positive quantities such that $\sum_j \omega_j = 1$, and $y_i(t)$ is the i -th component of the vector $\mathbf{y}(\mathbf{p}, t)$ of the predicted quantities corresponding to the parameters \mathbf{p} . As a consequence, the number $E = 100\sqrt{J}$ is a mean relative error in percentage. Each evaluation of the cost function J requires to solve the model, that is to find the solution of a system of differential equations. The goal is to obtain (a suitable approximation of) the *optimal* vector \mathbf{p}^* in the set P_{ad} of admissible parameters:

$$\text{find } \mathbf{p}^* : \quad J(\mathbf{p}^*) = \min_{\mathbf{p} \in P_{ad}} J(\mathbf{p}). \quad (1.26)$$

The set P_{ad} has to represent all the constraints on the parameters; for instance, every component of $\mathbf{p} \in P_{ad}$ has to be greater than zero.

Problem (1.26) is an *inverse problem*, expressed in the form of an *optimal control problem*.

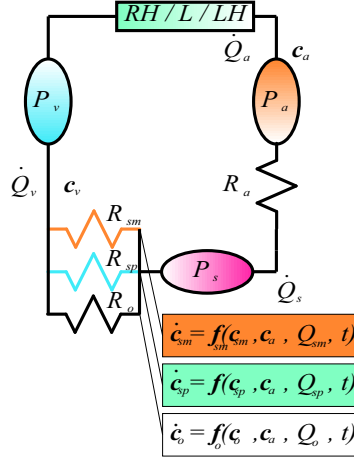


Figure 1.4: Coupling between cardiovascular system and metabolism.

1.4.1 Identification methods

In order to solve the identification problem (1.26), one could use standard line-search methods, based on the computation of the gradient of the cost function, or stochastic methods (in particular *genetic algorithms* [22], GA). There are two main differences between these algorithms. First, genetic algorithms are *global optimization methods*, while the line-search algorithms only find *local* minima (as a consequence, the starting guess for the parameters is critical). Second, usually line-search algorithms are computationally cheaper than stochastic algorithms.

Let us recall the abstract structure of a GA (the term *individual* means a parameter \mathbf{p}):

1. Supply a population P_0 of N “individuals”, together with their cost function; let $i = 1$;
2. $\tilde{P}_i = \text{selection}(P_{i-1})$;
3. $P_i = \text{reproduction}(\tilde{P}_i)$;
4. $i \leftarrow i + 1$;
5. If an exit condition on P_i is satisfied, then end; otherwise, $i \leftarrow i + 1$ and go to step 2.

At step 3, the genetic operators *mutation* and *crossover* act on the population \tilde{P}_i (which is selected on the basis of the cost function associated with each individual) in order to create the next generation P_{i+1} . If the mutation operator includes a few iterations of a line-search algorithm (such as a gradient method), the method belongs to the class of *hybrid genetic algorithms* (HGA); the introduction of the fast local optimization procedure greatly speeds up the convergence compared with standard GA.

We can apply gradient-based methods, GA and HGA to problems of type (1.26) to identify the set of unknown parameters of each compartment; for each $i = sm, sp$, this can be done by excluding the cardiovascular part of the model, assigning an *a priori* flow rate Q_i corresponding to the physiological conditions to which the available data \mathbf{y}_{ob} refer to, and then carrying out the optimization for this reduced state system, where the observed variables \mathbf{y} are the concentrations \mathbf{c}_i .

Due to the non-linearities in the Michaelis-Menten equations, the *sm* compartment is the only one for which the identification may be troublesome: when considering as objective variables the measurements obtained from a certain class of exercise protocols, the parameters which best fit the

data may not be as good for other protocols. For this reason, in the sequel the optimization results are discussed only for the skeletal muscle compartment, and the following vector of unknown parameters (see tab. 1.8):

$$\mathbf{p} = (\phi_{PCs}, \phi_{PCb}, \phi_{GLb}, \phi_{GYs}, \phi_{GYb}, \phi_{PYr}, \phi_{LAo}, \phi_{PYo}, V_{O_2}^{\max}, \phi_{FAo}). \quad (1.27)$$

As in [11], for each reaction R , the k_R constants of the Michaelis-Menten laws are assigned in such a way that the basal flux is small compared with the maximal one ϕ_R .

Fitting objective variables at rest

In principle, one may choose the vector of rest concentrations as observed variables, which are known (even though the measurement is not a straightforward procedure, and data strongly depend on the subject). This approach has been adopted in [11]. In order to compare the performances of different optimization algorithms, we fixed the rest flow rate $Q_{sm}(t) = Q_{sm}^0$ and rest skeletal muscle metabolic rate $MR(t) = MR^0$: then, we applied both gradient method (Matlab function `fminsearch`) and HGA (modifying the `gaot` Matlab library [42]) to minimize the cost function J defined by (1.25) with equal weights, being the objective variables the known rest concentrations c_{sm}^0 . In tab. 1.10 the identified parameters together with the minimum of the cost function obtained with standard gradient methods (mean relative error $E \simeq 10\%$) and with hybrid genetic algorithms ($E \simeq 6\%$) are shown. Standard values of Q_{sm}^0 and MR^0 have been used in the state equation: in particular, $Q_{sm}^0 = 1$ l/sec, and on the basis of the assumption that 6 molecules of ATP are formed from one oxygen molecule, $MR^0 = 6Q_{sm}^0([O_2]_a - [O_2]_{v,sm})$. If $[O_2]_a = 8.75$ mmol/l (see [55, 11]), and $[O_2]_{v,sm} = 6.75$ mmol/l (see [55] or apply the Fick's principle assuming $\dot{V}_{O_2} = 250$ ml min^{-1} at rest), then we get $MR^0 \simeq 12$ mmol(ATP) min^{-1} .

Parameter	Value	Parameter	Value
ϕ_{PCb}	41.09	ϕ_{PCb}	28.60
ϕ_{PCs}	84.24	ϕ_{PCs}	57.55
ϕ_{GYs}	0.29	ϕ_{GYs}	30.15
ϕ_{GYb}	0.001	ϕ_{GYb}	0.11
ϕ_{PYr}	2.69	ϕ_{PYr}	5.98
ϕ_{GLb}	0.23	ϕ_{GLb}	0.24
ϕ_{LAo}	0.15	ϕ_{LAo}	0.49
ϕ_{PYo}	0.26	ϕ_{PYo}	0.23
$V_{O_2}^{\max}$	3.33	$V_{O_2}^{\max}$	3.15
ϕ_{FAo}	0.02	ϕ_{FAo}	0.06
$J(\mathbf{p})$	0.014	$J(\mathbf{p})$	0.0042
E	11.8%	E	6.4%

a)

b)

Table 1.10: Parameter identification by fitting the rest metabolic state by a) the gradient method, and b) an HGA.

The fitting is satisfactory for both the algorithms, but the HGA allows a better minimization of the error (fig. 1.5), due to the fact that it is a global optimization method.

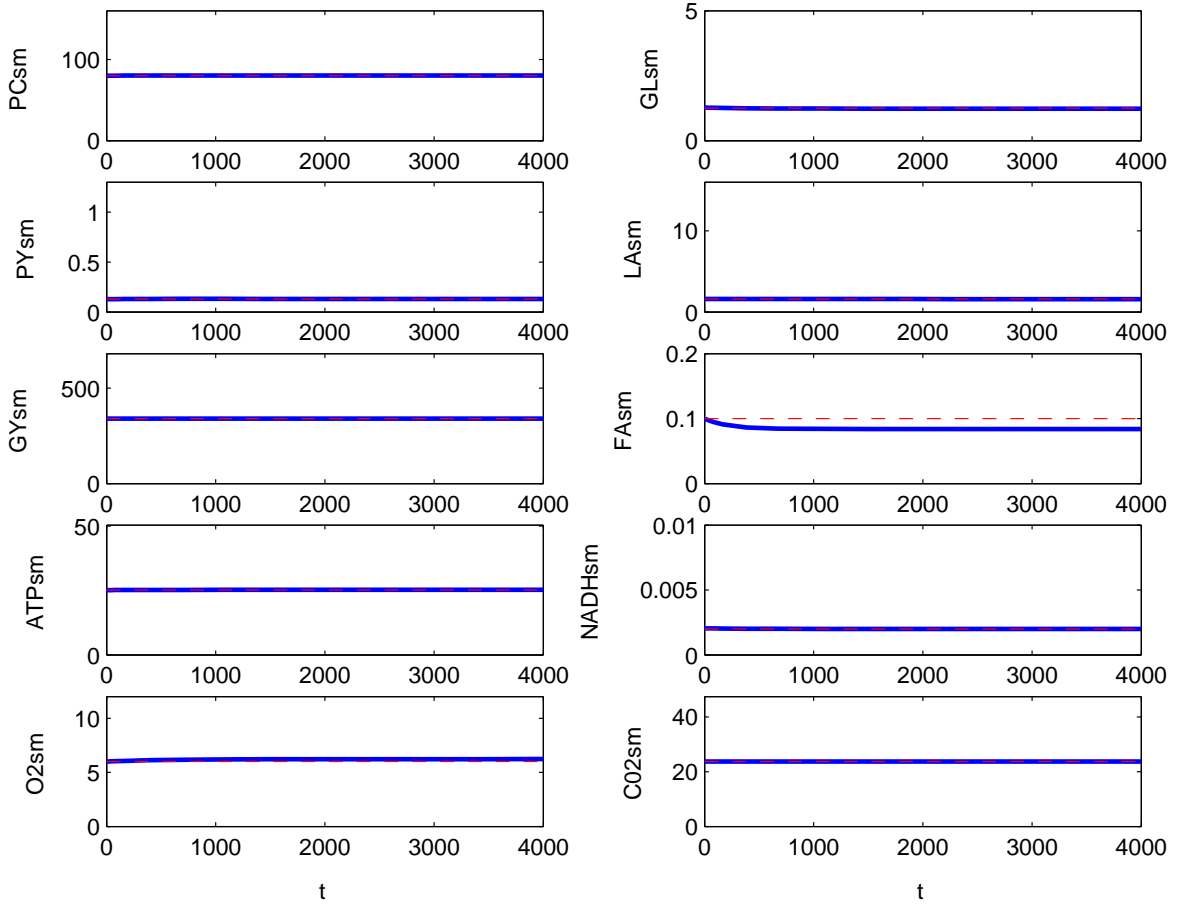


Figure 1.5: State variables corresponding to the parameters in tab. 1.10a) (continuous line) and objective values (dashed line) at rest. Concentrations are expressed in mmol/l , time in s .

As the fitting of basal concentrations is easily achieved, we wonder if it is possible to use parameters which have been identified by this procedure to simulate an effort condition. Unfortunately, this approach fails for heavy workloads: actually, if an exercise is simulated using parameters obtained by fitting the concentrations at rest \mathbf{c}_{sm}^0 , the results are often not physiological. For example, let us consider a rest/exercise transition at time \bar{t} , from the basal skeletal muscle metabolic rate MR^0 and blood flow rate Q_{sm}^0 to the respective increased values MR^1 and Q_{sm}^1 . We assume submaximal workload, for example $Q_{sm}^1 = 7Q_{sm}^0$ (the maximal Q_{sm}^1/Q_{sm}^0 is nearly 12, see tab. 1.2). Then, under the hypothesis that for submaximal effort the ATP breakdown is proportional to the oxygen extraction rate, by the Fick's equation we have

$$\frac{MR^1}{MR^0} = \frac{Q_{sm}^1}{Q_{sm}^0} \frac{\Delta_v^a [O_2]_{sm}^1}{\Delta_v^a [O_2]_{sm}^0}.$$

Actually, the former assumption does not consider an augmented anaerobic ATP production; however, we will accept it, even though the MR^1/MR^0 ratio obtained by the proposed formula could be underestimated. At rest, $\Delta_v^a [O_2]_{sm}^0 = [O_2]_a - [O_2]_{v,sm} = 0.22[O_2]_a$, that is the skeletal muscle oxygen extraction is 22%; assuming that during submaximal exercise the extraction raises up to 60% (the maximal value is about 85%, up to 90% for elite athletes), we get $MR^1 = \frac{Q_{sm}^1}{Q_{sm}^0} \frac{60\%}{22\%} \simeq 20$. Therefore,

we consider as input variables for our sm model the following functions:

$$MR(t) = \begin{cases} MR^0 & \text{if } 0 \leq t \leq \bar{t}, \\ 20MR^0 & \text{if } \bar{t} < t \leq T, \end{cases} \quad Q_{sm}(t) = \begin{cases} Q_{sm}^0 & \text{if } 0 \leq t \leq \bar{t}, \\ 7Q_{sm}^0 & \text{if } \bar{t} < t \leq T. \end{cases} \quad (1.28)$$

As we pointed out previously, we expect that 60% of arterial oxygen will be extracted by the sm compartment for $t > \bar{t}$: this means that the venous oxygen content should decrease from 6.75 to $0.4[O_2]_a^0 = 3.5$ mmol/l, that is about 50% of the rest value; being the tissue O_2 concentration proportional to the venous one, we have that a reduction of $[O_2]_{sm}$ down to an half of its rest value is expected.

Parameters identified by fitting the rest concentrations have been used to run the simulation of the rest to exercise transition: the results are shown in fig. 1.6, where one clearly sees that the O_2 concentration in the tissue does not decrease during exercise (actually it slightly increases), and CO_2 does not increase. Therefore, despite the good accuracy in fitting the rest concentrations, the identified parameters do not provide acceptable simulations of exercise. This issue is not addressed in [11], so in the next section we will detail how it is possible to improve the identification considering a rest-exercise transition and using HGA.

Fitting objective variables for a rest-exercise transition

If the parameters of the sm compartment are identified by solely observing a steady basal state; they will not include any information about the dynamics of the system. Consequently, as we have shown, it may happen that the model does not conform to physiological observations.

The simplest attempt to overcome this problem is to consider a *rest/exercise transition*, and to identify the unknown parameters by fitting some available data for this protocol. In this way, the observations are not merely static: they contain information about the characteristic time constants and concentration jumps associated with the transition.

However, due to the great amount of information we are trying to put into the objective variables, the optimization can converge toward a solution affected by a big error, even if global algorithms are used. This means that a compromise has to be found, for instance considering only a few relevant metabolite concentrations as observed variables. Let us show how this is possible by means of an example.

We consider protocol (1.28), with $\bar{t} = 1500$ s and $T = 4000$ s. We suppose that a description of oxygen and carbon dioxide expected dynamic in skeletal muscle tissue is available, at least in terms of concentration jumps and characteristic times. In particular, we assume an exponential transient:

$$y_{ob,O_2}(t) = \begin{cases} [O_2]_{sm}^0 & \text{if } 0 \leq t \leq \bar{t}, \\ [O_2]_{sm}^1 + e^{-(t-\bar{t})/\tau_{O_2}}([O_2]_{sm}^0 - [O_2]_{sm}^1) & \text{if } \bar{t} < t \leq T, \end{cases} \quad (1.29)$$

$$y_{ob,CO_2}(t) = \begin{cases} [CO_2]_{sm}^0 & \text{if } 0 \leq t \leq \bar{t}, \\ [CO_2]_{sm}^1 + e^{-(t-\bar{t})/\tau_{CO_2}}([CO_2]_{sm}^0 - [CO_2]_{sm}^1) & \text{if } \bar{t} < t \leq T, \end{cases}$$

where $[O_2]_{sm}^0$ and $[CO_2]_{sm}^0$ are the basal concentrations values, $[O_2]_{sm}^1$ and $[CO_2]_{sm}^1$ are the new concentrations after the transition to the effort condition, and τ_{O_2} and τ_{CO_2} are the respective time constants. An example of such functions y_{ob,O_2} and y_{ob,CO_2} are the dashed lines in fig. 1.6.

With regard to the other observed chemical concentrations, we suppose to have only the basal state data:

$$\forall C \notin \{O_2, CO_2\} : \quad y_{ob,C}(t) = [C]_{sm}^0, \quad 0 \leq t \leq \bar{t}. \quad (1.30)$$

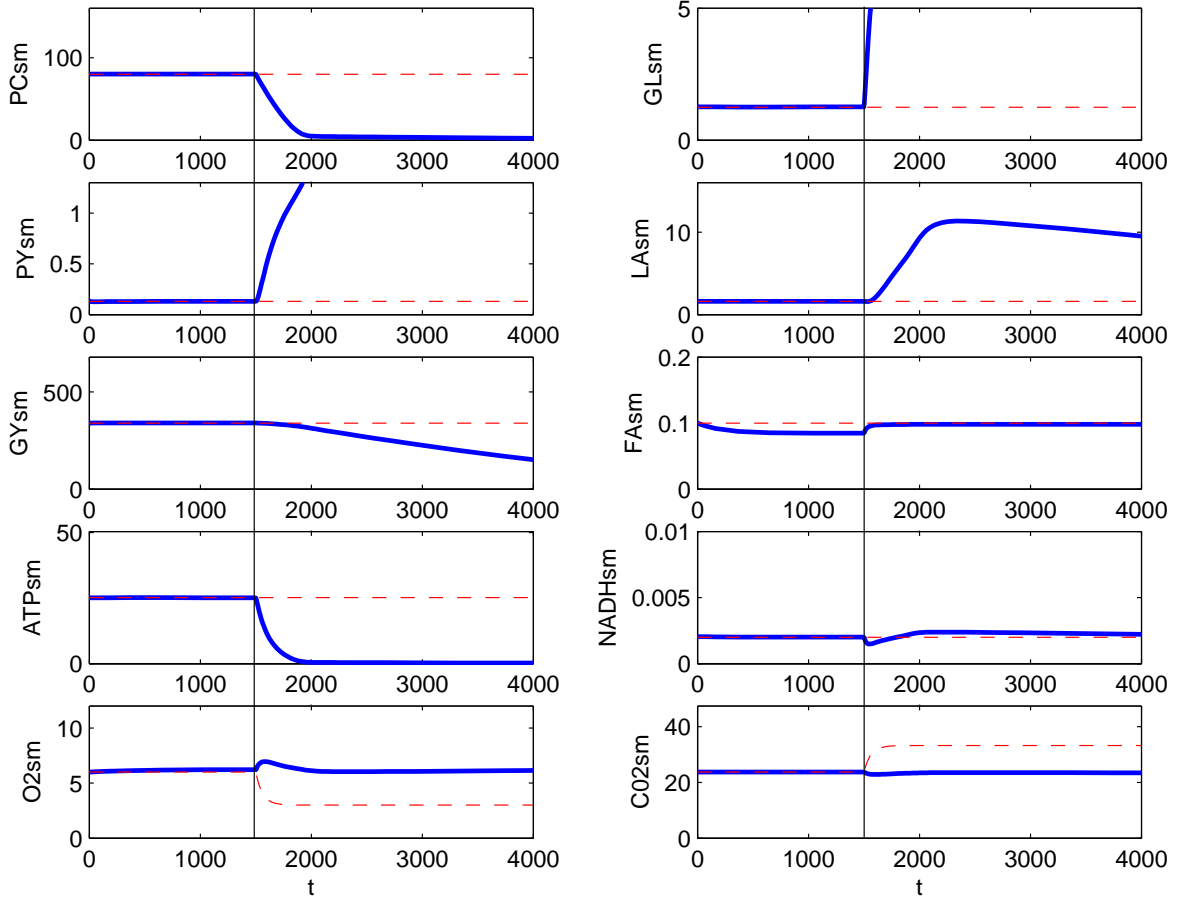


Figure 1.6: Rest/exercise transition: state variables (continuous line) corresponding to the parameters of tab. 1.10a) obtained by fitting the basal concentrations (dashed line). For O_2 and CO_2 , the dashed line during exercise represents expected values: in this case, simulations do not agree with observations. Concentrations are expressed in mmol/l, time in s.

Eq. (1.29) and (1.30) define our objectives. As the data y_{ob,O_2} and y_{ob,CO_2} are defined on a wider temporal frame, the expression of the cost functional to be minimized is the following one, where norms are taken on different intervals depending on the data:

$$\begin{aligned}
 J(\mathbf{p}) = & \omega_{O_2} \frac{\|y_{O_2}(\mathbf{p}) - y_{ob,O_2}\|_{[0,T]}}{\|y_{ob,O_2}(t)\|_{[0,T]}} + \omega_{CO_2} \frac{\|y_{CO_2}(\mathbf{p}) - y_{ob,CO_2}\|_{[0,T]}}{\|y_{ob,CO_2}\|_{[0,T]}} \\
 & + \sum_{C \notin \{O_2, CO_2\}} \omega_C \frac{\|y_C(\mathbf{p}) - y_{ob,C}\|_{[0,\bar{t}]}}{\|y_{ob,C}\|_{[0,\bar{t}]}} ,
 \end{aligned} \tag{1.31}$$

As usual we denote by $y_C(\mathbf{p}) = y_C(\mathbf{p})(t) = [C]_{sm}(t)$ the time-dependent concentration of the substance C given by the solution of the state equation with the parameters \mathbf{p} .

In tab. 1.11 and fig. 1.8-1.9 the results of two different parameter identifications are shown. The first optimization was carried out assuming the cost functional defined by eq. (1.31), that is taking both $[O_2]_{sm}$ and $[CO_2]_{sm}$ as observed variables for $t > \bar{t}$, while for the second optimization only the $[O_2]_{sm}$ variable was observed for $t > \bar{t}$.

Parameter	Value
ϕ_{PCb}	38.27
ϕ_{PCs}	61.25
ϕ_{GYs}	17.87
ϕ_{GYb}	15.24e-2
ϕ_{PYr}	23.57e-1
ϕ_{GLb}	11.85e-1
ϕ_{LAo}	86.50e-3
ϕ_{PYo}	87.78e-2
VO_2^{\max}	16.20
ϕ_{FAo}	37.60e-3
$J(\mathbf{p})$	0.047
E	21.6%

Weights:
 $\omega_{O_2} = \omega_{CO_2} = 0.30$;
 $\omega_C = 0.05$ if $C \notin \{O_2, CO_2\}$.

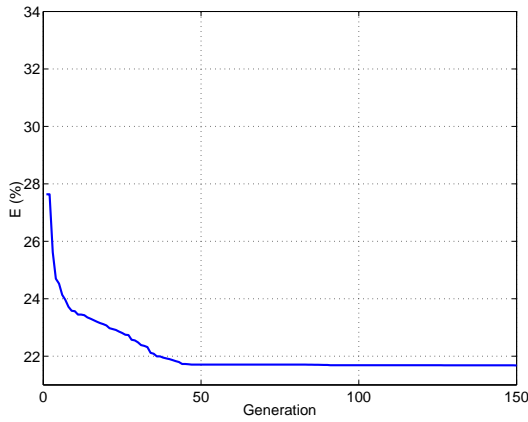
a)

Parameter	Value
ϕ_{PCb}	40.14
ϕ_{PCs}	70.60
ϕ_{GYs}	43.82
ϕ_{GYb}	30.18e-2
ϕ_{PYr}	26.33e-1
ϕ_{GLb}	19.67e-1
ϕ_{LAo}	43.30e-3
ϕ_{PYo}	12.76e-1
VO_2^{\max}	16.69
ϕ_{FAo}	31.90e-3
$J(\mathbf{p})$	0.057
E	24.0%

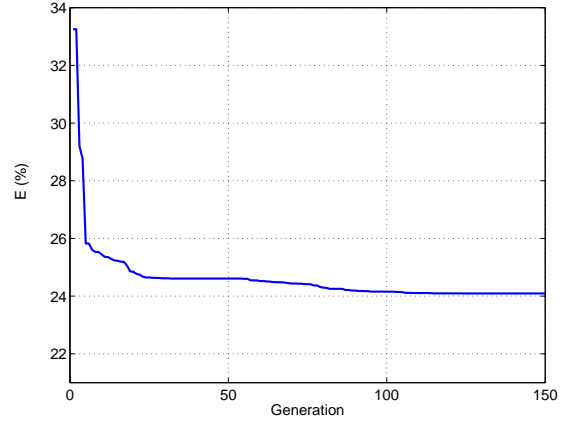
Weights:
 $\omega_{O_2} = 0.55$;
 $\omega_C = 0.05$ if $C \neq O_2$.

b)

Table 1.11: Parameter identification by fitting via weighted-HGA the rest metabolic state and a) both the O_2 and CO_2 concentrations during exercise, b) only the O_2 concentration during exercise.



a)



b)

Figure 1.7: Convergence history of HGA. The observed variables are: a) both O_2 and CO_2 , and b) only O_2 .

These results shows that the error E with respect to available data can be non negligible (20-25%, fig. 1.7, instead of 6% obtained with a basal state fitting) when fitting non-steady data. Nevertheless, the major expected features of the rest-to-exercise transition are obtained: the oxygen concentration in the skeletal muscle drops off (the reduction being 25%, the expected one 50%), and the carbon dioxide content increases (actual increment 8%, 33% expected). The discrepancy between the actual and the expected jumps of the O_2 and CO_2 concentrations can be reduced if a higher MR^1 is assumed

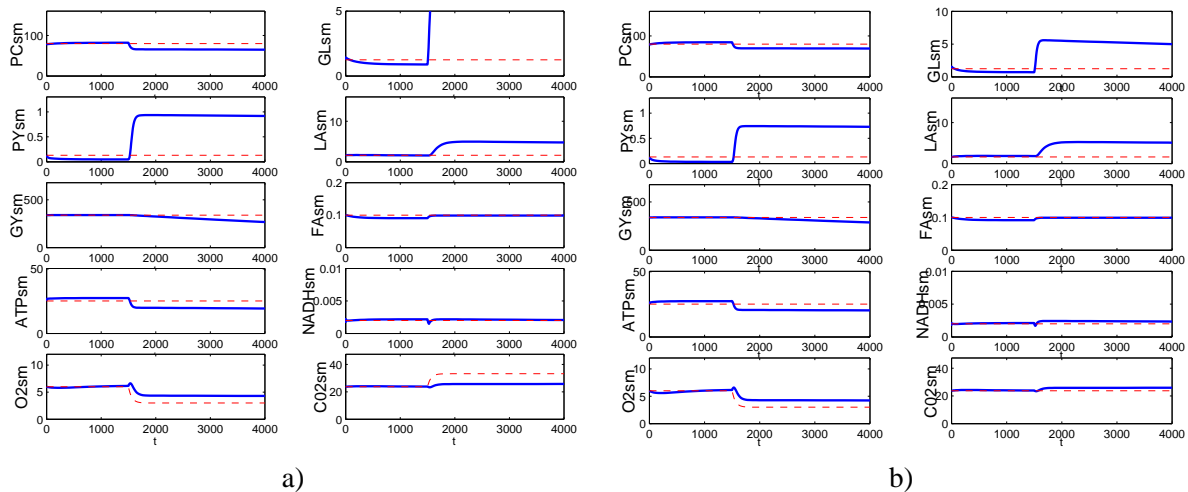


Figure 1.8: State variables corresponding respectively to the parameters in tab. 1.11a,b) (continuous line), and basal values (dashed line) for a rest-exercise transition. For O_2 and CO_2 , the dashed line during exercise represents the objective values. Concentrations are expressed in mmol/l, time in s.

in eq. (1.28), considering that we neglected any augmented anaerobic pathway in the estimation of the metabolic rate. Finally, it is remarkable that the time courses of muscle metabolites obtained first observing only the oxygen concentration, and then observing both the oxygen and carbon dioxide concentrations, do not differ substantially (see fig. 1.8), with the exception of glucose.

1.5 Simulations of coupled CVM and TMM

In this last section simulation results for the coupled models are discussed. To sustain the application of this kind of mathematical models in sport medicine and physiology, we consider realistic protocols, data and problems, and analyze the behaviour of relevant quantities related to cardiovascular system and biochemistry.

1.5.1 One-chemical model

We first present some results obtained with the simple one-chemical kinetic (1.22): therefore, in this preliminary investigation O_2 is the only chemical we account for. To test our results, we consider the measurements obtained in [81]; in this study the authors address an augmented sympathetic nerve activity as a possible mechanism contributing to the observed impaired leg vasodilatation during dynamic exercise in healthy older women. In the sequel, we will verify this hypothesis by our model.

The simulated protocol is the following one: starting from a rest condition, the subject is pedaling for 6 min at 20 W, then the power output is linearly increased by 10 W every 3 min up to 60 W. According to [81], several measurements have been made for this protocol (mean arterial pressure, leg blood flow, ...) for thirteen younger (20-27 yr) and older (60-71 yr) women: a reduced leg vasodilatation and blood flow response has been observed in the latter group.

The cardiovascular model coupled with the one-chemical TMM for the oxygen is solved over a time interval consisting of three subintervals: $[0, T_0]$ (rest), $[T_0, T_{20}]$ (pedaling at 20 W), $[T_{20}, T_{60}]$ (linear increasing in power output up to 60 W), where $T_0 = 12$ min, $T_{20} = 18$ min, $T_{60} = 30$ min.

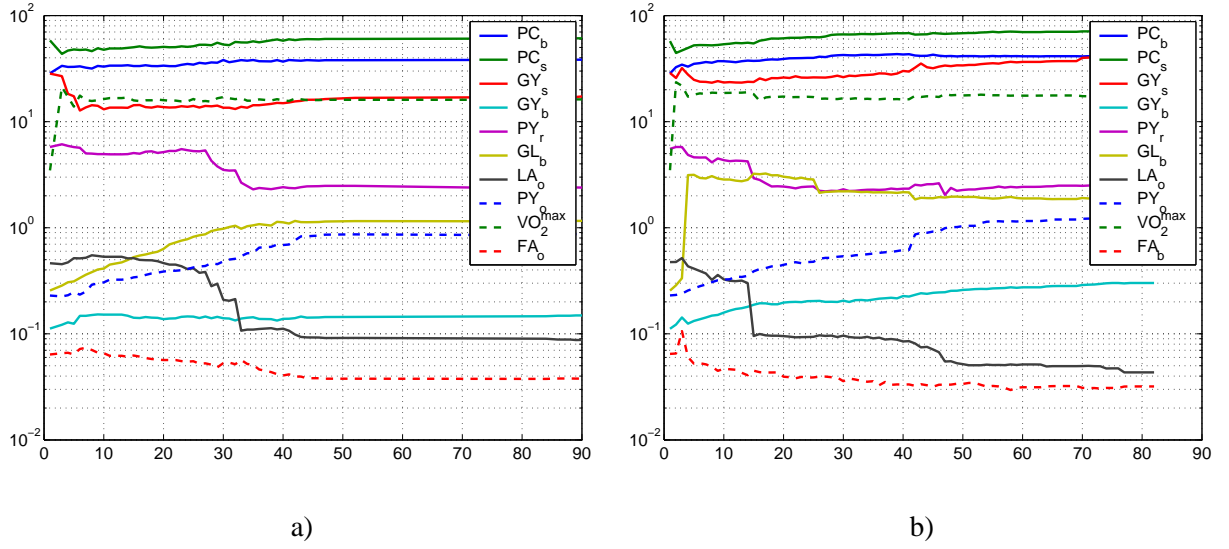


Figure 1.9: Trace of the best parameters obtained at each generation number (abscissa). The observed variables are: a) both O_2 and CO_2 , and b) only O_2 .

The oxygen consumption rate $OP_{sm}(t)$ in the skeletal muscle compartment, that represents the exercising legs, is expressed as follows:

$$OP_{sm}(t) = \begin{cases} OP_{sm}^0 & 0 \leq t \leq T_0, \\ OP_{sm}^0 + OP_{sm}^{20} & T_0 \leq t \leq T_{20}, \\ OP_{sm}^0 + OP_{sm}^{20} + \alpha \frac{t-T_{20}}{T_{60}-T_{20}} 40W & T_{20} \leq t \leq T_{60}, \end{cases}$$

where OP_{sm}^0 is the basal oxygen consumption rate ($2.4 \text{ mmol min}^{-1}$), OP_{sm}^{20} is the oxygen consumption rate at 20 W (calculated as in [12], 5 mmol min^{-1}) and α is a conversion factor: assuming that 30 KJ of mechanical energy are produced by the breakdown of a ATP molecule, and that 6 mol of ATP are formed for each mol of O_2 , then $\alpha = 5.6 \cdot 10^{-3} \text{ mmol } O_2 / \text{s/W}$. In fig. 1.10 exercise simulation for the younger women is presented. Some parameters among those in tab. 1.2 were adjusted to match the cardiac output, mean arterial pressure and blood flow distribution at rest and at 20 W, referring to data reported in [81]. We used $P_{n,0} = 75 \text{ mmHg}$, $G_{P_n} = 20 \text{ s} \cdot \text{mmHg}$, $k_{cm} = 0.7 \text{ kgdw}^2 / \text{mmol}^2 / \text{s}$, $[O_2]_{sm}^0 = 5.8 \text{ mmol/kgdw}$; we also increased the gain of the sympathetic control on the heart rate with $G_{T,s} = 0.9 \text{ s}^2$, and we changed the constants $\tilde{R}_{i,0}$ for $i = sm, sp, o$ respectively to 2, 1 and $0.6 \text{ mmHg} \cdot \text{s/ml}$.

Simulations for the older women are shown in fig. 1.11: in this case, modifications of the parameters were made to take into account the higher pressure and the lower cardiac output of older women in regard of the younger subjects. Particularly, in this case we considered $P_{n,0} = 90 \text{ mmHg}$, $G_{P_n} = 35 \text{ s} \cdot \text{mmHg}$, $G_{T,s} = 0.52 \text{ s}^2$, $G_{T,v} = 0.3 \text{ s}^2$; the constants $\tilde{R}_{i,0}$ for $i = sm, sp, o$ were changed to 2, 1 and $0.6 \text{ mmHg} \cdot \text{s/ml}$; and finally, a global increase of the efferent sympathetic activity was imposed by increasing the values of $f_{es,\infty}$ and $f_{es,0}$ in (1.10). Results with the same parameters but without the augmented sympathetic vasoconstriction are shown with dashed lines: we obtained a reduction in both arterial pressure and leg vascular resistance, and a more accurate fitting was provided by the previous simulation. This shows that our investigation is consistent with the hypothesis of an increased sympathetic nerve activity during exercise in older women.

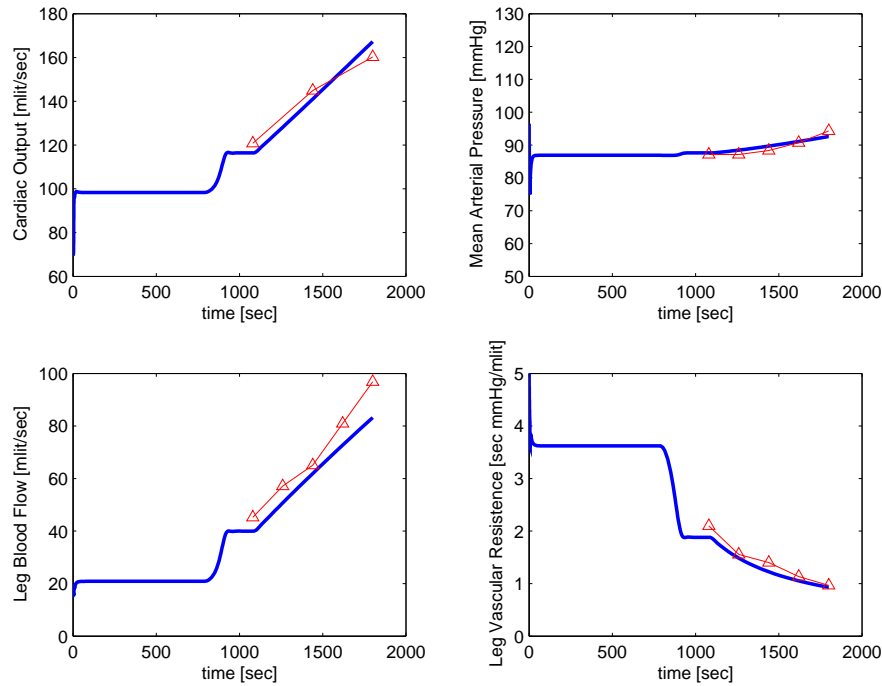


Figure 1.10: Younger women exercise: experimental measurements [81] (*triangles*) and simulation (*continuous line*) of cardiac output Q_a , mean arterial pressure P_a , leg blood flow Q_{sm} , and leg vascular resistance R_{sm} .

1.5.2 Multi-chemical model

The simple one-chemical model of the metabolism does not take into account the dynamic of several important metabolites such as lactate, glucose, pyruvate. Here we present numerical results obtained by coupling the extended metabolism model described in section 1.3.3 and the cardiovascular model (section 1.2).

We considered a 10 min incremental exercise, with a linear increasing workload: the metabolic rate $MR_{sm}(t)$ of the skeletal muscle compartment was increased starting from the basal value MR_{sm}^0 at $t = 0$ up to $30MR_{sm}^0$ at $t = 10$ min and then again set equal to MR_{sm}^0 . Being the energy expenditure of the whole body basal metabolism approximately equal to 75 W, and the skeletal muscle rest blood flow $Q_{sm}^0 \simeq Q_a^0/5$, we can estimate the rest skeletal muscle power to be 15 W. Therefore, if the power output was proportional to MR , the peak power of the exercise simulation would be about 450 W; however, as it has been discussed, *ATP* breakdown becomes less and less efficient as the workload increases, so that the power output/ MR ratio is not a constant, but rather a decreasing function of MR . If we assume that under high effort conditions the metabolic efficiency is reduced by 35% [50, 12], then we can estimate a 300 W peak power output.

The evolution in time of the main hemodynamical variables is shown in fig. 1.12. The time course of the vascular resistances, for instance, shows that during exercise the skeletal muscle becomes the most blood-demanding compartment; this perturbs the overall systemic resistance, which in turn causes the increase of heart rates (and stroke volume, not shown here) due to the baroreflex effector. Moreover, the shifting of the reference value for the pressure in the carotid sinus sigmoid curve causes an increase of the mean arterial pressure.

In fig. 1.13 a few relevant venous chemical concentrations are shown (O_2 , CO_2 , LA and PY).

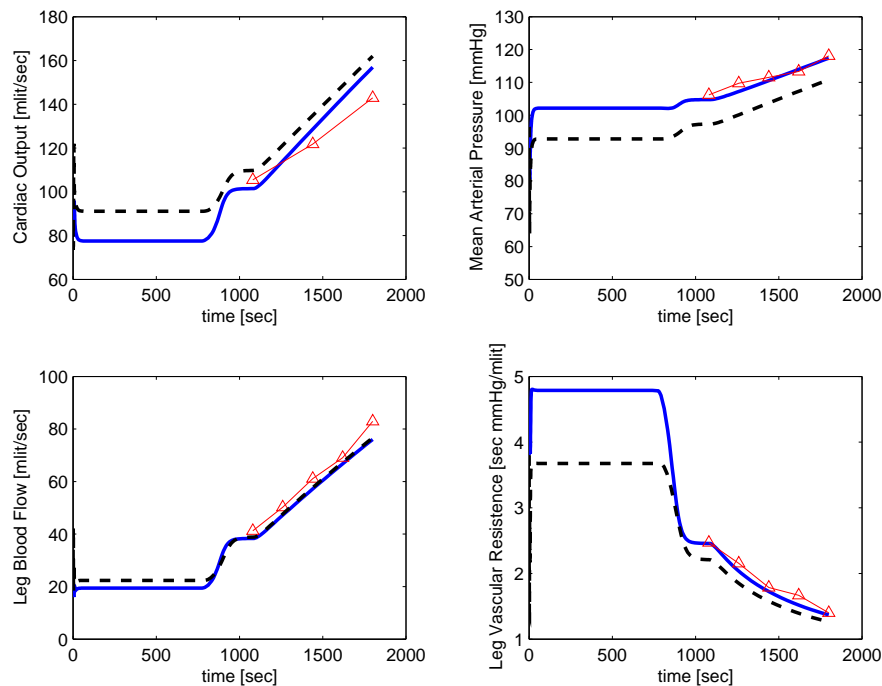


Figure 1.11: Older women exercise: experimental measurements [81] (*triangles*) and model simulations with enhanced (*continuous line*) sympathetic nerve activity. The dashed line shows the simulation results when no enhancement in sympathetic activity is considered.

As expected, a reduction in the venous O_2 content is observed; moreover the high level of skeletal muscle metabolic rate causes an increase in carbon dioxide (6.5%), and a significant accumulation of lactate (900%) and pyruvate (1000%). Increments in lactate level of the same order are found in the ramp tests described in [33].

1.6 Conclusions

In this chapter we have seen how it is possible model the complex interactions between cardiovascular system and local biochemical processes, such as those taking place in muscle cells. We have considered models for *a*) metabolism of relevant substrates in the tissues involved in exercise, and *b*) circulatory systems. Baroreflex and chemoreflex regulation effects have been taken into account in the coupling in order to describe the interplay between these subsystems. This approach allows to simulate the response of the body to exercise; it may also provide a tool to investigate several other aspects of interest in physiology, such as pharmacokinetics of a particular drug under effort conditions or hemodynamics and tissue perfusion during exercise.

We have adopted a *compartmental* approach: no geometrical descriptions of circulation and chemical distribution in the tissues have been considered, due to the complexity of the whole-body processes we were focusing on. In the following chapters, we will introduced more detailed models, that are able to describe the spatial distribution of important physiological quantities such as blood pressure or oxygen concentration. To provide finer tools allowing a more detailed analysis of local phenomena will be the aim of the next chapters. We will begin with one-dimensional models for blood flow and mass transport (chapter 2) and then we will introduce 1D-3D models of tissue perfu-

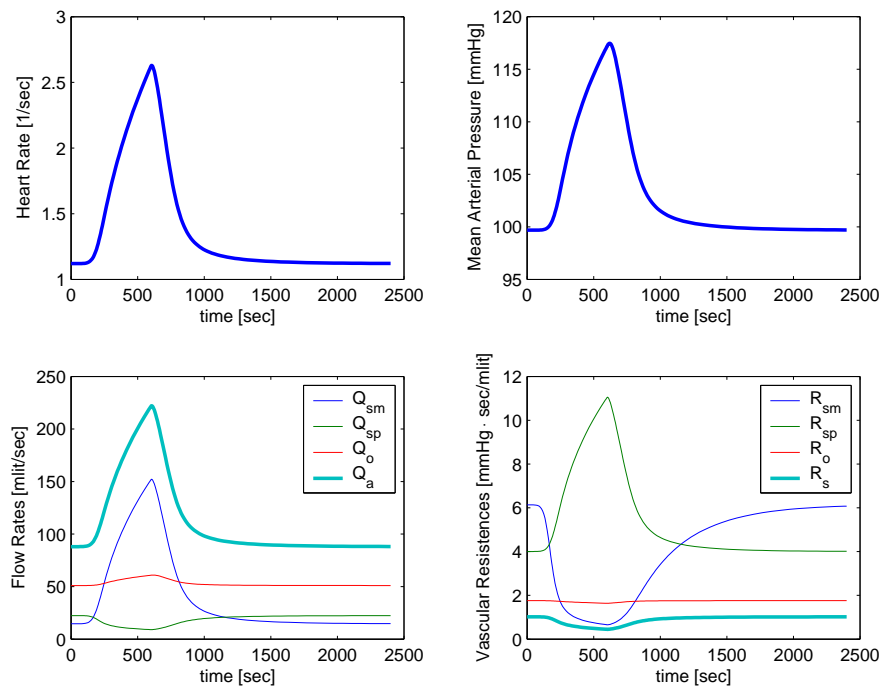


Figure 1.12: Heart rates, mean arterial pressure, flow rates and vascular resistances in a 10 minutes incremental exercise.

sion (from chapter 3). In case, the finer models can replace some of the “lumped” models we have considered in this chapter, providing a more accurate analysis of the processes at hand.

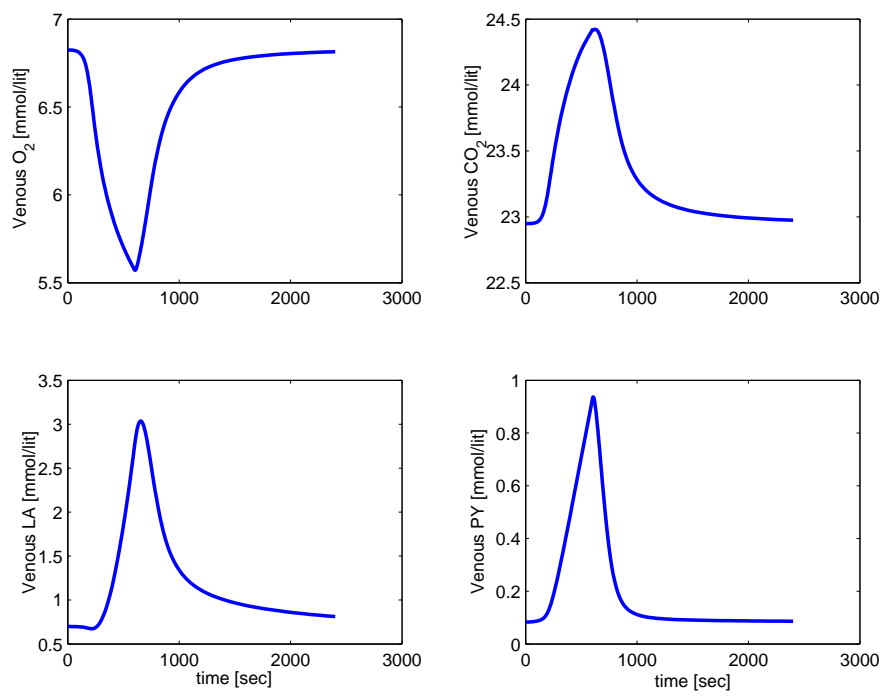


Figure 1.13: Venous concentrations of oxygen, carbon dioxide, lactate and pyruvate in a 10 minute incremental exercise.

Chapter 2

Reduced one-dimensional models for transport of chemicals in blood vessels

2.1 Introduction

We have seen in the previous chapter that the simulation of the exchanges of various chemical species (O_2 , CO_2 , lactate, ...) between blood vessels and tissues necessitates an accurate description of both the haemodynamics (fluid properties of blood) and mass transport. We have considered a compartmental analysis in order to keep the computational costs in reasonable ranges: however, by this approach any geometrical information about vessels and tissues is lost.

A compromise between the lumped models and the expensive three-dimensional convection-diffusion-reaction (CDR) models is provided by *reduced models*. As regards haemodynamics, the most important example is given by one-dimensional reduced models (we refer the reader to [84], [64], [13], [14] and [97]). From the full 3D Navier-Stokes equation coupled with the wall structure, a simplified axi-symmetric coupled problem can be derived; under suitable hypotheses one can further simplify these equations to obtain a reduced 2×2 hyperbolic system relating the local axial pressure to the flow-rate (see [13, 14] for a rigorous derivation).

In this chapter¹ we adapt the already existing analysis to treat the transport of a chemical in a one-dimensional vessel: we derive reduced CDR equations assuming some simplifying hypotheses. In this sense, we provide an extension of what has been achieved for haemodynamics [86, 29, 104, 31]. Namely, we study the solutions of the CDR equation in an axi-symmetric cylindrical vessel, and suppose that the length of the vessel is considerably much larger than its radius. Under these hypotheses, we derive a 1D model that describes the evolution of the flow rate, pressure and cross sectional averaged concentration transported by blood flow. We study the global existence of the solutions of such a system in the case of a finite vessel, basing our argument on [13]. We also provide numerical methods to solve these equations in the spirit of [23, 84] and references therein.

The subject of 1D CDR models will be extended in chapters 3 and 4, where 1D-3D coupled models will be considered.

¹Part of the chapter has been published as an internal report [20].

2.2 A reduced model for chemical transport

2.2.1 The transport diffusion equation

Let us consider an *axisymmetric* domain $\Omega \subset \mathbb{R}^3$ representing an arterial vessel. The equations which govern the fluid motion and the mass transport in the vessel are:

$$\begin{cases} \frac{\partial \mathbf{v}}{\partial t} + (\mathbf{v} \cdot \nabla) \mathbf{v} - \nu \Delta \mathbf{v} + \frac{1}{\rho} \nabla p = \mathbf{0} & \text{in } \Omega, \\ \nabla \cdot \mathbf{v} = 0 & \text{in } \Omega, \\ \frac{\partial c}{\partial t} + \mathbf{v} \cdot \nabla c - \mu \Delta c = 0 & \text{in } \Omega, \end{cases} \quad (2.1)$$

where \mathbf{v} is the blood velocity, ν and ρ are the blood viscosity and its density (which we assume constant), and p is the pressure; c is the concentration of the chemical under consideration (for example oxygen), and μ is its diffusivity in blood. Standard boundary and initial condition should be provided for these equations. A set of one-dimensional equations for the cross-sectional averaged pressure,

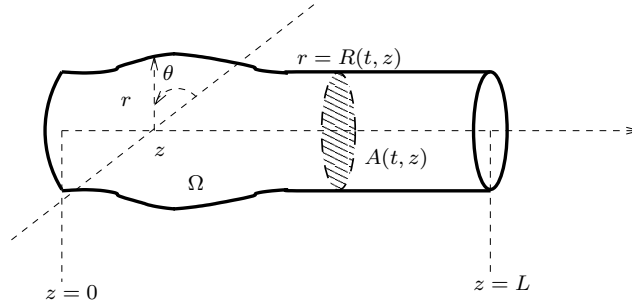


Figure 2.1: Vessel geometry.

flow rate and mass concentration can be found using standard asymptotic techniques, as discussed in [84] for the hydrodynamical part. In order to use similar arguments on the coupled system (2.1), we shall assume the following hypotheses:

1. The domain Ω is described at each time t in cylindrical coordinates by

$$\Omega(t) = \{(r, \theta, z) \in \mathbf{R}^3 \mid 0 \leq z \leq L, 0 \leq r \leq R(t, z)\},$$

where $R(t, z)$ is the radius of the vessel at time t at the section z (see fig. 2.2.1).

2. Both \mathbf{v} and c are axisymmetric functions of the space variables. We set

$$\mathbf{v} = v_r(t, r, z) \mathbf{e}_r + v_z(t, r, z) \mathbf{e}_z, \quad c = c(t, r, z),$$

where \mathbf{e}_r and \mathbf{e}_z are the radial and the longitudinal vectors of the cylindrical coordinate system. Moreover, we prescribe *a priori* the longitudinal velocity and concentration *profile*: that is, we assume

$$v_z(t, r, z) = U(t, z) f_v(r), \quad c(t, r, z) = C(t, z) f_c(r), \quad (2.2)$$

where f_v and f_c are shape function, while U and C are the mean longitudinal velocity and concentration:

$$\begin{aligned} U(t, z) &= \frac{1}{R(t, z)^2} \int_0^{R(t, z)} 2v_z(t, r, z)r dr, \\ C(t, z) &= \frac{1}{R(t, z)^2} \int_0^{R(t, z)} 2c(t, r, z)r dr. \end{aligned} \quad (2.3)$$

Thus, $\frac{1}{R^2} \int_0^R 2f_v r dr = 1$, and the same equality holds for f_c .

3. The “radial” scale is much smaller than the “longitudinal” one, that is

$$\frac{R_0}{L_0} \ll 1, \quad \frac{B_r}{B_z} \ll 1,$$

where R_0 , L_0 , B_r and B_z are typical values of respectively the vessel length, the vessel radius, the mean radial velocity and the mean longitudinal velocity.

4. The streamline boundary condition holds:

$$v_r(t, R, z) = \frac{\partial R(t, z)}{\partial z} v_z(t, R, z) + \frac{\partial R(t, z)}{\partial t}. \quad (2.4)$$

5. The blood pressure at the vessel wall and the wall displacement are related by a standard algebraic law, as follows:

$$p(t, z, R) = G_0 \left(\left(\frac{A(t, z)}{A_0} \right)^{1/2} - 1 \right), \quad (2.5)$$

where $A = \pi R^2$ is the section area, and A_0 the constant reference section area at rest. The reference pressure (for $A = A_0$) is assumed to be zero, and the coefficient G_0 is given by

$$G_0 = \frac{\sqrt{\pi} h_0 E}{\sqrt{A_0}},$$

where E is the Young modulus and h_0 the vessel thickness.

6. The concentration at the vessel wall satisfies a Robin boundary condition:

$$-\mu \frac{\partial c(t, z, R)}{\partial r} = Dc(t, z, R), \quad (2.6)$$

where D is a permeability coefficient.

2.2.2 Axisymmetric transport diffusion equation (TDE) in cylindrical coordinates

Using standard expressions for the differential operators in cylindrical coordinates, and noting that from assumption 2 we have that $(\partial c / \partial \theta = 0)$, we find:

$$\mathbf{v} \cdot \nabla c = v_r \frac{\partial c}{\partial r} + v_z \frac{\partial c}{\partial z}, \quad \Delta c = \frac{1}{r} \frac{\partial}{\partial r} c + \frac{\partial^2 c}{\partial r^2} + \frac{\partial^2 c}{\partial z^2},$$

which finally gives the transport-diffusion equation (TDE) for the concentration:

$$\partial_t c + v_r \frac{\partial}{\partial r} c + v_z \frac{\partial}{\partial z} c = \mu \left[\frac{1}{r} \frac{\partial}{\partial r} c + \frac{\partial^2 c}{\partial r^2} + \frac{\partial^2 c}{\partial z^2} \right]. \quad (2.7)$$

2.2.3 The reduced non-dimensional equation

Consider the characteristic quantities defined in assumption 3, and consider also a reference concentration C_0 ; it is possible to introduce non-dimensional variables (we denote them by a tilde) by setting:

$$r = R_0 \tilde{r}, \quad z = L_0 \tilde{z}, \quad t = \frac{L_0}{B_z} \tilde{t}, \quad c = C_0 \tilde{c}, \quad v_r = B_r \tilde{v}_r, \quad v_z = B_z \tilde{v}_z, \quad p = \rho B_z^2 \tilde{p}. \quad (2.8)$$

Moreover, following the assumption 3 we suppose that the characteristic quantities are chosen in such a way that

$$\frac{R_0}{L_0} = \frac{B_r}{B_z} = \epsilon,$$

where ϵ is small. Equation (2.7) becomes

$$\partial_{\tilde{t}}(\tilde{r}\tilde{c}) + \tilde{r}\tilde{v}_r\partial_{\tilde{r}}\tilde{c} + \tilde{r}\tilde{v}_z\partial_{\tilde{z}}\tilde{c} = \frac{L_0\mu\tilde{r}}{B_zR_0^2} \left[\frac{1}{\tilde{r}}\partial_{\tilde{r}}\tilde{c} + \partial_{\tilde{r}}^2\tilde{c} + \frac{R_0^2}{L_0^2}\partial_{\tilde{z}}^2\tilde{c} \right],$$

and neglecting terms of order ϵ^2 inside the brackets, we get

$$\partial_{\tilde{t}}(\tilde{r}\tilde{c}) + \tilde{r}\tilde{v}_r\partial_{\tilde{r}}\tilde{c} + \tilde{r}\tilde{v}_z\partial_{\tilde{z}}\tilde{c} = \frac{L_0\mu}{B_zR_0^2} [\partial_{\tilde{r}}(\tilde{r}\partial_{\tilde{r}}\tilde{c})] \quad (2.9)$$

Using the same techniques for the incompressibility condition we get

$$\partial_{\tilde{r}}(\tilde{r}\tilde{v}_r) + \partial_{\tilde{z}}(\tilde{r}\tilde{v}_z) = 0,$$

which transforms expression (2.9) in a conservative formulation that reads

$$\partial_{\tilde{t}}(\tilde{r}\tilde{c}) + \partial_{\tilde{r}}(\tilde{r}\tilde{v}_r\tilde{c}) + \partial_{\tilde{z}}(\tilde{r}\tilde{v}_z\tilde{c}) = \frac{L_0\mu}{B_zR_0^2} [\partial_{\tilde{r}}(\tilde{r}\partial_{\tilde{r}}\tilde{c})]. \quad (2.10)$$

2.2.4 The averaged equations

Next we reformulate equation (2.10) averaging it across the section of the vessel. Consider the non-dimensional mean concentration and the velocity-concentration correlation coefficient, defined as:

$$\tilde{C} = \frac{1}{\tilde{R}^2} \int_0^{\tilde{R}} 2\tilde{c}\tilde{r}d\tilde{r}, \quad \tilde{\omega} = \frac{1}{\tilde{R}^2\tilde{U}\tilde{C}} \int_0^{\tilde{R}} 2\tilde{v}_z\tilde{c}\tilde{r}d\tilde{r}.$$

We can integrate eq. (2.10) from $\tilde{r} = 0$ to $\tilde{r} = \tilde{R}$ and obtain a reduced equation for the averaged quantities. At this point we need to specify the boundary condition at the wall where $\tilde{r} = \tilde{R}$. By assumption 4 and the rescaling (2.8), the streamline boundary condition (2.4) holds also for the non-dimensional quantities:

$$[\tilde{v}_r]_{\tilde{r}=\tilde{R}} = \frac{\partial\tilde{R}}{\partial\tilde{z}} [\tilde{v}_z]_{\tilde{r}=\tilde{R}} + \frac{\partial\tilde{R}}{\partial\tilde{t}},$$

so that from eq. (2.10) we get:

$$\begin{aligned} & \frac{\partial}{\partial\tilde{t}} \int_0^{\tilde{R}} \tilde{c}\tilde{r}d\tilde{r} - \tilde{R} [\tilde{c}]_{\tilde{r}=\tilde{R}} \frac{\partial\tilde{R}}{\partial\tilde{t}} + \tilde{R} [\tilde{v}_r\tilde{c}]_{\tilde{r}=\tilde{R}} \\ & + \frac{\partial}{\partial\tilde{z}} \int_0^{\tilde{R}} \tilde{v}_z\tilde{c}\tilde{r}d\tilde{r} - [\tilde{R}\tilde{c}\tilde{v}_z]_{\tilde{r}=\tilde{R}} \frac{\partial\tilde{R}}{\partial\tilde{z}} = \frac{\mu L_0}{B_z R_0^2} \tilde{R} \left[\frac{\partial\tilde{c}}{\partial\tilde{r}} \right]_{\tilde{r}=\tilde{R}}. \end{aligned}$$

In terms of the averaged quantity \tilde{C} , the latter equation reads:

$$\frac{\partial}{\partial \tilde{t}} \left(\frac{\tilde{R}^2}{2} \tilde{C} \right) + \frac{\partial}{\partial \tilde{z}} \left(\frac{\tilde{\omega} \tilde{R}^2 \tilde{U} \tilde{C}}{2} \right) = \frac{\mu L_0}{B_z R_0^2} \tilde{R} \left[\frac{\partial \tilde{c}}{\partial \tilde{r}} \right]_{\tilde{r}=\tilde{R}}.$$

Combining this result with those presented in [13] for the momentum equation, we obtain a complete system of averaged Navier Stokes equations coupled with the concentration equation:

$$\begin{cases} \frac{\partial}{\partial \tilde{t}} \tilde{R}^2 + \frac{\partial}{\partial \tilde{z}} (\tilde{R}^2 \tilde{U}) = 0 \\ \frac{\partial}{\partial \tilde{t}} (\tilde{R}^2 \tilde{U}) + \frac{\partial}{\partial \tilde{z}} (\tilde{\alpha} \tilde{R}^2 \tilde{U}^2) + \tilde{R}^2 \frac{\partial \tilde{p}}{\partial \tilde{x}} = 2 \frac{\nu L_0}{B_z R_0^2} \left[\frac{\partial \tilde{v}_z}{\partial \tilde{r}} \right]_{\tilde{r}=\tilde{R}}, \\ \frac{\partial}{\partial \tilde{t}} (\tilde{R}^2 \tilde{C}) + \frac{\partial}{\partial \tilde{z}} (\tilde{\omega} \tilde{R}^2 \tilde{U} \tilde{C}) = \frac{2\mu L_0}{B_z R_0^2} \tilde{R} \left[\frac{\partial \tilde{c}}{\partial \tilde{r}} \right]_{\tilde{r}=\tilde{R}} \end{cases}$$

where the Coriolis coefficient $\tilde{\alpha}$ is defined as [13]:

$$\tilde{\alpha} = \frac{1}{\tilde{R}^2 \tilde{U}^2} \int_0^{\tilde{R}} 2\tilde{v}_z^2 \tilde{r} d\tilde{r}.$$

2.2.5 The reduced averaged equations in dimensional form

Consider the averaged cross-sectional velocity U , the concentration C defined by eq. (2.3), and the coefficients α and ω defined by

$$\alpha = \frac{1}{R^2} \int_0^R 2v_z^2 r dr, \quad \omega = \frac{1}{R^2} \int_0^R 2v_z c r dr.$$

From $U = B_z \tilde{U}$, $C = C_0 \tilde{C}$, we have $\alpha = \tilde{\alpha}$, $\omega = \tilde{\omega}$, and we can transform the reduced system into the following form:

$$\begin{cases} \frac{\partial}{\partial t} R^2 + \frac{\partial}{\partial z} (R^2 U) = 0 \\ \frac{\partial}{\partial t} (R^2 U) + \frac{\partial}{\partial z} (\alpha R^2 U^2) + \frac{R^2}{\rho} \frac{\partial p}{\partial z} = 2\nu R \left[\frac{\partial v_z}{\partial r} \right]_{r=R} \\ \frac{\partial}{\partial t} (R^2 C) + \frac{\partial}{\partial z} (\omega R^2 U C) = 2\mu R \left[\frac{\partial c}{\partial r} \right]_{r=R} \end{cases} \quad (2.11)$$

2.2.6 Closure of system (2.11)

System (2.11) involves 7 unknowns but has only 3 equations. We need therefore several closure assumptions.

- *The pressure.* In a standard way [84, 13, 84], we close system (2.11) by using hypothesis 5 to define the pressure p as an algebraic function of the section area $A = \pi R^2$.
- *The viscous term for the hydrodynamic part.* The coefficients α and ω as well as the viscous terms in (2.11) are affected by the choice of the velocity and concentration radial shape functions (f_v and f_c). Assuming hypothesis 2, it remains only to choose the function f_v . A typical approximation for the velocity profile is

$$f_v(r) = \frac{\gamma + 2}{\gamma} \left[1 - \left(\frac{r}{R} \right)^\gamma \right]. \quad (2.12)$$

This profile gives the following expression for the Coriolis parameter:

$$\alpha = \frac{1}{R^2} \int_0^R 2f_v^2(r)r \, dr = \frac{\gamma + 2}{\gamma + 1},$$

and an explicit formulation of the right hand side of the second equation in (2.11):

$$2\nu R \left[\frac{\partial v_z}{\partial r} \right]_{r=R} = -2\nu \left(\frac{\alpha}{\alpha - 1} \right) \frac{Q}{A}.$$

For blood flow, a suitable value for γ is 9, that gives $\alpha = 1.1$.

- *The viscous term of the TDE.* Thanks to (2.6), we have

$$2\mu R \left[\frac{\partial c}{\partial r} \right]_{r=R} = -2DRf_c(R)C.$$

We point out that, in order to have a concentration profile satisfying (2.6), f_c has to satisfy the compatibility condition

$$-\mu f_c'(R) = Df_c(R). \quad (2.13)$$

The normalized concentration profile can be for instance

$$f_c(r) = \frac{\kappa + 2}{\kappa + 2(1 - \delta)} \left[1 - \delta \left(\frac{r}{R} \right)^\kappa \right], \quad (2.14)$$

where κ and δ are constants that we can choose such that (2.13) holds. An explicit formula for ω is available in this case:

$$\begin{aligned} \omega &= \frac{1}{R^2} \int_0^R 2f_v(r)f_c(r)r \, dr \\ &= 2 \frac{(\gamma + 2)(\kappa + 2)}{\gamma(\kappa + 2(1 - \delta))} \left[1 - \frac{\delta}{\kappa + 2} - \frac{1}{\gamma + 2} + \frac{\delta}{\kappa + \gamma + 1} \right] \end{aligned}$$

and the following expression of the viscous term:

$$2\mu R \left[\frac{\partial c}{\partial r} \right]_{r=R} = -2DR \frac{(\kappa + 2)(1 - \delta)}{\kappa + 2(1 - \delta)} C.$$

Thanks to the closure assumptions, we end up with a 3×3 system for the unknowns

$$A = \pi R^2, \quad Q = AU, \quad \Gamma = AC,$$

that reads

$$\begin{cases} \partial_t A + \partial_z Q = 0, \\ \frac{\partial Q}{\partial t} + \frac{\partial}{\partial z} \left(\alpha \frac{Q^2}{A} \right) + c_1^2(A) \frac{\partial A}{\partial z} = -K_u \frac{Q}{A}, \\ \partial_t \Gamma + \partial_z \left(\omega \frac{\Gamma Q}{A} \right) = -K_C \frac{\Gamma}{A}, \end{cases} \quad (2.15)$$

where

$$\begin{aligned} K_u &= 2\pi\nu \left(\frac{\alpha}{\alpha - 1} \right), \\ K_C &= 2\pi DR \frac{(\kappa + 2)(1 - \delta)}{\kappa + 2(1 - \delta)}, \\ c_1^2(A) &= \frac{A}{\rho} \frac{\partial p(A)}{\partial z} = \frac{G_0}{2\rho A_0^{1/2}} A^{1/2}. \end{aligned}$$

Let $u = Q/A$ be the mean blood velocity; in eq. (2.15), the linear concentration Γ is transported by an "effective velocity" ωu . We point out that ω could be different than one. For instance, when Γ is the (linear) *hematocrit*, the well-known *Fahraeus-Lindqvist effect* (see for instance [78]) can be described by $\omega > 1$.

2.3 Characteristics

The reduced model (2.15) is hyperbolic, and admits the following conservation form:

$$\frac{\partial \mathbf{U}}{\partial t} + \frac{\partial}{\partial z} \mathbf{F}(\mathbf{U}) = \mathbf{S}(\mathbf{U}), \quad (2.16)$$

where

$$\mathbf{U} = \begin{bmatrix} A \\ Q \\ \Gamma \end{bmatrix}, \quad \mathbf{F}(\mathbf{U}) = \begin{bmatrix} Q \\ \alpha \frac{Q^2}{A^2} + \frac{G_0}{2\rho A_0^{1/2}} A^{3/2} \\ \omega \frac{Q\Gamma}{A} \end{bmatrix}, \quad \mathbf{S}(\mathbf{U}) = \begin{bmatrix} 0 \\ -K_u Q/A \\ -K_c \Gamma/A \end{bmatrix}.$$

Introducing the flux matrix

$$H(\mathbf{U}) = \frac{\partial \mathbf{F}}{\partial \mathbf{U}} = \begin{bmatrix} 0 & 1 & 0 \\ c_1^2(A) - \alpha \frac{Q^2}{A^2} & 2\frac{Q}{A} & 0 \\ -\omega \frac{Q\Gamma}{A^2} & \omega \frac{\Gamma}{A} & \omega \frac{Q}{A} \end{bmatrix}, \quad (2.17)$$

we obtain a non-conservative formulation:

$$\frac{\partial \mathbf{U}}{\partial t} + H(\mathbf{U}) \frac{\partial \mathbf{U}}{\partial z} = \mathbf{S}(\mathbf{U}). \quad (2.18)$$

All the properties of this system hold also when several chemical linear concentrations Γ_i , $i = 1, \dots, N$ are considered instead of one: each concentration Γ_i obeys to an equation like (2.15)₃.

We point out that even if the third equation in (2.15) does not influence the first two equations of (2.15), an analysis of the whole system is necessary, in order to set up the correct boundary conditions (based on the characteristic variables).

In what follows, we will use the notation

$$u = \frac{Q}{A}, \quad c_\alpha(A, Q) = \sqrt{c_1^2(A) + u^2 \alpha(\alpha - 1)},$$

where u is the *mean axial velocity*. Using Jensen's inequality, one can easily show that $\alpha \geq 1$, thus c_α is well-defined.

Property 2.3.1. *The matrix H admits three real eigenvalues:*

$$\lambda_1 = \alpha u - c_\alpha, \quad \lambda_2 = \alpha u + c_\alpha, \quad \lambda_3 = \omega u, \quad (2.19)$$

associated with the corresponding three left eigenvectors:

$$\mathbf{l}_1 = \zeta_1 \begin{bmatrix} -c_\alpha - \alpha u \\ 1 \\ 0 \end{bmatrix}, \quad \mathbf{l}_2 = \zeta_2 \begin{bmatrix} c_\alpha - \alpha u \\ 1 \\ 0 \end{bmatrix}, \quad \mathbf{l}_3 = \zeta_3 \begin{bmatrix} -\omega C \frac{1+u^2(1-\omega)(2-\omega)}{c_1^2+(2\omega-\omega^2-\alpha)u^2} \\ \omega u C \frac{1-\omega}{c_1^2+(2\omega-\omega^2-\alpha)u^2} \\ 1 \end{bmatrix},$$

$u = Q/A$ being the mean velocity, $C = \Gamma/A$ the (volumetric) concentration, and $(\zeta_1, \zeta_2, \zeta_3)$ arbitrary functions of the state variables.

For physiological values of the parameters, the *sound speed* c_α (at which a perturbation propagates in the vessel) is two orders of magnitude greater than the typical mean axial velocity u ; this means that in practical computations, the eigenvalues are always distinct; moreover λ_1 is expected to be negative and λ_2 positive.

A fundamental step, from both the theoretical and numerical points of view, is the study of characteristic variables of the system. This analysis is based on the solution of the following characteristic differential equation:

$$\begin{cases} \frac{\partial \mathbf{W}}{\partial \mathbf{U}} = L(\mathbf{U}), & L(\mathbf{U}) = \begin{bmatrix} \mathbf{l}_1^T \\ \mathbf{l}_2^T \\ \mathbf{l}_3^T \end{bmatrix}, & \mathbf{W} = \begin{bmatrix} W_1 \\ W_2 \\ W_3 \end{bmatrix}, \\ \mathbf{W}(U^0) = \mathbf{W}^0 \end{cases} \quad (2.20)$$

where W_1, W_2 and W_3 are the characteristic variables, and L is the matrix whose rows contain three left eigenvectors of H corresponding to each eigenvalue.

Suppose that a solution of the characteristic equations exists, at least locally. In this case, L being non singular, the mapping $\mathbf{W} = \mathbf{W}(\mathbf{U})$ between the state variables \mathbf{U} and the characteristic ones \mathbf{W} is one-to-one. Denote the inverse map by $\mathbf{U} = \mathbf{U}(\mathbf{W})$; if we adopt the characteristic variables to rewrite the system (2.16), we get

$$\frac{\partial \mathbf{W}}{\partial t} + \Lambda(\mathbf{W}) \frac{\partial \mathbf{W}}{\partial z} = L(\mathbf{W}) \mathbf{S}(\mathbf{W}), \quad (2.21)$$

where Λ is the diagonal matrix of eigenvalues $\lambda_i(\mathbf{U}(\mathbf{W}))$, while $L(\mathbf{W}) = L(\mathbf{U}(\mathbf{W}))$ and $\mathbf{S}(\mathbf{W}) = \mathbf{S}(\mathbf{U}(\mathbf{W}))$. System (2.21) is diagonal with respect to the derivatives of \mathbf{W} .

Remark 2.3.1. *The sign of the eigenvalues λ_i determines the number of boundary conditions to impose at each end. While for the haemodynamic part there is always one positive (resp. one negative) eigenvalue, for the transport equation the sign of λ_3 is not defined a priori. Thus, for the fluid equations, we will impose always one boundary condition at each end, while for the convection-reaction equation the number of boundary conditions depends on the sign of u at each boundary point.*

In the next section, we will study in detail the case of *flat profiles*, in which it is possible to explicitly solve (2.20) and compute the characteristic variables globally as functions of the physical ones.

2.4 Analysis of the system for *flat profile*

In the *flat profile* case (that is, $f'_v = f'_c = 0$), the averaged quantities α and ω are identically equal to 1, the source terms vanish, and equations (2.20) can be solved analytically.

The characteristic variables W_1 and W_2 , that will be denoted by r and s in this case, are independent of Γ (as the third component of \mathbf{l}_1 and \mathbf{l}_2 is zero), so we follow the method outlined in [84] to integrate the first two equations of (2.20). We adopt the integration factors $\zeta_1 = -A^{-1}$ and $\zeta_2 = A^{-1}$, and find

$$r = -u + 4c_1, \quad s = u + 4c_1. \quad (2.22)$$

The calculation of the third characteristic variable is easily done in the same manner (with $\mathbf{l}_3 = [-C, 0, 1]^t$ and $\zeta_3 = A^{-1}$), and we get

$$C \equiv W_3 = \Gamma/A. \quad (2.23)$$

Actually, defining z_c as a characteristic curve associated to the third equation

$$\begin{cases} \frac{dz_c}{dt} = u(z_c(t), t), & t \geq 0 \\ z_c(0) = \xi, & \xi \in [0, L_0] \end{cases},$$

we can see that C is constant along this trajectory. In fact:

$$\begin{aligned} 0 &= \frac{\partial \Gamma}{\partial t} + \frac{\partial}{\partial z} \left(\frac{Q}{A} \Gamma \right) = \frac{\partial A}{\partial t} C + A \frac{\partial C}{\partial t} + \frac{\partial Q}{\partial z} C + Q \frac{\partial C}{\partial z} \\ &= A \frac{\partial C}{\partial t} + Q \frac{\partial C}{\partial z} = A \left(\frac{\partial C}{\partial t} + u \frac{\partial C}{\partial z} \right) \\ &= A \frac{d}{dt} C(z_c(t), t), \end{aligned}$$

where we used (2.15)₁ and the definition of characteristic curve.

Let us write our system in terms of characteristic variables. Since we have no viscous terms, equations (2.21) read

$$\begin{cases} \frac{\partial r}{\partial t} + \lambda_1(r, s) \frac{\partial r}{\partial z} = 0, \\ \frac{\partial s}{\partial t} + \lambda_2(r, s) \frac{\partial s}{\partial z} = 0, \\ \frac{\partial C}{\partial t} + \lambda_3(r, s) \frac{\partial C}{\partial z} = 0, \end{cases} \quad (2.24)$$

where by eq. (2.19), (2.22) and (2.23) we have

$$\lambda_1(r, s) = -\frac{5}{8}r + \frac{3}{8}s, \quad \lambda_2(r, s) = -\frac{3}{8}r + \frac{5}{8}s, \quad \lambda_3(r, s) = -\frac{1}{2}r + \frac{1}{2}s. \quad (2.25)$$

The existence of a global solution for the first two equations (in the semi-infinite domain $z \geq 0, t \geq 0$) was proved in [56, 13] under certain assumptions on the boundary conditions. Here we follow a similar approach, in the case of a finite vessel with “resistive” load at the right end: this is often used in the multiscale modelling of the cardiovascular system to account for the remaining circulation, and in particular the capillary bed. Once r and s are found, the third transport equation

is easily solved: moreover, this equation can be coupled with “external” dynamical systems (we will present some numerical examples in the next section).

It has been shown in [13] that shocks can occur due to the non-linear nature of the fluid equations; thus, only under additional assumptions on the initial and boundary data a classical global solution exists. The initial data for problem (2.24) read

$$\begin{cases} r(z, 0) = r_0(z) & \text{for } 0 \leq z \leq L_0, \\ s(z, 0) = s_0(z) & \text{for } 0 \leq z \leq L_0, \\ C(z, 0) = C_0(z) & \text{for } 0 \leq z \leq L_0, \end{cases} \quad (2.26)$$

Moreover, we can assign a Dirichlet boundary data to each *incoming* characteristic, eventually dependent on time t and on the *outgoing* characteristic variable. If we suppose that $\lambda_1 < 0$, $\lambda_2 > 0$, and $\lambda_3 > 0$, we should consider the following boundary conditions:

$$\begin{cases} s(z, t) = g(t, r(z, t)) & \text{on } z = 0, t \geq 0, \\ r(z, t) = f(t, s(z, t)) & \text{on } z = L_0, t \geq 0, \\ C(z, t) = C_{in}(t) & \text{on } z = 0, t \geq 0. \end{cases} \quad (2.27)$$

The boundary and initial conditions satisfy the following *compatibility conditions*

$$\begin{aligned} g(0, r_0(0)) &= s_0(0), \\ f(0, s_0(L_0)) &= r_0(L_0), \\ C_{in}(0) &= C_0(0), \\ -\lambda_1(r_0(0), s_0(0))r'_0(0) &= -\partial_s g(0, s_0(0)) \lambda_2(r_0(0), s_0(0)) s'_0(0) \\ &\quad + \partial_t g(0, s_0(0)); \\ -\lambda_2(r_0(L_0), s_0(L_0))s'_0(L_0) &= -\partial_r f(0, r_0(L_0)) \lambda_1(r_0(L_0), s_0(L_0)) r'_0(L_0) \\ &\quad + \partial_t f(0, r_0(L_0)), \\ -\lambda_3(r_0(0), s_0(0))C'_0(0) &= C'_{in}(0), \end{aligned} \quad (2.28)$$

that is we require the continuity of the variables and their derivatives along the incoming characteristics for $t = 0$ at $z = 0$ and $z = L_0$.

Now we are able to state the global existence result:

Theorem 2.4.1. *Suppose that:*

- a) $r_0, s_0, C_0 \in C^1(0, L_0)$, $f, g \in C^1$, and equations (2.28) hold;
- b) $r'_0 \leq 0$, $s'_0 \geq 0$;
- c) (i) the function g satisfies $\partial g / \partial r \geq 0$, $\partial g / \partial t \leq 0$;
(ii) the function f satisfies $\partial f / \partial s \geq 0$ and $\partial f / \partial t \leq 0$;
- d) there exist $\eta \in (\frac{3}{5}, 1)$, $s_0^{\min} > 0$ and $s_0^{\max} > 0$ such that

$$\eta s_0(z) < r_0(z) < s_0(z), \quad s_0^{\min} < s_0(z) < s_0^{\max} \quad \forall z \in [0, L_0];$$

- e) The functions f and g satisfy the following estimates with respect to their arguments:

$$\eta s < f(t, s) < s, \quad \forall s \in (s_0^{\min}, s_0^{\max}), \quad s_0^{\min} < g(t, r) < s_0^{\max}, \quad \forall r \in (\eta s_0^{\min}, s_0^{\max});$$

f) There is $\epsilon > 0$ such that

$$\lambda_1(r(t, 0), s(t, 0)) < -\epsilon, \quad \lambda_2(r(t, L_0), s(t, L_0)) > \epsilon \quad \text{and} \quad \lambda_3(r(t, 0), s(t, 0)) > \epsilon, \quad \forall t > 0;$$

g) the eigenvalues satisfy $\partial\lambda_1/\partial r \leq 0$ and $\partial\lambda_2/\partial s \geq 0$.

Then, there exists a (unique) global classical solution $(r, s, C) \in C^1(\mathbb{R}^+ \times [0, L_0])^3$ for the problem (2.24, 2.25), satisfying (2.26) and (2.27).

Proof. If we prove that there is a classical solution of the (r, s) problem (2.24)_{1,2} such that $\lambda_3(r(t, z), s(t, z)) > 0$, $\forall (t, z) \in \mathbb{R}^+ \times [0, L_0]$, then theorem 2.4.1 follows from standard results applied to the linear scalar hyperbolic equation (2.24)₃. Therefore, in the sequel we focus on the problem (2.24)_{1,2} for r and s .

System (2.24)_{1,2} is strictly hyperbolic i.e.

$$\lambda_2(r(t, z), s(t, z)) > \lambda_1(r(t, z), s(t, z)), \quad \forall (t, z) \in \mathbb{R}^+ \times [0, L_0]$$

provided that $\lambda_2 - \lambda_1 > 0$ at $t = 0$ and on the boundary, as shown in [13] (and in [56] for the analogous case of isentropic 1D gas flow). By hypothesis d), at $t = 0$ we have $\lambda_2(r(0, z), s(0, z)) - \lambda_1(r(0, z), s(0, z)) = s_0(z) - r_0(z) > 0$; by f) we have $\lambda_2 - \lambda_1 > 2\epsilon > 0$ on the boundary. So the eigenvalues satisfy $\lambda_2 > \lambda_1$ everywhere. We denote by $z = z_s^0(t)$ the forward characteristic emanating from $(t, z) = (0, 0)$, and by $z = z_r^{L_0}(t)$ the backward one emanating from $(t, z) = (0, L_0)$. In what follows, $T > 0$ is the first time at which z_s^0 crosses $z_r^{L_0}$, that is $z_s^0(T) = z_r^{L_0}(T)$. Moreover, we define $D = [0, T] \times [0, L_0]$, $D_1 = \{(t, z) \in D : z_s^0(t) \leq z \leq z_r^{L_0}(t)\}$, $D_2 = \{(t, z) \in D : 0 \leq z \leq z_s^0(t)\}$, and $D_3 = \{(t, z) \in D : z_r^{L_0}(t) \leq z \leq L_0\}$.

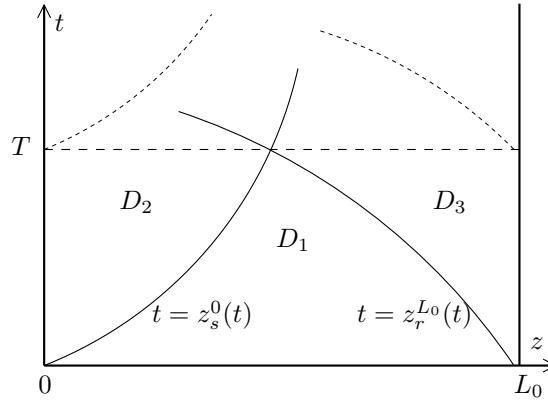


Figure 2.2: The domain $D = \bigcup_{i=1}^3 D_i$.

The smoothness of the initial data, together with hypothesis b) and the strict hyperbolicity of the system, guarantees [56] that there is a classical solution (r, s) in D_1 , such that

$$\partial r / \partial z \leq 0, \quad \partial s / \partial z \geq 0. \quad (2.29)$$

As in [13], due to the additional hypotheses b), c)_(i), g), and to the compatibility conditions (2.28), the solution is extended to D_2 where it still satisfies (2.29); moreover, the solution is $C^1(D_1 \cup D_2)$. Using exactly the same technique with c)_(ii) instead of c)_(i), the solution is extended to D_3 , where (2.29) holds, the extension being in $C^1(D)$ (see also the recent work [2]).

Now, to prove our assertion we have to consider the following steps.

1. *Sign of λ_3 .* Consider a generic forward characteristic curve z_s . As $\partial r/\partial z \leq 0$ and $\lambda_2 - \lambda_1 > 0$ everywhere, we have

$$\begin{aligned} \frac{d\lambda_3}{dt}(r(t, z_s(t)), s(t, z_s(t))) &= \frac{1}{2} \frac{d}{dt}(s(t, z_s(t)) - r(t, z_s(t))) = -\frac{1}{2} \frac{dr(t, z_s(t))}{dt} \\ &= -\frac{1}{2}(\lambda_2 - \lambda_1)|_{(r(t, z_s(t)), s(t, z_s(t)))} \frac{\partial r(t, z_s(t))}{\partial z} \geq 0, \end{aligned}$$

that is λ_3 increases along z_s . As $\lambda_3(r(0, z), s(0, z)) = (s(0, z) - r(0, z))/2 > 0$, $\forall z \in [0, L_0]$ by f) and $\lambda_3(r(t, 0), s(t, 0)) > \epsilon > 0$, $\forall t > 0$ by d), and as λ_3 increases on every forward characteristic, we obtain $\lambda_3 > \epsilon$ in the whole D , so that there exists a unique solution C of (2.24)₃ with initial and boundary data given by (2.26)₃, (2.27)₃.

2. *Global estimates.* We need some global estimates in order to increase the time of existence of our solution. Notice that along the backward characteristics $(ds/dt)_{z=z_r(t)} = (\lambda_1 - \lambda_2)\partial s/\partial z \leq 0$. Since $\eta s < r$ at $t = 0$ by d) and on $z = 0$ by e), and using the fact that along the backward characteristics r is constant and s is non-increasing, we have that $\eta s < r$ holds in the whole D . In the same way, as $s_0^{\min} < s < s_0^{\max}$ at $t = 0$ and on $z = 0$, propagating this inequality along the forward characteristics we obtain $s < s_0^{\max}$ in the whole D . Finally, $r - s = 2\lambda_3 > 0$ in D , and summarizing we have

$$\eta s < r < s, \quad s_0^{\min} < s < s_0^{\max} \quad \text{in } D. \quad (2.30)$$

Then, since $\eta > 3/5$, we get $\forall (t, z) \in D$

$$\lambda_1 < \frac{-5\eta + 3}{8}s < \frac{-5\eta + 3}{8}s_0^{\min} < 0, \quad \lambda_2 > \frac{s}{4} > \frac{s_0^{\min}}{4} > 0.$$

These estimates are uniform in time, because they only depend on the constants η and s_0^{\min} . Thus, we have a lower bound for the time T that it takes for the characteristics to cross:

$$T > \frac{L_0/2}{\min\{(5\eta - 3)s_0^{\min}/8, s_0^{\min}/4\}} = \frac{4L_0}{(5\eta - 3)s_0^{\min}} = T_{\min} > 0.$$

3. *Restart from $t = T$.* Now we can consider $t = T$ as a new initial time and $r(T, z)$, $s(T, z)$, $C(T, z)$ as new initial conditions. By (2.30), the new initial data satisfy the hypotheses b) and e); moreover, the compatibility conditions (2.28) hold at $(t, z) = (T, 0)$ and (T, L_0) as the solution is $C^1(D)$. It follows that we can extend the solution to a new domain $D' = [0, T'] \times [0, L_0]$, and so on recursively. At each prolongation we advance by a time greater than T_{\min} ; this proves that a global solution in $\mathbb{R}^+ \times [0, L_0]$ exists. ■

To show that theorem 2.4.1 can be applied to our blood flow problem with mass transport, we impose the blood velocity $u_{in}(t)$ (as in [13]) and the chemical concentration $C_{in}(t)$ at the inlet $z = 0$, and a generic (algebraic) constitutive law for the load at the outlet $z = L_0$. A constitutive law for a “resistive” load is a pressure vs. flow rate equation in the form $p = R(Q)$. However, we will suppose that the linearized equation $Q = Au \simeq A_0u$ holds at the vessel’s outlet, where A_0 is the reference section area. Hence, we will assume the following law for the load:

$$p = H(u), \quad (2.31)$$

where $H(u) = R(A_0u)$.

Property 2.4.1. *Define*

$$\begin{aligned} g(t, r) &= 2u_{in}(t) + r, \\ f(t, s) &= \phi(s), \end{aligned}$$

where ϕ is the solution of $F(\phi, s) = 0$, with

$$F(f, s) = p - H(u) = \frac{\rho}{32}(f + s)^2 - G_0 - H\left(\frac{-f + s}{2}\right). \quad (2.32)$$

Suppose that:

H1) there exists $u_{in}^{\min} > 0$ such that $u_{in}^{\min} < u_{in}(t) < \frac{4}{5}c_{1,0}$, where $c_{1,0} = c_1(A_0) = \sqrt{G_0/2\rho}$;

H2) the initial data r_0, s_0 satisfy hypotheses a), b), and d) of Theorem 2.4.1 with

$$s_0^{\min} = 4c_{1,0} \equiv \sqrt{8G_0/\rho}, \quad \eta = 1 - \frac{u_{in}^{\min}}{2c_{1,0}};$$

H3) the load function H satisfies $H(0) = 0$ and

$$H'(u) > m, \quad \forall u \in \mathbb{R},$$

$$\text{where } m = s_0^{\max} \rho \frac{2c_{1,0}}{u_{in}^{\min}}$$

If $u'_{in}(t) \leq 0$, then there exists a (unique) global classical solution $(r, s, C) \in C^1(\mathbb{R}^+ \times [0, L_0])^3$ for the problem (2.24), satisfying (2.26) and (2.27).

Proof. We have to show that hypotheses c)_(i), c)_(ii), e), f) and g) of Theorem 2.4.1 hold. Without loss of generality we consider only the domain D defined in the previous proof: propagating the initial data on the characteristics we have

$$\eta s_0^{\min} < r(t, 0) < s_0^{\max}, \quad s_0^{\min} < s(t, L_0) < s_0^{\max} \quad \forall t \in [0, T]. \quad (2.33)$$

Being $\partial g/\partial r = 1$ and $\partial g/\partial t = 2u'_{in} < 0$, hypothesis c)_(i) is satisfied. By H1 and H2, $\eta \in (\frac{3}{5}, 1)$ and hypothesis d) is satisfied as well.

Using (2.33) and hypotheses H1 and H2 we have that

$$s_0^{\min} = \frac{u_{in}^{\min}}{2c_{1,0}} s_0^{\min} + \eta s_0^{\min} < 2u_{in}^{\min}(t) + r < g(t, r) < g(0, r) = s_0(0) < s_0^{\max},$$

thus g satisfies e).

Now, we claim that the solution $\phi = \phi(s)$ of $F(\phi, s) = 0$ is in the interval $(\eta s, s)$ (note that if such a solution exists, it is unique because $H' > 0$ together with $s > 0$ imply that $\partial F/\partial \phi > 0$ for $\phi \in (\eta s, s)$). To show this, it suffices to prove that $F(s, s) > 0$ and $F(\eta s, s) < 0$, or, equivalently,

$$\frac{\rho}{8}s^2 - G_0 > 0 \text{ on } z = L_0, \quad (2.34)$$

$$\frac{\rho}{32}(\eta + 1)^2 s^2 - G_0 - H\left(\frac{\eta - 1}{2}s\right) < 0 \text{ on } z = L_0. \quad (2.35)$$

The inequality (2.34) is true by (2.33) and hypothesis H2. On the other hand, (2.35) is true if we show that

$$\frac{\rho}{32}(\eta + 1)^2 s^2 - G_0 - m \frac{\eta - 1}{2} s < 0,$$

which is satisfied if

$$0 < s < \frac{(1 - \eta)m + \sqrt{(1 - \eta)^2 m^2 + \rho(\eta + 1)^2 G_0/2}}{\rho(\eta + 1)^2/2}.$$

The latter inequality is true because $0 < s < s_0^{\max}$ and

$$\frac{(1 - \eta)m + \sqrt{(1 - \eta)^2 m^2 + \rho(\eta + 1)^2 G_0/2}}{\rho(\eta + 1)^2/2} > \frac{(1 - \eta)m}{\rho} = \frac{u_{in}^{\min} m}{\rho 2c_{1,0}} = s_0^{\max}.$$

Thus, f satisfies the hypothesis e) of Theorem 2.4.1.

Now we have to check that $\phi'(s) \geq 0$. From (2.32) we get

$$\frac{\rho}{16}(f(s) + s)(f'(s) + 1) - H' \left(\frac{-f + s}{2} \right) \frac{-f'(s) + 1}{2} = 0,$$

and then

$$\begin{aligned} f'(s) &= 1 - 2 \frac{\rho(f(s) + s)/16}{H'((-f(s) + s)/2)/2 + \rho(f(s) + s)/16} \\ &\geq 1 - 2 \frac{\rho(f(s) + s)}{8m + \rho(f(s) + s)} \geq 1 - 2 \frac{\rho s_0^{\max}}{4m + \rho s_0^{\max}}. \end{aligned}$$

As $m > \frac{5}{2} \rho s_0^{\max}$ by H3 and H1, we have that $f'(s) > 0$. So the function f satisfies the hypothesis c)_(ii) of Theorem 2.4.1.

Finally, consider the eigenvalues at the boundary: we have

$$\lambda_3(t, 0) = u_{in}(t) > u_{in}^{\min},$$

$$\lambda_1(t, 0) = -\frac{5}{8}r(t, 0) + \frac{3}{8}g(t, r(t, 0)) < -\frac{5}{8}r(t, 0) + \frac{3}{8}r(t, 0)/\eta < \frac{-5 + 3/\eta}{8}s_0^{\min},$$

$$\lambda_2(t, L_0) = -\frac{3}{8}f(t, s(t, L_0)) + \frac{5}{8}s(t, L_0) > -\frac{3}{8}s(t, L_0) + \frac{5}{8}s(t, L_0) > \frac{s_0^{\min}}{4}.$$

So f) holds with $\epsilon = \min \left\{ u_{in}^{\min}, \frac{5-3/\eta}{8}s_0^{\min}, \frac{s_0^{\min}}{4} \right\} > 0$. This completes the proof, g) having been fulfilled. ■

2.5 Taylor-Galerkin numerical approximation of the solution

We present the Taylor-Galerkin scheme for the system (2.18): this choice seems to be suitable as shock waves do not develop for the hydrodynamical variables in physiological conditions [13]. The last variable being the solution of a linear transport equation, we don't expect it to be discontinuous if the boundary/initial data are not. The scheme we will adopt is based on finite element, spatial

discretization and a second-order Taylor expansion for \mathbf{U} . We write the first and the second time derivatives of the unknown using (2.15), as follows:

$$\begin{aligned}\frac{\partial \mathbf{U}}{\partial t} &= \mathbf{S}(\mathbf{U}) - \frac{\partial}{\partial z} \mathbf{F}(\mathbf{U}), \\ \frac{\partial^2 \mathbf{U}}{\partial t^2} &= \frac{\partial \mathbf{S}(\mathbf{U})}{\partial \mathbf{U}} \left(\mathbf{S}(\mathbf{U}) - H(\mathbf{U}) \frac{\partial \mathbf{U}}{\partial z} \right) - \frac{\partial}{\partial z} \left[H(\mathbf{U}) \left(\mathbf{S}(\mathbf{U}) - H(\mathbf{U}) \frac{\partial \mathbf{U}}{\partial z} \right) \right],\end{aligned}$$

and the following semi-discrete time advancing scheme is considered:

$$\begin{aligned}\mathbf{U}^{n+1} &= \mathbf{U}^n + \Delta t \left(\mathbf{S}^n - \frac{\partial}{\partial z} \mathbf{F}^n \right) \\ &\quad + \frac{\Delta t^2}{2} \left\{ J^n \left(\mathbf{S}^n - H^n \frac{\partial \mathbf{U}^n}{\partial z} \right) - \frac{\partial}{\partial z} \left[H^n \left(\mathbf{S}^n - H^n \frac{\partial \mathbf{U}^n}{\partial z} \right) \right] \right\},\end{aligned}$$

where $\mathbf{U}^n(z)$ is the approximate solution at time $t_n = t_0 + n\Delta t$, and we set $\mathbf{S}^n = \mathbf{S}(\mathbf{U}^n)$, $\mathbf{F}^n = \mathbf{F}(\mathbf{U}^n)$, $J^n = \frac{\partial \mathbf{S}(\mathbf{U}^n)}{\partial \mathbf{U}}$, $H^n = H(\mathbf{U}^n)$.

Let $N_h \in \mathbb{N}$, $N_h > 0$, and $\{z_i = ih, i = 0, \dots, N_h\}$, being $h = \frac{L_0}{N_h}$. Consider the associated finite element space V_h of piecewise linear polynomials and the subspace $V_{0,h} = \{v \in V_h \mid v(0) = v(L_0) = 0\}$. We adopt the following Galerkin spatial discretization: *given \mathbf{U}_h^n , find $\mathbf{U}_h^{n+1} \in V_h^3$ such that for all $\phi_h \in V_{0,h}^3$*

$$\begin{aligned}(\mathbf{U}_h^{n+1}, \phi_h) &= (\mathbf{U}_h^n, \phi_h) - \frac{\Delta t^2}{2} (J^n H^n \frac{\partial \mathbf{U}^n}{\partial z}, \phi_h) - \frac{\Delta t^2}{2} (H^n H^n \frac{\partial \mathbf{U}^n}{\partial z}, \frac{\partial \phi_h}{\partial z}) \\ &\quad + (\Delta t \mathbf{S}^n + \frac{\Delta t^2}{2} J^n \mathbf{S}^n, \phi_h) + (\Delta t \mathbf{F}^n + \frac{\Delta t^2}{2} H^n \mathbf{S}^n, \frac{\partial \phi_h}{\partial z}),\end{aligned}$$

and

$$\mathbf{W}(\mathbf{U}_h^{n+1})|_{z=0} = \mathbf{W}_1^{n+1}, \quad \mathbf{W}(\mathbf{U}_h^{n+1})|_{z=L_0} = \mathbf{W}_2^{n+1},$$

where the components W_{ij}^{n+1} of \mathbf{W}_i^{n+1} , $i = 1, 2$, are the incoming characteristic boundary data or the outgoing characteristic extrapolation data at time t_{n+1} (depending on the sign of the associated eigenvalues, see [84]).

For instance, in $z = 0$ we extrapolate the outgoing variable W_1 and assign the corresponding boundary condition for W_2 and W_3 . Therefore, we set

$$\begin{aligned}W_{11}^{n+1} &:= W_1(t_n, -\lambda_1(t_n, 0)\Delta t) + \Delta t (\mathbf{I}_1^n(0))^T \mathbf{S}^n(0), \\ W_{12}^{n+1} &:= g(t_{n+1}, W_{11}^{n+1}), \\ W_{13}^{n+1} &:= C_{in}(t_{n+1}).\end{aligned}$$

This numerical method requires an analytic expression for the characteristic variables; therefore, we consider here the flat profile case. It is possible to use the same method but with a different treatment of boundary conditions also if non-flat velocity and/or concentration profiles are adopted [84]. Note that the extrapolation technique is based on a forward Euler step for the integration of characteristic equations (2.20). If flat profiles are assumed, we have $\mathbf{S} = \mathbf{0}$ and the characteristic variables are conserved along the characteristic curves. The numerical scheme entails a CFL stability condition with a CFL number equal to $1/\sqrt{3}$ [83], more precisely:

$$\Delta t \leq \frac{\Delta z}{\sqrt{3} (\max\{|\lambda_i(z_j)|, i \in \{1, \dots, 3\}, j \in \{1, \dots, N_h\}\})}.$$

Some numerical results with a pure resistive load and standard aorta parameters are reported in fig. 2.7, where the section area A , the flow rate Q and the oxygen linear concentration Γ are shown. The vessel reference section area is $A_0 = 3.14$ cm. We consider a pulsatile input blood velocity $u_{in}(t)$ at heart rates corresponding to rest conditions (1 bpm) and mean flow rate $Q_0 = 4.98$ lit min⁻¹, as in fig. 2.3. The oxygen concentration in blood is assumed [77] to be $C = \Gamma/A = 0.2$ ml O₂ ml⁻¹ blood =

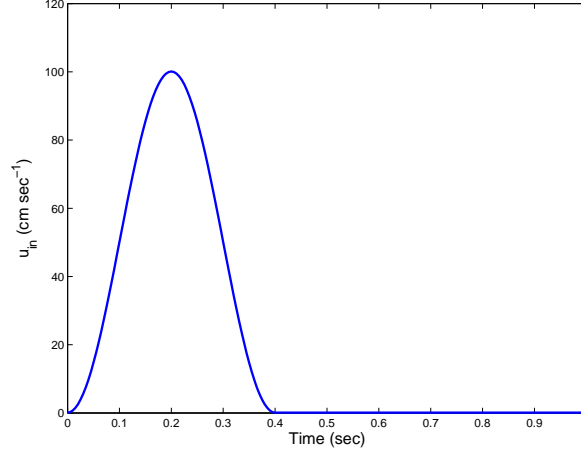


Figure 2.3: Imposed inlet blood velocity u_{in} (one period).

8.75 $\mu\text{mol ml}^{-1}$, with a step-shaped initial condition in order to display the wavefront progress. In one heart beat the wavefront moves on and covers 28 cm; this result is consistent with the mean blood velocity (that is $\int_0^1 Q(t,0)/A(t,0)dt$). In this simulation, the load is represented by a pure resistance $R = 0.3$ mmHg sec cm⁻³, that is a standard $\Delta p/\Delta Q$ ratio, where Δp and ΔQ are the mean variations of pressure and flow rate during an heart period in a large artery.

We choose a 60 cm vessel length in order to show the wave propagation. In our model the reference pressure value is zero: we only deal with *pressure variations*. The “physiological” pressure, is obtained by adding the pressure offset (90 mmHg), corresponding to rest condition, to the results. The resistive load causes the formation of several non negligible reflected waves: we observed three reflections, as it is shown by the pressure time course of fig. 2.4. Moreover, the smaller the peripheral resistance, the larger the reflected pressure waves: this is shown in fig. 2.5 where pressure profiles for $R = 0.08$ mmHg sec cm⁻³ are reported at the vessel inlet and outlet.

More realistic results are obtained with a *coupled system*, in which a 0D model described by *ordinary differential equations* represents the vessel load [29]. We point out that in this way we can take into account the substrate metabolism in tissues as well as the peripheral capillary resistance and compliance. The 0D model, depicted in fig. 2.5, has the following state equations:

$$\begin{cases} C \frac{dp_C(t)}{dt} = -\frac{p_C(t)}{R_2} + Q(t), \\ M \frac{dC_T(t)}{dt} = Q(t) \left(\frac{\Gamma(t)}{A(t)} - \sigma C_T(t) \right) - v(C_T(t), t) \end{cases}$$

where C and R_2 are respectively the hydraulic compliance and resistance of the load, p_C is the pressure on the compliance, C_T is the substrate concentration in the tissue, M is the tissue volume (or mass, depending on the C_T definition), σ is the a partition coefficient, and v is the metabolic rate of consumption of the substrate. The pressure p appearing as boundary value in the 1D model is given

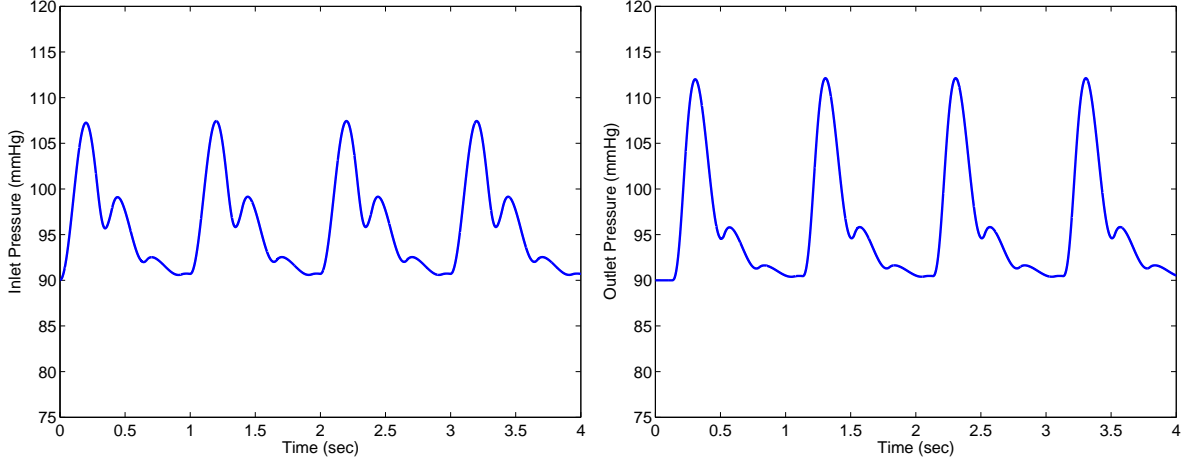


Figure 2.4: Inlet/outlet pressure time course in a 60 cm 1D model of a vessel with a pure resistive load $R = 0.3 \text{ mmHg sec cm}^{-3}$.

by

$$p(t) = p_C(t) + R_1 Q(t),$$

where R_1 is a further hydrodynamic resistance. As regards the blood-tissue exchanges, we proceed as in chapter 1: we assume that the relation between the tissue concentration C_T and the venous concentration C_v in the blood leaving the tissue is *linear*, $C_v = \sigma C_T$, being σ the partition coefficient.

A possible choice for the metabolic rate v is the Michaelis-Menten law that reads

$$v = V_{max}(t) \frac{C_T}{C_{0.5} + C_T}, \quad (2.36)$$

where $V_{max}(t)$ is the maximum consumption rate and $C_{0.5}$ is the characteristic concentration.

Here we detail the interface conditions used to couple both systems [29, 31]. Suppose that the boundary values $A^n(L_0)$, $Q^n(L_0)$, $\Gamma^n(L_0)$ of the 1D model are known at time t_n , and consider a forward Euler step on the 0D model, that is

$$\begin{aligned} Cp_C^{n+1} &= Cp_C^n + \Delta t \left(-\frac{p_C^n}{R_2} + Q^n(L_0) \right), \\ MC_T^{n+1} &= MC_T^n + \Delta t \left(Q^n(L_0) \left(\frac{\Gamma^n(L_0)}{A^n(L_0)} - \sigma C_T^n \right) - v(C_T^n, t_n) \right), \\ p^{n+1} &= p_C^{n+1} + R_1 Q^n. \end{aligned}$$

Then, the new value of the pressure p^{n+1} can be used to update the characteristic variables:

$$\begin{aligned} W_{22}^{n+1} &= W_2(t_n, -\lambda_2(t_n, L_0)\Delta t) + \Delta t (\mathbf{1}_2^n(0))^T \mathbf{S}^n(0), \\ W_{21}^{n+1} &= -W_{22}^{n+1} + 8 \left(\frac{G_0}{2\rho} \right)^{1/2} A_0^{1/2} \sqrt{p^{n+1}/G_0 + 1}, \end{aligned}$$

i.e. we extrapolate the outgoing characteristic variable and then we assign the incoming one using the boundary value provided by the 0D model.

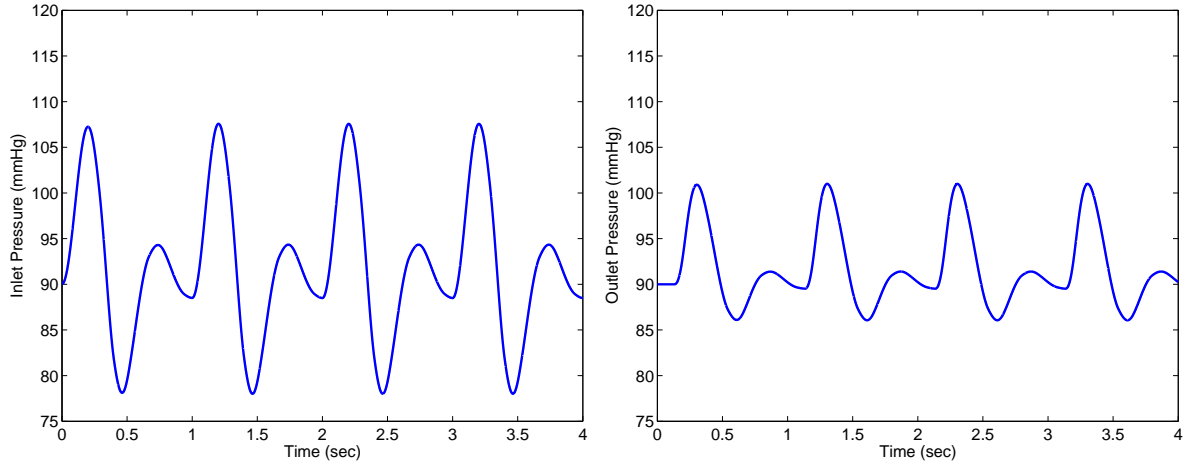


Figure 2.5: Inlet/outlet pressure time course in a 60 cm 1D model of a vessel with a pure resistive load $R = 0.08 \text{ mmHg sec cm}^{-3}$.

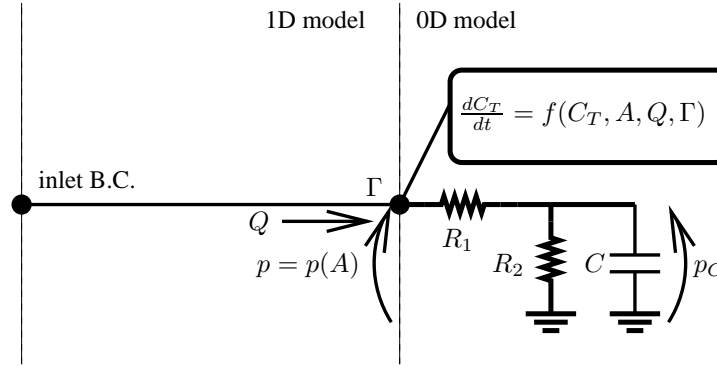


Figure 2.6: Multiscale coupling.

In fig. 2.8 the input/output pressure profiles during four heart beats are reported. We observe that the pressures are in the clinical range, and that the peripheral compliance acts like a damper with respects to the reflections, that were more important in fig. 2.4 and 2.5).

In fig. 2.9 we show the evolution in time of C_T for the coupled 1D-0D system with oxygen transport. For the sake of simplicity, the load is representative of all the tissues fed by the systemic circulation. In this simulation C and R are respectively the total arterial compliance and resistance (we considered $C = 0.1 \text{ cm}^3 \text{ mmHg}^{-1}$ [99] and $R_1 = 0.02 \text{ mmHg sec cm}^{-3}$, $R_2 = 0.08 \text{ mmHg sec cm}^{-3}$, in such a way that the total static resistance equals $0.1 \text{ mmHg sec cm}^{-3}$. The mean oxygen concentration in arterial blood, as well as the constant boundary value C_{in} , is $8.75 \mu\text{mol ml}^{-1}$; at rest the body consumes $V_0 = 0.18 \text{ mmol s}^{-1}$ of oxygen and the mean oxygen concentration² in tissues is $C_{T,0} = 6.5 \text{ mmol kgdw}^{-1}$, so that we use (2.36) with $V_{max} = 2V_0$ and $C_{0.5} = 6.5 \text{ mmol kgdw}^{-1}$. Finally, we assume that the total tissue dry weight is $M = 10 \text{ kgdw}$, and that the partition coefficient σ is such that the balance $Q_0(C_{in} - \sigma C_{T,0}) - V_0 = 0$ holds, that is $\sigma = (C_{in} - V_0/Q_0)/C_{T,0} =$

² Tissue concentrations are often measured in terms of millimoles per kilogram of *dry weight* of tissue is (mmol kgdw^{-1}). The values are extracted from [11].

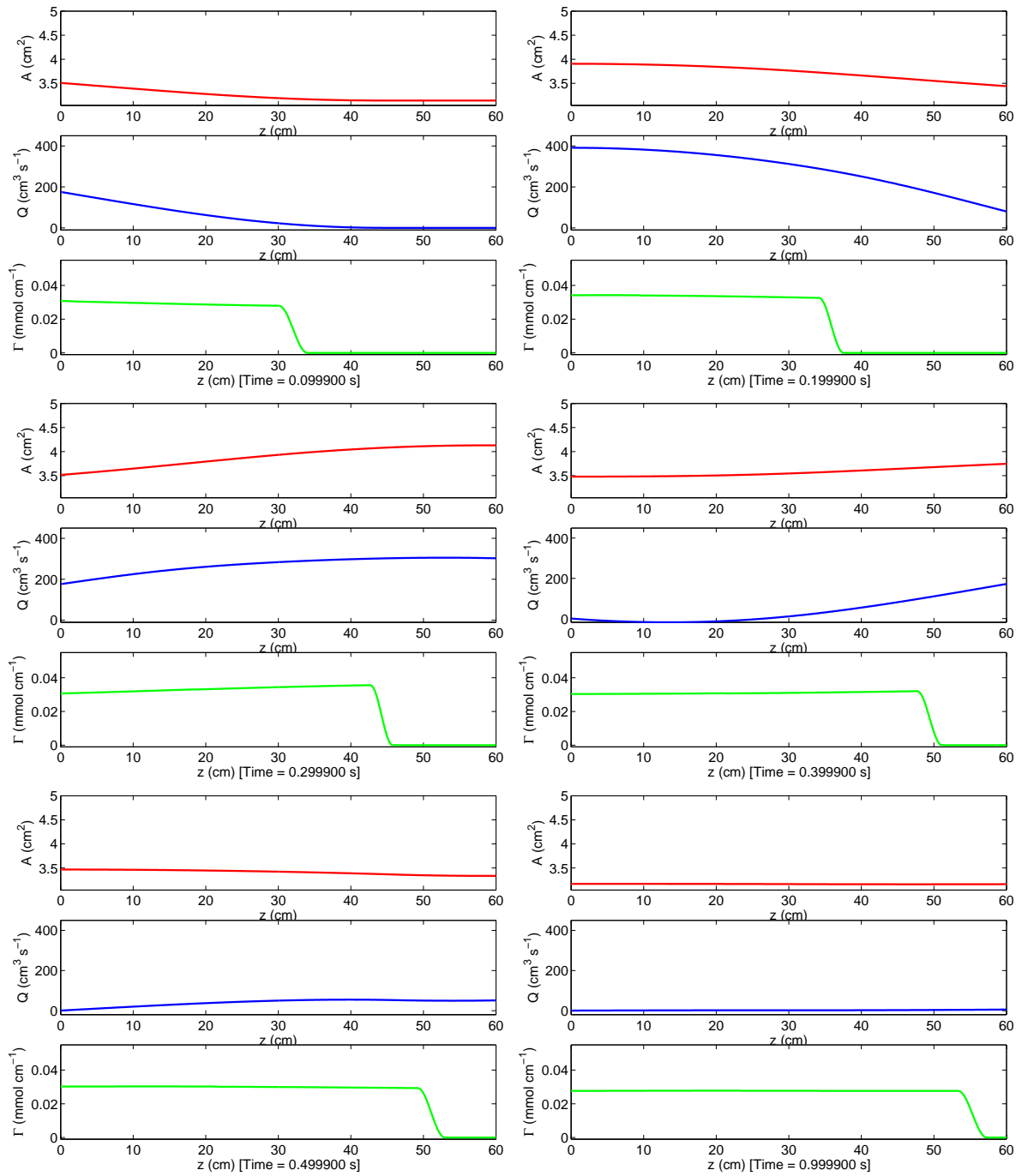


Figure 2.7: Section area (cm^2), flow rate ($\text{cm}^2 \text{sec}^{-1}$) and linear concentration (mmol cm^{-1}) waves in a 60 cm 1D model of a vessel with a load $R = 0.3 \text{ mmHg sec cm}^{-3}$.

$10^{-3} \text{ kgdw ml}^{-1}$.

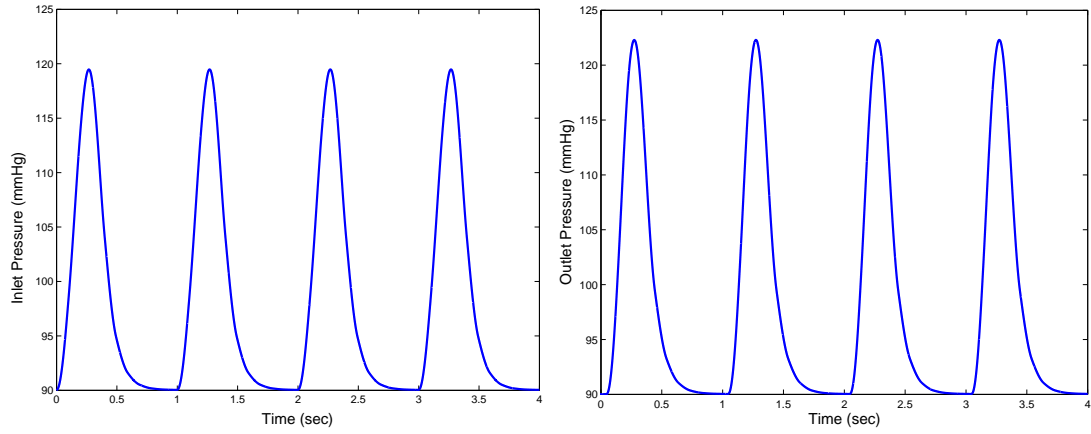


Figure 2.8: Inlet and outlet pressure (dynamic *RCR* load).

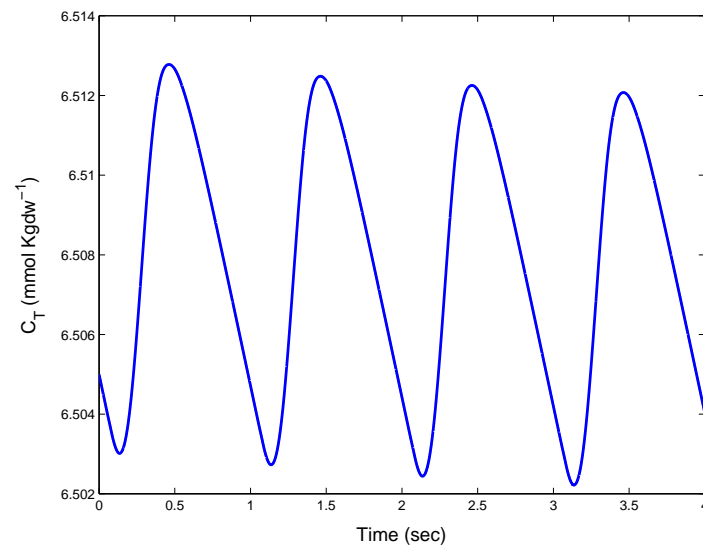


Figure 2.9: Oxygen concentration in the tissue compartment, dynamic *RCR* load.

Chapter 3

Introducing coupled 1D-3D diffusion-reaction models

3.1 Introduction

In this chapter, we are going to study the coupling between two diffusion-reaction phenomena, one taking place in a three-dimensional medium, the other on a one-dimensional subdomain, and both depending on each other by some exchange terms.

Our analysis is motivated by the increasing use of multi-scale approaches in biomathematics. As an example, let us consider variables like the partial pressure of oxygen (or its concentration), or the blood temperature: usually they are found to satisfy *fast* diffusion-reaction-advection equations (advection-dominated) in the net of “big to medium-scale” vessels (macroscale), while they feature a *slow* dynamics in the matrix of “small” vessels (microscale). Typically, homogenized 3D models can suitably represent the phenomena related to the microscale (for example Darcy flow) without resolving its fine structure. But this is not the case for the macroscale, where the branching vessel geometry has to be considered, and can still be too complex to afford the computational costs of a 3D model. A possible cure, supported by the extremely small ratio between the typical vessel diameter and the size of the tissue region, is to resort to 1D circulation models. The advantage of such an approach is clearly its efficiency: it does not need a very refined computational grid near the vessels, allowing for a large economy of memory and CPU utilization. The drawback is that the coupling conditions between tissue and vessels are non-standard.

This and the next chapter are devoted to the mathematical justification and analysis of such coupled problems, while the next one will focus on their applications. For the sake of simplicity, we first consider model problems only; in chapter 6 we will focus on applications.

To sum up, the plan of chapters 3 - 5 is as follows.

- In this chapter, we introduce the vessel-tissue coupling for our model equations, and derive an asymptotic 1D-3D problem. We will see that the asymptotic 3D problem has non-smooth (*measure*) data, so that its solution is somehow singular.
- In chapter 4, we consider suitable functional spaces in which the well-posedness of our 3D singular problem can be established. We use the results for the analysis of the coupled 1D-3D problem.
- In chapter 5, we study the numerical approximation of the solution of the 1D-3D coupled problem.

3.2 The problem and model equations

3.2.1 Geometry

In the sequel we shall consider a tissue domain $\Omega \subset \mathbb{R}^3$, containing a 1D manifold, like a line or a tree, that represents a blood vessel. We will introduce the actual 3D space occupied by the vessel as well, and the actual bidimensional interface between the vessel and the tissue, but only to recover physically meaningful coupling conditions. As shown in fig. 3.1, these objects can be mathematically defined as follows.

- The 1D manifold, representing the vessel, will be denoted by Λ . For the sake of simplicity, let us assume that Λ is a single line:

$$\Lambda = \{\mathbf{x} \in \Omega : \mathbf{x} = \mathbf{x}_v(s), s \in (s_1, s_2)\}, \quad (3.1)$$

where s is the curvilinear abscissa, and $\mathbf{x}_v : (s_1, s_2) \rightarrow \mathbb{R}^3$ is the related smooth parametrization. This assumption can easily be extended to consider branching geometries too, however this topic will be addressed only in the next chapter.

- We assume that the actual vessel radius is a positive constant $R > 0$. Then, we introduce the actual volume occupied by the vessel as the set of point closer than $R > 0$ to Λ :

$$\Omega_v^R := \{\mathbf{x} \in \mathbb{R}^n : \text{dist}(\mathbf{x}, \Lambda) < R\}.$$

We will use this domain to study the coupling conditions between the tissue and the one-dimensional vessel. Of course, we assume that R is small enough so that $\overline{\Omega_v^R} \subset \Omega$.

We will equip Ω_v^R with an atlas consisting of three local maps. To this end, define

$$\begin{aligned} \Omega_{v,0}^R &= \{\mathbf{x} \in \mathbb{R}^3 : \mathbf{x} = \mathbf{x}_{v,0}(s, r, \theta), (s, r, \theta) \in (s_1, s_2) \times [0, R] \times [0, 2\pi)\}, \\ \Omega_{v,1}^R &= \{\mathbf{x} \in \mathbb{R}^3 : \mathbf{x} = \mathbf{x}_{v,1}(r, \theta, \phi), (r, \theta, \phi) \in [0, R] \times [0, 2\pi) \times [0, \pi)\}, \\ \Omega_{v,2}^R &= \{\mathbf{x} \in \mathbb{R}^3 : \mathbf{x} = \mathbf{x}_{v,2}(r, \theta, \phi), (r, \theta, \phi) \in [0, R] \times [0, 2\pi) \times [0, \pi)\}, \end{aligned} \quad (3.2)$$

being

$$\begin{aligned} \mathbf{x}_{v,0}(s, r, \theta) &= \mathbf{x}_v(s) + \mathbf{n}(s)r \cos \theta + \mathbf{b}(s)r \sin \theta, \\ \mathbf{x}_{v,1}(r, \theta, \phi) &= \mathbf{x}_v(s_1) + \mathbf{n}(s_1)r \cos \theta \sin \phi + \mathbf{b}(s_1)r \sin \theta \sin \phi + \mathbf{t}(s_1)r \cos \phi, \\ \mathbf{x}_{v,2}(r, \theta, \phi) &= \mathbf{x}_v(s_2) + \mathbf{n}(s_2)r \cos \theta \sin \phi + \mathbf{b}(s_2)r \sin \theta \sin \phi + \mathbf{t}(s_2)r \cos \phi, \end{aligned} \quad (3.3)$$

where $\mathbf{t}(s)$, $\mathbf{n}(s)$ and $\mathbf{b}(s)$ are the tangent, normal and binormal versors on Λ . Roughly speaking, Ω_v^R can be parametrized as an overlapping union of one cylindrical coordinates local map on $\Omega_{v,0}^R$ and two spherical coordinates mappings on $\Omega_{v,1}^R, \Omega_{v,2}^R$.

- We will denote by

$$\Omega_t^R = \Omega \setminus \overline{\Omega_v^R}$$

the actual ‘‘tissue’’ domain. A special role will be played by the interface Γ^R between vessel and tissue:

$$\Gamma^R = \partial\Omega_v^R.$$

The “cylindrical” part of Γ^R that belongs to the boundary of $\Omega_{v,0}^R$ will be denoted by

$$\Gamma_0^R = \{\mathbf{x} \in \mathbb{R}^3 : \mathbf{x} = \mathbf{x}_{v,0}(s, R, \theta), \quad (s, \theta) \in (s_1, s_2) \times [0, 2\pi)\}.$$

This is the “leading order” surface because it scales as R for $R \rightarrow 0$, whereas the remaining “spherical” boundaries scale as R^2 .

Finally, we denote by

$$\Gamma_t = \partial\Omega$$

the surface of the tissue domain that is not shared with the vessel; being $\overline{\Omega_t^R} \subset \overline{\Omega}$, we have that $\partial\Omega_t^R = \Gamma^R \cup \Gamma_t$.

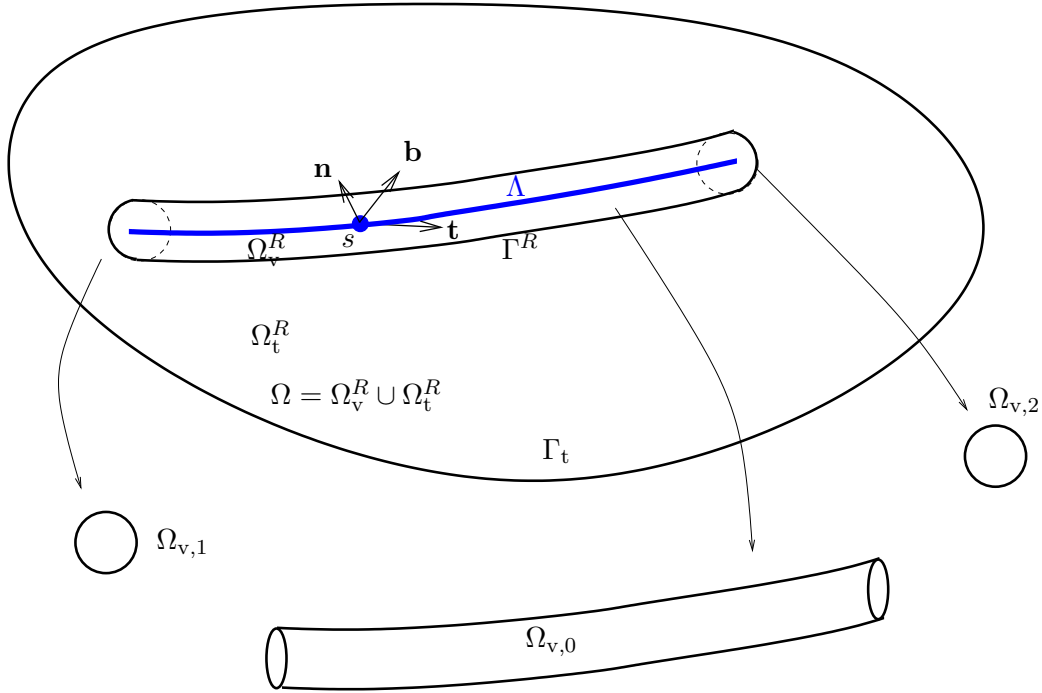


Figure 3.1: Subdomains in Ω : the 1D vessel domain Λ , the actual 3D vessel domain Ω_v^R , and the 3D tissue domain Ω_t^R . Shown is the covering of Ω_v by overlapping subsets $\Omega_{v,0}$, $\Omega_{v,1}$ and $\Omega_{v,2}$ where local cylindrical/spherical coordinates $\mathbf{x}_{v,0}$, $\mathbf{x}_{v,1}$, $\mathbf{x}_{v,2}$ are defined.

Our basic assumption on the vessel geometry is that the projection from Ω_v^R to Λ is unique:

$$\forall \mathbf{x} \in \Omega_v^R : \exists! \mathbf{x}_0 \in \Lambda : \text{dist}(\mathbf{x}, \Lambda) = \|\mathbf{x} - \mathbf{x}_0\|. \quad (3.4)$$

Notice that the projection \mathbf{x}_0 exists because Λ is compact. One can show that eq. (3.4) is satisfied if Λ is smooth enough and R is small. A consequence of (3.4) is that

$$\text{dist}(\mathbf{x}_{v,0}(s, r, \theta), \Lambda) = r \quad \forall (r, s, \theta) \in [0, R) \times [s_1, s_2] \times [0, \pi). \quad (3.5)$$

Let $\{\varphi_{v,i}\}$ be a partition of the unity such that, for $i = 0, 1, 2$, $\varphi_{v,i} : \Omega_v^R \rightarrow \mathbb{R}$ is a non-negative smooth function with $\text{supp}(\varphi_{v,i}) \subset \Omega_{v,i}^R$, and $\sum_i \varphi_{v,i} = 1$ on Ω_v^R . For every measurable function

$g : \Omega_v^R \rightarrow \mathbb{R}$, we have

$$\int_{\Omega_v^R} g \, d\mathbf{x} = \int_{s_1}^{s_2} \int_0^R \int_0^{2\pi} g_0(s, r, \theta) r \, ds \, dr \, d\theta + \sum_{i=1,2} \int_0^R \int_0^{2\pi} \int_0^\pi g_i(r, \theta, \phi) r^2 \sin \phi \, dr \, d\theta \, d\phi, \quad (3.6)$$

where

$$g_i = (g\varphi_{v,i}) \circ \mathbf{x}_{v,i}^{-1}, \quad i = 0, 1, 2.$$

Moreover, we have the formula

$$\int_{\Gamma^R} g \, d\sigma = \int_{s_1}^{s_2} \int_0^{2\pi} g_0(s, R, \theta) R \, ds \, d\theta + \sum_{i=1,2} \int_0^{2\pi} \int_0^\pi g_i(R, \theta, \phi) R^2 \sin \phi \, d\theta \, d\phi. \quad (3.7)$$

From this equation, we have that if g is continuous on Ω_v^R , then

$$\lim_{\epsilon \rightarrow 0} \frac{1}{\epsilon} \int_{\Gamma^{\epsilon R}} g \, d\sigma = \lim_{\epsilon \rightarrow 0} \int_{s_1}^{s_2} \int_0^{2\pi} g_0(s, \epsilon R, \theta) R \, ds \, d\theta = \int_{s_1}^{s_2} 2\pi g(s) R \, ds = 2\pi R \int_\Lambda g \, ds, \quad (3.8)$$

where $g(s) = g(\mathbf{x}_{v,0}(s, 0, 0))$.

We will denote by a bar the following averaging operator on circles of radius R laying on the cylindrical surface Γ_0^R and normal to the line Λ :

$$\bar{g}(s) = \frac{1}{2\pi} \int_0^{2\pi} g(\mathbf{x}_{v,0}(s, R, \theta)) \, d\theta. \quad (3.9)$$

The area of surface Γ_0^R scales as R , so that, using local coordinates $\mathbf{x}_{v,0}$, and defining $g_\epsilon(s, r, \theta) = g(s, r/\epsilon, \theta)$, we have

$$\lim_{\epsilon \rightarrow 0} \frac{1}{\epsilon} \int_{\Gamma^{\epsilon R}} g_\epsilon \, d\sigma = 2\pi R \int_{s_1}^{s_2} \bar{g}(s) \, ds. \quad (3.10)$$

3.2.2 Diffusion-advection-reaction equations

Now we can focus on the interplay between the actual 3D tissue domain Ω_t^R and the 1D vessel domain Λ , and study the behavior of the solutions when a suitable rescaling is applied and $R \rightarrow 0$ so that Ω_t^R expands to the whole Ω . We point out that in this investigation, the starting equation for the vessel variable is already one-dimensional, while it would have been preferable to “obtain” this one-dimensional equation starting from the actual 3D vessel domain Ω_v^R by “shrinking” it to its 1D axis. We did not follow this (interesting) approach because we are mostly interested in the singularity of the asymptotic 3D solution. Moreover, the same asymptotic analysis for the vessel region has been considered in the previous chapter on one-dimensional models for mass transport in blood vessels¹.

¹Nevertheless, a coupled vessel-tissue asymptotic analysis, justifying the 1D-3D model starting from the 3D-3D one, is still lacking and would represent an interesting complement to this work.

Let us denote by u_t the unknown variable in the tissue and by u_v the one in the vessel; the model problem we will consider reads

$$\left\{ \begin{array}{ll} -\nabla \cdot (k_t \nabla u_t) + m_t u_t + r_t = 0 & \text{in } \Omega_t^R, \\ u_t = 0 & \text{on } \Gamma_t, \\ -k_t \partial_{\mathbf{n}} u_t = -q & \text{on } \Gamma^R, \\ -\frac{d}{ds} \left(k_v \frac{du_v}{ds} \right) + b_v \frac{du_v}{ds} + f = 0 & \text{in } \Lambda, \\ u_v(s_1) = u_{v,1}, \\ -k_v \frac{du_v}{ds}(s_2) = 0, \end{array} \right. \quad (3.11)$$

where k_t , m_t and r_t are respectively a diffusion, reaction and source term in the tissue domain, while k_v and b_v are the diffusion and convective term in the vessel domain.

The q term, defined on the actual interface Γ^R between vessel and tissue, represents the mass transfer term (per unit surface) from the vessel to the tissue: for the moment it is assumed to be a known function, such that $\text{supp}(q) \subset \Gamma_0^R$. By conservation of the global flux Φ across Γ^R , a related term f appears in the vessel equation, such that

$$\int_{s_1}^{s_2} f(s) ds = \int_{\Gamma^R} q d\sigma = \Phi.$$

The boundary conditions for the tissue are of mixed Dirichlet/Neumann type: $\partial_{\mathbf{n}}$ denotes the outer normal derivative (with respect to Ω_t^R). For the vessel we have a Dirichlet condition at $s = s_1$ and a homogeneous Neumann condition at $s = s_2$ (other combinations could be considered as well).

Once q and f are given, under standard hypotheses system (3.11) consists of two decoupled elliptic equations. However, we wonder if some ‘‘asymptotic’’ problem for u_t on Ω can be recovered by letting $R \rightarrow 0$ and by rescaling properly q in order to keep the total flux across Γ^R unchanged. Therefore, for $\epsilon \in (0, 1]$, we consider the problem corresponding to the scaled vessel radius ϵR :

$$\left\{ \begin{array}{ll} -\nabla \cdot (k_t \nabla u_t^\epsilon) + m_t u_t^\epsilon + r_t = 0 & \text{in } \Omega_t^{\epsilon R}, \\ u_t^\epsilon = 0 & \text{on } \Gamma_t^{\epsilon R}, \\ -k_t \partial_{\mathbf{n}} u_t^\epsilon = -q_\epsilon & \text{on } \Gamma^{\epsilon R}, \end{array} \right. \quad (3.12)$$

for which we would like to find a limit solution when $\epsilon \rightarrow 0$. Using local variables, the flux q_ϵ on $\Gamma_0^{\epsilon R}$ for the scaled problem must be equal to

$$q_\epsilon(s, \epsilon R, \theta) = \frac{1}{\epsilon} q(s, R, \theta),$$

if we want the total flux $\Phi = \int_{\Gamma^{\epsilon R}} k_t \partial_{\mathbf{n}} u_t^\epsilon d\Gamma$ to be independent of ϵ . In fact, by changing the integration variables we have

$$\Phi = \int_{\Gamma_0^{\epsilon R}} q_\epsilon d\sigma = \int_{\Gamma_0^R} q d\sigma = \int_{s_1}^{s_2} f(s) ds \quad \forall \epsilon \in (0, 1] \quad (3.13)$$

Let $C_0^\infty(\Omega)$ be the space of smooth functions with compact support in Ω . If we multiply the equation in (3.12) by an arbitrary test function in $C_0^\infty(\Omega)$ and integrate over $\Omega_t^{\epsilon R}$, we get

$$\int_{\Omega_t^{\epsilon R}} k_t \nabla u_t^\epsilon \cdot \nabla \phi d\Omega + \int_{\Omega_t^{\epsilon R}} m_t u_t^\epsilon \phi d\Omega + \int_{\Omega_t^{\epsilon R}} r_t \phi d\Omega = \int_{\Gamma_0^{\epsilon R}} q_\epsilon \phi d\sigma \quad \forall \phi \in C_0^\infty(\Omega). \quad (3.14)$$

Since

$$\int_{\Gamma_0^{\epsilon R}} q_\epsilon \phi \, d\sigma = \int_0^L \int_0^{2\pi} q(\mathbf{x}_{v,0}(s, R, \theta)) \phi(s, \epsilon R, \theta) R \, ds \, d\theta$$

we have, similarly to eq. (3.10),

$$\lim_{\epsilon \rightarrow 0} \int_{\Gamma_0^{\epsilon R}} q_\epsilon \phi \, d\sigma = 2\pi R \int_\Lambda \bar{q} \phi \, ds, \quad \text{where} \quad \bar{q}(s) = \frac{1}{2\pi} \int_0^{2\pi} q(s, R, \theta) \, d\theta.$$

In particular, thanks to (3.13), we see that f can be given the following expression:

$$f(s) = 2\pi R \bar{q}(s).$$

Suppose now that $u_t^\epsilon \rightarrow u_t$ with respect to a suitable norm so that the limit of (3.14) for $\epsilon \rightarrow 0$ is

$$\int_\Omega k_t \nabla u_t \cdot \nabla \phi \, d\Omega + \int_\Omega m_t u_t \phi \, d\Omega + \int_\Omega r_t \phi \, d\Omega = \int_\Lambda f(s) \, ds \quad \forall \phi \in C_0^\infty(\Omega). \quad (3.15)$$

Then, eq. (3.15) is the candidate for our asymptotic problem, whose strong form reads:

$$\begin{cases} -\nabla \cdot (k_t \nabla u_t) + m_t u_t + r_t = f(s) \delta_\Lambda & \text{in } \Omega, \\ u_t = 0 & \text{on } \partial\Omega, \end{cases} \quad (3.16)$$

being δ_Λ the Dirac measure concentrated on Λ : in this work, we will adopt the following convention: for $f \in L^2(\Lambda)$, we denote by $f \delta_\Lambda$ the linear operator on $C(\Omega)$, the space of continuous functions on Ω , defined by

$$(f \delta_\Lambda, \phi) = \int_\Lambda f \phi \, ds. \quad (3.17)$$

In particular, $f \delta_\Lambda$ is a *measure* (for $f = 1$, it is exactly the Dirac measure on Λ). Notice that $f(s)$ appears in turn as a sink term in the one-dimensional transport subproblem in (3.11):

$$\begin{cases} -\frac{d}{ds} \left(k_v \frac{du_v}{ds} \right) + b_v \frac{du_v}{ds} + f(s) = 0 & \text{in } \Lambda, \\ u_v(0) = u_{v,D}, \\ -k_v u_v'(L) = 0, \end{cases}$$

In practice, *the mass exchange term f appears as a function in the 1D equation, and as a measure in the 3D one.* The first remark we can make is that $\delta_\Lambda \notin H^{-1}(\Omega)$, so that if a solution u_t exists, it will be not in $H^1(\Omega)$. It is known that a 3D solution to a Poisson problem with a line source has a logarithmic singularity near the line, whose gradient does not belong to $L^2(\Omega)$.

In applications, q (and so f) is not known *a priori*. Usually a constitutive law for q has to be chosen: this makes the derivation of the asymptotic problem more complicated. Even if more complex non-linear models (like the Kedem-Katchalsky equations) could be adopted, let us consider as an example the following linear filtration law in local coordinates $\mathbf{x}_{v,0}$:

$$q(s, \theta) = D(u_v(s) - u_t(\mathbf{x}_{v,0}(s, R, \theta))), \quad (3.18)$$

In this case system (3.11) is no longer decoupled. Moreover, it is not immediately clear how to choose the scaling of the flux $-k_t \partial_n u_t^\epsilon$, as q depends on the solution itself, so that a simple formula preserving

the total flux Φ is not available. For certain scalings, the reduced problem still has the form

$$\begin{cases} -\nabla \cdot (k_t \nabla u_t) + m_t u_t + r_t = f(u_v, u_t, s) \delta_\Lambda & \text{in } \Omega, \\ u_t = 0 & \text{on } \partial\Omega, \\ -\frac{d}{ds} \left(k_v \frac{du_v}{ds} \right) + b_v \frac{du_v}{ds} + f(u_v, u_t, s) = 0 & \text{in } \Lambda, \\ u_v(0) = u_{v,D}, \\ -k_v u'_v(L) = 0, \end{cases} \quad (3.19)$$

where f is a suitable functional, representing a *linear flux* (i.e. rate of transfer per unit *length*). In general, it is not a simple function, but rather an integral operator. For example, if we adopt the ϵ^{-1} -scaling of the flux q , we find

$$\begin{aligned} f(u_v, u_t, s) &= 2\pi RD \left(u_v(s) - \frac{1}{2\pi} \int_0^{2\pi} u_t(\mathbf{x}_{v,0}(s, R, \theta)) d\theta \right) \\ &= 2\pi RD (u_v(s) - \bar{u}_t(s)). \end{aligned} \quad (3.20)$$

We might wonder if this ϵ^{-1} scaling associated with form (3.20) of the exchange term does preserve the total flux. Actually we will show by some examples that this is the case. We will provide test cases with an available analytical solution, that allow the investigation of the typical behavior of the asymptotic solution.

Examples

For $\delta \in (0, 1)$ we define the following simple domain in cylindrical coordinates (see fig. 3.2):

$$\Omega_t^\delta = \{(z, r, \theta) \in \mathbb{R}^3 : \delta < r < 1, 0 < z < 1\}.$$

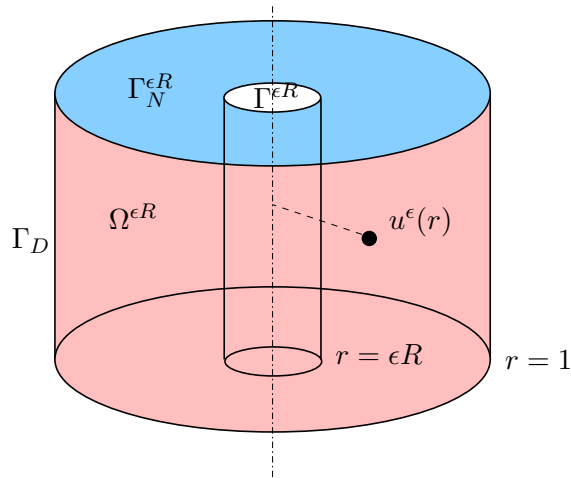


Figure 3.2: Axisymmetric model problem.

We have $\partial\Omega = \Gamma^\delta \cup \Gamma_D \cup \Gamma_N^\delta$, where

$$\begin{aligned}\Gamma^\delta &= \{(z, r, \theta) \in \mathbb{R}^3 : r = \delta, 0 < z < 1\}, \\ \Gamma_D &= \{(z, r, \theta) \in \mathbb{R}^3 : r = 1, 0 < z < 1\}, \\ \Gamma_N^\delta &= \{(z, r, \theta) \in \mathbb{R}^3 : \delta \leq r \leq 1, z \in \{0, 1\}\}.\end{aligned}$$

Moreover, we define the segment

$$\Lambda = \{(z, r, \theta) \in \mathbb{R}^3 : (z, r, \theta) = (s, 0, 0), s \in [0, 1]\}.$$

Let $\epsilon \in (0, 1)$ be the scaling coefficient, and denote by $0 < R < 1$ a reference radius, thought to be $\ll 1$ (this could be the case of the actual vessel radius). We will focus on the scaling of two model Laplace problems, respectively considering Neumann and Robin conditions.

The Neumann case. Consider a constant Neumann datum q on Γ^R . The associated ϵ -scaled model problem reads:

$$\begin{cases} -\Delta u^\epsilon = 0 & \text{in } \Omega_t^{\epsilon R}, \\ -\partial_{\mathbf{n}} u^\epsilon = 0 & \text{on } \Gamma_N^{\epsilon R}, \\ -\partial_{\mathbf{n}} u^\epsilon = -q_\epsilon & \text{on } \Gamma^{\epsilon R} \\ u^\epsilon = 0 & \text{on } \Gamma_D, \end{cases} \quad (3.21)$$

where q_ϵ is the scaled flux. The scaling has to be such that the total flux across the surface $\Gamma^{\epsilon R}$

$$\Phi(\epsilon) = \int_{\Gamma^{\epsilon R}} q_\epsilon R d\Gamma = \int_0^1 \int_0^{2\pi} q_\epsilon \epsilon R dz d\theta = 2\pi \epsilon R q_\epsilon$$

is constant with respect to ϵ . This obviously implies

$$q_\epsilon = \frac{1}{\epsilon} q.$$

As the problem is θ, z -symmetric, we can look for radial solutions, in the form $u^\epsilon = u^\epsilon(r)$. With this choice, Neumann conditions on $\Gamma_N^{\epsilon R}$ are automatically satisfied; moreover, $\Delta u^\epsilon = \frac{1}{r} \frac{d}{dr} \left(r \frac{d}{dr} u^\epsilon \right)$, so that the problem is reduced to

$$\begin{cases} -\frac{d}{dr} \left(r \frac{d}{dr} u^\epsilon(r) \right) = 0, & \epsilon R < r < 1, \\ \frac{d}{dr} u^\epsilon(\epsilon R) = -q/\epsilon, \\ u^\epsilon(1) = 0, \end{cases} \quad (3.22)$$

whose solution is

$$u^\epsilon(r) = -Rq \ln(r), \quad r \in [\epsilon R, 1], \forall \epsilon \in (0, 1).$$

Since this function is independent of ϵ , it is already the asymptotic solution for $\epsilon \rightarrow 0$ that we are looking for. This is given by

$$u(r) = -Rq \ln(r),$$

and defined on the whole $\Omega = (0, 1) \times (0, 1) \times (0, 2\pi)$. One can easily verify that u is the weak solution of the following Poisson problem with a measure as a right hand side:

$$\begin{cases} -\Delta u = 2\pi Rq \delta_\Lambda & \text{in } \Omega, \\ -\partial_{\mathbf{n}} u = 0 & \text{on } \Gamma_N, \\ u = 0 & \text{on } \Gamma_D. \end{cases} \quad (3.23)$$

Notice that the Dirac density $2\pi Rq$ on the one-dimensional vessel Λ is just the integral of the surface flux q on each cross-section of the actual vessel.

The Robin case. Consider a linear Robin condition:

$$-\partial_{\mathbf{n}}u = -q_1(u) = -D(u - u_v) \quad \text{on } \Gamma^R,$$

being D and u_v constants. When ϵ -scaling the problem, the total flux across the surface $\Gamma^{\epsilon R}$ becomes now dependent on the solution. For $\epsilon > 0$, denote by D_ϵ the rescaled conductive coefficient, such that $D_1 = D$. In our axisymmetric problem, we have:

$$\Phi(\epsilon) = \int_{\Gamma^{\epsilon R}} D_\epsilon(u^\epsilon - u_v)R d\Gamma = D_\epsilon \int_0^1 \int_0^{2\pi} (u^\epsilon(\epsilon R) - u_v)\epsilon R dz d\theta = 2\pi D_\epsilon \epsilon R (u^\epsilon(\epsilon R) - u_v).$$

In order to preserve the flux, one should impose $\Phi(\epsilon) = \Phi(1) \forall \epsilon \in (0, 1]$, which gives

$$D_\epsilon = D \frac{1}{\epsilon} \left(\frac{u^1(R) - u_v}{u^\epsilon(\epsilon R) - u_v} \right).$$

In this equation, we have the same ϵ^{-1} term we met in the Neumann case, plus another term which involves the actual and the rescaled solutions. The latter, in particular, it is not known *a priori*. The correspondent rescaled problem

$$\begin{cases} -\frac{d}{dr} \left(r \frac{d}{dr} u^\epsilon(r) \right) = 0, & \epsilon R < r < 1, \\ \frac{d}{dr} u^\epsilon(\epsilon R) = D_\epsilon (u^\epsilon(\epsilon R) - u_v) \\ \quad = D \frac{1}{\epsilon} (u^1(R) - u_v), \\ u^\epsilon(1) = 0, \end{cases} \quad (3.24)$$

admits the following solution: for $\epsilon = 1$ we find

$$u^1(r) = -\frac{DRu_v}{1 - DR \ln R} \ln(r), \quad r \in [R, 1],$$

that is the actual solution in the non-rescaled domain. Solving (3.24) for $\epsilon \in (0, 1]$ using u^1 as datum, we obtain once again

$$u^\epsilon(r) = -\frac{DRu_v}{1 - DR \ln R} \ln(r), \quad r \in [\epsilon R, 1],$$

which is, as in the Neumann case, depending on ϵ only via the domain, so that the asymptotic solution for $\epsilon \rightarrow 0$ is the singular function

$$u(r) = -\frac{DRu_v}{1 - DR \ln R} \ln(r)$$

defined on the whole $\Omega = (0, 1) \times [0, 1) \times (0, 2\pi)$. As in the Neumann case, one can verify that u is the weak solution of problem (3.23), if we take

$$q = 2\pi \frac{Du_v}{1 - DR \ln R}.$$

We point out that this expression for q has been obtained by means of the actual solution u^1 , and it may change when different geometries and Dirichlet data are considered. However, we draw the reader's attention on the fact that this example is a particular case of problem (3.19), namely:

$$\begin{cases} -\Delta u = 2\pi Rq\delta_\Lambda & \text{in } \Omega, \\ -\partial_{\mathbf{n}}u = 0 & \text{on } \Gamma_N, \\ u = 0 & \text{on } \Gamma_D, \end{cases} \quad (3.25)$$

where

$$\begin{aligned} q(s) &= D(u_v(s) - \bar{u}(s)), \\ \bar{u}(s) &= \frac{1}{2\pi} \int_0^{2\pi} u(\mathbf{x}(s, R, \theta)) d\theta, \end{aligned} \quad (3.26)$$

being $\mathbf{x}(r, s, \theta)$ the parametrization of Ω_t^R appearing in (3.3). This means that for $s \in [0, L]$, $\bar{u}(s)$ is the mean value of the unknown u on the circle of radius R centered at the point s on the line Λ , and laying on the plane normal to Λ . Notice that (3.25, 3.26) form an *integro-differential* problem, and one has to show that this problem makes sense in a suitable functional space. In our axisymmetric example, we have $\bar{u} = -\frac{DRu_v \ln R}{1-DR \ln R}$, so that we obtain once again the expression $\frac{Du_v}{1-DR \ln R}$ for q . We point out that, in this case, the asymptotic problem is preserving the total flux.

The former examples show how the asymptotic singular solution can approximate the actual one at least for $r > R$ (in the simple axisymmetric problem we considered, the actual and asymptotic solution are the same function on Ω_t^R). To summarize, by means of the asymptotic solution we can avoid to resolve the 3D geometry of small vessels, but the elliptic problem we have to consider has a right hand side which is a *measure*, that has the form $f(s)\delta_\Lambda$. Of course, for $r < R$ the singular solution ceases to have a physical meaning, since it is not bounded near the singularity.. However, since R is a known parameter, this is not a drawback of the asymptotic solution approach: for $r \geq R$, u is expected to be a good approximation of the actual solution u^1 .

A numerical experiment. Having presented through a couple of examples the typical behavior of the asymptotic solution, let us investigate its numerical approximation by the finite element method.

We will consider the simple problem (3.23) on Ω , with $Rq = 1$: the exact solution is $u(r) = -\ln r$. Basis functions of standard FEM are continuous, so that the Galerkin approximation u_h of u is well defined: that is, we are allowed to consider $u_h \in V_h$ such that

$$a(u_h, v) = \int_0^1 2\pi v(z, 0, 0) dz \quad \forall v \in V_h, \quad (3.27)$$

where V_h is a suitable finite element space (in this example, we use \mathbb{P}^1 elements with maximum element size h), and a is the following bilinear form:

$$a(u, v) = (\nabla u, \nabla v)_{L^2(\Omega)} = \int_\Omega \nabla u \cdot \nabla v \, dx.$$

As we already pointed out, we cannot expect convergence $u_h \rightarrow u$ in H^1 norm for $h \rightarrow 0$. In fact, we have:

$$\|u\|_{L^2}^2 = 2\pi \int_0^1 r \ln^2 r \, dr < \infty, \quad \|\nabla u\|_{L^2}^2 = 2\pi \int_0^1 r \frac{1}{r^2} \, dr = \infty,$$

so that $u \in L^2(\Omega)$ but $u \notin H^1(\Omega)$. As we will see, even if we cannot rely on the standard H^1 convergence, we still have L^2 convergence. Moreover, it is possible to introduce other spaces in which

we can study the convergence of the FEM. To this end, we introduce the weighted space $L_\alpha^2(\Omega)$, (see definition A.1.1) as the space of square integrable functions with respect to the measure μ_α defined by

$$d\mu_\alpha(\mathbf{x}) = \text{dist}(\mathbf{x}, \Lambda)^{2\alpha} d\mathbf{x}.$$

The space of functions in $L_\alpha^2(\Omega)$ whose first derivatives are in $L_\alpha^2(\Omega)$ is defined as the weighted Sobolev space $H_\alpha^1(\Omega)$. It is a Hilbert space (see [51]), with

$$(u, v)_{H_\alpha^1(\Omega)} = \int_\Omega u(\mathbf{x})v(\mathbf{x})d\mu_\alpha(\mathbf{x}) + \int_\Omega \nabla u(\mathbf{x}) \cdot \nabla v(\mathbf{x})d\mu_\alpha(\mathbf{x}).$$

In our axis-symmetric case, we have $\text{dist}(\mathbf{x}, \Lambda) = r$, and the function r^{-1} belongs to $L_\alpha^2(\Omega)$ for any $\alpha > 0$. In particular, we have

$$\|\nabla u\|_{L_\alpha^2}^2 = 2\pi \int_0^1 r^{1+2\alpha} \frac{1}{r^2} dr = \frac{\pi}{\alpha}$$

and $u \in H_\alpha^1(\Omega)$ for $\alpha > 0$. We will show that $H_\alpha^1(\Omega)$ is a “good” space to study the both well-posedness and FEM convergence for our singular problem.

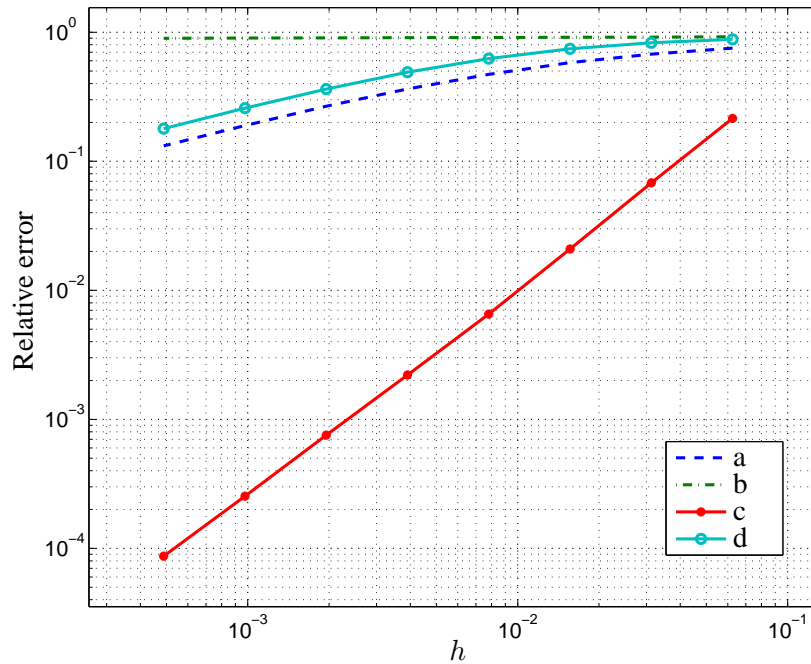


Figure 3.3: Relative approximation error in different norms, namely a: $L^2(\Omega)$, b: $H^1(\Omega)$, c: $L_\alpha^2(\Omega)$ ($\alpha = 0.5$), d: $H_\alpha^1(\Omega)$ ($\alpha = 0.5$), as a function of the mesh size h .

In fig. (3.3) the convergence history of FEM with respect of different norms is shown. For the sake of simplicity, we considered an axisymmetric case in which the independent variables are $(r, z) \in [0, 1]^2$, the symmetry condition defining our 3D solution on the whole cylinder Ω . We can see that the approximate solution does not converge in $H^1(\Omega)$, but it does in $L^2(\Omega)$, $L_{1/2}^2(\Omega)$ and $H_{1/2}^1(\Omega)$. The

slope of the bilogarithmic plot gives the order of convergence with respect to h , which is in particular more than linear for the $L^2_{1/2}(\Omega)$ norm, and $O(h^\eta)$, with $\eta \simeq 1/3$, for the L^2 and $H^1_{1/2}(\Omega)$ norms. The slow convergence rate is mainly due to the singularity near Λ (i.e. for $r = 0$): as it is seen in fig. 3.4, “large” errors are localized only on those elements having at least one node on Λ ; on the other elements, the approximate solution is very accurate, even if a relatively coarse mesh ($h = 1/10$) is used. This fact shows that a good accuracy in the solution far away from the 1D vessel Λ can be achieved by a coarse grid, without resolving the actual 3D structure of the vessel.

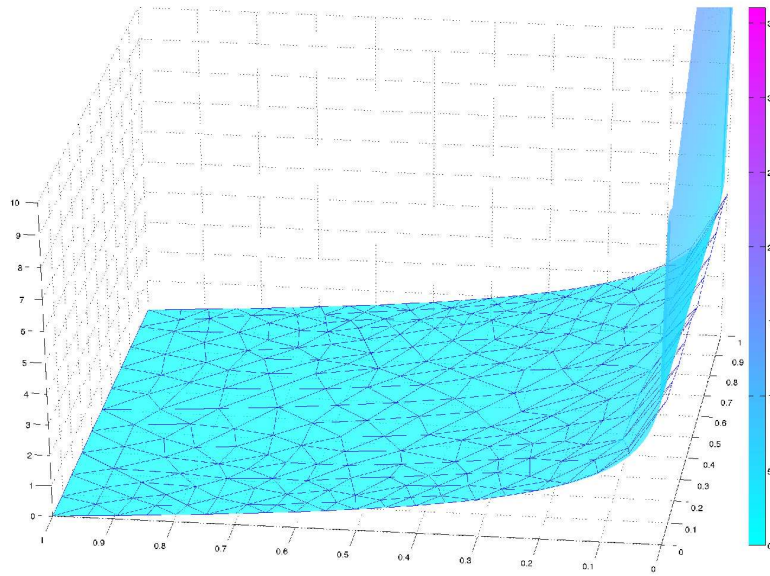


Figure 3.4: Surfaces representing the numerical solution $u_h(r, z)$ (mesh) and the exact solution $u(r, z) = -\ln r$ (shaded with color), for $h = 1/10$.

In our simulation, we considered an assigned source term q on Λ ; but in applications this term is not known *a priori*, and it depends on the solution itself via a constitutive law, as in (3.26). The constitutive law usually depends on the solution values near the 1D source, typically at distances of the order of R . Hence, the following questions naturally arise:

- Does the FEM converge to the singular solution for Robin coupling conditions?
- In order to obtain an approximate solution with a reasonable tolerance on the error, is it mandatory to refine the mesh and take h of the order of the vessel radius, at least in a neighborhood of the corresponding 1D axis Λ ? If the answer is yes, the major advantage of the asymptotic solution approach will be lost.
- Can we eliminate the singularity? A typical procedure is to find $w = u - \xi$, where the function ξ is chosen in such a way that w satisfies a “standard” problem. Is this approach preferable to the FEM one?

These issues will be addressed in the next chapter.

Chapter 4

Analysis of 1D-3D coupled problems

In the previous chapter we found that the modelling of small vessels by 1D manifolds embedded in a 3D tissue gives rise to elliptic problems with measure data, namely Dirac measures concentrated on lines. Further difficulties arise when considering the coupling between 3D and 1D problems: for instance, a meaning has to be assigned to the “1D-projection” \bar{u} (see (3.26)) of the 3D solution u , and the solvability of the coupled problem has to be investigated.

Results already known on standard problems do not apply directly to our equations: for instance, due to the singularity of solutions we cannot rely on usual Sobolev spaces for studying well-posedness or FEM convergence. Existence and uniqueness result for a Dirichlet problem with measure data was proven by Stampacchia [98], whereas the semilinear case has been treated by Brezis (for instance in [9]): in these papers the authors have proven the existence of a solution in $W^{1,q}(\Omega)$, with $0 < q < N/(N - 1)$, N being the dimension of Ω (in the linear case uniqueness is obtained as well).

In view of the numerical approximation of the solution, we prefer to work with Hilbert spaces. Moreover, the measures involved by the problems we will consider, like (3.16), or more generally (3.19), are not arbitrary: we will always deal with Dirac measures on lines only. For these reasons we introduce an “*ad hoc*” functional setting, specifically designed for our case, based on weighted Sobolev spaces $H_\alpha^1(\Omega)$.

We point out that Babuška [5] and Scott [94] have already studied the numerical approximation of Dirichlet problems with Dirac δ -functions as data. Nevertheless, their approach in the case of Laplace operator is essentially based on spaces $H^s(\Omega)$ with $s \in [0, \frac{1}{2})$, and it fails to extend to Robin problems (where at least an L^2 -valued trace operator has to be defined). Moreover, the assumption of the smoothness of the domain is crucial in the work of Scott, who is the only one that addresses the 3D problem. Our functional setting will encompass this case.

We consider the notations introduced in section 3.2, with $\Omega \subset \mathbb{R}^3$ and $\Lambda \subset \Omega$ denoting our 3D and 1D domains respectively; in particular, the assumptions of subsection 3.2.1 hold.

For $\alpha \in (-1, 1)$, we define the following weighted Sobolev space

$$H_\alpha^1(\Omega) = \{f \in L_\alpha^2(\Omega) : \nabla f \in L_\alpha^2(\Omega)^3\},$$

where $L_\alpha^2(\Omega)$ has been introduced in Definition A.1.1. The scalar product in $H_\alpha^1(\Omega)$ is defined by

$$(f, g)_{H_\alpha^1(\Omega)} = (f, g)_{L_\alpha^2(\Omega)} + (\nabla f, \nabla g)_{L_\alpha^2(\Omega)^3},$$

being

$$(f, g)_{L_\alpha^2(\Omega)} = \int_\Omega f(\mathbf{x})g(\mathbf{x})d\mu_\alpha(\mathbf{x}) = (d^\alpha f, d^\alpha g)_{L^2},$$

where μ_α is the measure defined in Definition A.1.1, that is $d\mu_\alpha(\mathbf{x}) = d(\mathbf{x})^{2\alpha} d\mathbf{x}$. Here d is distance from Λ , $d(\mathbf{x}) = \text{dist}(\mathbf{x}, \Lambda)$. More generally, one could consider any “equivalent” function such that $C_1 \text{dist}(\mathbf{x}, \Lambda)^{-1} \leq d(\mathbf{x}) \leq C_2 \text{dist}(\mathbf{x}, \Lambda)$, where C_1 and C_2 are positive constants.

For the basic properties of $H_\alpha^1(\Omega)$ that we shall need, the reader can refer to Appendix A.

We shall consider the following steps:

1. To provide a suitable functional setting and a finite element convergence analysis in the case of Dirichlet problem for the Laplace operator with a Dirac datum on a line;
2. To extend the analysis of the previous point to the coupled 3D-1D problem.

4.1 Dirichlet problem with source term on a line

The model problem we will focus on in this section is:

$$\begin{cases} -\nabla \cdot (k\nabla u) = f\delta_\Lambda & \text{in } \Omega, \\ u = 0 & \text{on } \partial\Omega, \end{cases} \quad (4.1)$$

where $f \in L^2(\Lambda)$, and $f\delta_\Lambda$ is the measure defined by (3.17). This problem has to be considered in a weak sense: to this end, we introduce the following bilinear form

$$a(u, v) := \int_\Omega k\nabla u \cdot \nabla v \, d\mathbf{x} \quad (4.2)$$

and the linear functional

$$F(v) = \int_\Lambda f(s)v(s) \, ds. \quad (4.3)$$

Let

$$V_\alpha = \{u \in H_\alpha^1(\Omega) : u|_{\partial\Omega} = 0\} \quad (4.4)$$

be the subspace of H_α^1 of functions vanishing on $\partial\Omega$ (in the sense of traces). We say that $u \in V_\alpha$ solves problem (4.1) if it satisfies the variational problem

$$a(u, v) = F(v) \quad \forall v \in C_0^\infty(\Omega). \quad (4.5)$$

This is the basic paradigm of more complex problems, for instance featuring perfusion and reaction terms as in (3.16), or nonlinearities. The extension of the theory to handle these modifications is trivial: in this section we are interested above all in the handling the measure data.

First of all, we point out that certain singular problems in the form (4.1) can be solved by “removing” the singular part. This is the case for instance if k is a positive constant: we have a “representation formula” for the solution in terms of a line potential and of a nonsingular elliptic problem, as it is stated by the following result.

Lemma 4.1.1. *Let $f \in L^2(\Lambda)$, and assume that $k > 0$ is constant in Ω . Then, for every $\alpha \in (0, 1)$ there exists a unique solution $u \in V_\alpha \cap L^2(\Omega)$ of problem (4.5), and two positive constants C and C' such that*

$$\|u\|_{H_\alpha^1} \leq C\|f\|_{L^2(\Lambda)}, \quad \|u\|_{L^2} \leq C'\|f\|_{L^2(\Lambda)}. \quad (4.6)$$

Moreover, the following representation formula holds:

$$u = \tilde{u} + \xi, \quad (4.7)$$

where $\tilde{u} \in V_0$ is defined by

$$\begin{cases} -\Delta \tilde{u} = 0 & \text{in } \Omega, \\ \tilde{u} = -\xi & \text{on } \partial\Omega, \end{cases} \quad (4.8)$$

and $\xi \in H_\alpha^1(\Omega) \cap L^2(\Omega)$ is the following line potential:

$$\xi(\mathbf{x}) := \frac{1}{4\pi k} \int_\Lambda \frac{f(\mathbf{y})}{|\mathbf{x} - \mathbf{y}|} ds(\mathbf{y}).$$

Proof. It is not difficult to verify that a constant $c > 0$ exists such that

$$|\nabla \xi(\mathbf{x})| \leq c \|f\|_{L^2(\Lambda)} \frac{1}{\text{dist}(\mathbf{x})}. \quad (4.9)$$

Therefore, thanks to lemma A.1.1, we have that $|\nabla \xi| \in H_\alpha^1(\Omega)$. An estimate similar to (4.9) is easily found for $|\xi(\mathbf{x})|$ too. Hence, $\xi \in H_\alpha^1(\Omega)$ and

$$\|\xi\|_{H_\alpha^1(\Omega)} \leq C_1 \|f\|_{L^2(\Lambda)}, \quad \|\xi\|_{L^2(\Omega)} \leq C'_1 \|f\|_{L^2(\Lambda)}.$$

Being $f\delta_\Lambda$ a measure with compact support in Ω , the potential ξ satisfies $-k\Delta\xi = f\delta_\Lambda$ in the sense of distributions [108, th. 4.1]. Due to the density of smooth functions (theorem A.2.1) the Green's formula holds in $H_\alpha^1(\Omega)$, so that $F(v) = (\xi, -k\Delta v)_{L^2} = (k\nabla\xi, \nabla v)_{L^2} \forall v \in C_0^\infty(\Omega)$. Therefore, ξ satisfies

$$a(\xi, v) = F(v) \quad \forall v \in C_0^\infty(\Omega).$$

Moreover, by theorem A.3.2, we have that $\xi|_{\partial\Omega} \in H^{1/2}(\Omega)$. Being a V_0 -elliptic, problem (4.8) has a unique solution $\tilde{u} \in H^1(\Omega)$ such that $\tilde{u}|_{\partial\Omega} = -\xi|_{\partial\Omega}$, and $\|\tilde{u}\|_{H^1} \leq C_2 \|\xi\|_{H_\alpha^1}$, C_2 being a positive constant. Hence $u = \tilde{u} + \xi \in V_\alpha$, and

$$a(u, v) = a(\tilde{u}, v) + a(\xi, v) = F(v) \quad \forall v \in C_0^\infty(\Omega).$$

On the other hand, any solution u to problem (4.5) can be written in the form (4.7) since $u - \xi$ solves (4.8).

To complete the proof, we observe that

$$\|u\|_{V_\alpha} \leq \|\tilde{u}\|_{H_\alpha^1} + \|\xi\|_{H_\alpha^1} \leq C \|f\|_{L^2(\Lambda)},$$

where $C = \text{diam}(\Omega)^\alpha C_1 C_2 + C_1$. In the same way we can choose $C' = \text{diam}(\Omega)^\alpha C_1 C_2 + C'_1$. The uniqueness of u follows. \square

Lemma 4.1.1 provides a first method to numerically approximate the solution of problem (4.1). Since it is possible to compute the singular part ξ with an “arbitrary” accuracy by numerical integration, one is left with the approximation of \tilde{u} , which is a “standard” problem.

However, we will not adopt this method, although it allows for very accurate numerical solutions. A few drawbacks are: *i*) we can only use it for problem (4.1) where k is constant, and more generally only for those operators such that a fundamental solution is known: this is not the case in hemodynamics, where the tissue diffusivity can vary and nonlinear perfusion terms have to be considered; *ii*) every evaluation of the approximate solution requires a line integration on Λ . When Λ represents a complex vessel geometry, this can be quite expensive in terms of computing.

In our opinion, a direct FEM discretization of the variational problem (4.5), which is possible since basis functions are continuous, provides a more flexible approach. In the sequel we introduce the special functional setting that is needed to use this approximation method. The idea underlying our approach is to consider in (4.5) test functions v belonging to the wider space $V_{-\alpha} \supset C_0^\infty(\Omega)$.

4.1.1 Analysis in weighted Sobolev spaces

First, let us state some preliminary lemmas; they are interesting *per se*, for our weighted Sobolev spaces approach entirely relies on them. We consider the variational formulation (4.5), and we seek a solution in V_α considering test functions in $V_{-\alpha}$. In order to have existence and uniqueness for this problem, we will make use of the generalized Lax-Milgram theorem A.4.1, due to Nečas. In particular, we have to show that:

- i) bilinear form a defined in (4.2) is continuous on $V_\alpha \times V_{-\alpha}$ and satisfies the inf-sup inequalities (A.10), (A.11);
- ii) functional F defined in (4.3) is continuous on $V_{-\alpha}$.

Let us start with point ii): we can show that if $0 < \alpha < 1$, functions of $V_{-\alpha}$ admit a continuous trace operator on the 1D manifold Λ . This implies that $F \in V'_{-\alpha}$. We will make use of the following weighted Hardy's inequality (see [70]):

Property 4.1.1 (Weighted Hardy's inequality). *Let $0 < p \leq q < \infty$, $0 < R \leq \infty$ and let u and v be weight functions defined on $(0, \infty)$. Assume that, for every $r > 0$,*

$$\int_0^r v(t)^{\frac{1}{1-p}} dt < \infty.$$

Then, the inequality

$$\left(\int_0^R \left(\int_0^r f(t) dt \right)^q u(r) dr \right)^{\frac{1}{q}} \leq C \left(\int_0^R f(r)^p v(r) dr \right)^{\frac{1}{p}} \quad (4.10)$$

holds for all positive functions f on $(0, \infty)$ if and only if

$$D = \sup_{r \in (0, R)} \left(\int_r^R u(t) dt \right)^{\frac{1}{q}} \left(\int_0^r v(t)^{\frac{1}{1-p}} dt \right)^{\frac{p-1}{p}} < \infty.$$

Moreover, the best constant in (4.10) satisfies the estimate

$$D \leq C \leq k(p, q)D$$

where

$$k(p, q) = \left(\frac{p + qp - q}{p} \right)^{\frac{1}{q}} \left(\frac{p + qp - q}{(p-1)q} \right)^{\frac{p-1}{p}}.$$

Theorem 4.1.1 (Λ -trace operator). *If $0 < \alpha < 1$, then there exists a unique linear continuous map*

$$\gamma_\Lambda : H^1_{-\alpha}(\Omega) \rightarrow L^2(\Lambda)$$

such that $\gamma_\Lambda u = u|_\Lambda$ for each smooth function $u \in C^\infty(\Omega)$. In particular, we have

$$\|\phi\|_{L^2(\Lambda)} \leq C_\Lambda(\alpha) \|\phi\|_{H^1_{-\alpha}(\Omega)}.$$

Proof. Let $\phi \in C^\infty(\Omega)$. By using local cylindrical coordinates $\mathbf{x}_{v,0}$ and integrating in $\Omega_{v,0}^R$ along the radial direction, we have for every $\theta \in [0, 2\pi)$:

$$\phi(s, 0, 0) = \phi(s, r, \theta) - \int_0^r \frac{\partial \phi}{\partial r}(s, t, \theta) dt,$$

so that, using the inequality $(a + b)^2 \leq 2a^2 + 2b^2$, and integrating on $\Omega_{v,0}^R$ we get

$$\pi R^2 \int_{\Lambda} \phi(s)^2 ds \leq 2 \int_{\Omega_{v,0}^R} \phi(s, r, \theta)^2 r ds dr d\theta + 2 \int_{\Omega_{v,0}^R} \left(\int_0^r \frac{\partial \phi}{\partial r}(s, t, \theta) dt \right)^2 r ds dr d\theta. \quad (4.11)$$

Now we can use theorem 4.1.1 and inequality (4.10) with $p = q = 2$, the weight functions being

$$u(t) = t, \quad v(t) = t^{1-2\alpha},$$

and $f(t) = |\partial \phi / \partial r(s, t, \theta)|$. We have

$$\int_0^r v(t)^{\frac{1}{1-p}} dt = \int_0^r t^{2\alpha-1} dt = \frac{r^{2\alpha}}{2\alpha} < \infty \quad \forall r > 0,$$

and

$$\begin{aligned} D &:= \sup_{r \in (0, R)} \left(\int_r^R t dt \right)^{\frac{1}{2}} \left(\int_0^r t^{2\alpha-1} dt \right)^{\frac{1}{2}} \\ &\leq \sup_{r \in (0, R)} \left[\frac{1}{4\alpha} (R^2 - r^2) r^{2\alpha} \right]^{\frac{1}{2}} = R^{\alpha+1} \frac{\alpha^{(-1+\alpha)/2}}{2(\alpha+1)^{(1+\alpha)/2}} \leq \frac{R^{1+\alpha}}{2\sqrt{\alpha}}, \end{aligned}$$

so that, since $r = \text{dist}(\mathbf{x}, \Lambda)$ on $\Omega_{v,0}^R$,

$$\int_0^R \left(\int_0^r \left| \frac{\partial \phi}{\partial r}(s, t, \theta) \right| dt \right)^2 r dr \leq C(\alpha)^2 \int_0^R \text{dist}(\mathbf{x}, \Lambda)^{-2\alpha} \left| \frac{\partial \phi}{\partial r}(s, r, \theta) \right|^2 r dr, \quad (4.12)$$

where

$$R^{\alpha+1} \frac{\alpha^{(-1+\alpha)/2}}{2(\alpha+1)^{(1+\alpha)/2}} \leq C(\alpha) \leq R^{1+\alpha} / \sqrt{\alpha}. \quad (4.13)$$

Using estimates (4.12) and $1 \leq d(\mathbf{x}, \Lambda)^{-2\alpha} R^{2\alpha} \forall \mathbf{x} \in \Omega_{v,0}^R$ in (4.11), we obtain

$$\begin{aligned} \pi R^2 \int_{\Lambda} \phi(s)^2 ds &\leq 2R^\alpha \int_{\Omega_{v,0}^R} \phi(s, r, \theta)^2 d(\mathbf{x}, \Lambda)^{-2\alpha} r ds dr d\theta + \\ &\quad 2C(\alpha)^2 \int_{\Omega_{v,0}^R} \left(\frac{\partial \phi}{\partial r}(s, r, \theta) \right)^2 d(\mathbf{x}, \Lambda)^{-2\alpha} r ds dr d\theta \\ &\leq 2 \max\{R^\alpha, C(\alpha)^2\} \|\phi\|_{H_{-\alpha}^1(\Omega)}^2, \end{aligned} \quad (4.14)$$

Hence the following continuity estimate holds:

$$\|\phi\|_{L^2(\Lambda)} \leq C_\Lambda(\alpha) \|\phi\|_{H_{-\alpha}^1(\Omega)}$$

where $C_\Lambda = \sqrt{\max\{R^\alpha, C(\alpha)^2\} / (\pi R^2)}$, and ϕ is a smooth function. The extension to $\phi \in H_{-\alpha}^1(\Omega)$ follows by a density argument (see theorem A.2.1). Notice that the constant C_Λ depends on α : actually from (4.13) we have that $C_\Lambda = \mathcal{O}(\alpha^{-1/2})$, and $C_\Lambda \rightarrow \infty$ for $\alpha \rightarrow 0$: this confirms that the result is not true anymore if $\alpha = 0$ (non-weighted case). \square

We are left with *i*). The continuity of a is straightforward; the non-trivial point is rather the inf-sup inequality (A.11). To show it, we need the following technical lemma, that we adapted to our case from [105]. Recall that we are allowed to use local coordinates (s, r, θ) for the “cylinder” $\Omega_{v,0}^R$, and local coordinates (r, θ, ϕ) for the “hemi-spheres” $\Omega_{v,1}^R \setminus \Omega_{v,0}^R$ and $\Omega_{v,2}^R \setminus \Omega_{v,0}^R$, see equations (3.3).

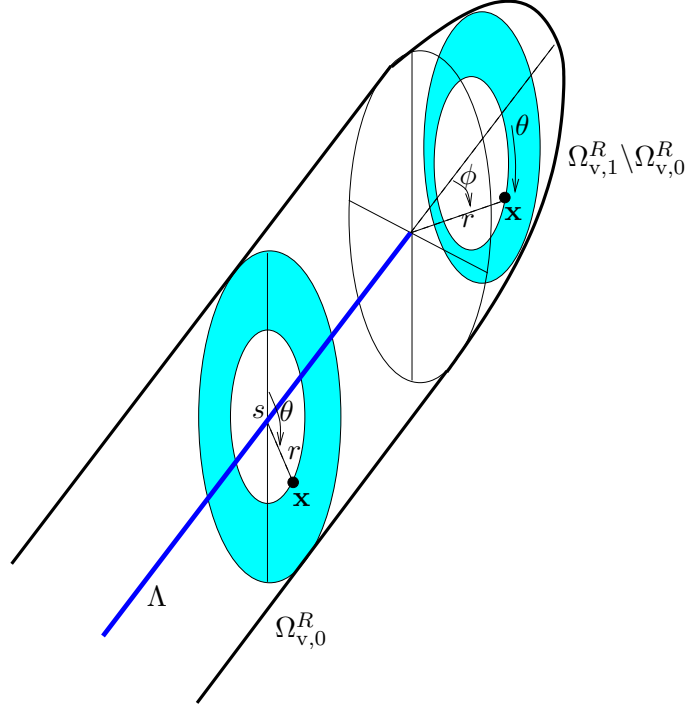


Figure 4.1: Local coordinates on subdomains of Ω_v^R .

Lemma 4.1.2. *Let $\delta \in (0, 1)$ and $u \in H_\alpha^1(\Omega)$ for some $0 < \alpha < \delta$. Consider the θ -Fourier expansions in local coordinates given by*

$$u(s, r, \theta) = \sum_{k \in \mathbb{Z}} A_{k,0}(r, s) e^{ik\theta} \quad \text{in } \Omega_{v,0}^R, \quad (4.15)$$

$$u(r, \theta, \phi) = \sum_{k \in \mathbb{Z}} A_{k,1}(r, \phi) e^{ik\theta} \quad \text{in } \Omega_{v,1}^R \setminus \Omega_{v,0}^R, \quad (4.16)$$

$$u(r, \theta, \phi) = \sum_{k \in \mathbb{Z}} A_{k,2}(r, \phi) e^{ik\theta} \quad \text{in } \Omega_{v,2}^R \setminus \Omega_{v,0}^R. \quad (4.17)$$

Consider the real function

$$A_0(\mathbf{x}) = \begin{cases} A_{0,0}(r, s) & \text{in } \Omega_{v,0}^R \\ A_{0,1}(r, \phi) & \text{in } \Omega_{v,1}^R \setminus \Omega_{v,0}^R \\ A_{0,2}(r, \phi) & \text{in } \Omega_{v,2}^R \setminus \Omega_{v,0}^R \end{cases}$$

defined on the whole Ω_v^R . Furthermore, define

$$\Psi(\mathbf{x}) = \begin{cases} \Psi(r, y) = \int_r^R t^{2\alpha-1} A_0(t, y) dt & \text{in } \Omega_v^R, \\ 0 & \text{elsewhere,} \end{cases} \quad (4.18)$$

where y can be either the s or the ϕ local variable, depending on the subdomain of Ω_{ν}^R in which \mathbf{x} is (in particular, Ψ is independent of θ).

There are positive constants C_1, C_2, C_3 independent of $\alpha \in (0, \delta)$ and R , such that the following estimates hold:

$$\|u - A_0\|_{L_{\alpha-1}^2(\Omega_{\nu}^R)} \leq C_1 \|\nabla u\|_{L_{\alpha}^2(\Omega)}, \quad (4.19)$$

$$\|\Psi\|_{L_{-\alpha}^2(\Omega)} \leq C_2 \|u\|_{L_{\alpha}^2(\Omega)}, \quad (4.20)$$

$$\|d^{2\alpha-1}u\nabla d + \nabla\Psi\|_{L_{-\alpha}^2(\Omega_{\nu}^R)} \leq C_3 \|\nabla u\|_{L_{\alpha}^2(\Omega_{\nu}^R)}, \quad (4.21)$$

where $d(\mathbf{x}) = \text{dist}(\mathbf{x}, \Lambda)$.

Proof. Some preliminary remarks: the coefficients of Fourier expansions are given by standard formulas, for example in $\Omega_{\nu,0}^R$ we have

$$A_{k,0}(r, s) = \frac{1}{2\pi} \int_0^{2\pi} u(s, r, \theta) e^{-ik\theta} d\theta.$$

Since $A_{-k,0}(r, s) = \overline{A_{k,0}(r, s)}$, $A_{0,0}$ is a real function. Actually, $A_0(\mathbf{x})$ is the average of u on the circle described by $\theta \in [0, 2\pi]$, keeping the other local variables constant and equal to those of point \mathbf{x} (notice that this circle varies continuously with respect to \mathbf{x}). Incidentally, this gives a geometrical interpretation for Ψ too, as the integral of $\frac{1}{2\pi} \text{dist}(\mathbf{x}, \Lambda)^{2\alpha-1} u(\mathbf{x})$ on the shaded areas associated with \mathbf{x} in fig. 4.1. Even if we have two kinds of local variables (spherical and cylindrical), we will consider only the cylindrical subdomain $\Omega_{\nu,0}^R$, since calculations for the remaining hemispherical subdomains are carried on in the same way.

From now, if we omit the integration intervals, it is understood that they are $r \in (0, R)$, $\theta \in (0, 2\pi)$, $s \in (s_1, s_2)$, and $\phi \in (0, \pi/2)$. Thanks to Parseval's equality

$$\int_0^{2\pi} (u(s, r, \theta) - A_{0,0}(r, s))^2 d\theta = 2\pi \sum_{k \in \mathbb{Z} \setminus \{0\}} |A_{k,0}(r, s)|^2 \quad (4.22)$$

we can write

$$\begin{aligned} \|u - A_0\|_{L_{\alpha-1}^2(\Omega_{\nu,0}^R)}^2 &= \int r^{2\alpha-2} [u(s, r, \theta) - A_{0,0}(r, s)]^2 r dr ds d\theta \\ &= 2\pi \sum_{k \in \mathbb{Z} \setminus \{0\}} \int r^{2\alpha-1} |A_{k,0}(r, s)|^2 dr ds. \end{aligned} \quad (4.23)$$

On the other hand, being $|\nabla u|^2 \geq \frac{1}{r^2} \left(\frac{\partial u}{\partial \theta}\right)^2$, we have

$$\begin{aligned} \|\nabla u\|_{L_{\alpha}^2(\Omega)}^2 &\geq \int r^{2\alpha} \frac{1}{r^2} \left(\frac{\partial u}{\partial \theta}\right)^2 r ds dr d\theta = 2\pi \sum_{k \in \mathbb{Z}} \int r^{2\alpha-1} k^2 |A_{k,0}(r, s)|^2 dr ds \\ &= 2\pi \sum_{k \in \mathbb{Z} \setminus \{0\}} \int r^{2\alpha-1} k^2 |A_{k,0}(r, s)|^2 dr ds, \end{aligned}$$

where Parseval's formula for the θ -derivative has been used. Since in the last sum $k^2 \geq 1$, comparing with (4.23) we have

$$\|u - A_0\|_{L_{\alpha-1}^2(\Omega_{\nu,0}^R)} \leq \|\nabla u\|_{L_{\alpha}^2(\Omega)}.$$

Analogous estimates on $\Omega_{v,1}^R \setminus \Omega_{v,0}^R$ and $\Omega_{v,2}^R \setminus \Omega_{v,0}^R$ follow in a similar way and (4.19) is proven.

The $L_{-\alpha}^2$ norm of Ψ on $\Omega_{v,0}^R$ is given by

$$\|\Psi\|_{L_{-\alpha}^2(\Omega_{v,0}^R)}^2 = 2\pi \int r^{-2\alpha} \left(\int_r^R t^{2\alpha-1} A_{0,0}(t, s) dt \right)^2 r ds dr.$$

Now we use the following weighted Hardy's inequality (see [105])

$$\int_0^R r^{-\beta} \left(\int_r^R t^{\beta-1} f(t) dt \right)^2 dr \leq \left(\frac{2}{1-\beta} \right)^2 \int_0^R r^\beta f(r)^2 dr, \quad \beta < 1, \quad (4.24)$$

with $f(t) = tA_{0,0}(t, s)$, $\beta = 2\alpha - 1$ (which is < 1 since $\alpha \in (0, \delta)$, $\delta < 1$). We get

$$\begin{aligned} \|\Psi\|_{L_{-\alpha}^2(\Omega_{v,0}^R)}^2 &\leq 2\pi \left(\frac{1}{1-\alpha} \right)^2 \int A_{0,0}(r, s)^2 r^{2\alpha+1} dr ds \\ &= \left(\frac{1}{1-\alpha} \right)^2 \|\sqrt{2\pi} A_{0,0}\|_{L_\alpha^2(\Omega_{v,0}^R)}^2 \leq \left(\frac{1}{1-\delta} \right)^2 \|u\|_{L_\alpha^2(\Omega_{v,0}^R)}^2, \end{aligned} \quad (4.25)$$

where last inequality is due to Parseval's formula. Analogous estimates are found on $\Omega_{v,1}^R \setminus \Omega_{v,0}^R$ and $\Omega_{v,2}^R \setminus \Omega_{v,0}^R$, where we make use of (4.24) with $f(t) = A_{0,i}(t, \phi)t^2$ and $\beta = 2\alpha - 2$ due to the extra r term coming from the integration formula in spherical coordinates; therefore, since $\Psi = 0$ outside Ω_v^R , (4.20) is proven.

Now let us show (4.21). We recall the following formulas in $\Omega_{v,0}^R$

$$\frac{\partial u}{\partial s}(s, r, \theta) = \sum_{k \in \mathbb{Z}} \frac{\partial A_{k,0}}{\partial s}(r, s) e^{ik\theta}, \quad (4.26)$$

and

$$\nabla \Psi = -\mathbf{e}_r r^{2\alpha-1} A_{0,0}(r, s) + \mathbf{e}_s \int_r^R t^{2\alpha-1} \frac{\partial A_{0,0}}{\partial s}(t, s) dt, \quad d^{2\alpha-1} \nabla d = r^{2\alpha-1} \mathbf{e}_r,$$

where \mathbf{e}_r and \mathbf{e}_s are the versors associated to the r and s local coordinates. We have

$$\|d^{2\alpha-1} u \nabla d + \nabla \Psi\|_{L_{-\alpha}^2(\Omega_{v,0}^R)}^2 \leq \|u - A_0\|_{L_{\alpha-1}^2(\Omega_{v,0}^R)}^2 + 2\pi \int r^{-2\alpha} \left(\int_r^R t^{2\alpha-1} \frac{\partial A_{0,0}}{\partial s}(t, s) dt \right)^2 r ds dr.$$

The first term can be estimated by means of (4.19), so that we are left with the second one. We can proceed as for eq. (4.25), using (4.24) and Parseval's equality for the Fourier expansion (4.26); we get

$$\begin{aligned} 2\pi \int r^{-2\alpha} \left(\int_r^R t^{2\alpha-1} \frac{\partial A_{0,0}}{\partial s}(t, s) dt \right)^2 r ds dr &\leq \left(\frac{1}{1-\alpha} \right)^2 \left\| \sqrt{2\pi} \frac{\partial A_{0,0}}{\partial s} \right\|_{L_\alpha^2(\Omega_{v,0}^R)}^2 \\ &\leq \left(\frac{1}{1-\delta} \right)^2 \left\| \frac{\partial u}{\partial s} \right\|_{L_\alpha^2(\Omega_{v,0}^R)}^2 \leq \left(\frac{1}{1-\delta} \right)^2 \|\nabla u\|_{L_\alpha^2(\Omega)}^2. \end{aligned} \quad (4.27)$$

Analogous estimates come from integration over the remaining subdomains of Ω_v^R . The proof is complete. \square

At this point we are able to state our well-posedness result.

Theorem 4.1.2. *Let $f \in L^2(\Lambda)$, $k \in L^\infty(\Omega)$, and assume that there exists a constant $k_0 > 0$ such that $k \geq k_0$ in Ω . Then, there is $\delta \in (0, 1)$, $\delta = \delta(k_0, R)$ such that for each $\alpha \in (0, \delta)$ there exists a unique $u \in V_\alpha$ such that*

$$a(u, v) = F(v) \quad \forall v \in V_{-\alpha},$$

where a and F are defined by (4.2), (4.3). Moreover, there exists a constant $C = C(k_0, R) > 0$ such that:

$$\|u\|_{V_\alpha} \leq C\|f\|_{L^2(\Lambda)}. \quad (4.28)$$

Proof. The idea is to apply the Nečas' theorem A.4.1, with $H_1 = V_\alpha$, $H_2 = V_{-\alpha}$. We already observed that since $\alpha > 0$, and thanks to property 4.1.1, F is a bounded linear functional on $V_{-\alpha}$, and

$$\|F\|_{V'_{-\alpha}} \leq \|\gamma_\Lambda\| \|f\|_{L^2(\Lambda)}, \quad (4.29)$$

where $\|\gamma_\Lambda\| = \|\gamma_\Lambda\|_{\mathcal{L}(V_{-\alpha}; L^2(\Lambda))}$. Furthermore, the bilinear form a is continuous:

$$|a(u, v)| = \left| \int_\Omega k d^\alpha \nabla u \cdot d^{-\alpha} \nabla v \, d\mathbf{x} \right| \leq \|k\|_\infty \|d^\alpha \nabla u\|_{L^2(\Omega)} \|d^{-\alpha} \nabla v\|_{L^2(\Omega)} \leq \|k\|_\infty \|u\|_{V_\alpha} \|v\|_{V_{-\alpha}}. \quad (4.30)$$

Now, let $v \in V_{-\alpha}$, $v \neq 0$; since $\alpha > 0$, we have $V_{-\alpha} \subset V_\alpha$. Choosing $u = v$ yields

$$\sup_{u \in V_\alpha} a(u, v) \geq a(v, v) \geq k_0 \|\nabla v\|_{L^2(\Omega)}^2 > 0.$$

In fact, if $\|\nabla v\|_{L^2(\Omega)} = 0$ then v is a constant, which is necessarily zero, due to the Dirichlet boundary conditions: this is in contrast with our assumption $v \neq 0$. Hence, a is non-degenerate and hypothesis (A.10) is satisfied.

To prove that (A.11) holds, it is sufficient to show that there are positive constants m, M , such that for every $u \in V_\alpha$ there is $v \in V_{-\alpha}$ satisfying

$$\|v\|_{V_{-\alpha}} \leq m\|u\|_{V_\alpha}, \quad (4.31)$$

$$a(u, v) \geq M\|u\|_{V_\alpha}^2. \quad (4.32)$$

Then, (A.11) holds with $C_2 = M/m$. Set

$$v(\mathbf{x}) = \tilde{d}(\mathbf{x})^{2\alpha} u(\mathbf{x}) + 2\alpha \Psi(\mathbf{x}), \quad (4.33)$$

where \tilde{d} is the following Lipschitz continuous function

$$\tilde{d}(\mathbf{x}) = \max\{\text{dist}(\mathbf{x}, \Lambda), R\} = \begin{cases} \text{dist}(\mathbf{x}, \Lambda) & \text{in } \Omega_v^R, \\ R & \text{elsewhere,} \end{cases} \quad (4.34)$$

and Ψ is the auxiliary function introduced in lemma 4.1.2. Notice that \tilde{d} is equivalent to the distance function d in the sense that

$$\left(\frac{R}{\text{diam}(\Omega)} \right) d \leq \tilde{d} \leq d \quad \text{on } \Omega. \quad (4.35)$$

Thanks to (4.35) and (4.20) we have

$$\|v\|_{L^2_{-\alpha}} \leq \|u\|_{L^2_\alpha} + 2\|\Psi\|_{L^2_{-\alpha}} \leq m_1 \|u\|_{V_\alpha}$$

where m_1 is independent of α . Moreover, since

$$\nabla v = \tilde{d}^{2\alpha} \nabla u + 2\alpha(\tilde{d}^{2\alpha-1} u \nabla \tilde{d} + \nabla \Phi)$$

observing that $\tilde{d} = d$ on Ω_V^R , $\nabla \tilde{d} = \nabla \Psi = \mathbf{0}$ on $\Omega \setminus \Omega_V^R$, and using estimate (4.21) of lemma 4.1.2, we have

$$\|\nabla v\|_{L_{-\alpha}^2} \leq \|\nabla u\|_{L_{\alpha}^2} + 2\|d^{2\alpha-1} u \nabla d + \nabla \Phi\|_{L_{-\alpha}^2(\Omega_V^R)} \leq m_2 \|u\|_{V_{\alpha}},$$

where m_2 is independent of α . Hence (4.31) is satisfied with $m^2 = m_1^2 + m_2^2$. Now, since

$$a(u, v) \geq k_0 \int_{\Omega} \tilde{d}^{2\alpha} |\nabla u|^2 \, dx + 2\alpha \int_{\Omega_V^R} \nabla u \cdot (\tilde{d}^{2\alpha-1} u \nabla \tilde{d} + \nabla \Phi) \, dx,$$

we can use estimate (4.35), and once again (4.21) to obtain

$$a(u, v) \geq k_0 \|\nabla u\|_{\tilde{L}_{\alpha}^2(\Omega)}^2 - 2\alpha \|\nabla u\|_{\tilde{L}_{\alpha}^2(\Omega_V^R)} \|d^{2\alpha-1} u \nabla d + \nabla \Phi\|_{\tilde{L}_{-\alpha}^2(\Omega_V^R)} \geq \|\nabla u\|_{\tilde{L}_{\alpha}^2(\Omega)}^2 (k_0 - 2\alpha C_3),$$

where C_3 is the constant in estimate (4.21), and, for $A \subset \Omega$, we define

$$\|f\|_{L_{\alpha}^2(A)}^2 := \int_A \tilde{d}^{2\alpha} |f|^2 \, dx.$$

Of course $\|f\|_{L_{\alpha}^2(\Omega_V^R)}^2 = \|f\|_{\tilde{L}_{\alpha}^2(\Omega_V^R)}^2$, and $\|\cdot\|_{\tilde{L}_{\alpha}^2(\Omega)}$, $\|\cdot\|_{L_{\alpha}^2(\Omega)}$ are equivalent norms, since thanks to (4.35) we have

$$\frac{R^{\alpha}}{\text{diam}(\Omega)^{\alpha}} \|f\|_{L_{\alpha}^2(\Omega)} \leq \|f\|_{\tilde{L}_{\alpha}^2(\Omega)} \leq \|f\|_{L_{\alpha}^2(\Omega)}.$$

Let $0 < \delta < k_0/(2C_3)$: for $0 < \alpha < \delta$ we have $0 < (k_0 - 2\delta C_3) < (k_0 - 2\alpha C_3)$, so that

$$a(u, v) \geq (k_0 - 2\delta C_3) \|\nabla u\|_{\tilde{L}_{\alpha}^2(\Omega)}^2 \geq \frac{R^{2\alpha} (k_0 - 2\delta C_3)}{\text{diam}(\Omega)^{2\alpha}} \|\nabla u\|_{L_{\alpha}^2(\Omega)}^2. \quad (4.36)$$

Therefore (4.32) holds with $M = \frac{(k_0 - 2\delta C_3) R^{2\alpha}}{(1 + C_P^2) \text{diam}(\Omega)^{2\alpha}}$ where C_P is the Poincaré's constant for V_{α} (see property A.2.1).

Therefore we can apply theorem A.4.1, and the proof is complete. The constant C in (4.28) is estimated by

$$C \leq \left(1 + \frac{m}{M}\right) \|\gamma_{\Lambda}\|.$$

□

4.2 Neumann-Robin problem with exchange term on a line

The analytical tools we introduced in previous sections may be used to give the following Neumann-Robin problem a proper mathematical setting:

$$\begin{cases} -\nabla \cdot (k \nabla u) + \beta(\bar{u} - u_0) \delta_{\Lambda} = 0 & \text{in } \Omega, \\ -\frac{\partial u}{\partial \mathbf{n}} = 0 & \text{on } \partial \Omega, \end{cases} \quad (4.37)$$

where $\beta > 0$ is a constant permeability coefficient (actually we have $\beta = 2\pi R D$, where D is the vessel surface permeability) and $u_0 \in L^2(\Lambda)$ is a given function. Before applying those tools to

(4.37), let us make a few remarks. First, we recall that \bar{u} is the average of u on circles lying in the normal plane to Λ , centered at point s , and with radius R , as in (3.9). With notations from lemma 4.1.2, we can write $\bar{u}(s) = A_{00}(R, s)$. Problem (4.37) has been named “Neumann-Robin” due to the Neumann boundary condition on $\partial\Omega$ and to the “Robin-like” exchange term on the line Λ . We will see that under suitable assumptions the Robin term can make the bilinear form “coercive enough” (in the sense of theorem A.4.1) even without Dirichlet boundary conditions. This is rather important, because problem (4.37) is our model problem for a wide range of typical applications (see the next section), in which diffusion from a 1D vessel into the tissue is driven by a concentration gap. Furthermore, extensions to fully coupled 1D-3D problems such as (3.19) are easily derived from the analysis of problem (4.37). The assumptions to have a well-posed problem concern the radius R : it has to be small enough.

First we have to give \bar{u} a meaning and introduce a special inequality, in the sense of the following lemmas.

Lemma 4.2.1. *Let $\alpha \in (0, 1)$: the mapping $u \rightarrow \bar{u}$ is continuous from $H_\alpha^1(\Omega)$ to $L^2(\Lambda)$, and*

$$\|\bar{u}\|_{L^2(\Lambda)} \leq C(R, \alpha) \|u\|_{H_\alpha^1(\Omega)}$$

where C is a positive constant.

Proof. We have

$$\int_\Lambda \bar{u}(s)^2 ds = \int_\Lambda \left(\frac{1}{2\pi} \int_0^{2\pi} u(s, R, \theta) d\theta \right)^2 ds \leq \int_\Lambda \frac{1}{2\pi} \int_0^{2\pi} u(s, R, \theta)^2 d\theta ds \leq \frac{1}{2\pi R} \|u\|_{L^2(\Gamma^R)}^2,$$

where Γ^R is the “actual” vessel surface (see sec. 3.2.1). Since $\text{dist}(\Gamma^R, \Lambda) = R > 0$, the trace operator from $H_\alpha^1(\Omega)$ to $L^2(\Gamma^R)$ is continuous (see property A.3.2) and the lemma follows. \square

Lemma 4.2.2. *Let a, b, c be positive constants. There are positive numbers $\xi_1 = \xi_1(a, b, c)$, $\lambda_0 = \lambda_0(b, c)$ such that if*

$$0 < \xi < \xi_1$$

then, for all $(x_1, x_2) \in \mathbb{R}^2$, we have the inequality

$$ax_1^2 + b\xi x_2^2 - 2c\xi x_1 x_2 \geq \xi \lambda_0 (x_1^2 + x_2^2).$$

In particular, the inequality is satisfied with $\xi_1 = \frac{ab}{2c^2}$ and $\lambda_0 = \frac{b}{2+b^2/c^2}$.

Proof. Set $A = \begin{bmatrix} a & -c\xi \\ -c\xi & b\xi \end{bmatrix}$ and $\mathbf{x} = \begin{bmatrix} x_1 \\ x_2 \end{bmatrix}$. We want to show that under the assumptions at hand, $\mathbf{x}^\top A \mathbf{x} \geq \xi \lambda_0 \|\mathbf{x}\|^2$ where λ_0 is positive and only depends on b, c . To this end, it is sufficient to prove that the smallest eigenvalue of A is greater than $\xi \lambda_0$. The smallest eigenvalue of A is given by

$$\lambda_{\min}(A) = \frac{1}{2} \left[(a + b\xi) - \sqrt{(a + b\xi)^2 + 4(c^2\xi^2 - ab\xi)} \right] \geq \frac{ab\xi - c^2\xi^2}{a + b\xi}$$

where inequality $\sqrt{t_0 + t} \leq \sqrt{t_0} + \frac{t}{2\sqrt{t_0}}$ has been used, with $t_0 = (a + b\xi)^2$, $t = 4(c^2\xi^2 - ab\xi)$.

If $\xi_1 = \frac{ab}{2c^2}$ and $0 < \xi < \xi_1$ we have

$$\lambda_{\min}(A) \geq \xi \frac{ab/2}{a + \frac{ab^2}{2c^2}} = \xi \frac{b}{2 + b^2/c^2},$$

so that the inequality holds true with $\lambda_0(b, c) = \frac{b}{2+b^2/c^2}$. \square

We state our well-posedness result as follows.

Theorem 4.2.1. *Let $k \in L^\infty(\Omega)$, $u_0 \in L^2(\Lambda)$, and assume that $k \geq k_0$ in Ω , k_0 being a strictly positive constant. Let $\beta > 0$, and*

$$\begin{aligned} a(u, v) &= \int_{\Omega} k \nabla u \cdot \nabla v \, d\mathbf{x} + \beta \int_{\Lambda} \bar{u}(s) v(s) \, ds, \\ F(v) &= \beta \int_{\Lambda} u_0(s) v(s) \, ds. \end{aligned} \quad (4.38)$$

Then, there is a constant $\delta \in (0, 1)$ such that if $\alpha \in (0, \delta)$ and $0 < R < R_1(\alpha, \beta, k_0)$, problem

$$a(u, v) = F(v) \quad \forall v \in H_{-\alpha}^1(\Omega),$$

admits a unique solution $u \in H_{\alpha}^1(\Omega)$.

Moreover, there is a constant $C(\alpha, \beta, R) > 0$ such that:

$$\|u\|_{H_{\alpha}^1(\Omega)} \leq C \|u_0\|_{L^2(\Lambda)}. \quad (4.39)$$

Proof. We adopt the same technique we used for theorem 4.1.2: in particular, the first term of a in (4.38) is continuous on $H_{\alpha}^1(\Omega) \times H_{-\alpha}^1(\Omega)$. The second term is also continuous, since we have

$$\beta \int_{\Lambda} \bar{u}(s) v(s) \, ds \leq \beta \|\bar{u}\|_{L^2(\Lambda)} \|v\|_{L^2(\Lambda)},$$

and we know that operators $u \mapsto \bar{u}$ and $v \mapsto \gamma_{\Lambda} v$ are respectively continuous from $H_{\alpha}^1(\Omega)$, $H_{-\alpha}^1(\Omega)$ to $L^2(\Lambda)$ (lemma 4.2.1 and theorem 4.1.1).

Similarly, F is a continuous linear functional on $H_{-\alpha}^1(\Omega)$, and

$$\|F\| \leq \|\gamma_{\Lambda}\| \|u_0\|_{L^2(\Lambda)}. \quad (4.40)$$

Let $v \in H_{-\alpha}^1(\Omega)$, $v \neq 0$; to show that bilinear form a is non-degenerate, we take $u = v$ as in the proof of theorem 4.1.2. We have

$$a(v, v) = \int_{\Omega} k |\nabla v|^2 \, d\mathbf{x} + \frac{\beta}{2\pi} \int_{s_1}^{s_2} \left(\int_0^{2\pi} v(s, R, \theta) \, d\theta \right) v(s) \, ds.$$

Since

$$v(s, R, \theta) = v(s) + \int_0^R \frac{\partial v}{\partial r}(s, r, \theta) \, dr,$$

integrating on $(0, 2\pi)$ and substituting in the previous equation gives

$$a(v, v) = \int_{\Omega} k |\nabla v|^2 \, d\mathbf{x} + \beta \left[\|v\|_{L^2(\Lambda)}^2 - \frac{1}{2\pi} \int_{s_1}^{s_2} \left(\int_0^{2\pi} \int_0^R \frac{\partial v}{\partial r}(s, r, \theta) \, dr \, d\theta \right) v(s) \, ds \right]. \quad (4.41)$$

By Schwarz inequality

$$\begin{aligned} \left(\int_0^R \frac{\partial v}{\partial r}(s, r, \theta) \, dr \right)^2 &= \left(\int_0^R r^{\alpha-\frac{1}{2}} r^{\frac{1}{2}-\alpha} \frac{\partial v}{\partial r}(s, r, \theta) \, dr \right)^2 \\ &\leq \int_0^R r^{2\alpha-1} \, dr \int_0^R r^{-2\alpha} \left(\frac{\partial v}{\partial r} \right)^2 r \, dr = \frac{R^{2\alpha}}{2\alpha} \int_0^R r^{-2\alpha} \left(\frac{\partial v}{\partial r} \right)^2 r \, dr \end{aligned} \quad (4.42)$$

so that

$$\begin{aligned} \int_{s_1}^{s_2} \left(\int_0^{2\pi} \int_0^R \frac{\partial v}{\partial r}(s, r, \theta) dr d\theta \right)^2 ds &\leq 2\pi \int_{s_1}^{s_2} \int_0^{2\pi} \int_0^R \left(\frac{\partial v}{\partial r}(s, r, \theta) \right)^2 d\theta ds \\ &\leq 2\pi \frac{R^{2\alpha}}{2\alpha} \|\nabla v\|_{L^2_{-\alpha}(\Omega^R_\Psi)}^2. \end{aligned} \quad (4.43)$$

Using (4.43) in (4.41) together with Schwarz inequality gives

$$a(v, v) \geq k_0 \|\nabla v\|_{L^2(\Omega)}^2 + \beta \|v\|_{L^2(\Lambda)}^2 - \beta \frac{R^{2\alpha}}{2\alpha} \|v\|_{L^2(\Lambda)} \|\nabla v\|_{L^2(\Omega)}.$$

Since $\|v\|_{L^2(\Lambda)} \|\nabla v\|_{L^2(\Omega)} \leq \frac{1}{2} \|v\|_{L^2(\Lambda)}^2 + \frac{1}{2} \|\nabla v\|_{L^2(\Omega)}^2$, we have

$$a(v, v) \geq \left(k_0 - \beta \frac{R^{2\alpha}}{4\alpha} \right) \|\nabla v\|_{L^2(\Omega)}^2 + \beta \left(1 - \frac{R^{2\alpha}}{4\alpha} \right) \|v\|_{L^2(\Lambda)}^2. \quad (4.44)$$

The expression on the right hand side of the last equation is a squared norm on $H^1_{-\alpha}(\Omega)$ if

$$R^{2\alpha} < 4\alpha \min\{k_0/\beta, 1\}. \quad (4.45)$$

In this case, the bilinear form a is non-degenerate.

Now, let $u \in H^1_\alpha(\Omega)$, and set

$$v = \tilde{d}^{2\alpha} u + 2\alpha \Psi,$$

as in the proof of theorem 4.1.2. It has already been shown that $\|v\|_{H^1_{-\alpha}} \leq m \|u\|_{H^1_\alpha}$, and that a constant $\delta > 0$, independent of α and R , exists such that

$$\int_\Omega \nabla u \cdot \nabla v dx \geq k_0(1 - \alpha/\delta) \|\nabla u\|_{L^2_\alpha(\Omega)}^2.$$

Hence we have

$$a(u, v) \geq k_0(1 - \alpha/\delta) \|\nabla u\|_{L^2_\alpha(\Omega)}^2 + \beta \int_\Lambda \bar{u}(s)v(s) ds. \quad (4.46)$$

Let us estimate the line integral. First of all, due to a density argument, we may assume u is smooth. Then, $\tilde{d}^{2\alpha} u$ vanishes on Λ , so that

$$v(s) = 2\alpha \Psi(s) = \frac{2\alpha}{2\pi} \int_0^{2\pi} \int_0^R r^{2\alpha-1} u(s, r, \theta) dr d\theta. \quad (4.47)$$

Furthermore, we have

$$\begin{aligned} v(s) &= \frac{1}{2\pi} \int_0^{2\pi} \int_0^R \frac{\partial}{\partial r} (r^{2\alpha} u) dr d\theta - \frac{1}{2\pi} \int_0^{2\pi} \int_0^R r^{2\alpha} \frac{\partial u}{\partial r} dr d\theta \\ &= R^{2\alpha} \bar{u}(s) - \frac{1}{2\pi} \int_0^{2\pi} \int_0^R r^{2\alpha} \frac{\partial u}{\partial r} dr d\theta. \end{aligned} \quad (4.48)$$

Thanks to Schwarz inequality

$$\left(\int_0^R r^{2\alpha} \frac{\partial u}{\partial r} dr \right)^2 \leq \int_0^R r^{2\alpha-1} dr \int_0^R r^{1+2\alpha} \left(\frac{\partial u}{\partial r} \right)^2 dr = \frac{R^{2\alpha}}{2\alpha} \int_0^R r^{1+2\alpha} \left(\frac{\partial u}{\partial r} \right)^2 dr, \quad (4.49)$$

and using (4.48) and the last estimate, we can write

$$\begin{aligned} \beta \int_{\Lambda} \bar{u}(s)v(s) \, ds &= \beta R^{2\alpha} \|\bar{u}\|_{L^2(\Lambda)}^2 - \frac{\beta}{2\pi} \int_{\Lambda} \bar{u}(s) \int_0^{2\pi} \int_0^R r^{2\alpha} \frac{\partial u}{\partial r} \, dr \, d\theta \, ds \\ &\geq \beta R^{2\alpha} \|\bar{u}\|_{L^2(\Lambda)}^2 - \beta \frac{R^{2\alpha}}{4\pi\alpha} \|\bar{u}\|_{L^2(\Lambda)} \|\nabla u\|_{\tilde{L}^2_{\alpha}(\Omega_{\mathbb{R}}^3)}. \end{aligned}$$

Therefore, we have

$$a(u, v) \geq k_0(1 - \alpha/\delta) \|\nabla u\|_{\tilde{L}^2_{\alpha}(\Omega)}^2 + \beta R^{2\alpha} \|\bar{u}\|_{L^2(\Lambda)}^2 - \beta \frac{R^{2\alpha}}{4\pi\alpha} \|\bar{u}\|_{L^2(\Lambda)} \|\nabla u\|_{\tilde{L}^2_{\alpha}(\Omega_{\mathbb{R}}^3)}.$$

Now we can use lemma 4.2.2, with $x_1 = \|\nabla u\|_{\tilde{L}^2_{\alpha}(\Omega)}$, $x_2 = \|v\|_{L^2(\Lambda)}$, $a = k_0(1 - \alpha/\delta)$, $b = \beta$, $c = \beta/(8\pi\alpha)$, and $\xi = R^{2\alpha}$: for

$$R^{2\alpha} < \frac{32\pi^2\alpha^2 k_0(1 - \alpha/\delta)}{\beta}, \quad (4.50)$$

we have

$$a(u, v) \geq R^{2\alpha} \lambda_0 \left[\|\nabla u\|_{\tilde{L}^2_{\alpha}(\Omega)}^2 + \|\bar{u}\|_{L^2(\Lambda)}^2 \right], \quad (4.51)$$

where $\lambda_0 = \frac{\beta}{2+64\pi^2\alpha^2}$. Since the L^2_{α} and \tilde{L}^2_{α} norms are equivalent (see the proof of theorem 4.1.2), $\|\bar{u}\|_{L^2(\Lambda)}$ is a seminorm and $\|\bar{u}\|_{L^2(\Lambda)} \neq 0$ if u is a 0^{th} -order polynomial, $u \neq 0$, we have that $(\|\nabla u\|_{\tilde{L}^2_{\alpha}}^2 + \|\bar{u}\|_{L^2(\Lambda)}^2)^{1/2}$ is a norm equivalent to $\|u\|_{H^1_{\alpha}}$ (see [61] pag. 27; however, the proof is the same of Poincaré inequality A.3.2). Therefore, defining $R_1^{2\alpha} = R_1^{2\alpha}(\alpha, \beta, k_0)$ as the smallest of the right hand sides of eq. (4.50) and (4.45), for $R < R_1$ Nečas' theorem applies and the theorem follows; in particular, (4.40) implies estimate (4.39). \square

4.3 1D-3D coupled problems with exchange term on a line

Our theory applies without substantial modifications to the coupled 3D-1D problem that has been introduced in section 3.2.2. This is actually the more interesting case in which two problems having a dimensional mismatch of order 2 are coupled via a ‘‘Robin-like’’ exchange term on a line: all multiscale models of physiological phenomena concerning blood flow and mass transport considered in the next chapter (except the hyperbolic models), basically refer to this paradigm.

The strong form of our model problem is the following one:

$$\begin{cases} -\nabla \cdot (k_t \nabla u_t) + \beta(\bar{u}_t - u_v) \delta_{\Lambda} = 0 & \text{in } \Omega, \\ -\frac{d}{ds} (k_v \frac{d}{ds} u_v) + \beta(u_v - \bar{u}_t) = 0 & \text{in } \Lambda, \end{cases} \quad (4.52)$$

where we have a tissue variable u_t and a diffusivity k_t , as well as a vessel variable u_v and diffusivity k_v . The two variables interact by an exchange term. This problem is a simplified version of (3.19) in which $\beta = 2\pi RD$, but this is not restrictive since the needed modifications for handling the reaction and advection terms are trivial. On the boundary, we shall consider standard mixed conditions:

$$\begin{aligned} -\frac{\partial u_t}{\partial \mathbf{n}} &= 0 & \text{on } \partial\Omega, \\ u_v(s_1) &= u_{v,0}, \\ -\frac{d}{ds} u_v(s_2) &= 0. \end{aligned} \quad (4.53)$$

The non-homogeneous Dirichlet boundary condition can be converted to a homogeneous one by means of an extension of the Dirichlet data (in the 1D case, we have simply to consider $\tilde{u}_v = u_v - u_{v,0}$ as the new unknown). For this reason we are going to consider a weak formulation of (4.52) in term of the (u_t, \tilde{u}_v) variables.

Theorem 4.3.1. *Let $k_t, k_v \in L^\infty(\Omega)$, and assume that $k_t, k_v \geq k_0$, in Ω , with $k_0 > 0$, constant. Define $V_\alpha = H_\alpha^1(\Omega)$, and \hat{V} the subspace of functions $f \in H^1(\Lambda)$ such that $f(s_1) = 0$. Let $\beta > 0$.*

Then, there is a positive constant $\delta \in (0, 1)$ such that if $\alpha \in (0, \delta)$ and $0 < R < R_1(\alpha, \beta, k_0)$, there exists a unique solution $\mathbf{u} \in V_\alpha \times \hat{V}$ of

$$a(\mathbf{u}, \mathbf{v}) = F(\mathbf{v}) \quad \forall \mathbf{v} \in V_{-\alpha} \times \hat{V},$$

where $\mathbf{u} = (u_t, \tilde{u}_v)$, $\mathbf{v} = (v_t, v_v)$,

$$\begin{aligned} a(\mathbf{u}, \mathbf{v}) &= \int_{\Omega} k_t \nabla u_t \cdot \nabla v_t \, d\mathbf{x} + \int_{\Lambda} k_v u'_v v'_v \, ds + \beta \int_{\Lambda} (\bar{u}_t - u_v)(v_t - v_v) \, ds, \\ F(\mathbf{v}) &= \beta u_{v,0} \int_{\Lambda} [v_t(s) - v_v(s)] \, ds. \end{aligned} \quad (4.54)$$

Moreover, there is a constant $C = C(\alpha, \beta, R, u_{v,0}) > 0$ such that:

$$\|\mathbf{u}\|_{V_\alpha \times \hat{V}} \leq C |u_{v,0}|. \quad (4.55)$$

Proof. But for minor modifications, it is identical to the proof of theorem 4.2.1. Namely, we choose $\mathbf{u} = \mathbf{v}$ to show that a is non-degenerate, and $\mathbf{v} = (\tilde{d}^{2\alpha} u_t + 2\alpha \Psi, u_v)$ to prove the inf-sup condition of Nečas' theorem, using lemma 4.2.2 to get the necessary inequalities to hold for R small enough. \square

Chapter 5

Finite element approximation of 1D-3D coupled problems

The advantage of using Hilbert functional spaces is that we can state convergence results for the finite element approximation. Together with theorem A.4.2, the main ingredients are regularity results for the solution and finite element approximation properties in Sobolev spaces. For weighted functional spaces, these subjects are not standard. A similar matter has been studied for axisymmetric Stokes flow in [7]; however, the issue of whether their results could be adapted or not to our case, has not been addressed in this work. For this reason, we do not treat the finite element convergence rates. Nevertheless, concerning the Neumann-Robin problem (4.37) (the same considerations clearly hold for the simpler Dirichlet problem with Dirac source), we will verify that finite element approximation is convergent in the H_α^1 norm. Results from numerical experiments will be discussed in order to suggest guidelines for further developments concerning the convergence rates.

The full 1D-3D coupled model requires the discretization of the line Λ as well: this introduces some more difficulties, so that we will discuss only the algorithmic aspects.

In what follows, we assume that domain Ω is a polyhedron; for the sake of simplicity, we only consider \mathbb{P}^1 finite elements, and introduce a regular family of “triangulations” $\{\mathcal{T}_h\}$ of Ω with the following standard properties:

- (i) The domain Ω is the union of the (tetrahedral) elements of \mathcal{T}_h .
- (ii) If $T_k \neq T_j$ and their intersection is non empty, then $T_k \cap T_j$ is either a face, a side or a node. We denote by $\mathbf{x}_i, i = 1, \dots, N_h$ the mesh nodes.
- (iii) There exists a constant σ independent of h , such that for all $T \in \mathcal{T}_h$, $\text{diam}(T) < h$ and T contains a sphere of radius σh_T .

Then, we define the family $\{V_h\}$ of \mathbb{P}^1 finite element spaces

$$V_h = \{f \in C(\Omega) : f|_{T_i} \in \mathbb{P}^1(T_i) \forall T_i \in \mathcal{T}_h\}. \quad (5.1)$$

As usual, we will equip V_h with its Lagrangian finite element base $\{\psi_i\}, i = 1, \dots, N_h$, satisfying

$$\psi_i(\mathbf{x}_j) = \delta_{ij}.$$

Property 5.0.1. *Let the assumption of theorem 4.2.1 be fulfilled. Then, for each $h > 0$, there exists a unique $u_h \in V_h$ such that*

$$a(u_h, v_h) = F(v_h) \quad \forall v_h \in V_h, \quad (5.2)$$

being a and F defined by eq. (4.38). Moreover, if $u \in H_\alpha^1(\Omega)$ is such that

$$a(u, v) = F(v) \quad \forall v \in H_{-\alpha}^1(\Omega),$$

then, there is a positive constant C such that

$$\|u - u_h\|_{H_\alpha^1} \leq C \inf_{\tilde{u} \in V_h} \|u - \tilde{u}\|_{H_\alpha^1}. \quad (5.3)$$

Proof. The idea is to use th. A.4.2, with $M_1 = M_2 = V_h \subset H_{-\alpha}^1(\Omega) \subset H_\alpha^1(\Omega)$. Let us prove that the hypotheses of the theorem are satisfied. For all $v \in V_h$, $v \neq 0$, we have:

$$\sup_{u \in V_h} a(u, v) \geq a(v, v) \geq c \|v\|_{H_{-\alpha}^1}^2 > 0, \quad (5.4)$$

since we proved in the proof of theorem 4.3.1, eq. (4.44), that last inequality is indeed true $\forall v \in H_{-\alpha}^1(\Omega)$, $v \neq 0$, with $c = c(\alpha, \beta, k_0, R)$.

In the sequel we denote by $(\cdot, \cdot)_{H_{-\alpha}^1}$ the $H_{-\alpha}^1(\Omega)$ scalar product; obviously, it is a scalar product on the discrete space V_h as well, and in the sequel we will always equip V_h with the $\|\cdot\|_{H_{-\alpha}^1}$ norm. All norms are equivalent on a finite dimensional space: hence $a(\cdot, \cdot)$ is continuous on $V_h \times V_h$, since it is continuous on $(\tilde{V}_h, \|\cdot\|_{H_\alpha^1}) \times (\tilde{V}_h, \|\cdot\|_{H_\alpha^1})$. Therefore, thanks to the Riesz theorem, we can introduce the linear operator $A : V_h \rightarrow V_h$ defined by

$$(w_h, Av_h)_{H_{-\alpha}^1} = a(w_h, v_h) \quad \forall w_h, v_h \in V_h. \quad (5.5)$$

Thanks to inequality (5.4), we have

$$c \|v_h\|_{H_{-\alpha}^1}^2 \leq a(v_h, v_h) = (v_h, Av_h)_{H_{-\alpha}^1} \leq \|v_h\|_{H_{-\alpha}^1} \|Av_h\|_{H_{-\alpha}^1}. \quad (5.6)$$

This yields

$$\|Av_h\|_{H_{-\alpha}^1} \geq c \|v_h\|_{H_{-\alpha}^1}, \quad (5.7)$$

so that A is an isomorphism from V_h to V_h^1 .

Consider a given $u_h \in V_h$, and the related function Ψ constructed as in lemma 4.1.2. As done in theorem 4.2.1, we introduce the function

$$\tilde{v} = \tilde{d}^{2\alpha} u_h + 2\alpha \Psi,$$

where \tilde{d} is the modified distance function (4.34). We recall that the following estimate holds true (see the proof of eq. (4.31) in th. 4.1.2):

$$\|\tilde{v}\|_{H_{-\alpha}^1} \leq m \|u_h\|_{H_\alpha^1} \quad (5.8)$$

Obviously, in general $\tilde{v} \notin V_h$. However, there is a unique $v_h \in V_h$ such that

$$(w_h, v_h)_{H_{-\alpha}^1} = a(w_h, \tilde{v}) \quad \forall w_h \in V_h. \quad (5.9)$$

¹ Since all scalar products on a finite-dimensional space are equivalent, the same result holds when (u, v) is given by the Euclidean scalar product of the coordinates of u, v with respect to a finite element basis. As a consequence, we have that the *finite element matrix* (which is the linear operator A corresponding to this scalar product) is non-singular. We recall that this is true only under the assumptions of theorem 4.3.1, namely the radius R has to be small enough.

Moreover, taking $w_h = v_h$, we have

$$c_1 \|v_h\|_{H_\alpha^1} \|v_h\|_{H_{-\alpha}^1} \leq \|v_h\|_{H_{-\alpha}^1}^2 = (v_h, v_h)_{H_{-\alpha}^1} = a(v_h, \tilde{v}) \leq c_2 \|v_h\|_{H_\alpha^1} \|\tilde{v}\|_{H_{-\alpha}^1}, \quad (5.10)$$

being c_1 the norm of the continuous embedding $H_{-\alpha}^1 \hookrightarrow H_\alpha^1$, c_2 the continuity constant of a . Hence, the following estimation holds:

$$\|v_h\|_{H_{-\alpha}^1} \leq c_3 \|\tilde{v}\|_{H_{-\alpha}^1}, \quad (5.11)$$

with $c_3 = c_2/c_1$. Since A is an isomorphism, using (5.5), (5.9), (5.7) and (5.11), we can write

$$\begin{aligned} \sup_{\substack{v \in V_h, \\ \|v\|_{H_{-\alpha}^1} \leq 1}} a(u_h, v) &\geq \frac{1}{\|A^{-1}v_h\|_{H_{-\alpha}^1}} a(u_h, A^{-1}v_h) = \frac{(u_h, v_h)_{H_{-\alpha}^1}}{\|A^{-1}v_h\|_{H_{-\alpha}^1}} \\ &= \frac{a(u_h, \tilde{v})}{\|A^{-1}v_h\|_{H_{-\alpha}^1}} \geq c_3 c \frac{a(u_h, \tilde{v})}{\|\tilde{v}\|_{H_{-\alpha}^1}} \end{aligned}$$

In the proof of th. 4.3.1, see eq. (4.51), we have proven that a constant $c_4 = c_4(\alpha, \beta, k_0, R) > 0$ exists such that

$$a(u_h, \tilde{v}) \geq c_4 \|u_h\|_{H_\alpha^1}^2;$$

thanks to estimate (5.8) we have finally

$$\sup_{\substack{v \in V_h, \\ \|v\|_{H_{-\alpha}^1} \leq 1}} a(u_h, v) \geq \frac{cc_4}{c_3 m} \|u_h\|_{H_\alpha^1},$$

so that the hypotheses of th. A.4.2 are satisfied.

As a consequence, there exist a unique finite element solution u_h of (5.2), and

$$\|u - u_h\|_{H_\alpha^1} \leq C \inf_{\tilde{u} \in V_h} \|u - \tilde{u}\|_{H_\alpha^1}, \quad (5.12)$$

being

$$C = 1 + \frac{c_2 c_3 m}{cc_4}.$$

□

We point out that as a corollary of property 5.0.1, we have the *convergence* of the finite element scheme in the H_α^1 norm. In fact, it is known that under our assumptions (i)-(iii) on \mathcal{T}_h , for all $u \in C^\infty(\Omega)$ we have

$$\lim_{h \rightarrow 0} \inf_{\tilde{u} \in V_h} \|u - \tilde{u}\|_{H^1(\Omega)} = 0;$$

since the embedding $H^1(\Omega) \hookrightarrow H_\alpha^1(\Omega)$ is continuous, we have

$$\lim_{h \rightarrow 0} \inf_{\tilde{u} \in V_h} \|u - \tilde{u}\|_{H_\alpha^1(\Omega)} = 0.$$

Due to the density of smooth functions, the result is extended to all $u \in H_\alpha^1(\Omega)$.

On the other hand, results about finite element convergence rates cannot be that easily extended to encompass our problem. Although Bramble-Hilbert and Deny-Lions lemmas (see [85]) hold true in weighted spaces, one needs regularity results to obtain an a priori error estimate with respect to h . For

example, if the results from [7] could be extended to our case, and a weighted Clément interpolation operator $\Pi_h : L^2_\alpha(\Omega) \rightarrow V_h$ could be constructed such that

$$\|u - \Pi_h u\|_{L^2_\alpha(\Omega)} \leq Ch^l |u|_{H^l_\alpha(\Omega)}$$

for integers $l = 0, 1, 2$ (we are using \mathbb{P}^1 elements), and, for $l = 1, 2$,

$$|u - \Pi_h u|_{H^1_\alpha(\Omega)} \leq Ch^{l-1} |u|_{H^l_\alpha(\Omega)},$$

where $|\cdot|$ denotes the standard Sobolev seminorm, these estimations would apply in our case for $l = 0, 1$ only: in fact, $u \notin H^2_\alpha(\Omega)$ (the second radial derivative near the line is $\mathcal{O}(r^{-2})$, so that $u \in H^2_{1+\alpha}(\Omega) \not\subset H^2_\alpha(\Omega)$). Therefore, we could justify the first order $L^2_{1/2}$ convergence in figure 3.3 for the simple example with Dirac source, but we could not use the former results to estimate the convergence rate for the H^1_α norm (which is actually < 1 , as we found in the numerical experiment).

5.1 FEM discretization of the coupled 1D-3D problem

Although for the Neumann/Robin problem there is no need of discretizing Λ , this becomes necessary when considering the coupled 1D-3D problem. Unless we consider spline FEM or similar techniques, we loose our smoothness assumption on Λ , and we are not allowed to use the theory previously exposed: this is the reason why we are not considering the finite element convergence for the fully coupled problem. The case in which Λ is only piecewise differentiable is remarkable also from a practical standpoint: we are mostly interested to the special situation in which the mesh of the 1D problem is *extracted* from the 3D mesh, being actually built on its *edges*. Indeed, in this case the finite element implementation is much simpler. This suggests also a 1D segmentation technique: we will show that in applications to tissue perfusion, it is possible to automatically build the 1D mesh directly from a medical image and an already available “superposed” 3D mesh, owing to proper path extraction algorithms. In the sequel we will discuss some algorithmic aspects of FEM discretization for the coupled problem, and we will present the convergence results for a test case in which an analytical solution is available.

Assumption. We assume that a collection \mathcal{I}_h of *edges* I_m of tetrahedra in \mathcal{T}_h is given, such that Λ is the union

$$\Lambda = \bigcup_{I_m \in \mathcal{I}_h} I_m.$$

This assumptions (see fig. 5.1) allows to inherit the 1D finite element space from the 3D one (this is true for polynomial degrees higher than 1 as well). Namely, we define the following space (notice that we include the homogeneous Dirichlet condition in this definition):

$$\hat{V}_h = \{f \in C(\Lambda) : f(s_1) = 0, f|_{I_m} \in \mathbb{P}^1(I_m) \forall I_m \in \mathcal{I}_h\}. \quad (5.13)$$

Then, we observe that we can choose a Lagrangian basis of \hat{V}_h , denoted by $\{\hat{\psi}_i\}$, $i = 1, \dots, \hat{N}_h$, such that elements $\hat{\psi}_i$ are the restriction on Λ of the 3D basis functions ψ_i whose node is lying on Λ (with the exception of the node where the Dirichlet condition is imposed). As for space \hat{V}_h , in the sequel objects related to the 1D discretization will be denoted with a hat. So, we denote by $\hat{\mathbf{x}}_i$, $i = 1, \dots, \hat{N}_h$

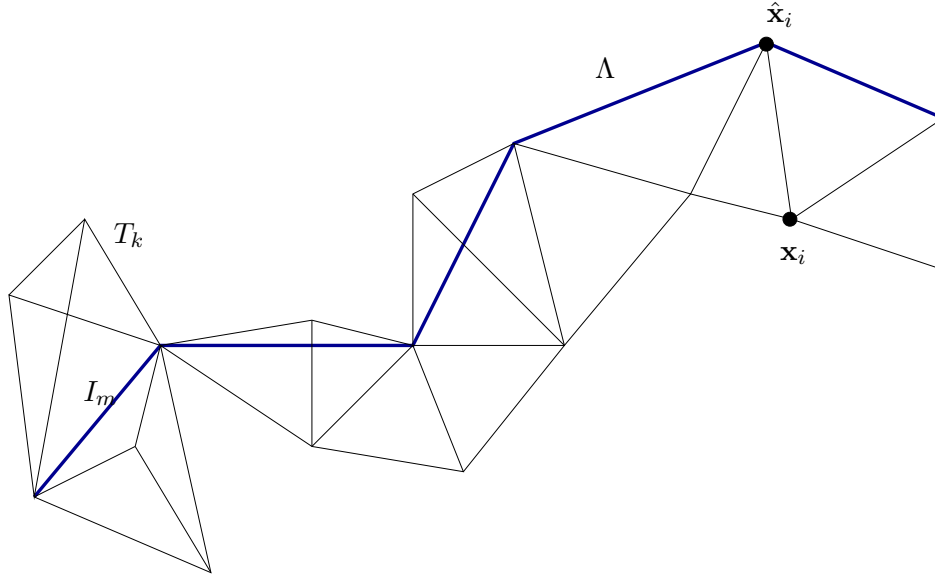


Figure 5.1: The domain Λ is composed by edges I_m of elements T_k of the 3D mesh

the nodes of the 1D mesh. Being those nodes a subset of the 3D mesh nodes, there is a function, that we call $r_\Lambda(\cdot)$, that maps each 1D node index to the corresponding 3D one:

$$[1, \dots, \hat{N}_h] \rightarrow [1, \dots, N_h], \quad i \mapsto r_\Lambda(i),$$

and is such that

$$\forall i \in [1, \dots, \hat{N}_h] : \quad \mathbf{x}_{r_\Lambda(i)} = \hat{\mathbf{x}}_i, \quad \text{and} \quad \hat{\psi}_i = \psi_{r_\Lambda(i)} \quad \text{on } \Lambda.$$

We also introduce the *extension matrix* R_Λ , defined as

$$(R_\Lambda)_{ij} = \begin{cases} 1 & \text{if } i = r_\Lambda(j), \\ 0 & \text{otherwise,} \end{cases} \quad i = 1, \dots, N_h, \quad j = 1, \dots, \hat{N}_h. \quad (5.14)$$

Matrix R_Λ has the following property: if $\hat{\mathbf{u}}$ are the components (with respect to the basis $\{\hat{\psi}_i\}$) of a function $\hat{u} \in \hat{V}_h$, then $\mathbf{u} = R_\Lambda \hat{\mathbf{u}}$ are the components (with respect to the basis $\{\psi_i\}$) of a function $u \in V_h$ such that $u = \hat{u}$ on Λ , and $u = 0$ on elements that are not sharing an edge or a node with Λ .

The finite element approximation of problem (4.52) reads: *find* $(u_h, \hat{u}_h) \in V_h \times \hat{V}_h$ *such that*

$$a((u_h, \hat{u}_h), (\psi, \hat{\psi})) = F(\psi, \hat{\psi}) \quad \forall (\psi, \hat{\psi}) \in V_h \times \hat{V}_h, \quad (5.15)$$

where bilinear form a and linear functional F are defined in (4.54). Let us focus on the matrix form of problem (5.15). Let $\mathbf{u} = (u_h^1, \dots, u_h^{N_h})$ and $\hat{\mathbf{u}} = (\hat{u}_h^1, \dots, \hat{u}_h^{\hat{N}_h})$ be the components of the approximate solutions with respect to the basis functions ψ_i and $\hat{\psi}_i$; eq. (5.15) is equivalent to the

following conditions:

$$\sum_{j=1}^{N_h} u_h^j \left(\int_{\Omega} k_t \nabla \psi_j \cdot \nabla \psi_i + \beta \int_{\Lambda} \bar{\psi}_j \psi_i \right) - \sum_{j=1}^{\hat{N}_h} \hat{u}_h^j \beta \int_{\Lambda} \hat{\psi}_j \psi_i = \beta u_{v,0} \int_{\Lambda} \psi_i, \quad (5.16)$$

$$i = 1, \dots, N_h,$$

$$- \sum_{j=1}^{N_h} u_h^j \beta \int_{\Lambda} \bar{\psi}_j \hat{\psi}_i + \sum_{j=1}^{\hat{N}_h} \hat{u}_h^j \left(\int_{\Lambda} k_v \frac{d}{ds} \hat{\psi}_j \frac{d}{ds} \hat{\psi}_i + \beta \int_{\Lambda} \hat{\psi}_j \hat{\psi}_i \right) = -\beta u_{v,0} \int_{\Lambda} \hat{\psi}_i, \quad (5.17)$$

$$i = 1, \dots, \hat{N}_h,$$

where we recall that $\bar{\psi}_j$ is the averaging of function ψ_j according to eq. (3.9). Equations (5.16) and (5.17) form a linear system, that in matrix form reads

$$\begin{pmatrix} A & B \\ \hat{B} & \hat{A} \end{pmatrix} \begin{pmatrix} \mathbf{u} \\ \hat{\mathbf{u}} \end{pmatrix} = \begin{pmatrix} \mathbf{b} \\ \hat{\mathbf{b}} \end{pmatrix} \quad (5.18)$$

The components of the right hand side vectors $\mathbf{b} = (b^1, \dots, b^{N_h})$ and $\hat{\mathbf{b}} = (\hat{b}^1, \dots, \hat{b}^{\hat{N}_h})$ read

$$b^i = \beta u_{v,0} \int_{\Lambda} \psi_i d\mathbf{x} \quad i = 1, \dots, N_h,$$

$$\hat{b}^i = -\beta u_{v,0} \int_{\Lambda} \hat{\psi}_i d\mathbf{x} \quad i = 1, \dots, \hat{N}_h. \quad (5.19)$$

Using the extension matrix R_{Λ} defined in (5.14), we have $\mathbf{b} = R_{\Lambda} \hat{\mathbf{b}}$.

To study the blocks of the global matrix of the previous system, let us introduce the 3D and 1D stiffness matrices K and \hat{K} , whose elements are respectively

$$K_{ij} = \int_{\Omega} k_t \nabla \psi_i \cdot \nabla \psi_j d\mathbf{x} \quad i, j = 1, \dots, N_h,$$

$$\hat{K}_{ij} = \int_{\Lambda} k_v \frac{d}{ds} \hat{\psi}_j \frac{d}{ds} \hat{\psi}_i ds \quad i, j = 1, \dots, \hat{N}_h, \quad (5.20)$$

and matrices \hat{M}, \bar{M} , whose elements are

$$\hat{M}_{ij} = \beta \int_{\Lambda} \hat{\psi}_i \hat{\psi}_j ds \quad i, j = 1, \dots, \hat{N}_h,$$

$$\bar{M}_{ij} = \beta \int_{\Lambda} \hat{\psi}_i \bar{\psi}_j ds \quad i = 1, \dots, N_h; j = 1, \dots, \hat{N}_h. \quad (5.21)$$

Observing that

$$\beta \int_{\Lambda} \bar{\psi}_j \psi_i ds = \begin{cases} \bar{M}_{kj} & \text{if } i = r_{\Lambda}(k), \\ 0 & \text{otherwise,} \end{cases} \quad \beta \int_{\Lambda} \hat{\psi}_j \psi_i ds = \begin{cases} \hat{M}_{kj} & \text{if } i = r_{\Lambda}(k), \\ 0 & \text{otherwise,} \end{cases}$$

and

$$\beta \int_{\Lambda} \bar{\psi}_j \psi_i ds = \sum_{k=1}^{\hat{N}_h} (R_{\Lambda})_{ik} \bar{M}_{kj}, \quad \beta \int_{\Lambda} \hat{\psi}_j \psi_i ds = \sum_{k=1}^{\hat{N}_h} (R_{\Lambda})_{ik} \hat{M}_{kj},$$

we obtain the following expressions for the blocks of our system:

$$\begin{pmatrix} A & B \\ \hat{B} & \hat{A} \end{pmatrix} = \begin{pmatrix} K + R_\Lambda \bar{M} & -R_\Lambda \hat{M} \\ -\bar{M} & \hat{K} + \hat{M} \end{pmatrix}$$

This means that the only matrices we need to build are stiffness and mass matrices on the 3D and 1D mesh, plus the matrix \bar{M} , which contains the averaging operator. The elements of this matrix are given by

$$\bar{M}_{ij} = \beta \int_\Lambda \hat{\psi}_i \bar{\psi}_j ds = \beta \sum_{I_m \in \mathcal{I}_m} \int_{I_m} \hat{\psi}_i(s) \left(\frac{1}{2\pi} \int_0^{2\pi} \psi_j(s, R, \theta) d\theta \right) ds, \quad (5.22)$$

where the term inside the parentheses is a function of s that we have to know in order to compute \bar{M}_{ij} . Although this can be done by numerical integration, it will require *interpolations* over the 3D mesh: that is, we will need to compute the value of a basis function at a certain point $\mathbf{x} \in \Omega$, namely a point lying on the circle described in local coordinates by (s, R, θ) for $\theta \in [0, 2\pi]$. This is due to the non-local nature of our problem. In general, interpolation is a computationally expensive procedure: we will show how its use can be minimized or even avoided, but for the moment let us postpone this issue.

To approximate the integral on I_m in eq. (5.22), it will suffice to use a quadrature formula on the reference interval $[0, 1]$, with nodes ξ_k and weights ω_k , $k = 1, \dots, \bar{N}$. If s_k is the curvilinear abscissa corresponding to the image of ξ_k by the geometrical transformation that maps $[0, 1]$ on the element I_m (see fig. 5.2), we can write

$$\int_{I_m} \hat{\psi}_i(s) \left(\frac{1}{2\pi} \int_0^{2\pi} \psi_j(s, R, \theta) d\theta \right) ds \simeq \sum_{k=1}^{\bar{N}} \hat{\psi}_i(s_k) \left(\sum_{l=1}^{\bar{N}} \psi_j(s_k, R, 2\pi\xi_l) \omega_l \right) J_k \omega_k \quad (5.23)$$

where J_k is the (absolute value of the determinant of the) Jacobian of the transformation at ξ_k (for linear elements, $J_k = |I_m| = \text{const.}$). We remark that in eq. (5.23), the same quadrature formula has been used for both the integrals over I_m and over the circles with radius R , normal to I_m and centered at points s_k (different formulae may be used as well). To apply any integration formula like (5.23), we will have to know the values of function ψ_j at points $\bar{\mathbf{x}}_{k,l} = \mathbf{x}_{v,0}(s_k, R, 2\pi\xi_l) \in \Omega$, $k, l = 1, \dots, \bar{N}$, where $\mathbf{x}_{v,0}$ are the local cylindrical coordinates around I_m , see eq. (3.3). This is the interpolation step: it requires finding the 3D element in which point $\bar{\mathbf{x}}_{k,l}$ is, tracking it back to the reference element, and then computing the corresponding values of the local basis functions. Of course, since R is expected to be small, only a very few elements will contain at least one interpolation point; but as there are \bar{N}^2 interpolations to perform for each 1D element I_m , this procedure can be very time consuming when \bar{N} is large.

There are two techniques that have been tested and employed in this work in order to overcome the problem. The first method simply consists in choosing \bar{N} small enough to keep the CPU time spent for interpolation in a reasonable range. The second, completely removes the interpolation step and leads to what we will call the

lumped approximation: if R is much smaller than the mesh size h , then we have $\bar{\psi}_j(s) \simeq \psi_j(s)$ in eq. (5.23). If we take $\psi_j(s)$ as an approximation of $\bar{\psi}_j(s)$, we have the following expression for matrix \bar{M}

$$\bar{M} \simeq \hat{M} R_\Lambda^\top \quad (5.24)$$

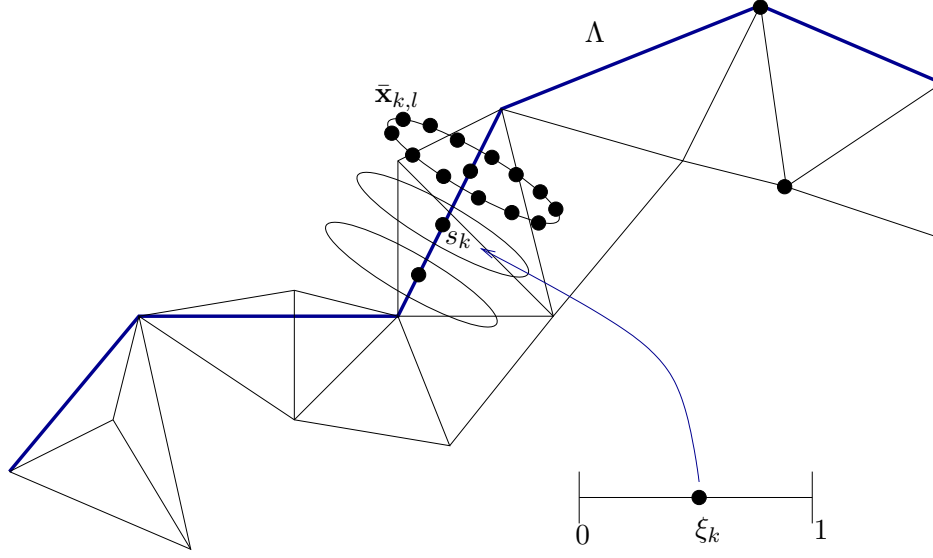


Figure 5.2: The 3D mesh and the 1D domain Λ , composed by edges of the 3D mesh. Shown are the circles around Λ used to compute the \bar{M}_{ij} terms by integration.

and the matrix of system (5.18) becomes

$$\begin{pmatrix} A & B \\ \hat{B} & \hat{A} \end{pmatrix} = \begin{pmatrix} K + R_\Lambda \hat{M} R_\Lambda^\top & -R_\Lambda \hat{M} \\ -\hat{M} R_\Lambda^\top & \hat{K} + \hat{M} \end{pmatrix} \quad (5.25)$$

In particular, this matrix is always symmetric and positive definite.

The symmetry of the global matrix coming from the lumped approximation is trivial; to see that it is positive definite as well, it suffices to observe that

$$\begin{pmatrix} \mathbf{u} \\ \hat{\mathbf{u}} \end{pmatrix}^\top \begin{pmatrix} R_\Lambda \hat{M} R_\Lambda^\top & -R_\Lambda \hat{M} \\ -\hat{M} R_\Lambda^\top & \hat{M} \end{pmatrix} \begin{pmatrix} \mathbf{u} \\ \hat{\mathbf{u}} \end{pmatrix} = (\hat{\mathbf{u}} - R_\Lambda^\top \mathbf{u})^\top \hat{M} (\hat{\mathbf{u}} - R_\Lambda^\top \mathbf{u})$$

and write

$$\begin{pmatrix} \mathbf{u} \\ \hat{\mathbf{u}} \end{pmatrix}^\top \begin{pmatrix} K + R_\Lambda \hat{M} R_\Lambda^\top & -R_\Lambda \hat{M} \\ -\hat{M} R_\Lambda^\top & \hat{K} + \hat{M} \end{pmatrix} \begin{pmatrix} \mathbf{u} \\ \hat{\mathbf{u}} \end{pmatrix} = \mathbf{u}^\top K \mathbf{u} + \hat{\mathbf{u}}^\top \hat{K} \hat{\mathbf{u}} + (\hat{\mathbf{u}} - R_\Lambda^\top \mathbf{u})^\top \hat{M} (\hat{\mathbf{u}} - R_\Lambda^\top \mathbf{u}).$$

Now, \hat{M} is positive definite; \hat{K} is also positive definite due to the homogeneous Dirichlet condition in the definition of the space \hat{V}_h ; matrix K is positive semidefinite, with only one null eigenvalue, corresponding to the eigenspace generated by vector $(1, 1, \dots, 1)^\top$. Therefore, the last expression is equal to zero only if $\hat{\mathbf{u}} = \mathbf{0}$, all components of \mathbf{u} are equal, and $R_\Lambda^\top \mathbf{u} = \hat{\mathbf{u}} = \mathbf{0}$; but this implies $\mathbf{u} = \mathbf{0}$ since $R_\Lambda(1, 1, \dots, 1)^\top \neq \mathbf{0}$.

We point out that we cannot expect the finite element scheme with lumped approximation to be convergent: we are replacing the \bar{u}_t term in eq. (4.52) by u_t , and this does not make sense from the analytical point of view, since u_t does not admit a trace on Λ . The goal of the lumped approximation is to simplify the assembling of the \hat{M} block if the characteristic mesh size h that we are using is sufficiently greater than the vessel radius R . Since this is actually the case in which 1D models are

introduced, we expect that at least for the typical applications we have in mind, the approximation (5.24) does not introduce a significant error. It is interesting to observe that a 1D-3D approach similar to the one we are proposing in this work, has been used (without any mathematical justification) for instance in [1], in the context of geothermal heating systems modelling. In this paper, a heat transfer problem is solved in a 3D soil domain, where the mesh size is in the range of 20 m, considering heat exchange with a 1D pipe (16 cm radius); the authors implicitly use lumped approximation (besides, the pipe radius is 125 times smaller than the mesh size h).

5.2 Convergence tests

We report hereafter some numerical results for a coupled 1D-3D problem with an available analytical solution. We consider again the simple geometry of the examples of section 3.2.2 (see fig 3.2); namely, using cylindrical coordinates, we set

$$\Omega = \{(z, r, \theta) \in (0, 1) \times [0, 1] \times [0, 2\pi)\}$$

and

$$\Lambda = \{(z, r, \theta) \in \Omega : r = 0\}.$$

Notice that the curvilinear abscissa of Λ is $s = z$. Then, we consider problem (4.52), that we report here for the reader's convenience

$$\begin{cases} -\nabla \cdot (k_t \nabla u_t) + \beta(\bar{u}_t - u_v) \delta_\Lambda = 0 & \text{in } \Omega, \\ -\frac{d}{dz} (k_v \frac{d}{dz} u_v) + \beta(u_v - \bar{u}_t) = 0 & \text{in } \Lambda, \end{cases} \quad (5.26)$$

with

$$k_t = 1, \quad k_v = k_v(z) = 1 + z + \frac{1}{2}z^2, \quad \beta = \frac{2\pi}{2\pi + \log R},$$

and boundary conditions

$$\begin{cases} u_t = 0 & \text{on } \Gamma_D, \\ \frac{\partial u_t}{\partial \mathbf{n}} = -\frac{1}{2\pi} \log r & \text{on } \partial\Omega \cap \{z = 1\}, \\ \frac{\partial u_t}{\partial \mathbf{n}} = \frac{1}{2\pi} \log r & \text{on } \partial\Omega \cap \{z = 0\}, \end{cases} \quad \begin{cases} u_v(0) = 1, \\ u_v(1) = 2, \end{cases}$$

where $\Gamma_D = \{(z, r, \theta) \in \{1\} \times [0, 1] \times [0, 2\pi)\} \subset \partial\Omega$ is the lateral surface of the cylinder Ω . In this case, it is easy to verify² that the exact solution is given by

$$u_t(z, r, \theta) = -\frac{1+z}{2\pi} \log r, \quad u_v(z) = 1 + z.$$

Let us consider the weak formulation of our problem: to deal with homogeneous Dirichlet conditions only, we set $u_v = 1 + z + \tilde{u}_v$, and we reformulate the problem using the “translated” unknown \tilde{u}_v . Introducing the spaces

$$V_\alpha = \{f \in H^1_\alpha(\Omega) : f|_{\Gamma_D} = 0\}, \quad \hat{V} = \{f \in H^1(\Lambda) : f(0) = f(1) = 0\},$$

² In fact, boundary conditions are satisfied; moreover, we have $\bar{u}_t = -\frac{1+z}{2\pi} \log R$, so that $\beta(\bar{u}_t - u_v) = -(1+z) = f(z)$, where f is such that $-\Delta u_t + f \delta_\Lambda = 0$ (in the sense of distributions) and $\frac{d}{dz} (-k_v \frac{d}{dz} u_\Lambda) - f = 0$. Hence, (u_t, u_v) solves our problem.

and using notations from theorem 4.3.1, the weak form of this problem reads: *find* $\mathbf{u} = (u_t, \tilde{u}_v) \in V_\alpha \times \hat{V}$ such that

$$a(\mathbf{u}, \mathbf{v}) = F(\mathbf{v}) \quad \forall \mathbf{v} = (v_t, v_v) \in V_{-\alpha}(\Omega) \times \hat{V},$$

where

$$\begin{aligned} a(\mathbf{u}, \mathbf{v}) &= \int_{\Omega} k_t \nabla u_t \cdot \nabla v_t \, d\mathbf{x} + \int_{\Lambda} k_v(z) \frac{d\tilde{u}_v}{dz} \frac{dv_v}{dz} \, dz + \beta \int_{\Lambda} (\bar{u}_t - \tilde{u}_v)(v_t - v_v) \, dz, \\ F(\mathbf{v}) &= \beta \int_{\Lambda} (1+z)(v_t - v_v) \, dz - \int_{\Lambda} k_v(z) v_v \, dz. \end{aligned} \quad (5.27)$$

We want to study the finite element convergence of our numerical schemes to the exact solution, and the error introduced by the lumped approximation. To this end, we perform two numerical experiments. First, a 2D-axisymmetric finite element discretisation of Ω is considered: in this case the interpolation is affordable even for a very small h , and convergence results are easier to obtain. Then, results for a 3D unstructured mesh are presented. We will see that, if the vessel radius R is sufficiently smaller than h , the lumped approximation gives almost the same results than a proper finite element discretisation with numerical quadrature of the non-local term.

5.2.1 2D-axisymmetric discretization.

If we take advantage of the cylindrical symmetry of our problem, assuming that all our variables depend only on the cylindrical coordinates (r, z) , we can rewrite equations (5.27) in the following form:

$$\begin{aligned} a(\mathbf{u}, \mathbf{v}) &= 2\pi \int_{[0,1]^2} k_t \left(\frac{\partial u_t}{\partial r} \frac{\partial v_t}{\partial r} + \frac{\partial u_t}{\partial z} \frac{\partial v_t}{\partial z} \right) r \, dr \, dz \\ &\quad + \int_0^1 k_v(z) \frac{d\tilde{u}_v}{dz} \frac{dv_v}{dz} \, dz + \beta \int_0^1 (\bar{u}_t - \tilde{u}_v)(v_t - v_v) \, dz, \\ F(\mathbf{v}) &= \beta \int_0^1 (1+z)(v_t - v_v) \, dz - \int_0^1 k_v(z) \frac{dv_v}{dz} \, dz, \end{aligned} \quad (5.28)$$

where, thanks to the θ -symmetry, we have

$$\bar{u}_t(z) = u_t(R, z).$$

Therefore, we can introduce a 2D finite element space V_h related to the triangulation \mathcal{T}_h of the square $[0, 1]^2$, and the corresponding 1D space \hat{V}_h induced on Λ , which is the $r = 0$ edge of the square, and use the expressions in (5.28) to compute the finite element solution $\mathbf{u}_h = (u_{t,h}, u_{v,h}) \in V_h \times \hat{V}_h$ of

$$a(\mathbf{u}_h, \mathbf{v}_h) = F(\mathbf{v}_h) \quad \forall \mathbf{v}_h \in V_h \times \hat{V}_h.$$

We used a composite trapezium rule with 10 subintervals to compute the integrals in (5.22).

In fig. 5.3 we report the computed approximation errors $E_{t,h}(V) = \|u_{t,h} - u_t\|_V$ and $E_{v,h}(\hat{V}) = \|u_{v,h} - u_v\|_{\hat{V}}$ for several spaces V, \hat{V} (for weighted norms we consider $\alpha = 1/2$), for $R = 0.05$ (that is 20 times smaller than the radius of Ω), corresponding to $\beta \simeq 1.911$, and for different mesh sizes h (from 0.0625 to 0.00097). The convergence of the numerical scheme is respectively of order 0.51 and 1.86 in the $H_{1/2}^1$ and $L_{1/2}^2$ norms for the 3D solution $u_{t,h}$, and of order 2.1 in both the H^1 and L^2 norms for the 1D solution $u_{v,h}$.

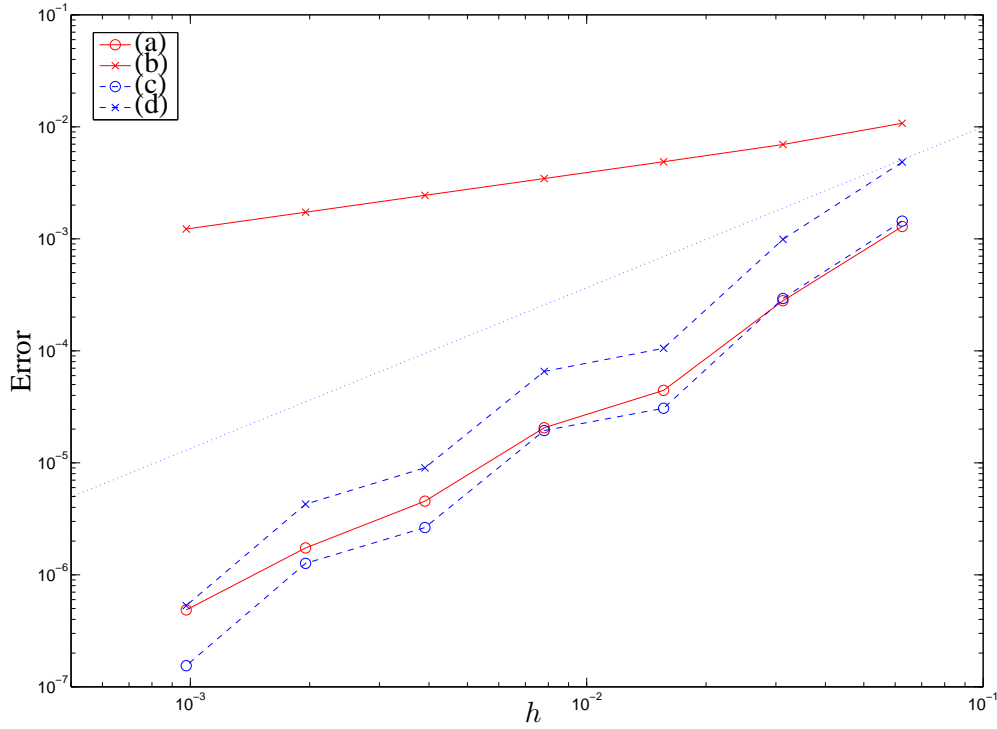


Figure 5.3: Computed errors for the 2D-axisymmetric FE approximation in different norms: the blue dotted line corresponds to a convergence rate equal to 1. Solid lines: $E_{t,h}(V)$ errors for $V = L^2_{1/2}(\Omega)$, (a), and $V = H^1_{1/2}(\Omega)$, (b). Dashed lines: $E_{v,h}(\hat{V})$ errors for $\hat{V} = L^2(\Lambda)$, (c), and $\hat{V} = H^1(\Lambda)$, (d). The mean rates (from regression lines) are: 1.86 (a), 0.51 (b), 2.1 (c), 2.1 (d).

5.2.2 Full 3D-1D discretization : the error introduced by the lumped approximation.

In order to study the effectiveness of the 1D-3D approach in a more realistic situation, we have computed finite element approximations using a full 3D unstructured mesh for the domain Ω , and an *extracted* 1D mesh built with the edges that are the closest to the actual $r = 0$ line (for the description of the extraction algorithm, we refer to the next chapter). Moreover, the same experiments were done first using interpolation and eq. (5.23) to compute the \bar{M}_{ij} elements (IN), then using the lumped approximation (LA), and for two values of the vessel radius, $R = 0.1$ and $R = 0.01$. Relative errors are reported in table 5.1: the solution for the (IN) case with the finest mesh is shown in fig. 5.4. From these results, the following observations can be made:

1. As expected, convergence for $h \rightarrow 0$ is achieved by the (IN) approach only.
2. The relative error affecting the 3D numerical (LA)-solution is almost equal to the one of the (IN)-solution when h is at least a few times bigger than R ; in this case the (LA) best error is about 10% in the $H^1_{1/2}$ and $L^2_{1/2}$ norms.
3. The relative error affecting the 1D numerical solution with (LA), is about 1-3%, for both values of R .

$R = 0.01, \text{IN}$	h	$E_{t,h}^r(L_\alpha^2)$	$E_{t,h}^r(H_\alpha^1)$	$E_{v,h}^r(L^2)$	$E_{v,h}^r(H^1)$
	0.200	0.2462	0.2659	0.0121	0.0342
	0.100	0.1143	0.1171	0.0060	0.0169
	0.050	0.0360	0.0379	0.0018	0.0053
	0.025	0.0100	0.0124	0.0005	0.0014
$R = 0.01, \text{LA}$	h	$E_{t,h}^r(L_\alpha^2)$	$E_{t,h}^r(H_\alpha^1)$	$E_{v,h}^r(L^2)$	$E_{v,h}^r(H^1)$
	0.200	0.21873	0.23964	0.01078	0.03036
	0.100	0.07795	0.08225	0.00409	0.01146
	0.050	0.00128	0.02505	0.02310	0.00360
	0.025	0.09674	0.09470	0.00527	0.01475

$R = 0.1, \text{IN}$	h	$E_{t,h}^r(L_\alpha^2)$	$E_{t,h}^r(H_\alpha^1)$	$E_{v,h}^r(L^2)$	$E_{v,h}^r(H^1)$
	0.200	0.03191	0.06352	0.00077	0.00219
	0.100	0.00893	0.02107	0.00035	0.00100
	0.050	0.00127	0.01172	0.000009	0.00002
	0.025	0.00331	0.00817	0.000009	0.00002
$R = 0.1, \text{LA}$	h	$E_{t,h}^r(L_\alpha^2)$	$E_{t,h}^r(H_\alpha^1)$	$E_{v,h}^r(L^2)$	$E_{v,h}^r(H^1)$
	0.200	0.14484	0.14694	0.00773	0.02194
	0.100	0.21300	0.20915	0.01156	0.03244
	0.050	0.26739	0.26196	0.01462	0.04092
	0.025	0.30912	0.30281	0.01693	0.04737

Table 5.1: Relative errors (normalized to the norm of the exact solution; for weighted norms, $\alpha = 1/2$) for $R = 0.01$ (top) and $R = 0.1$ (bottom). For each value of R , errors are reported for the interpolation (IN) and the lumped approximation (LA) case.

4. Despite the larger values of the global errors affecting the 3D solutions, as we already observed in fig. 3.4, the local error is always much smaller far away from Λ , and is mostly concentrated on elements sharing an edge or a node with Λ .

From these observations, we can conclude that (i) our 1D-3D finite element discretization allows for the numerical approximation of problem (5.26), and (ii) the lumped approximation may be adopted at least when the mesh size h is several times greater than the typical vessel radius R . This result is comforting: the critical applications, in which the (IN) approach would be computationally too expensive, are perfusion simulations with a consistent number of 1D vessels in a given 3D tissue, and usually, if the vessels are many and small, the 3D spatial resolution needed in practice is always sufficiently bigger than R .

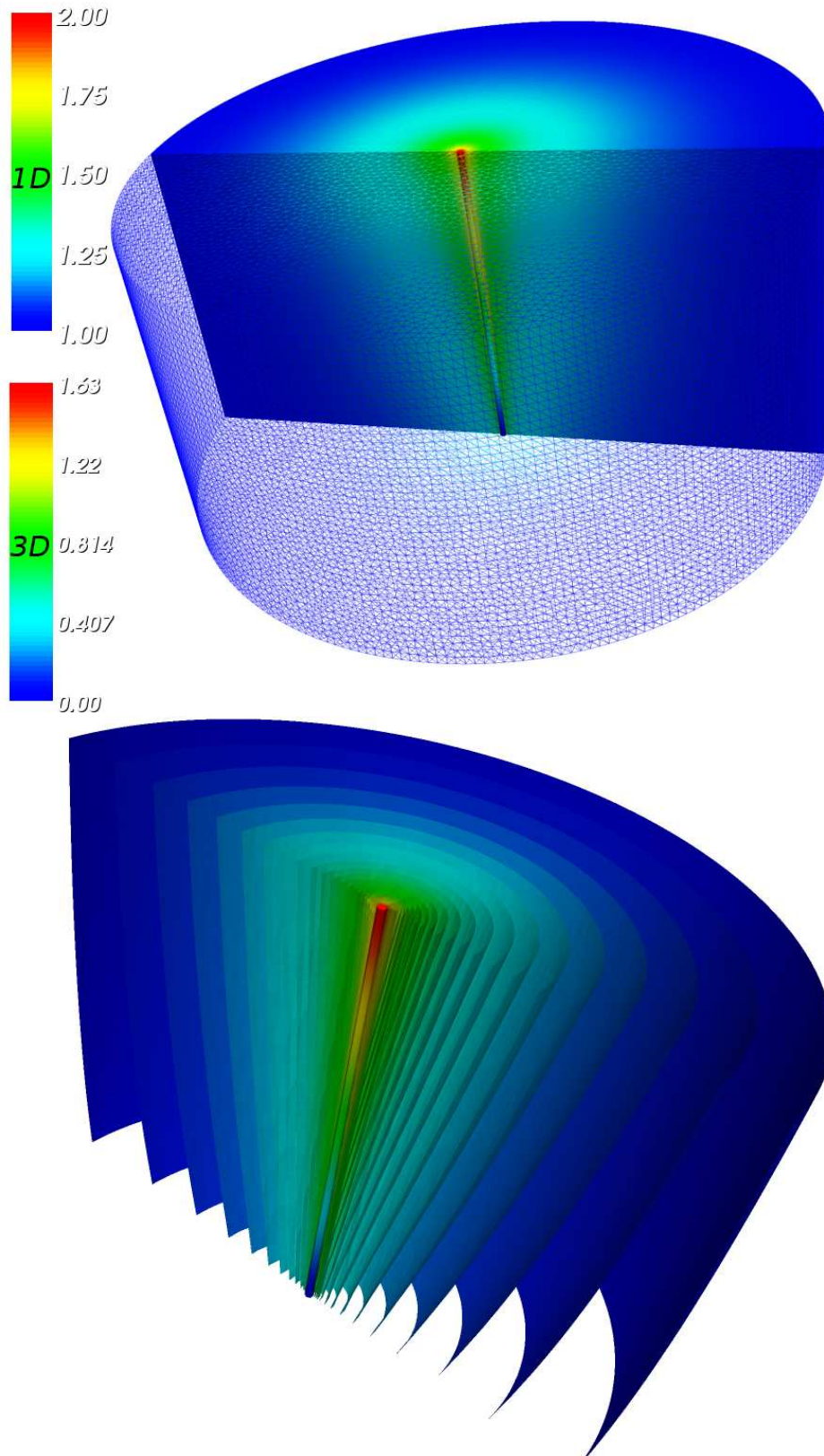


Figure 5.4: Computed approximate solutions for the full 3D-1D FE approximation. Top: shown are the surface mesh of the 3D domain Ω , the solution $u_{t,h}$ in a half of Ω , and the solution $u_{v,h}$ on Λ . In the picture, the 1D domain Λ has been rendered as a “tube” only for visualization purposes. Bottom: isosurfaces of the solution $u_{t,h}$ in a half of Ω , and the solution $u_{v,h}$ on Λ .

Chapter 6

Modelling blood flow and mass transport in vascularized tissues

6.1 Introduction

The simulation of biological transfer mechanisms between blood and tissues is of primary interest for several reasons. Circulation is responsible for a number of exchange processes between blood and cells, most remarkably:

- oxygen delivery to the tissues (blood as a carrier of chemicals)
- thermal regulation (blood as a heat exchanger)

These two examples are sufficient to explain how circulation and related transport phenomena are strongly affecting the body vital functions. In general, the study of the interaction between vessels and tissues is a valuable tool in biomedical engineering and medicine: we cite for instance applications in pharmacokinetics, design of biomedical devices such as *drug eluting stents* for arterial diseases, *implanted insulin pumps or patches* (possibly sensible to glucose concentration) for diabetes therapy, and *hyperthermia treatment* in some cancer therapies. In these cases, mathematical modelling might provide new insights to the biomedical engineer. Moreover, pathological or extreme conditions may be studied by means of simulations before starting any *in vivo* investigation.

Most of the relevant transfer processes between blood and tissues are due to small vessels (arterioles and capillaries) rather than large vessels. Among these processes, there is oxygen delivery, carbon dioxide removal, transfer of other chemicals (e.g. glucose, lactate drugs, see chapter 1), and heat exchange. It is known that small vessels strongly respond to modifications of the metabolic and hemodynamic state, by changing their resistance to blood flow. This makes the picture rather complex, since both microcirculation hemodynamics and autoregulation have to be taken into account. Now, any autoregulation model needs basically two input variables: local blood flow rate and local chemical concentrations¹: for this reason, this chapter will focus on modelling of perfusion and mass transport in tissues.

Vasculature shows very different space scales. It is organized in a hierarchical way: a given vessel may branch into several children vessels, and this splitting is repeated until the lowest level of the hierarchy (the capillary bed) is reached. The very particular hierarchical structure is indispensable, because of the small oxygen diffusion distance in the *interstitium*, as shown by the next example.

¹see for instance the works by Pries, Secomb and Gaetgens: [79], [80].

Example. The effective diffusion constant D_{O_2} of oxygen by myoglobin in skeletal muscle is about $10^{-4} \text{ cm}^2 \text{ s}^{-1}$ [77], and the (volume) concentration of oxygen when myoglobin is 100% saturated is $[O_2] = 11.2 \cdot 10^{-3} \text{ ml}(O_2) \text{ ml}^{-1}$. Let A be the area through which oxygen is transferred from blood to tissue, d the distance between the source of oxygen (blood) and the target (mitochondria), and q the rate of oxygen consumption in tissues ($q \simeq 1.3 \cdot 10^{-3} \text{ ml}(O_2) \text{ ml}^{-1} \text{ s}^{-1}$ in exercising muscle, [77]). Thanks to Fick's law the mass balance reads

$$D_{O_2}[O_2] \frac{A}{d} = qV,$$

where V is the volume of the tissue; if $V \simeq Ad$, then we get

$$d \simeq \sqrt{\frac{D_{O_2}[O_2]}{q}} \simeq 3 \cdot 10^{-2} \text{ cm}.$$

Actually, physiological measurements show that d is even smaller: for example in the hamster cheek pouch retractor muscle the number of capillaries per unit area is $N = 1.4 \cdot 10^5 \text{ cm}^{-2}$ [25], from which $d = \sqrt{1/N} = 2 \cdot 10^{-3} \text{ cm}$ (see fig. 6.1).

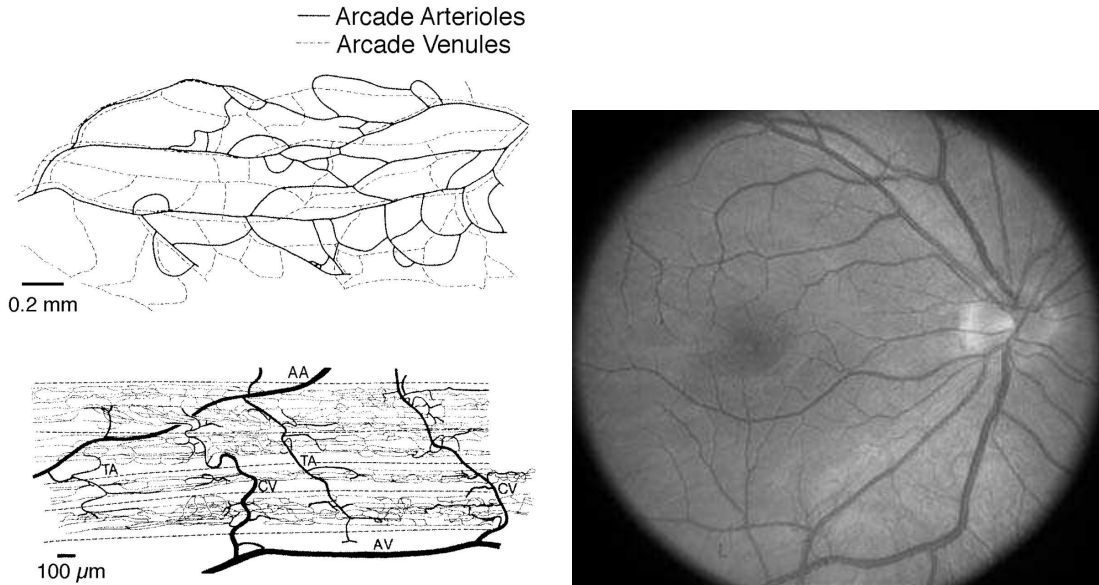


Figure 6.1: (From [96, 93]) Examples of vascular networks. On the left, top: tracing of arcade arterioles (AA) and arcade venules (AV) in the rat spinotrapezius muscle. The arcade network spans the entire muscle, and there are multiple connections of this network to the central arteries. The side branches to the capillary network (bottom) are provided by the terminal (transverse) arterioles (TA), which form asymmetric trees and directly connect to the capillary meshwork. Capillaries are predominantly aligned with the muscle fibers and give rise to the collecting venules (CV), which return the blood to the arcade venules. On the right: retinal imaging. An optical camera is used to see through the pupil of the eye to the rear inner surface of the eyeball. Shown are the retinal layer and its vessels, with their complex branching patterns.

Due to this multiscale structure of a tissue, the most suitable mathematical models for studying perfusion and mass transport should have multiscale nature too. Multiscale models of the cardiovascular system have already been introduced by several authors (for example [31], [84], [76], only to cite a few of them); the relatively large number of works on this topic has concerned most of the times the use of highly accurate models (for example, Navier-Stokes equations for blood flow with

a structure model for the vessel wall) for *large vessels*, coupled with reduced models (1D models or lumped parameter models) representing the remaining part of the circulation. The intrinsic power of such an approach is the capability to simulate in a very accurate manner the behaviour of a given blood vessel or small arterial tree (the carotid bifurcation, for example) without neglecting the influence of the whole circulatory system.

The idea of using a similar approach for tissue perfusion naturally comes up. More precisely, we can distinguish between blood flow at *macroscale*, that is in large and medium-size vessels, that one wants to describe with their geometry, and blood flow at *microscale* (small vessels, capillary bed), where reduced models involving average quantities are preferable. The key point from which this work has been motivated is that, when dealing with tissue perfusion and metabolism, the two scales have very specific properties:

- The macroscale is usually given by *complex arterial trees* (see fig. 6.1), rather than a few large blood vessels. Here we have *fast* blood flow and mass transport.
- In general, transfer processes take place at the microscale; at this scale, blood flow is quite *slow*.

These properties have to be taken into account when developing specific mathematical models for tissue perfusion:

- The geometrical complexity of the macroscale asks for models apt to resolve the vessel geometry and capture the behavior of the main physiological variables (blood pressure, concentrations, temperature, . . .) without being too computationally expensive. In this regard, 1D models seem to be the natural choice.
- Concerning the microscale, one would better resort to *averaged* quantities to describe the processes of interest: in fact, the geometrical data as well as other fine properties of microcirculation are usually not known in detail, and, on the other hand, computations with a very fine resolution are often beyond the needs. Actually, special 3D models from homogenization theory (or mixture theory²) have been developed in order to describe the evolution of the (volume) average of the physiological variables in a tissue.
- The 1D domain (the arterial tree) is a *subset* of the 3D domain (the tissue), and the geometry of the former influences the flow in the latter. Borrowing the terminology from geomechanics, the 1D domain can be seen as a *fracture* in the 3D one.

Thus, in this chapter we will consider 1D-3D models of blood flow and mass transport in tissues. In this regard, we will take advantage of the results of the chapters 3, 4 and 5 on the 1D-3D coupling. As schematically depicted in fig. 6.2, the final goal is to employ a two-stages model, the first stage being blood flow computation, the second mass transport simulation; at each stage, two coupled problems, respectively for the tissue (3D) and the vessel tree (1D), interact (the interactions being denoted by I_1 and I_2 in the figure); we will see that this situation falls in the class of problems we considered in the aforementioned chapters. Fig. 6.2 is only meant to sketch the basic ideas: several models of increasing complexity can be used in this scenario. We will study some of the possible choices, discussing the role of the interactions I_1 and I_2 . When needed, numerical techniques will be discussed as well.

²Mixture theory [24] provides an axiomatic framework for the dynamics of multiphase flow; it has been used for example by [44] to model blood flow in tissues

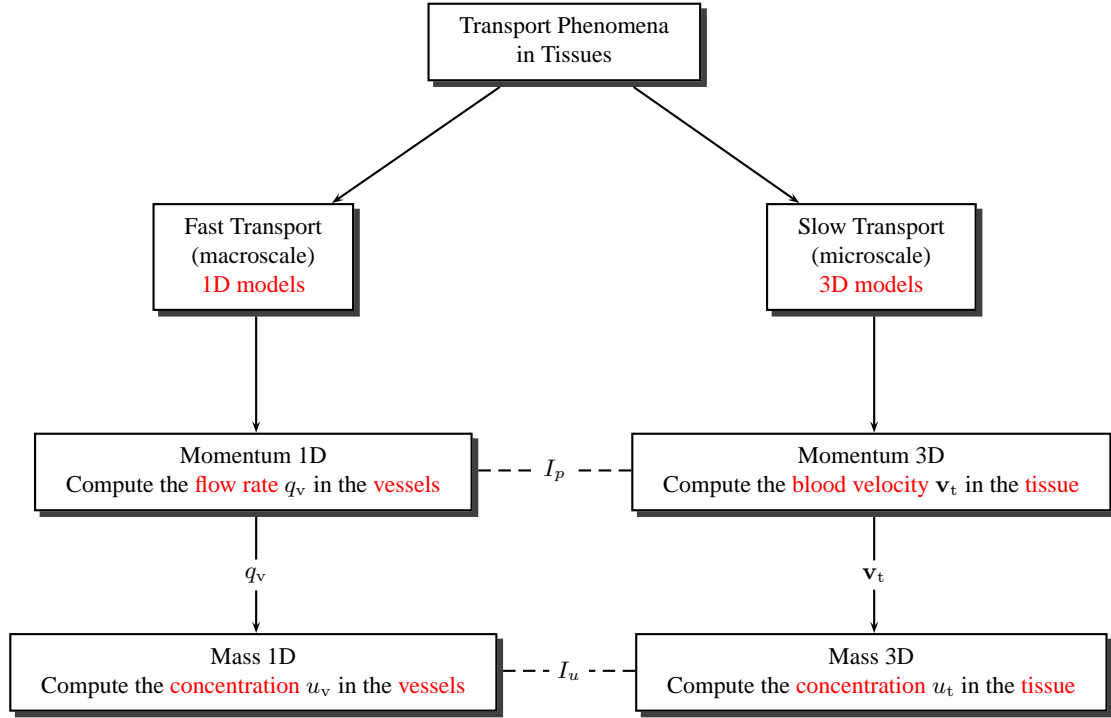


Figure 6.2: Multiscale approach in modelling transport phenomena in tissues

6.2 Macroscale: 1D and $\frac{1}{2}$ D models for blood flow and transport

One-dimensional models have been widely applied in hemodynamics to represent systems composed by a large number of blood vessels. From the mathematical and numerical point of view, they have been extensively studied for instance in [31], [84], [30], [75]; we refer to these articles for a thorough introduction to the subject, or to chapter 2.

One-dimensional models were introduced to study large vessels, with inner radius greater than a few millimeters. When considering small portion of tissue, the vessels at the macroscale are often smaller than that, and some simplifications of the existing models are possible. Let us recall the 1D model of blood flow in a single 1D vessel described by the spatial variable $s \in [0, L]$. For the sake of simplicity we shall consider the case of parabolic velocity profile, in which we have

$$\begin{cases} \frac{\partial A}{\partial t} + \frac{\partial Q}{\partial s} = 0, \\ \frac{\partial Q}{\partial t} + \frac{\partial}{\partial s} \left(\alpha \frac{Q^2}{A} \right) + \frac{A}{\rho} \frac{\partial P}{\partial s} + \frac{8\pi\nu}{A} Q = 0, \end{cases} \quad (6.1)$$

where t is the time, $A = A(t, s)$ is the cross-sectional area, $Q = Q(t, s)$ the blood flow rate, α is the Coriolis coefficient, ρ is the blood density and ν is the blood kinematic viscosity [84].

The equations are closed by a pressure-strain relation for the wall displacement. If we assume that Hooke's law holds, we have [84]:

$$P = P_0 + \frac{4}{3} \frac{Eh}{R_0} \left(\frac{R - R_0}{R_0} \right), \quad (6.2)$$

being h the wall thickness, E the Young's modulus, R the vessel radius, R_0 the reference radius corresponding to $P = P_0$ (here the Poisson ratio has been set to 0.5). Starting from these equations, it is possible to introduce two simplified models, the linearized 1D model and its quasistatic approximation, that will be referred to as the $\frac{1}{2}$ D model. Both of them allow the computation of blood flow rate, that in turn can be used in a one-dimensional mass transport model, as in chapter 2.

6.2.1 The linearized 1D model for blood flow

Using the small displacements hypothesis $A \simeq A_0 = \pi R_0^2$, (6.2) gives

$$\frac{\partial A}{\partial t} = \sqrt{A} \left(\frac{3\sqrt{\pi} R_0^2}{2Eh} \right) \frac{\partial P}{\partial t} \simeq c \frac{\partial P}{\partial t}, \quad \text{where} \quad c = \frac{3\pi R_0^3}{2Eh}.$$

Moreover, under the same assumption, and for small vessels, the convective terms can be neglected (see the derivation of the 0D model from the 1D model in [84]), and we can set $A \simeq A_0$ in the second equation of (6.1). In this case the following linearized model is obtained (see also [64]):

$$\begin{cases} c \frac{\partial P}{\partial t} + \frac{\partial Q}{\partial s} = 0, \\ \frac{\partial Q}{\partial t} + \frac{1}{l} \frac{\partial P}{\partial s} + rQ = 0, \end{cases} \quad (6.3)$$

where the constants

$$r = \frac{8\pi\nu}{A_0}, \quad l = \frac{\rho}{A_0} \quad (6.4)$$

have the physical meaning of an hydraulic *resistance* and *inductance* (whereas c is a *compliance*), and are depending only on the vessel stiffness and geometry and blood mechanical properties. With suitable initial and boundary conditions, this is a linear hyperbolic system of second order equations, that has been studied for multiscale coupling with 0D models for example in [29].

The model can immediately be extended to treat

- a flow rate loss term ϕ_v along the vessel (measured in square length on time);
- a concentrated load (hydraulic conductance G) at the end of the vessel ($s = L$).

To summarize, to introduce the symbols that we will use later on to distinguish between vessel (subscript “v”) and tissue (subscript “t”) variables, and to take into account the fluid loss, we restate the 1D linearized problem as follows:

Problem 6.2.1. Find the vessel pressure $p_v(t, s)$ and flow rate $q_v(t, s)$ such that:

$$\frac{\partial}{\partial t} \begin{bmatrix} p_v \\ q_v \end{bmatrix} + H \frac{\partial}{\partial s} \begin{bmatrix} p_v \\ q_v \end{bmatrix} + \mathbf{r}(p_v, q_v) = \mathbf{0}, \quad t > 0, s \in (0, L), \quad (6.5)$$

where

$$H = \begin{bmatrix} 0 & c^{-1} \\ l^{-1} & 0 \end{bmatrix}, \quad \mathbf{r}(p_v, q_v) = \begin{bmatrix} c^{-1} \phi_v \\ r q_v \end{bmatrix}, \quad (6.6)$$

given suitable boundary and initial conditions (BC and IC).

The BC that we can consider for problem 6.2.1 are in number of one for each boundary point, corresponding to the fact that the eigenvalues of matrix H have opposite signs. For example we can prescribe the input pressure $p_{\text{in}}(t)$ at $s = 0$, and the concentrated load at $s = L$, assuming a linear relation between flow rate and pressure via the conductance G . Concerning the IC, we have simply to assign the functions $p_v(0, s)$ and $q_v(0, s)$, $s \in (0, L)$. The BC/IC corresponding to this case are the following:

$$\begin{cases} p_v(t, 0) = p_{\text{in}}(t), & q_v(t, L) - Gp_v(t, L) = 0, & t > 0, \\ p_v(0, s) = p_{v,0}(s), & q_v(0, s) = q_{v,0}(s), & s \in (0, L). \end{cases} \quad (6.7)$$

6.2.2 Quasistatic approximation: the $\frac{1}{2}$ D model

The constant r in (6.4) has the units of a frequency [s^{-1}]. Let us assume to know the pressure P and consider the second equation in (6.3) as an evolution equation for Q with data $f(t, s) = -\frac{1}{l}\partial P/\partial s$:

$$\frac{\partial Q}{\partial t} = -rQ + f.$$

If r is much greater than the frequency spectrum of f , the following *quasistatic approximation* can be adopted:

$$Q = \frac{1}{r}f = -\frac{A_0^2}{8\pi\rho\nu} \frac{\partial P}{\partial s} \quad (6.8)$$

In other words, in this case Q follows the input signal f with a negligible time lag.

Now, being $\nu \simeq 0.033 \text{ cm}^2 \text{ s}^{-1}$, for “large” vessels, say with $A_0 > 0.1 \text{ cm}^2$ ($R_0 > 1.8 \text{ mm}$), the characteristic time $\tau_r = 1/r = A_0/(8\pi\nu)$ is about 0.12 s or greater. If one is interested in capturing the pressure pulse propagation in such vessels, that moves with velocity

$$c_{\text{pulse}} = \frac{1}{\sqrt{cl}} = \sqrt{\frac{2Eh}{3\pi\rho R_0}} \simeq 150 \text{ cm s}^{-1},$$

quasistatic approximation should be avoided, since τ_r is greater than the pulse travelling time $\tau_{\text{pulse}} = L/c_{\text{pulse}}$ (that is in the range of 0.03 for vessels of a few centimeters in length). But, when smaller vessels are considered, τ_r drops like R_0^2 ; on the other hand, the ratio h/R_0 and the Young modulus do not change considerably, so that c_{pulse} remains in the same order of magnitude and τ_{pulse} is proportional to the vessel length, which usually scales less than linearly with respect to R_0 . This means that for “small to medium” size vessels, $\tau_r \ll \tau_{\text{pulse}}$ so that the quasistatic approximation can be applied. For instance, considering arterioles with $A_0 = 2 \cdot 10^{-5} \text{ cm}^2$, we have $1/r = 2.4 \cdot 10^{-5} \text{ s}$: in this case the quasistatic approximation is more than justified. As a matter of fact, this simplified model is always the starting point for applications in microcirculation, see for example [54], part I, chapter 7.

We point out that one can look at the quasistatic approximation as the limit of the momentum conservation equation to the *Poiseuille’s law*: in fact, since $\rho\nu = \mu$ where μ is the *dynamic* blood viscosity, eq. (6.8) reads

$$Q = -\frac{\pi R_0^4}{8\mu} \frac{\partial P}{\partial s}, \quad (6.9)$$

which is nothing else than the well known Hagen-Poiseuille formula for laminar stationary flow of incompressible uniform viscous liquid through a cylindrical tube with radius R_0 .

Under this assumption, the model for pressure propagation in the vessel becomes *parabolic*: using (6.9) in the first equation (mass conservation) of (6.3), we have

$$c \frac{\partial P}{\partial t} - \frac{1}{lr} \frac{\partial^2 P}{\partial s^2} = 0, \quad (6.10)$$

that we will call “ $\frac{1}{2}$ D” model since the flow rate variable is now related to the pressure by the Poiseuille’s law (as if we had lost half of the independent variables).

As done for the linearized 1D model, we restate our problem, taking into account a fluid loss ϕ_v :

Problem 6.2.2. Find the vessel pressure $p_v(t, s)$ and flow rate $q_v(t, s)$ such that:

$$C_v \frac{\partial}{\partial t} p_v - \frac{\partial}{\partial s} K_v \frac{\partial p_v}{\partial s} + \phi_v = 0, \quad t > 0, s \in (0, L) \quad (6.11)$$

where

$$C_v = \frac{3\pi R_0^3}{2Eh}, \quad K_v = \frac{1}{lr} = \frac{\pi R_0^4}{8\mu}, \quad q_v = -K_v \frac{\partial}{\partial s} p_v,$$

with suitable boundary and initial conditions (BC and IC).

If we consider problem 6.11 with prescribed input pressure and a concentrated load with conductance G , we have the following BC/IC, obtained by (6.7):

$$\begin{cases} p_v(t, 0) = p_{in}(t), & q_v(t, L) - Gp_v(t, L) = 0, & t > 0, \\ p_v(0, s) = p_{v,0}(s), & & s \in (0, L). \end{cases} \quad (6.12)$$

6.2.3 The 1D transport model

The one-dimensional model for mass transport we have derived in chapter 2, starting from the actual 3D advection-diffusion problem in the vessel lumen, falls in the category of general 1D advection-reaction-diffusion problems. The variable transported in the vessel had the meaning of a *linear concentration* (for instance mol per unit length) of a chemical.

Here we consider a similar model for the *volume* concentration of a chemical inside the vessel, that we denote by u_v . Of course, the linear concentration is given by Au_v , A being the cross-sectional area. The governing equations for u_v we propose here are obtained from those of chapter 2, under the following assumptions:

- i) we neglect the variation of the cross-sectional area, and set $A = A_0$, where A_0 is time independent;
- ii) we consider also a diffusive term, that may be important in small vessels. The diffusion coefficient will be denoted by D_v ;
- iii) we consider a concentration loss term θ_v (measured in mol per unit time and unit length; we will define it more specifically later on when the 1D-3D coupling will be considered).

From these assumptions, the following 1D model for mass transport in the vessel is obtained:

Problem 6.2.3. Find the (volume) concentration $u_v(t, s)$ that satisfies:

$$A_0 \frac{\partial}{\partial t} u_v + \frac{\partial}{\partial s} \left(q_v u_v - A_0 D_v \frac{\partial}{\partial s} u_v \right) + \theta_v = 0, \quad t > 0, s \in (0, L), \quad (6.13)$$

with suitable BC/IC.

Concerning the BC/IC, we can prescribe for example the value of the concentration at the inlet, and a homogeneous Neumann condition (that means to neglect the diffusive terms with respect to the advective terms) at the other boundary point:

$$\begin{cases} u_v(t, 0) = u_{\text{in}}(t), & \partial u_v(0, s)/\partial s = 0 & t > 0, \\ u_v(0, s) = u_{v,0}(s), & & s \in (0, L). \end{cases} \quad (6.14)$$

We also point out that, if the $\frac{1}{2}$ D model is used for blood flow, then we can express the blood flow rate in (6.13) using the Poiseuille's formula and have:

$$A_0 \frac{\partial}{\partial t} u_v - \frac{\partial}{\partial s} \left(\frac{\pi R_0^4}{8\mu} \frac{\partial p_v}{\partial s} u_v + A_0 D_v \frac{\partial}{\partial s} u_v \right) + \theta_v = 0. \quad (6.15)$$

6.3 Microscale: 3D models for blood flow and transport

In this section, we consider homogenized mathematical models governing blood flow and mass transport at the microscale. The fundamental idea is that only averaged quantities are considered: the size of vessels belonging to the microscale is so small that we consider them as the pores of a *porous medium*, the microvascular matrix. Specific constitutive laws can be adopted for this medium: basically, they are extensions of Darcy's law for multiporous media. Multiporosity models are currently used to simulate groundwater flows and other geological phenomena: their application to biological flows is quite recent. In what follows, we introduce such models and discuss related numerical issues that have not been discussed in the previous chapters.

6.3.1 Hierarchical perfusion model for blood flow in the tissue

The system of blood vessels in a tissue has a *hierarchical* structure: vessels can belong to several branching orders, each order having its specific properties, depending first of all on the radius. Therefore, rather than associate single values to the hydraulic tissue permeability, porosity, mean blood velocity and other classical porous medium averaged quantities, we must consider a *distribution* of values depending on the vessel level in the hierarchy.

To this end, a *hierarchical parameter* $\vartheta \in [0, 1]$ is introduced: it is an auxiliary variable representing the level a given vessel belongs to, that has been considered first by Huyghe and Vancampen [45].

In this work, ϑ spans the range from the smallest vessels (capillaries) for $\vartheta = 0$, to largest ones for $\vartheta = 1$. We will not include the venous system in the hierarchy (even if one could use "negative" values of ϑ); rather, this system will be described by some reduced model.

In several papers by Huyghe and coworkers (see for instance [103], [45]), constitutive laws for hierarchical blood flow have been theoretically developed starting from fundamental conservation

principles³. Each unknown related to blood flow is expressed as a function of both spatial variables and hierarchical coordinate ϑ , as well as flow takes place both in the “spatial” direction (through vessels of comparable porosity) and the “hierarchical” direction (usually passing from a hierarchical level to a lower one).

In porous medium theory, the averaged variables are defined by means of a “reference elementary volume” (REV) whose size h_{REV} is negligible with respect to the characteristic length of the macroscale, but still big enough to allow a meaningful averaging on the microscale (see [6]). In our case, the REV has 4 dimensions (three in space, one for hierarchy).

Let $\Omega \subset \mathbb{R}^3$ be the tissue domain, and Ω_b the subdomain occupied by blood vessels (that are the *pores* of our medium); for $\mathbf{x} \in \Omega$ and $\vartheta \in [0, 1]$, we define a REV corresponding to (\mathbf{x}, ϑ) by

$$\mathcal{U}_0(\mathbf{x}, \vartheta) = \{(\mathbf{x}', \vartheta') \in \Omega_b \times [0, 1] : \|(\mathbf{x}', \vartheta') - (\mathbf{x}, \vartheta)\| < h_{\text{REV}}\}.$$

Several microscopic physiological variables are defined on Ω_b :

- the pore pressure p_b ;
- the pore *spatial* velocity \mathbf{v}_b , defined by $\mathbf{v}_b = \frac{D\mathbf{x}}{Dt}$, where D/Dt denotes a material derivative;
- the pore *hierarchical* blood velocity $\omega_b = \frac{D\vartheta}{Dt}$; this quantity represents the rate at which blood moves up in the hierarchy, through a given level ϑ , at a given point \mathbf{x} . Notice that if the highest hierarchal level corresponds to the largest arterial blood vessels, in normal conditions blood will move down in the hierarchy, thus producing a negative value of ω_b .

Taking the average of the microscopic physiological quantities we can define the corresponding macroscopic variables on Ω :

- $p = p(t, \mathbf{x}, \vartheta) = \frac{1}{|\mathcal{U}_0|} \int_{\mathcal{U}_0(\mathbf{x}, \vartheta)} p_b(t, \mathbf{x}', \vartheta') d\mathbf{x}' d\vartheta'$: the mean blood pressure.
- $\mathbf{v} = \mathbf{v}(t, \mathbf{x}, \vartheta) = \frac{1}{|\mathcal{U}_0|} \int_{\mathcal{U}_0(\mathbf{x}, \vartheta)} \mathbf{v}_b(t, \mathbf{x}', \vartheta') d\mathbf{x}' d\vartheta'$: the mean *spatial* blood velocity.
- $\omega = \omega(t, \mathbf{x}, \vartheta) = \frac{1}{|\mathcal{U}_0|} \int_{\mathcal{U}_0(\mathbf{x}, \vartheta)} \omega_b(t, \mathbf{x}', \vartheta') d\mathbf{x}' d\vartheta'$: the mean *hierarchical* blood velocity.

Starting from fundamental conservation laws and using mixture theory, in [103] the admissible models for hierarchical flow have been completely described, including poroelastic effect. Neglecting the solid matrix displacements, and introducing a compliance effect, we have that the following four-dimensional Darcy equation in mixed form (here ∇ operates on \mathbf{x} only) is one of the admissible models:

$$\begin{cases} C \frac{\partial}{\partial t} p + \nabla \cdot (n_b \mathbf{v}) + \frac{\partial}{\partial \vartheta} (n_b \omega) + \phi_t = 0, & t > 0, \mathbf{x} \in \Omega, \vartheta \in (0, 1), \\ n_b \mathbf{v} = -K_t \nabla p, & t > 0, \mathbf{x} \in \Omega, \vartheta \in (0, 1), \\ n_b \omega = -\alpha \frac{\partial}{\partial \vartheta} p, & t > 0, \mathbf{x} \in \Omega, \vartheta \in (0, 1). \end{cases} \quad (6.16)$$

In this model the following quantities are defined:

- i) the *porosity* $n_b = n_b(\mathbf{x}, \vartheta)$, defined as the ratio between the blood volume $|\mathcal{U}_0|$ and the total volume (blood and tissue) in the REV (in other words, n_b is the *fluid fraction*);
- ii) the compliance $C = C(\mathbf{x}, \vartheta)$;

³Actually a complete poroelastic theory is developed by the cited authors.

iii) the four-dimensional hierarchical permeability tensor

$$\tilde{K}(\mathbf{x}, \vartheta) = \begin{bmatrix} K_t(\mathbf{x}, \vartheta) & 0 \\ 0 & \alpha(\mathbf{x}, \vartheta) \end{bmatrix}.$$

This tensor can be computed experimentally, but also theoretically, from the microscale geometry [44, 43];

iv) the generic tissue fluid loss term ϕ_t .

Of course some boundary and initial conditions have to be assigned to (6.16). Restating problem (6.16) in non-mixed form, introducing the subscript “t” to emphasize that the unknown lives in the tissue region, and assigning suitable BC/IC, we have:

Problem 6.3.1. Find the tissue blood pressure $p_t(t, \mathbf{x}, \vartheta)$ such that

$$C_t \frac{\partial}{\partial t} p_t - \nabla \cdot K_t \nabla p_t - \frac{\partial}{\partial \vartheta} \alpha \frac{\partial p_t}{\partial \vartheta} + \phi_t = 0, \quad t > 0, s \in (0, L), \quad (6.17)$$

satisfying

$$\begin{cases} n_b \omega(t, \mathbf{x}, 0) = G_0 (p_t(t, \mathbf{x}, 0) - p_v(t, \mathbf{x})), & t > 0, \mathbf{x} \in \Omega, \\ n_b \omega(t, \mathbf{x}, 1) = G_1 (p_t(t, \mathbf{x}, 1) - p_a(t, \mathbf{x})), & t > 0, \mathbf{x} \in \Omega, \\ n_b \mathbf{v}(t, \mathbf{x}, \vartheta) \cdot \mathbf{n} = 0, & t > 0, \mathbf{x} \in \partial\Omega, \vartheta \in [0, 1]; \\ p_t(0, \mathbf{x}, \vartheta) = p_{t,0}(\mathbf{x}, \vartheta), & \mathbf{x} \in \Omega, \vartheta \in [0, 1], \end{cases} \quad (6.18)$$

where

$$\mathbf{v} = -\frac{1}{n_b} K_t \nabla p_t, \quad \omega = -\frac{1}{n_b} \alpha \frac{\partial p_t}{\partial \vartheta},$$

are respectively the spatial and hierarchical blood velocities.

The BC we have considered in (6.18) correspond to the following situation: p_v and p_a are the venous and arterial pressure in the tissue region Ω , G_0 and G_1 are the hydraulic conductivities respectively between the lowest hierarchy and draining veins, and between the highest hierarchy and feeding arteries. Dirichlet boundary conditions at $\vartheta = 0, 1$, such as $p_t(t, \mathbf{x}, 1) = p_a(t, \mathbf{x})$ are also admissible; they correspond to high values of conductances G_0, G_1 .

Remark. In physiology, tissue perfusion ω_t is defined as the volume of blood moving down in the hierarchy per unit volume of tissue and per unit time. For a given hierarchical level ϑ , this is exactly

$$\omega_t = -n_b \omega, \quad (6.19)$$

and is usually a positive value.

6.3.2 Multi-pressure models (hierarchical discretization)

Despite the fact that in mixture theory the hierarchy level ϑ is a continuous variable, in practice one considers only a few discrete levels (see table 6.1). So, even if problem (6.16) is four-dimensional, the

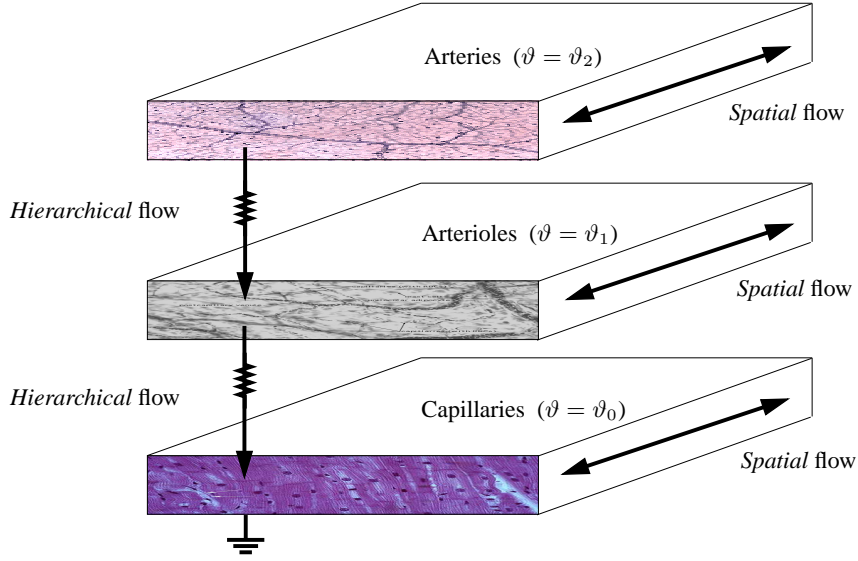


Figure 6.3: Spatial and hierarchical flows in biological tissues

number N_ϑ of degrees of freedom for the ϑ -variable is usually very small (for instance considering arteries / arterioles / pre-capillaries / capillaries, we have $N_\vartheta = 4$).

Huyghe, Vankan and coworkers did not address this issue (for example their FEM calculations in [103] are 2D in space, so that a standard 3D solver can be used for the simulation of the hierarchical model), but we think it is possible to take advantage of the smallness of N_ϑ to simplify the model. We will thus introduce a special semi-discretized model, in which the four-dimensional problem (6.16) is split into N_ϑ three-dimensional ones.

For the sake of simplicity, let us consider problem (6.17) in the steady case: then we have

$$-\nabla \cdot K_t \nabla p - \frac{\partial}{\partial \vartheta} \alpha \frac{\partial p}{\partial \vartheta} + \phi_t = 0 \quad \text{in } \Omega \times [0, 1]. \quad (6.20)$$

Let $n = N_\vartheta - 1$, $h_\vartheta = n^{-1}$, and for $i = 0, \dots, n$ define $\vartheta_i = ih_\vartheta$. We will consider N_ϑ pressures corresponding to each hierarchical level ϑ_i , that is we set

$$p_i(\mathbf{x}) := p(\mathbf{x}, \vartheta_i), \quad i = 0, \dots, n. \quad (6.21)$$

The hierarchical discretization of (6.20) leads to a (tridiagonal) system of coupled equations for the pressures p_i , which reads as follows:

$$\begin{bmatrix} \mathcal{L}_{00} & \mathcal{L}_{01} & & & & & & \\ \mathcal{L}_{10} & \mathcal{L}_{11} & \mathcal{L}_{12} & & & & & \\ & \mathcal{L}_{21} & \mathcal{L}_{22} & \mathcal{L}_{23} & & & & \\ & & \ddots & \ddots & \ddots & & & \\ & & & & & \ddots & & \\ & & & & & & \mathcal{L}_{nn-1} & \mathcal{L}_{nn} \end{bmatrix} \begin{bmatrix} p_0 \\ p_1 \\ p_2 \\ \vdots \\ p_n \end{bmatrix} = \begin{bmatrix} f_0 \\ f_1 \\ f_2 \\ \vdots \\ f_n \end{bmatrix} \quad (6.22)$$

where \mathcal{L}_{ij} is a linear differential operator given by

$$\mathcal{L}_{ij} = -\nabla \cdot K_{ij}(\mathbf{x}) \nabla + \alpha_{ij}(\mathbf{x}), \quad (6.23)$$

being K_{ij} , α_{ij} and f_i suitable functions of spatial coordinates that we will derive in the sequel. System (6.22) is given n homogeneous Neumann boundary conditions:

$$\mathbf{n} \cdot K_{ii}(\mathbf{x}) \nabla p_i(\mathbf{x}) = 0 \quad \text{on } \partial\Omega, \quad i = 0, \dots, n. \quad (6.24)$$

	$K \left[\frac{\text{mm}^2}{\text{s kPa}} \right]$	$\alpha \left[\frac{1}{\text{s kPa}} \right]$	$C \left[\frac{1}{\text{kPa}} \right]$
Arterial	100	0.0025	0.001
Arteriolar	0.05	0.000325	0.001
Venous	100	0.0025	0.1

Table 6.1: Hierarchical vessel parameters used by Huyghe and coworkers for *rat calf muscle* (permeabilities K and α , and compliance C .)

To derive model (6.22), let us introduce the \mathbb{P}^1 finite element basis functions $\{\varphi_i\}_{i=0,\dots,n}$ on $[0, 1]$, corresponding to the nodes $\{\vartheta_i\}$:

$$\varphi_i \in C([0, 1]) : \varphi_i \in \mathbb{P}^1([\vartheta_j - 1, \vartheta_j]) \forall j = 1, \dots, n, \quad \varphi_i(\vartheta_j) = \delta_{ij} \forall i, j = 0, \dots, n.$$

We assume that the elements of the permeability tensor \tilde{K} and the pressure p are piecewise \mathbb{P}^1 interpolations of their known hierarchical values:

$$K_t(\mathbf{x}, \vartheta) = \sum_{k=0}^n K_t(\mathbf{x}, \vartheta_k) \varphi_k(\vartheta), \quad \alpha(\mathbf{x}, \vartheta) = \sum_{k=0}^n \alpha(\mathbf{x}, \vartheta_k) \varphi_k(\vartheta), \quad p(\mathbf{x}, \vartheta) = \sum_{k=0}^n p(\mathbf{x}, \vartheta_k) \varphi_k(\vartheta). \quad (6.25)$$

Let q , φ be smooth functions respectively defined on Ω and $[0, 1]$; if we multiply the first equation in (6.16) times $q(\mathbf{x})\varphi(\vartheta)$ after substituting \mathbf{v} and ω in terms of p , and we integrate by parts over $\Omega \times [0, 1]$ taking into account the boundary conditions (6.17), we obtain a weak formulation that reads

$$\begin{aligned} & \int_0^1 \varphi(\vartheta) \int_{\Omega} (K_t(\mathbf{x}, \vartheta) \nabla p, \nabla q) \, d\mathbf{x} \, d\vartheta + \int_{\Omega} q(\mathbf{x}) \int_0^1 \alpha(\mathbf{x}, \vartheta) \frac{\partial p}{\partial \vartheta} \frac{\partial \varphi}{\partial \vartheta} \, d\vartheta \, d\mathbf{x} + \\ & \quad \varphi(0) \int_{\Omega} G_0 p(\mathbf{x}, 0) q(\mathbf{x}) \, d\mathbf{x} + \varphi(1) \int_{\Omega} G_1 p(\mathbf{x}, 1) q(\mathbf{x}) \, d\mathbf{x} = \\ & - \int_0^1 \int_{\Omega} \phi_t(\mathbf{x}, \vartheta) q(\mathbf{x}) \varphi(\vartheta) \, d\mathbf{x} \, d\vartheta + \varphi(0) \int_{\Omega} G_0 p_v(\mathbf{x}) q(\mathbf{x}) \, d\mathbf{x} + \varphi(1) \int_{\Omega} G_1 p_a(\mathbf{x}) q(\mathbf{x}) \, d\mathbf{x}. \end{aligned} \quad (6.26)$$

Now, we use expressions (6.25) in (6.26), where we choose $\varphi = \varphi_i$, $i = 0, \dots, n$: after elementary computations, we get

$$\sum_{j=0}^n \int_{\Omega} (K_{ij}(\mathbf{x}) \nabla p_j, \nabla q) \, d\mathbf{x} + \sum_{j=0}^n \int_{\Omega} \alpha_{ij}(\mathbf{x}) p_j q \, d\mathbf{x} = \int_{\Omega} f_i(\mathbf{x}) q(\mathbf{x}) \, d\mathbf{x}, \quad (6.27)$$

being

$$K_{ij}(\mathbf{x}) = \sum_{k=0}^n K(\mathbf{x}, \vartheta_k) \int_0^1 \varphi_k(\vartheta) \varphi_i(\vartheta) \varphi_j(\vartheta) d\vartheta, \quad (6.28)$$

$$\alpha_{ij}(\mathbf{x}) = \sum_{k=0}^n \alpha(\mathbf{x}, \vartheta_k) \int_0^1 \varphi_k(\vartheta) \varphi_i'(\vartheta) \varphi_j'(\vartheta) d\vartheta + \delta_{i0} \delta_{ij} G_0 + \delta_{in} \delta_{ij} G_1 \quad (6.29)$$

$$f_i(\mathbf{x}) = \delta_{i0} G_0 + \delta_{in} G_1 - \int_0^1 \phi_t(\mathbf{x}, \vartheta) \varphi_i(\vartheta) d\vartheta, \quad (6.30)$$

where δ_{ij} is the Kronecker delta. Now, (6.27) is exactly the weak formulation of system (6.22) with boundary conditions (6.24). Moreover, equations (6.28-6.30) define the coefficients of operators \mathcal{L}_{ij} in (6.23). Finally, if $|i - j| > 1$ then $K_{ij} = 0$, $\alpha_{ij} = 0$ due to the finite support of basis functions in equations (6.28-6.29), so that system (6.22) is tridiagonal.

One easily finds that in the non-steady case the hierarchical discretization leads to the following problem:

$$C_i \frac{\partial p_i}{\partial t} + \sum_{j=0}^n \mathcal{L}_{ij} p_j = f_i, \quad i = 0, \dots, n,$$

where

$$C_i(\mathbf{x}) = \int_0^1 C(\mathbf{x}, \vartheta) \varphi_i(\vartheta) d\vartheta, \quad (6.31)$$

while the operators \mathcal{L}_{ij} are always those of eq. (6.23).

6.3.3 The transport model in the tissue

In what follows, we model the dynamics of a chemical in a biological tissue using the porous medium description of the microscale, introduced in section 6.3. Although we mainly consider oxygen transfer in a skeletal muscle, the same methodology applies for all chemicals transported by the blood (about this subject, we refer the reader to chapter 1), and to temperature and heat transfer as well.

Blood acts as a carrier for chemicals, whereas the main reaction processes take place at a cellular level and in the extravasal solid matrix, the *interstitium*. Moreover, usually the blood-to-interstitium transfer only concerns low vessel hierarchies, such as capillaries. For these reasons, a general framework to study the mass transport and reaction in a biological tissue according to a macroscopic viewpoint is a so-called *double porosity* model, where both the blood and the interstitial concentration satisfy an advection-diffusion-reaction equation, in which the exchange term depends on the concentration gap. In some special cases, a model reduction to a single equation for the blood concentration can be considered as well.

Double porosity model

Let $\Omega \subset \mathbb{R}^3$ be the tissue domain; for $\mathbf{x} \in \Omega$ we denote by $u_{t,b}(\mathbf{x})$ the blood volume concentration of oxygen (in the considered hierarchical range, for example in capillaries) at $\mathbf{x} \in \Omega$, and by $u_{t,i}(\mathbf{x})$ the concentration in the *interstitium*.

Making use of the mass conservation principle, we propose the following double-porosity model:

Problem 6.3.2. Find the concentrations $u_{t,b}(t, \mathbf{x})$ and $u_{t,i}(t, \mathbf{x})$ such that

$$\left\{ \begin{array}{ll} \frac{\partial u_{t,b}}{\partial t} + \nabla \cdot (-D_{t,b} \nabla u_{t,b} + \mathbf{v} u_{t,b}) + \omega_t (u_{t,b} - u_a) + \frac{1}{\tau} (u_{t,b} - u_{t,i}) = 0, & t > 0, \mathbf{x} \in \Omega, \\ \frac{\partial u_{t,i}}{\partial t} + \nabla \cdot (-D_{t,i} \nabla u_{t,i}) + \frac{1}{\tau} (u_{t,i} - u_{t,b}) + \theta_{t,i} = 0, & t > 0, \mathbf{x} \in \Omega, \\ u_{t,b}(0, \mathbf{x}) = u_{b,0}(\mathbf{x}), \quad u_{t,i}(0, \mathbf{x}) = u_{i,0}(\mathbf{x}), & \mathbf{x} \in \Omega, \\ D_{t,b} \partial u_{t,b}(t, \mathbf{x}) / \partial \mathbf{n} = 0, & t > 0, \mathbf{x} \in \partial \Omega, \\ D_{t,i} \partial u_{t,i}(t, \mathbf{x}) / \partial \mathbf{n} = 0, & t > 0, \mathbf{x} \in \partial \Omega. \end{array} \right. \quad (6.32)$$

Here, $D_{t,b}$ is the (effective) oxygen diffusivity in blood, \mathbf{v} the blood velocity, ω_t the *tissue perfusion* (although it can be extremely variable, a “reference” value is $2.5 \cdot 10^{-3} \text{ s}^{-1}$ at rest), $D_{t,i} = 1.7 \cdot 10^{-5} \text{ cm}^2 \text{ s}^{-1}$ the (effective) oxygen diffusivity in *interstitium*, τ is the time constant for oxygen diffusion from blood vessels to *interstitium* (for capillaries, $d \simeq 2 \cdot 10^{-3} \text{ cm}$ is the diffusion distance and $\tau \simeq d^2/D = 0.2 \text{ s}$), $\theta_{t,i} = \theta_{t,i}(t, u_{t,i})$ is a reaction term (for example, the basal consumption rate $5 \cdot 10^{-8} \text{ mol cm}^{-3} \text{ s}^{-1}$ at rest, or more generally a function accounting for the dynamics of *ATP*, *CO*₂ and other chemicals), and $u_a = 8.75 \cdot 10^{-6} \text{ mol cm}^{-3}$ the arterial oxygen concentration.

We point out that the effective diffusion coefficients depend on the microscale geometry of the tissue via the *tortuosity* λ of the microvessel matrix (we refer the reader to the well known work of Nicholson and Phillips for mass transport in the brain [68]; for heat transfer the same theory is applied, see for instance [47]). In particular, $D_{t,b} = D_b/\lambda^2$ where D_b is the diffusivity in blood.

One porosity model

If reaction is dominating the diffusion processes in the interstitium, like for example in skeletal muscle during exercise, then we can assume that $D_{t,i} = 0$, obtaining an integro-differential problem.

Problem 6.3.3. Find the tissue concentrations $u_{t,b}(t, \mathbf{x}, \vartheta)$ and $u_{t,i}(t, \mathbf{x}, \vartheta)$ such that

$$\left\{ \begin{array}{ll} \frac{\partial u_{t,b}}{\partial t} + \nabla \cdot (-D_{t,b} \nabla u_{t,b} + \mathbf{v} u_{t,b}) + \omega_t (u_{t,b} - u_a) + \frac{1}{\tau} (u_{t,b} - u_i) = 0, & t > 0, \mathbf{x} \in \Omega, \\ \frac{d u_{t,i}}{d t} + \frac{1}{\tau} (u_{t,i} - u_{t,b}) + \theta_{t,i} = 0, & t > 0, \mathbf{x} \in \Omega, \\ u_{t,b}(0, \mathbf{x}) = u_{b,0}(\mathbf{x}), \quad u_{t,i}(0, \mathbf{x}) = u_{i,0}(\mathbf{x}), & \mathbf{x} \in \Omega, \\ D_{t,b} \partial u_{t,b}(t, \mathbf{x}) / \partial \mathbf{n} = 0, & t > 0, \mathbf{x} \in \partial \Omega. \end{array} \right. \quad (6.33)$$

Finally, if the characteristic time of the reaction in the interstitium is small enough, we can assume that $du_{t,i}/dt = 0$, then after expressing $u_{t,i} = u_{t,i}(u_{t,b})$ as a function of $u_{t,b}$ in the second equation in (6.33), we obtain a single equation for *utissue* = $u_{t,b}$ in the following form:

$$\frac{\partial u_t}{\partial t} + \nabla \cdot (-D_t \nabla u_t + \mathbf{v} u_t) + \omega_t (u_t - u_a) + \theta_t = 0, \quad (6.34)$$

where $D_t = D_{t,b}$, and $\theta_t(t, u_t) = \theta_t(t, u_{t,i}(u_t))$.

Eq. (6.34) is a very simplified model for mass transport in tissues; nevertheless, it encompasses the Pennes bioheat equation [74] as a particular case, so that u could represent also a temperature field in the tissue.

Typically, mass transport models such as those presented so far, need a regional capillary perfusion measure to provide values for \mathbf{v} and ω , allowing to solve for the concentration. Despite the fact that several techniques are available to provide clinical data for ω (MR perfusion imaging or Laser Doppler perfusion imaging, for instance), a perfusion model such as (6.16) or (6.22) can provide an useful alternative. There is a number of reasons supporting the argument that blood perfusion computations are worth the effort. For example, by numerical simulations it is possible to investigate extreme conditions such as hypoxia, circulation diseases, or make prognoses about the evolution of a tissue; moreover, numerical techniques are already widely used for design purposes in artificial organs and biodevices development.

6.4 Some examples of blood perfusion simulations

We have already presented some examples of application of the 1D mass transport model in chapter 2. Here we want to show some significant tissue perfusion simulations, using distributed microscale models. For the first time we introduce 1D vessels as *data* for our problems: we will consider 1D arteries/veins, with given blood pressure, embedded in a 2D tissue domain, and study how they behave as blood *sources/sinks*. At this stage, this approach is easy to handle, since

- i) the vessel pressure is given;
- ii) a 1D source in a 2D domain does not induce a singular solution.

When the full coupled 3D-1D problem will be considered, both i) and ii) will not hold anymore; nevertheless, we can take advantage of the special analysis carried out in chapter 4 and of the numerical techniques introduced in chapter 5.

6.4.1 A three-hierarchies perfusion model for the tissue

We consider a three-level hierarchical model ($n = 2$), in which the capillary ($\vartheta_0 = 0$), the pre-capillary ($\vartheta_1 = 1/2$), and the arteriolar ($\vartheta_2 = 1$) scales are taken into account. We suppose that the hierarchical permeability tensor is space-independent and isotropic, so that we have

$$K = K(\vartheta)I,$$

being $K(\theta)$ a scalar function and I the identity tensor. We will consider an simple case in which values for $K(\theta)$ are obtained by standard data. Thanks to the Poiseuille's law, we can relate the velocity v and the pressure drop δp in a vessel by

$$v = \frac{r^2}{8\mu} \frac{\delta p}{\delta l},$$

where μ is the dynamic blood viscosity, r is the vessel radius and δl the vessel length; so one can assume that

$$K(\vartheta) \simeq n_b(\vartheta) \frac{r(\vartheta)^2}{8\mu(\vartheta)}$$

is an approximation for K . As we neglected the solid displacements, the porosity n_b is a constant for each phase. Since the global blood volume fraction $\int_0^1 n_b(\vartheta) d\vartheta$ is about 0.1 (5 liters blood for 50 liters tissue), let us consider that $n_b = 0.1 = \text{const}$.

Typical radii [mm] and apparent blood viscosities [kPa s] corresponding to capillary, pre-capillary, and the arteriolar scales are

$$\begin{aligned} r(\vartheta_0) &= 4.3 \cdot 10^{-3}, & \mu(\vartheta_0) &= 15 \cdot 10^{-6}, \\ r(\vartheta_1) &= 12.9 \cdot 10^{-3}, & \mu(\vartheta_1) &= 4.9 \cdot 10^{-6}, \\ r(\vartheta_2) &= 51 \cdot 10^{-3}, & \mu(\vartheta_2) &= 2.8 \cdot 10^{-6}, \end{aligned}$$

so that we get the following estimations for $K(\vartheta_i) = K_i$ in $[\frac{\text{mm}^2}{\text{s kPa}}]$:

$$K_0 = 0.016, \quad K_1 = 0.43, \quad K_2 = 12.05.$$

Coefficient α is the (hydrodynamic) conductance per unit volume between contiguous hierarchical levels. Assuming to know typical mean values \bar{p}_i and $\bar{\omega}_i$ for pressures and hierarchical velocities, we can extrapolate standard conductance values in the following way:

$$n_b \bar{\omega}_i = -\alpha_i \left(\frac{\partial p}{\partial \vartheta} \right)_{\vartheta=\vartheta_i} \simeq -\alpha_i \frac{\Delta \bar{p}_i}{\Delta \vartheta_i} \implies \alpha_i \simeq -n_b \bar{\omega}_i \frac{\Delta \vartheta_i}{\Delta \bar{p}_i}.$$

Using standard mean values of pressures ($\bar{p}_0 \simeq 3.7, \bar{p}_1 \simeq 4.2, \bar{p}_2 \simeq 8.6$ kPa) and tissue perfusion ($-n_b \bar{\omega}_i = \omega_t \simeq 2.5 \cdot 10^{-3} \text{ s}^{-1} \text{ mm}^3$ of blood per mm^3 of tissue), we obtain the following estimates for α (units are $[\text{s}^{-1} \text{ kPa}^{-1}]$):

$$\alpha_0 = \omega_t \frac{h_\vartheta}{\bar{p}_1 - \bar{p}_0} = 2.5 \cdot 10^{-3}, \quad \alpha_1 = \omega_t \frac{2h_\vartheta}{\bar{p}_2 - \bar{p}_0} = 0.51 \cdot 10^{-3}, \quad \alpha_2 = \omega_t \frac{h_\vartheta}{\bar{p}_2 - \bar{p}_1} = 0.28 \cdot 10^{-3}.$$

In our case, using equations (6.28-6.30), system (6.22) reads:

$$\begin{bmatrix} -K_{00}\Delta + \alpha_{00} & -K_{01}\Delta + \alpha_{01} & 0 \\ -K_{10}\Delta + \alpha_{10} & -K_{11}\Delta + \alpha_{11} & -K_{12}\Delta + \alpha_{12} \\ 0 & -K_{21}\Delta + \alpha_{21} & -K_{22}\Delta + \alpha_{22} \end{bmatrix} \begin{bmatrix} p_0 \\ p_1 \\ p_2 \end{bmatrix} = \begin{bmatrix} f_0 \\ f_1 \\ f_2 \end{bmatrix}, \quad (6.35)$$

where

$$\begin{aligned} \begin{bmatrix} K_{00} & K_{01} & K_{02} \\ K_{10} & K_{11} & K_{12} \\ K_{20} & K_{21} & K_{22} \end{bmatrix} &= \begin{bmatrix} \frac{3K_0+K_1}{24} & \frac{K_0+K_1}{24} & 0 \\ \frac{K_0+K_1}{24} & \frac{K_0+6K_1+K_2}{24} & \frac{K_1+K_2}{24} \\ 0 & \frac{K_1+K_2}{24} & \frac{K_1+3K_2}{24} \end{bmatrix}, \\ \begin{bmatrix} \alpha_{00} & \alpha_{01} & \alpha_{02} \\ \alpha_{10} & \alpha_{11} & \alpha_{12} \\ \alpha_{20} & \alpha_{21} & \alpha_{22} \end{bmatrix} &= \begin{bmatrix} \alpha_0 + \alpha_1 + G_0 & -\alpha_0 - \alpha_1 & 0 \\ -\alpha_0 - \alpha_1 & \alpha_0 + 2\alpha_1 + \alpha_2 & -\alpha_1 - \alpha_2 \\ 0 & -\alpha_1 - \alpha_2 & \alpha_1 + \alpha_2 + G_1 \end{bmatrix}, \end{aligned}$$

and

$$f_0 = G_0 p_v, \quad f_1 = 0, \quad f_2 = G_1 p_a,$$

with homogeneous Neumann boundary conditions for pressures:

$$\frac{\partial p_i}{\partial \mathbf{n}} = 0 \quad \text{on } \partial\Omega, \quad i = 0, 1, 2.$$

We point out that a finite element discretization of the system (6.35) of partial differential equations, leads to a linear system with a block-structured matrix (blockwise tridiagonal). It easily found that in this case the block Gauss-Seidel iterative method [88] can be employed successfully to solve the global system by iterating the solution of three “standard” problems (one for each unknown p_i).

In fig. 6.5 results of a FEM 2D simulation for this model are reported, when a 1D feeding artery Λ_a and a 1D collecting vein Λ_v are embedded in a $15 \text{ mm} \times 15 \text{ mm}$ square tissue; moreover, a distributed microvenous bed is communicating with the capillary compartment. The presence of 1D vessels in this case is modelled by concentrating on Λ_a and Λ_v the venous and arterial conductances, that is by taking

$$G_0 = \alpha_{v,\text{bed}} + \alpha_v \delta_{\Lambda_v}, \quad G_1 = \alpha_a \delta_{\Lambda_a},$$

in eq. (6.35), where we denote δ_E the Dirac distribution concentrated on the set E . Constants α_v and α_a have been computed using

$$\alpha_v = \omega_t \frac{|\Omega|}{|\Lambda_v|(\bar{p}_0 - \bar{p}_v)}, \quad \alpha_a = \omega_t \frac{|\Omega|}{|\Lambda_a|(\bar{p}_a - \bar{p}_2)},$$

with reference mean values for arterial and venous pressures ($\bar{p}_a \simeq 13, \bar{p}_v \simeq 2.9 \text{ kPa}$), that gives

$$\alpha_v = 9.3 \cdot 10^{-5}, \quad \alpha_a = 7.5 \cdot 10^{-3} \text{ s}^{-1} \text{ kPa}^{-1} \text{ mm}.$$

We see that computed hierarchical pressures are of the form $p_i(\mathbf{x}) = \bar{p}_i + \delta p_i(\mathbf{x})$, where \bar{p}_i are

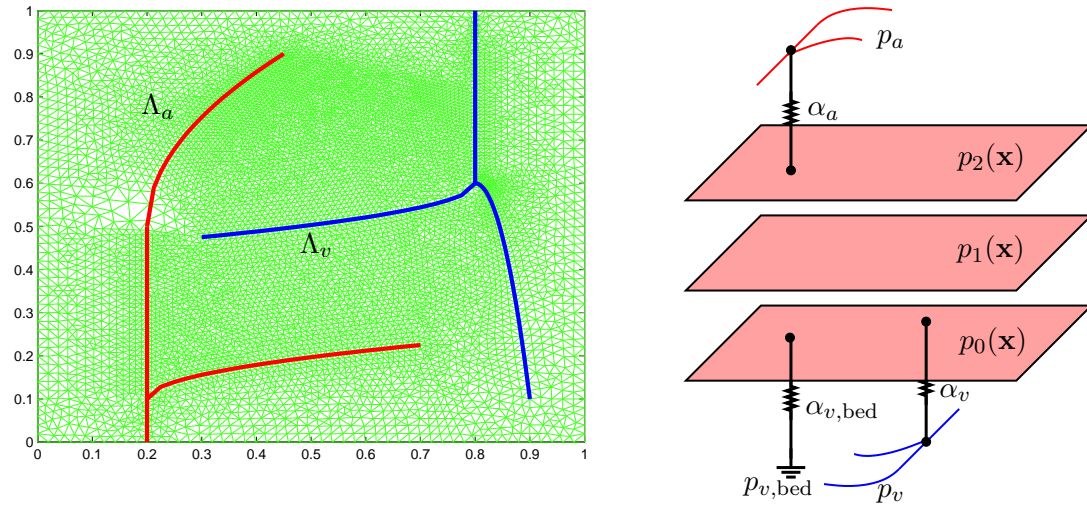


Figure 6.4: The mesh and three-level hierarchy of the tissue with external hydraulic conductances.

mean values and δp_i are pressure oscillations, that are responsible for the spatial blood flow. Using these values for pressures, one can compute tissue perfusion by using the third equation in (6.16) (actually we consider an L^2 projection on the same pressure FEM space): mean values for perfusions are respectively $0.0043, 0.0025, 0.0029 \text{ s}^{-1}$ for the capillary, pre-capillary and arteriolar levels.

The blood flow entering the tissue by the incoming artery Λ_a is computed as

$$q_a = \int_{\Lambda_a} \alpha_a (p_a - p_2(s)) ds = 0.68 \text{ mm}^3 \text{ s}^{-1},$$

while the outfluxes flowing from the capillary compartment respectively to the microvascular venous bed and to the vein Λ_v are found to be

$$q_{v,\text{bed}} = \int_{\Omega} \alpha_{v,\text{bed}}(p_0(\mathbf{x}) - p_{v,\text{bed}}) d\mathbf{x} = 0.23 \text{ mm}^3 \text{ s}^{-1}, \quad q_v = \int_{\Lambda_v} \alpha_v(p_0(s) - p_v) ds = 0.45 \text{ mm}^3 \text{ s}^{-1}.$$

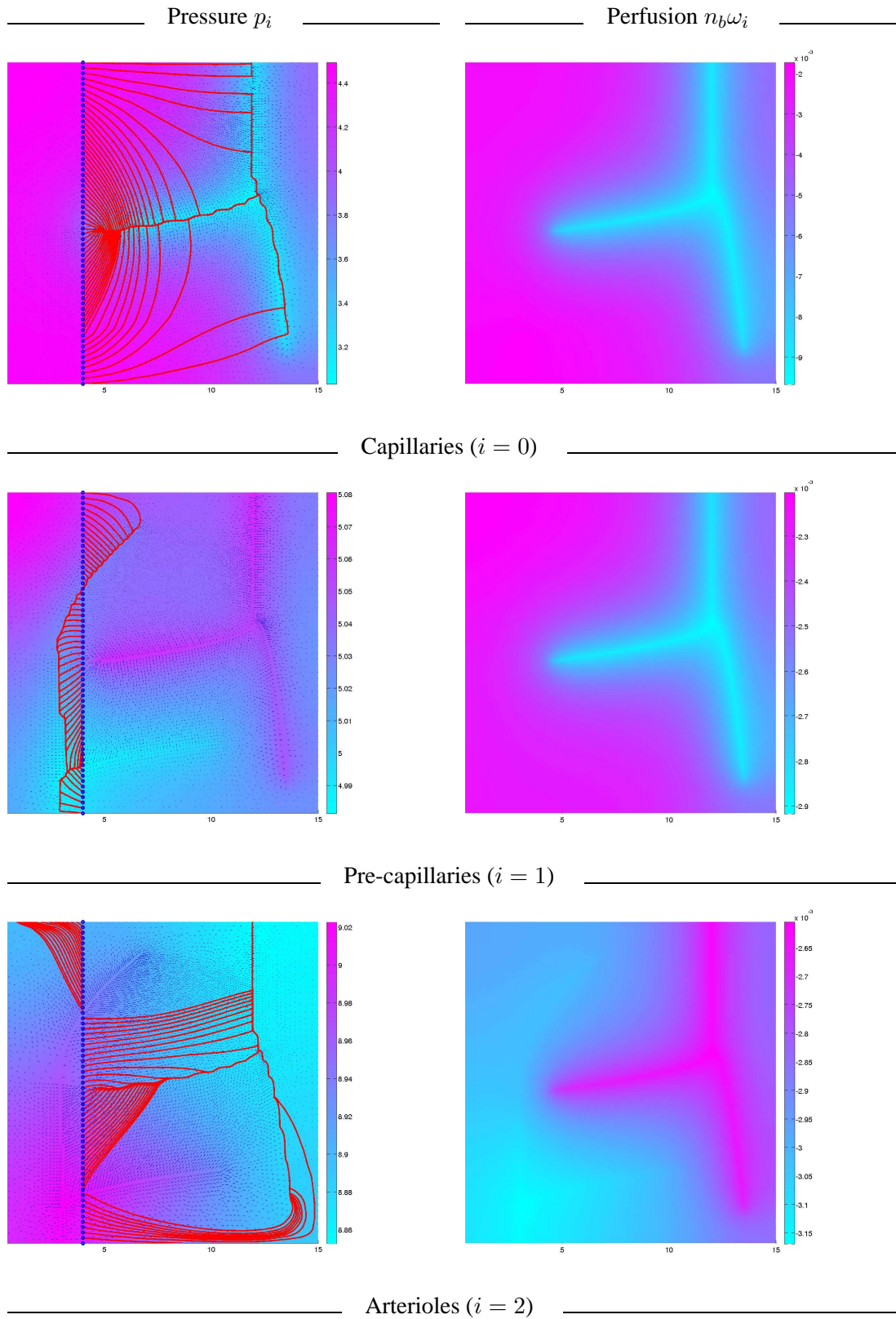


Figure 6.5: Perfusion simulation. Arteriolar, pre-capillary and capillary pressures (respect. p_2 , p_1 and p_0) are expressed in kPa; the corresponding tissue perfusion (respect. $n_b\omega_2$, $n_b\omega_1$ and $n_b\omega_0$) in s^{-1} (that is cc of blood per second per cc of tissue). On pressure plots, the spatial velocity field \mathbf{v}_i and some streamlines are reported to emphasize the spatial blood flow within each hierarchical compartment.

6.4.2 From retinal imaging to retinal perfusion simulation

Let us apply the tools we used in example (6.35) in a “real case” of tissue perfusion. Since here we deal with a 2D microscale, we will consider a “quasi-planar” tissue: the *retina*. It is an interesting case due to the well known *retinal imaging* technique, that consists in taking a picture of the rear inner eye surface by an optical camera in order to visualize its blood vessels. The impaired retina circulation is responsible of a number of sight diseases, this is why retinal imaging is so widely practiced. Being a relatively easy-to-apply technique, several tools to make automatic the prognosis by retinal imaging have been proposed (see for instance [40]): they rely on the automatic detection of the vessels geometry by suitable algorithms.

We used such kind of algorithms to extract the 1D geometry of the largest retinal vessels from an image, and then to simulate the perfusion using the microscale model, as we did in example (6.35). In fig. 6.6 are shown the major steps that lead to the 1D geometry extraction. We summarize them as follows.

1. **Segmentation.** A saturation threshold is used to convert the input image from the 256 gray levels format to the *bit* image format, so that each pixel is either “on” (black) or “off” (white). The goal is to have a first sketch of the vessels location, but of course the resulting segmented image is very irregular.
2. **Skeletonization.** A linear transformation is iteratively applied to the pixel matrix to extract its *skeleton*. We say that a bit image is a skeleton if each “on” pixel has at most 2 neighboring “on” pixels: intuitively, if a bit image is a skeleton, it describes 1D filaments.
3. **Tree topology identification.** Once the image is reduced to a skeleton, one is left with the last and most expensive step: the tree topology identification. This task consists in describing the skeleton as a *tree*, identifying each branch with a label and building the “child-of” table, that is to assign to each branch its father branch. To do that, first the skeleton *junctions* are identified, then the disconnected components have to be ordered according to their “genealogy”. In spite of the intuitiveness of this problem, its solution algorithm is computationally expensive: see for instance [18]. The tree topology identification is not necessary when the blood pressure on the tree is known, as in this example; but, if this is not the case, then 1D models usually will require suitable interface conditions at the tree nodes: to impose this conditions the tree topology has to be computed.

After the arterial tree is identified, its branches are geometrically defined as a set of points (the image pixels), so that to build the 1D vessel mesh, one has two possible approaches:

1. Interpolate this set of points, for example by least-square polynomial approximation;
2. Build the 1D mesh as an *edge path* in the 3D (or 2D) tissue mesh.

In this example, we used the first approach: we wrote a simple Matlab script in which first each branch is interpolated by a polynomial line, and then a FreeFem++ meshing code is automatically created that generates the arterial tree 1D grid. The same code solves the blood flow problem at the microscale level. Some results are shown in fig. 6.7, 6.8.

6.4.3 Brain Angiography

As show in fig. 6.9, the same computation can be carried out in a completely different situation, starting from a medical image obtained with a different technique. Here we consider a *brain angiography*,

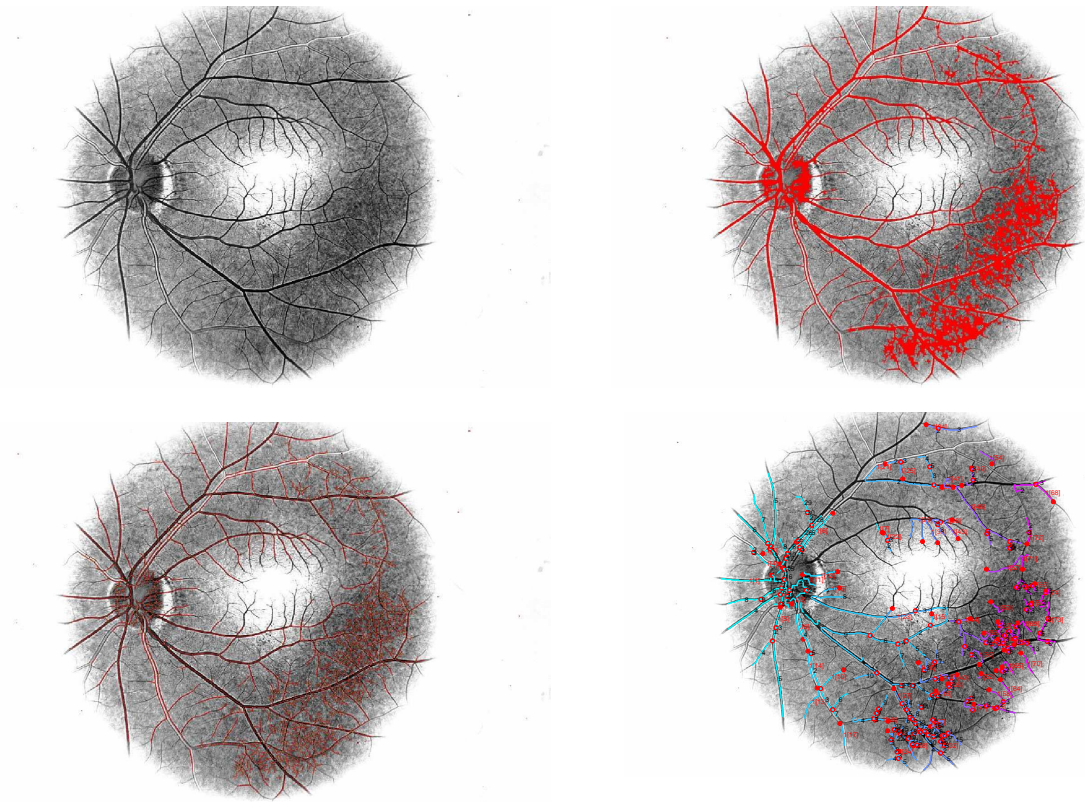


Figure 6.6: Some tools used in extracting vessel geometries for our numerical simulations. Top-left: retinal imaging bitmap. Top-right: segmentation of the image. Bottom-left: skeleton of the segmented image. Bottom-right: reconstruction of vessel tree topology with branch pruning and labelling (different colors correspond to different connected components).

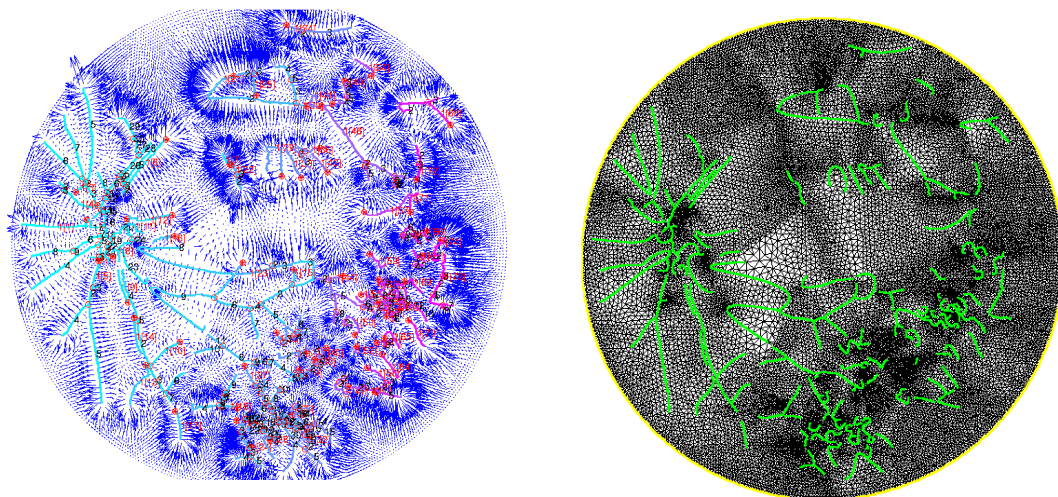


Figure 6.7: On the left: blood velocity at the capillary level. On the right: mesh of the retina, with least-square polynomial lines approximating the vessels (with branch labels).

in which brain vessels are detected using a contrast agent. In the case of fig. 6.9, the circle of Willis is visualized. In this case, the vessel sizes are quite large, nevertheless the skeletonization filtering still allows to get the 1D representation of the arterial tree. Of course, if one has to decide which 1D model is the most appropriate, the quasistatic approximation should be discarded, due to the large vessel radius. Nevertheless, models like (6.5) may accurately represent blood flow and blood pressure propagation in the circle of Willis, as we will see further on in this chapter.

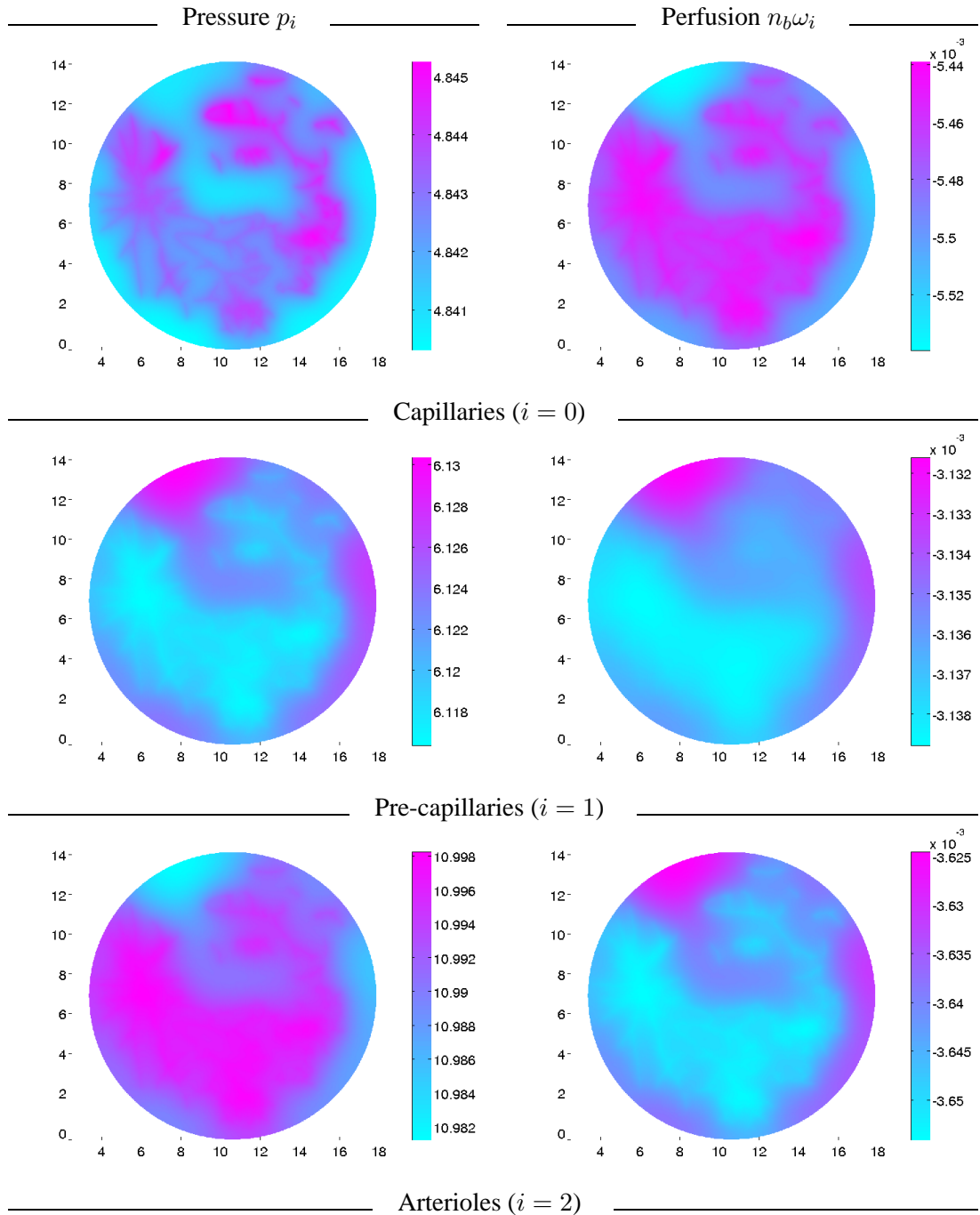


Figure 6.8: Pressures and perfusions for the 3-hierarchies model, in the retinal layer.

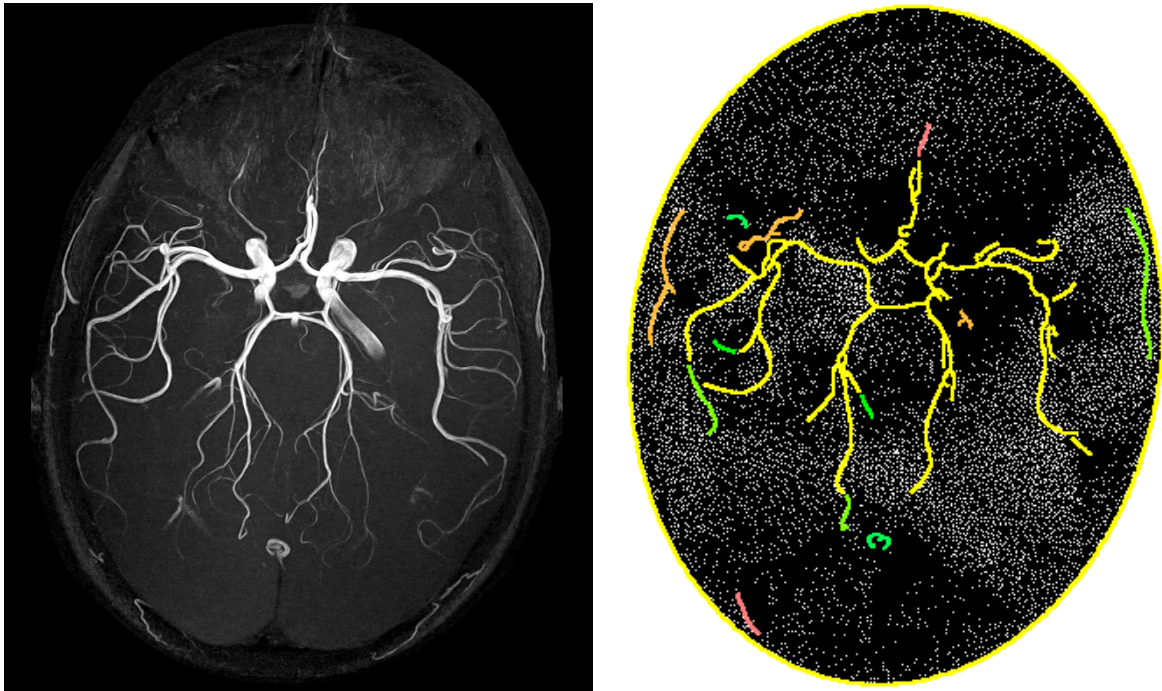


Figure 6.9: On the left: brain angiography. On the right: computational grid, with least-square polynomial approximation of the brain blood vessels. The vessel tree has been extracted from the medical image by means of an automatic algorithm.

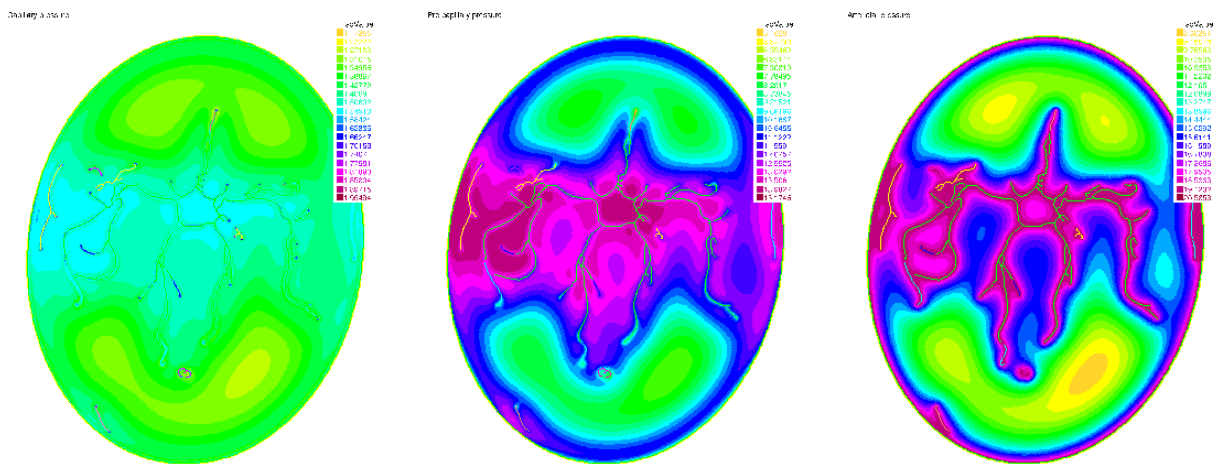


Figure 6.10: From left to right: hierarchical pressures p_0 , p_1 , p_2 at the capillary, pre-capillary and arteriolar levels.

6.5 1D-3D coupling between blood vessels and surrounding tissue

The most interesting problem, among those we have outlined at the beginning of this chapter, has still to be investigated: the coupling between the “fast” flow and transport in a net of 1D vessels, and the same “slow” phenomena in the surrounding 3D tissue where suitable “homogenized” models, such as those presented so far, are assumed. In this section we study the coupled models. To avoid irrelevant complications, we make the following assumptions.

1. A simple one-level hierarchy is considered for the microscale: we will deal with only one tissue permeability, the one referred to the microscale. This does not represent a limitation of our approach, since additional hierarchical levels can be accounted for easily, and will allow us to make the exposition more clear.
2. Blood flow is described by the $\frac{1}{2}$ D or the linearized 1D model. When the $\frac{1}{2}$ D model is considered, the two coupled problems are parabolic, so that the analytical and numerical techniques to treat them are similar; moreover, for the steady (elliptic) case, they have been studied in chapters 4, 5, respectively. If the linearized 1D model is used instead, then we have a coupling between a 3D parabolic and a 1D hyperbolic problem: we will discuss the extensions of our methods needed to treat this more complex case.
3. We consider the simple model (6.34) for mass transport in the tissue. Model (6.13) is assumed to describe mass transport in the vessels.
4. The blood flow from the vessels to the tissue is positive, and linearly dependent on the pressure gap. More precisely:
 - a) The volume of blood per unit time and surface exiting from the vessel wall, and entering into the vessel matrix of the tissue, is positive and proportional to the difference between blood pressure in the vessel and in the tissue, across the vessel wall. The proportionality constant is the (effective) hydraulic *conductivity* L_p . We say *effective* since it could not have the same value of the actual wall conductivity. In fact, we are taking into account also small branches, that provide blood to the surrounding regions, and that are not resolved by our 1D geometry: this *hierarchical* flow can be accounted for precisely by coefficient L_p .
 - b) Since blood exits from the vessels, the tissue concentration on the actual vessel surface is equal to the vessel concentration: in other words, the actual interface between vessel and tissue is the *inlet* of the tissue domain.

In particular, by assumption 4 the coupling conditions for tissue and vessel pressure on the surface of the actual 3D vessel are of Robin type. We have already seen that, starting from a diffusion problem in a domain $\Omega \in \mathbb{R}^3$, with Robin boundary conditions assigned on the surface of a thin tube “drilled” into Ω , a limit problem is obtained by a suitable “flux-preserving” rescaling in which the tube diameters tends to zero. The limit problem has a measure datum and an integral term. Specific formulas have been given for both these terms in section 3.2.2. The coupled 3D- $\frac{1}{2}$ D model of tissue perfusion is directly obtained using the latter results, in the limit case in which the 3D vessel tree is collapsed to its 1D skeleton $\Lambda \in \Omega$:

Problem 6.5.1. (Blood Flow, 3D- $\frac{1}{2}$ D)

Find the tissue and vessel blood pressures (p_t, p_v) satisfying

$$\begin{cases} C_t \frac{\partial}{\partial t} p_t + \nabla \cdot (K_t \nabla p_t) + \alpha p_t - \phi(p_t, p_v) \delta_\Lambda = f_p & t > 0, \mathbf{x} \in \Omega, \\ C_v \frac{\partial}{\partial t} p_v - \frac{\partial}{\partial s} K_v \frac{\partial p_v}{\partial s} + \phi(p_t, p_v) = 0, & t > 0, s \in \Lambda, \end{cases} \quad (6.36)$$

with suitable BC/IC. The term $\phi \delta_\Lambda$ has to be understood as Dirac measure concentrated on Λ and having line density ϕ , where

$$\phi(p_t, p_v) = 2\pi R L_p (p_v - \bar{p}_t), \quad \text{being} \quad \bar{p}_t(s) = \frac{1}{2\pi} \int_0^{2\pi} p_t(s, R(s), \theta) d\theta, \quad (6.37)$$

This model can be seen as the coupling between a one-hierarchy discretization of problem 6.3.1 (see section 6.3.2) with $\phi_t = -\phi(p_t, p_v) \delta_\Lambda$, and problem 6.2.2, with $\phi_v = \phi(p_t, p_v)$. Notice that the actual vessel radius $R = R(s)$ appears as a datum in the expression (6.37) of the coupling term. The coupling term ϕ represents the blood flow leakage from the vessel to the tissue (per unit length).

The term

$$\omega_t = \alpha p_t - f_p \quad (6.38)$$

is the tissue perfusion (see sec. 6.3), more precisely it is the blood flow rate leaving the tissue (and collected by the venous bed) per unit tissue volume. We assume it is positive, since in this work the ‘‘source’’ term f_p describes lower hierarchical compartments only, such as the venous microvascular bed; in this case, if p_{bed} is the related (known) blood venous pressure, we have

$$f_p = \alpha p_{\text{bed}}.$$

The blood velocity in the tissue is given by

$$\mathbf{v} = -\frac{1}{n_b} K_t \nabla p_t. \quad (6.39)$$

Admissible BC are (6.7) for the 1D problem, and homogeneous Neumann conditions (no blood flow across the tissue boundaries) for the 3D one. For example, we can consider the following boundary/initial conditions for problem (6.36):

$$\begin{cases} \mathbf{n} \cdot K_t \partial p_t(t, \mathbf{x}) / \partial \mathbf{n} = 0, & t > 0, \mathbf{x} \in \partial\Omega, \\ p_v(t, 0) = p_{\text{in}}(t), \quad q_v(t, L) - G p_v(t, L) = 0, & t > 0, \\ p_t(0, \mathbf{x}) = p_{t,0}(s), & \mathbf{x} \in \Omega, \\ p_v(0, s) = p_{v,0}(s), & s \in \Lambda, \end{cases} \quad (6.40)$$

where $q_v = -K_v \partial p_v / \partial s$. As usual, G is the hydraulic conductance seen from the end point of the 1D vessel.

When assuming a full 1D model for blood flow in the vessels, we have:

Problem 6.5.2. (Blood Flow, 3D-1D)

Find the tissue pressure p_t and vessel blood pressure and flow rate (p_v, q_v) satisfying

$$\begin{cases} C_t \frac{\partial}{\partial t} p_t + \nabla \cdot (K_t \nabla p_t) + \alpha p_t - \phi(p_t, p_v) \delta_\Lambda = f_p & t > 0, \mathbf{x} \in \Omega, \\ \frac{\partial}{\partial t} \begin{bmatrix} p_v \\ q_v \end{bmatrix} + H \frac{\partial}{\partial s} \begin{bmatrix} p_v \\ q_v \end{bmatrix} + \mathbf{r}(p_v, q_v) = \mathbf{0}, & t > 0, s \in \Lambda, \end{cases} \quad (6.41)$$

with suitable BC/IC, and where $\phi(p_t, p_v)$, H and $\mathbf{r}(p_t, p_v)$ are defined by (6.37), (6.6).

For this problem, (6.40) are still admissible BC/IC.

Similarly, we consider a coupled mass transfer problem obtained starting from the 3D problem 6.3.3 in its version (6.34), and the 1D problem 6.2.3. The interface condition obtained from assumption 4.b is $\bar{u}_t = u_v$ on Λ : this can be enforced by penalization, as we will see. The model we propose is the following one:

Problem 6.5.3. (Mass Transport)

Find the tissue and vessel concentrations (u_t, u_v) satisfying

$$\begin{cases} \frac{\partial}{\partial t} u_t + \nabla \cdot (-D_t \nabla u_t + \mathbf{v} u_t) + \omega_t u_t - \theta(u_t, u_v) \delta_\Lambda = f_u, & t > 0, \mathbf{x} \in \Omega, \\ A_0 \frac{\partial}{\partial t} u_v + \frac{\partial}{\partial s} \left(-A_0 D_v \frac{\partial u_v}{\partial s} + q_v u_v \right) + \phi(p_t, p_v) u_v = 0, & t > 0, s \in \Lambda, \end{cases} \quad (6.42)$$

with suitable BC/IC, where ω_t and \mathbf{v} are given by (6.38), (6.39), and

$$\theta(u_t, u_v) = 2\pi R L_u (u_v - \bar{u}_t). \quad (6.43)$$

Let us make some comments about the proposed model. As regards the first equation in (6.42), the reaction term f_u may describe metabolic or biochemical processes (see chapter 1). The coupling term θ represents a fictitious diffusion (corresponding to the L_u constant, which is a *permeability*). This is actually a *penalization* term to weakly enforce the condition $\bar{u}_t = u$: that is, the mean cross-sectional concentration at the actual vessel surface equals the vessel concentration. Obviously this is the case when the net blood flow ϕ leaving the vessel and entering into the tissue is positive, which is our hypothesis. In the general case, a test has to be made in order to treat Λ as an inlet for the tissue domain only if $\phi > 0$: we do not consider this possibility, since in physiological conditions ϕ is always positive.

The second equation in (6.43) expresses the conservation of the mass of transported chemical in the vessel. We neglected the variations in cross-sectional area; neglecting the rate of variation, that corresponds to a rigid walls assumption, by the conservation of blood flow rate we have that ϕ is such that

$$\frac{\partial q_v}{\partial s} + \phi \simeq 0,$$

so that in this cas an alternative formulation of the vessel transport equation is

$$A_0 \frac{\partial}{\partial t} u_v + \frac{\partial}{\partial s} \left(-A_0 D_v \frac{\partial u_v}{\partial s} \right) + q_v \frac{\partial u_v}{\partial s} = 0. \quad (6.44)$$

As regards BC/IC, we can assume for instance a prescribed input concentration at the vessel inlet and impose a zero diffusive flux elsewhere:

$$\begin{cases} \partial u_t(t, \mathbf{x})/\partial \mathbf{n} = 0, & t > 0, \mathbf{x} \in \partial\Omega, \\ u_v(t, 0) = u_{\text{in}}(t), \quad \partial u_v(t, L)/\partial s = 0, & t > 0, \\ u_t(0, \mathbf{x}) = u_{t,0}(s), & \mathbf{x} \in \Omega, \\ u_v(0, s) = u_{v,0}(s), & s \in \Lambda. \end{cases} \quad (6.45)$$

6.6 Algorithmic and numerical aspects

6.6.1 1D diffusion-advection equations on trees

In chapters 3, 4, 5, we have always considered a one-dimensional vessel domain without branching. However, 1D modelling is suited to represent complex branching geometries as well: in this section we are going to explain how this can be accomplished in an efficient way. A wide literature exists about the use of nonlinear hyperbolic 1D models for arterial trees, see for instance [84], [30] (and [8] for similar fluid-dynamic models of traffic flows on road networks). In these papers, techniques are described that allow to impose physiological meaningful interface conditions at the nodes of a given 1D network, namely the conservation of blood flow, and the continuity of the (possibly total) pressure. Basically, in a given internal branching point with n branches, these conditions are given in the form of n equations for the set of $2n$ characteristic variables, so that the ingoing variables are expressed as functions of the outgoing ones (see also chap. 2). Although we could take advantage of these already established techniques, we will adopt different strategies that are available in our simpler case, in which the equation at hand is either parabolic or linear hyperbolic.

The case of the $\frac{1}{2}$ D model

Let us consider the simple configuration of fig. 6.11 featuring three 1D vessels Λ_i , $i = 1, 2, 3$, connected by the branching point B . We consider a stationary flow, without any fluid loss. We denote by

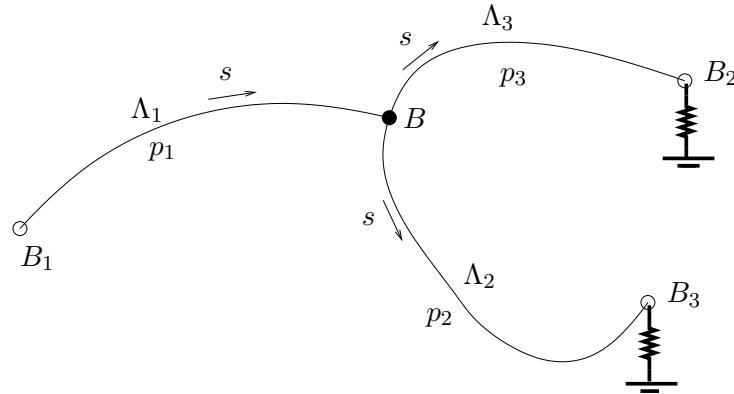


Figure 6.11: 1D domain with a bifurcation.

$p_i(s)$, $p_i : [0, L_i] \rightarrow \mathbb{R}$, the pressure on the branch Λ_i , L_i being the length of Λ_i and s the curvilinear abscissa. To fix the ideas, let us assume that the s positive directions on each branch are oriented as indicated in the figure. We denote by $q_i(s)$ the flow rates in the positive direction on Λ_i . Our assumptions concerning the conditions at the end points of the branches are the following:

- (i) in B_1 , the flow rate is q_{in} ;
- (ii) in B_i , $i = 2, 3$, a lumped hydraulic conductance G_i is relating pressure and flow rate according to $q_i = G_i(p_i - p_{e,i})$, where $p_{e,i}$ is an external reference pressure;
- (iii) at the branching node B the pressures p_i have the same value, and the flow rate is conserved (the sum of the flow rates entering in the node is zero).

According to eq. (6.10), the flow rate is given by $q_i(s) = -K_i p'_i(s)$ where K_i is the hydraulic conductivity per unit length of the i -th branch. Since we are in the steady case, the strong formulation of our problem is

$$(-K_i p'_i(s))' = 0 \quad 0 < s < L_i, \quad i = 1, 2, 3, \quad (6.46)$$

with “external” boundary conditions (i-ii) in B_i :

$$-K_1 p'_1(0) = q_{\text{in}}, \quad -K_2 p'_2(L_2) = G_2(p_2(L_2) - p_{e,2}), \quad -K_3 p'_3(L_3) = G_3(p_3(L_3) - p_{e,3}) \quad (6.47)$$

and “internal” boundary conditions (iii) in B :

$$p_1(L_1) = p_2(0) = p_3(0), \quad -K_1 p'_1(L_1) + K_2 p'_2(0) + K_3 p'_3(0) = 0. \quad (6.48)$$

Notice that we have 6 boundary conditions, namely 2 for each 1D subdomain Λ_i . Consider three smooth test functions $\psi_i : [0, L_i] \rightarrow \mathbb{R}$; multiplying the i -th equation in (6.46) times ψ_i , summing and integrating by parts we get

$$\sum_{i=1}^3 \left[\int_0^{L_i} K_i p'_i(s) \psi'_i(s) ds + (K_i p'_i(0) \psi_i(0) - K_i p'_i(L_i) \psi_i(L_i)) \right] = 0. \quad (6.49)$$

We can define functions on the whole Λ by using the local parametrizations $[0, L_i] \rightarrow \Lambda_i$ of each subdomain Λ_i in term of the respective curvilinear abscissa s . In this way, we can also define the derivatives with respect to s almost everywhere on Λ , since once again they are defined separately on each subdomain. In the sequel we will denote the argument of such functions either by s or with the corresponding point on Λ : this abuse of notation is only meant to simplify the exposition. In order to obtain a weak formulation of our problem on the whole manifold $\Lambda = \bigcup_i \Lambda_i$, let us introduce the space

$$\hat{V} = \{p : \Lambda \rightarrow \mathbb{R}, \quad p|_{\Lambda_i} \in H^1(\Lambda_i), \quad p|_{\Lambda_i}(B) = p|_{\Lambda_j}(B), \quad i, j = 1, 2, 3\}, \quad (6.50)$$

where the interface conditions in B make sense thanks to the trace operator. We observe that \hat{V} is endowed with a natural product norm, given by

$$\|p\|_{\hat{V}}^2 = \sum_i \|p|_{\Lambda_i}\|_{H^1(\Lambda_i)}^2. \quad (6.51)$$

Due to the first condition in (6.48), we can look at p_i as the restrictions $p|_{\Lambda_i}$ of a function $p \in \hat{V}$. Now, if we make the same *ansatz* for the test functions, letting $\psi_i = \psi|_{\Lambda_i}$ where $\psi \in \hat{V}$, thanks to the continuity condition in B

$$\psi_1(L_1) = \psi_2(0) = \psi_3(0)$$

and to (6.48), the sum of the boundary terms involving the point B is zero. Therefore, expressing the sum of integrals in (6.49) as an integral on the whole tree, and expressing the boundary terms at points B_i using eq. (6.47), we can restate our problem in the following weak form: *find* $p \in \hat{V}$ *such that*

$$\int_{\Lambda} K p' \psi' ds + G_2 p(B_2) \psi(B_2) + G_3 p(B_3) \psi(B_3) = q_{in} \psi(B_1) + G_2 p_{e,2} \psi(B_2) + G_3 p_{e,3} \psi(B_3) \quad \forall \psi \in \hat{V}, \quad (6.52)$$

where K is the function such that $K|_{\Lambda_i} := K_i$.

The advantage of such a formulation is that the constraints at the internal branching point B are “automatically” imposed: the continuity of the pressure, by construction of the space \hat{V} , and the conservation of the flow rate by natural conditions. This yields a very simple finite element approximation of the problem. Assume that Λ is a connected piecewise affine 1D domain, as in

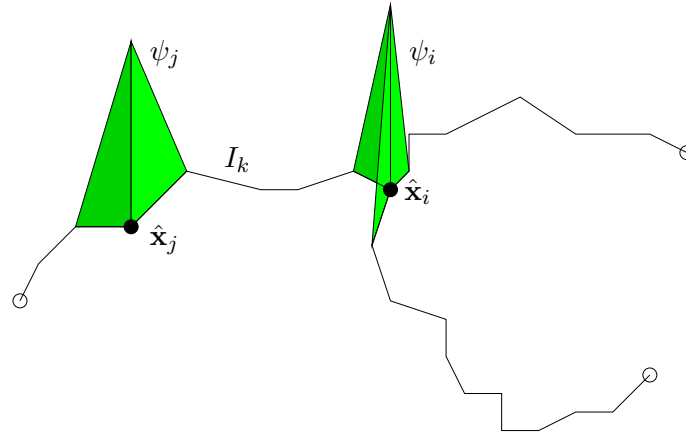


Figure 6.12: Representation of finite element basis functions on a 1D domain with a bifurcation.

fig. 6.12, that a family $\{\mathcal{I}_h\}$, $h > 0$, of sets of segments is given such that $|I_k| \leq h \forall I_k \in \mathcal{I}_h$, and $\Lambda = \bigcup_{I_k \in \mathcal{I}_h} I_k$. We define the discrete \mathbb{P}^1 finite element space as usual, namely

$$\hat{V}_h = \{p \in C(\Lambda) : p|_{I_k} \in \mathbb{P}^1(I_k) \forall I_k \in \mathcal{I}_h\}. \quad (6.53)$$

Since functions in \hat{V}_h are continuous on Λ , we have $\hat{V}_h \subset \hat{V}$. We denote by \hat{x}_i the nodes of Λ , as in chapter 5, and by ψ_i the corresponding Lagrange basis function, defined by $\psi_i \in \hat{V}_h$, $\psi_i(\hat{x}_j) = \delta_{ij}$. We observe that even when ψ_i corresponds to a branching node, its support is given by the union of all elements sharing that node: they may be more than two, as shown in figure 6.12. The finite element approximation of problem (6.52) is thus simply reduced to solve the same problem in the finite dimensional space \hat{V}_h : the corresponding bilinear form and linear functional will contain only the boundary terms (6.47), while the “internal” boundary conditions (6.48) are naturally imposed by the variational formulation. This is very convenient when dealing with complex branching patterns.

Remark. If we include in eq. (6.46) a reaction term (representing fluid losses), still the use of the space \hat{V} enforces automatically the conditions (6.48): in fact, the reaction term is not integrated by parts.

Until now, we have considered the steady problem; to approximate the solution of the non-steady problem, we can first perform a semi-discretization in space by the approach described above, then

employ any time advancing scheme, implicit or explicit (we refer for more details to [85]). This is a rather standard technique; therefore, as a non-steady example, we will consider directly the hyperbolic case, and describe how it is again possible to impose “naturally” the internal boundary conditions at branching nodes by a proper choice of the finite element spaces for the pressure and the flow rate.

The linearized 1D model

We consider again the branching geometry of fig. 6.11. Now we assume that the problem is time dependent, and that the pressure $p_i(t, s)$ and flow rate $q_i(t, s)$ in the i -th branch satisfy the linear 1D model (6.3), that is

$$\begin{cases} c \frac{\partial p_i}{\partial t} + \frac{\partial q_i}{\partial s} = 0, \\ \frac{\partial q_i}{\partial t} + \frac{1}{l} \frac{\partial p_i}{\partial s} + r q_i = 0, \end{cases} \quad (t, s) \in \mathbb{R}^+ \times (0, L_i), \quad i = 1, 2, 3. \quad (6.54)$$

The boundary/interface conditions (i)-(iii) become

$$q_1(t, 0) = q_{\text{in}}(t), \quad q_2(t, L_2) = G_2(p_2(t, L_2) - p_{e,2}), \quad q_3(t, L_3) = G_3(p_3(t, L_3) - p_{e,3}), \quad (6.55)$$

and

$$p_1(t, L_1) = p_2(t, 0) = p_3(t, 0), \quad q_1(t, L_1) + q_2(t, 0) + q_3(t, 0) = 0. \quad (6.56)$$

We assign initial conditions as well:

$$p_i(0, s) = p_{i,0}(s), \quad q_i(0, s) = q_{i,0}(s), \quad s \in [0, L_i], \quad i = 1, 2, 3, \quad (6.57)$$

that of course have to satisfy the compatibility conditions

$$q_{1,0}(0) = q_{\text{in},1}(0), \quad q_{i,0}(L_i) = G_i(p_{i,0}(L_i) - p_{e,i}), \quad i = 2, 3.$$

Remark. We point out that the boundary conditions can be reformulated in terms of characteristic variables. In our linear case, it is easy to see that the “forward” and “backward” characteristic variables in the i -th branch are given by

$$w_{1,i} = \frac{1}{2} \left(\sqrt{\frac{c}{l}} p_i + q_i \right), \quad w_{2,i} = \frac{1}{2} \left(-\sqrt{\frac{c}{l}} p_i + q_i \right), \quad (6.58)$$

associated to the eigenvalues $\lambda_1 = 1/\sqrt{cl}$, $\lambda_2 = -1/\sqrt{cl}$ of matrix H of problem 6.2.1. For example, the boundary condition $q_1(t, 0) = q_{\text{in}}(t)$ reads

$$w_{1,1}(t, 0) = q_{\text{in}}(t) - w_{2,1}(t, 0), \quad (6.59)$$

that is the incoming characteristic variable $w_{1,1}$ at B_1 is expressed as a function of the outgoing one $w_{2,1}$. A similar form is obtained for the remaining conditions (this is a quite general class of admissible boundary conditions for hyperbolic problems, see chapter 2 where the non-linear case has been addressed). It is easily found that characteristic variables for problem (6.54) satisfy

$$\frac{d}{dt} w_{k,i}(t, s_0 + \lambda_k t) + \frac{r}{2} [w_{1,i}(t, s_0 + \lambda_k t) + w_{2,i}(t, s_0 + \lambda_k t)] = 0, \quad k = 1, 2; \quad (6.60)$$

these relations will be used later on to extrapolate boundary values for our numerical scheme. We point out that if a fluid loss term ϕ_i is considered in the left hand side of the first equation in (6.54), then these relations have to be modified⁴.

Let us consider the finite element discretization of system (6.54). The idea is again to multiply each equation by a test function, and then integrate in space: this approach belongs to the class of Galerkin methods for hyperbolic equations, for which we refer the reader to [85, sec. 14.3.1]. We consider again the space \hat{V} defined in (6.50) for the pressure, whereas for the flow rate we introduce the space

$$\hat{W} = \{q : \Lambda \rightarrow \mathbb{R}, \quad q_{|\Lambda_i} \in H^1(\Lambda_i), \quad i, j = 1, 2, 3\}, \quad (6.61)$$

without any continuity condition in B , since of course the flow rate will be discontinuous at the branching point.

If we multiply the first equation in (6.54) by $\psi \in \hat{V}$, the second by $l\varphi$, $\varphi \in \hat{W}$, and then integrate by parts the $\partial q_i / \partial s$ term in the first equation, we have:

$$\begin{cases} \sum_{i=1}^3 \frac{d}{dt} \int_{\Lambda_i} cp_i \psi ds - \int_{\Lambda_i} q_i \frac{d\psi}{ds} ds + [q_i(t, L_i) \psi_{|\Lambda_i}(L_i) - q_i(t, 0) \psi_{|\Lambda_i}(0)] = 0, \\ \sum_{i=1}^3 \frac{d}{dt} \int_{\Lambda_i} lq_i \varphi ds + \int_{\Lambda_i} \frac{\partial p_i}{\partial s} \varphi ds + \int_{\Lambda_i} rlq_i \varphi ds = 0. \end{cases} \quad (6.62)$$

The boundary terms can be treated as in the previous case: in particular, letting $p_i(t, \cdot) = p_{|\Lambda_i}(t, \cdot)$, $q_i(t, \cdot) = q_{|\Lambda_i}(t, \cdot)$ where $p(t, \cdot) \in \hat{V}$, $q(t, \cdot) \in \hat{W}$, thanks to (6.56) we obtain the following problem: for $t \geq 0$, find $p(t, \cdot) \in \hat{V}$ and $q(t, \cdot) \in \hat{W}$ satisfying (6.55), (6.57), and such that

$$\begin{cases} \frac{d}{dt} \int_{\Lambda} cp\psi ds - \int_{\Lambda} q \frac{d\psi}{ds} ds - [q(t, B_1) \psi(B_1) - q(t, B_1) \psi(B_2) - q(t, B_3) \psi(B_3)] = 0 & \forall \psi \in \hat{V}, \\ \frac{d}{dt} \int_{\Lambda} lq\varphi ds + \int_{\Lambda} \frac{\partial p}{\partial s} \varphi ds + \int_{\Lambda} rlq\varphi ds = 0 & \forall \varphi \in \hat{W}. \end{cases} \quad (6.63)$$

Formulation (6.63), similarly to (6.52), automatically enforces the internal interface conditions in B : the only terms that have to be considered explicitly are those related to the end points B_i of Λ , appearing in the first equations between the brackets.

This advantage can be transferred to the finite element semi-discretization of our problem: we define the discrete space for the pressure \hat{V}_h as in (6.53), and the discrete space for the flow rate as

$$\hat{W}_h = \{q : \Lambda \rightarrow \mathbb{R}, \quad q_{|I_k} \in \mathbb{P}^0(I_k) \quad \forall I_k \in \mathcal{I}_h\}. \quad (6.64)$$

Notice that since no space derivative of q appears in the weak formulation (6.63), we can use \mathbb{P}^0 elements for the flow rate: the finite element semidiscrete approximation is immediately obtained by replacing \hat{V} , \hat{W} by their discrete counterparts \hat{V}_h and \hat{W}_h in (6.63).

⁴ They become

$$\begin{aligned} \frac{d}{dt} w_{1,i}(t, s_0 + \lambda_1 t) + \frac{r}{2} [w_{1,i}(t, s_0 + \lambda_1 t) + w_{2,i}(t, s_0 + \lambda_1 t)] + \frac{1}{2} \frac{1}{\sqrt{cl}} \phi_i(t, s_0 + \lambda_1 t) &= 0, \\ \frac{d}{dt} w_{2,i}(t, s_0 + \lambda_2 t) + \frac{r}{2} [w_{1,i}(t, s_0 + \lambda_2 t) + w_{2,i}(t, s_0 + \lambda_2 t)] - \frac{1}{2} \frac{1}{\sqrt{cl}} \phi_i(t, s_0 + \lambda_2 t) &= 0. \end{aligned}$$

Moreover, if we provide Dirichlet data for both p and q at the end points B_i , we can take the test functions ψ and φ respectively in the spaces

$$\hat{V}_{0,h} = \{p \in \hat{V}_h : p(B_i) = 0, i = 1, 2, 3\}, \quad \hat{W}_{0,h} = \{q \in \hat{W}_h : q(B_i) = 0, i = 1, 2, 3\};$$

in particular, all boundary terms in the first equation of (6.63) vanish.

We are allowed to provide 2 boundary values (p and q) instead of a single one as the continuous problem would require, when applying a time advancing scheme to the semidiscrete approximation. As we have seen in chapter 2 in the framework of a Taylor-Galerkin scheme, (see also [84], [73]), the “missing” boundary condition is obtained by *extrapolation* of the outgoing characteristic variable. Let $\Delta t > 0$ the time step, and $n \in \mathbb{N}$: denote $p_i^{(n)}(s) = p_i(n\Delta t, s)$, $q_i^{(n)}(s) = q_i(n\Delta t, s)$, $i = 1, 2, 3$. Consider for instance the node B_1 , in which $q = q_{\text{in}}(t)$ is prescribed. The outgoing characteristic in B_1 is the backward variable w_2 , we can extrapolate its value by using (6.60) with $k = 2$. Since $\frac{r}{2}(w_{1,i} + w_{2,i}) = rq_i$, using the backward Euler advancing scheme for eq. (6.60) with $s_0 = -\Delta t\lambda_2 = \Delta t/\sqrt{cl}$, we have:

$$w_{2,1}(t + \Delta t, 0) \simeq w_{2,1}\left(t, \frac{\Delta t}{\sqrt{cl}}\right) - r\Delta tq_{\text{in}}(t + \Delta t).$$

Therefore, thanks to (6.58), we have

$$p_1(t + \Delta t, 0) \simeq p_1\left(t, \frac{\Delta t}{\sqrt{cl}}\right) + \sqrt{\frac{l}{c}} \left[(1 + 2r\Delta t)q_{\text{in}}(t + \Delta t) - q_1\left(t, \frac{\Delta t}{\sqrt{cl}}\right) \right].$$

This yields the following boundary value extrapolation rule:

$$\begin{aligned} p_1^{(n+1)}(0) &= p_{\text{ex},1}(p_1^{(n)}, q_1^{(n)}) \\ &:= p_1^{(n)}\left(\frac{\Delta t}{\sqrt{cl}}\right) + \sqrt{\frac{l}{c}} \left[(1 + 2r\Delta t)q_{\text{in}}(t + \Delta t) - q_1\left(t, \frac{\Delta t}{\sqrt{cl}}\right) \right]. \end{aligned} \quad (6.65)$$

We see that the boundary value of pressure at time $t + \Delta t$ is expressed as a function of the flow rate boundary value, and other terms that are evaluated at the previous time step: therefore, when using a time advancing scheme, (6.65) can be used to prescribe the boundary value for the pressure in B_1 .

At the end points B_2, B_3 , the boundary value for the flow rate is given by

$$q_i^{(n+1)}(L_i) = G_i(p_i^{(n+1)}(L_i) - p_{e,i}), \quad i = 2, 3, \quad (6.66)$$

while the boundary value for the pressure is obtained by extrapolating the outgoing characteristic is w_1 ; by the same technique we used for (6.65), and substituting $q_i^{(n+1)}(L_i)$ using eq. (6.66), we get

$$\begin{aligned} p_i^{(n+1)}(L_i) &= p_{\text{ex},i}(p_i^{(n)}, q_i^{(n)}) \\ &:= \frac{1}{1 + \sqrt{\frac{l}{c}}G_i(1 + 2r\Delta t)} \left[p_i^{(n)}\left(L_i - \frac{\Delta t}{\sqrt{cl}}\right) + \sqrt{\frac{l}{c}} \left[q_i^{(n)}\left(L_i - \frac{\Delta t}{\sqrt{cl}}\right) + (1 + 2r\Delta t)G_i p_{e,i} \right] \right], \end{aligned} \quad (6.67)$$

for $i = 2, 3$.

Remark (Non-reflecting boundary conditions). We point out that, since we are using a hyperbolic model, a concentrated load at the end of a vessel induces *reflected waves*. If the load represents a

physical discontinuity in the vessel, this is an expected behavior; otherwise, it is more convenient to consider *non-reflecting boundary conditions*. In this case, the outgoing characteristic variable is extrapolated, and the ingoing variable is set to its reference value. This boundary conditions allows waves to exit from the 1D domain without being reflected. In our case, if non reflecting boundary conditions are assumed at end points B_2, B_3 , and $w_{2,i} = -\sqrt{\frac{c}{l}}p_{i,0} + q_{i,0}, i = 2, 3$, are the corresponding reference values of the incoming variables, the extrapolation formulas become:

$$\begin{aligned} p_i^{(n+1)}(L_i) = p_{\text{ex},i}(p_i^{(n)}, q_i^{(n)}) &:= \frac{1}{2(1+r\Delta t)} \left[p_i^{(n)} \left(L_i - \frac{\Delta t}{\sqrt{cl}} \right) + (1 + 2r\Delta t)p_{i,0} \right] + \\ &\frac{\sqrt{l/c}}{2(1+r\Delta t)} \left[q_i^{(n)} \left(L_i - \frac{\Delta t}{\sqrt{cl}} \right) - (1 + 2r\Delta t)q_{i,0} \right], \\ q_i^{(n+1)}(L_i) = q_{\text{ex},i}(p_i^{(n)}, q_i^{(n)}) &:= \frac{1}{2(1+r\Delta t)} \left[q_i^{(n)} \left(L_i - \frac{\Delta t}{\sqrt{cl}} \right) + q_{i,0} + \right. \\ &\left. \sqrt{\frac{c}{l}} \left(p_i^{(n)} \left(L_i - \frac{\Delta t}{\sqrt{cl}} \right) - p_{i,0} \right) \right], \end{aligned} \quad (6.68)$$

for $i = 2, 3$.

In the literature (see for example [30], [95] and references therein) boundary conditions have been imposed explicitly for all end points of the vessel net, as well as branching points. However, in our linear case we have that the boundary conditions at branching points are naturally imposed by the variational formulation. This means that we do not have to enforce that the test functions vanish at those points, they are considered just as any other internal node of our 1D mesh.

To sum up, the fully discrete implicit Euler scheme corresponding to our approach reads: for $n \in \mathbb{N}$, find $p^{(n+1)} \in \hat{V}_h$ and $q^{(n+1)} \in \hat{W}_h$ such that

$$\begin{cases} \int_{\Lambda} cp^{(n+1)}\psi \, ds - \Delta t \int_{\Lambda} q^{(n+1)} \frac{d\psi}{ds} \, ds = \int_{\Lambda} cp^{(n)}\psi \, ds & \forall \psi \in \hat{V}_{0,h}, \\ \int_{\Lambda} lq^{(n+1)}\varphi \, ds + \Delta t \left(\int_{\Lambda} \frac{\partial p^{(n+1)}}{\partial s} \varphi \, ds + \int_{\Lambda} rlq^{(n+1)}\varphi \, ds \right) = \int_{\Lambda} lq^{(n)}\varphi \, ds & \forall \varphi \in \hat{W}_{0,h}, \end{cases} \quad (6.69)$$

satisfying

$$p^{(n+1)}(B_1) = p_{\text{ex},1}(p^{(n)}, q^{(n)}), \quad q^{(n+1)}(B_1) = q_{\text{in}}((n+1)\Delta t),$$

where $p_{\text{ex},1}$ is given by (6.65), and

$$p^{(n+1)}(B_i) = p_{\text{ex},i}(p^{(n)}, q^{(n)}), \quad q^{(n+1)}(B_i) = G_i(p^{(n+1)}(B_i) - p_{e,i}), \quad i = 2, 3,$$

where $p_{\text{ex},i}$ are given by eq. (6.67). When non-reflecting boundary conditions are employed, the latter equations become

$$p^{(n+1)}(B_i) = p_{\text{ex},i}(p^{(n)}, q^{(n)}), \quad q^{(n+1)}(B_i) = q_{\text{ex},i}(p^{(n)}, q^{(n)}), \quad i = 2, 3,$$

where now $p_{\text{ex},1}$ and $q_{\text{ex},1}$ are the extrapolation formulas in eq. (6.68).

Remark (Stability). We have proposed an implicit time advancing scheme; according to this choice, the characteristic extrapolation was obtained using the implicit Euler scheme, to preserve the stability of our method. In fact, we observed that when explicit Euler characteristic extrapolation is performed, scheme (6.69) shows a very strict stability condition on Δt for high values of the conductances G_i .

In figures 6.13 and 6.14, results obtained by this scheme applied to a simple branching geometry are shown. We consider three vessels Λ_i (see the snapshots in the figures: Λ_1 is the parent vessel on

the bottom, while Λ_2 is the right child vessel, and Λ_3 is the left child vessel), having the parameters reported in table 6.2. The vessels are piecewise linear curves: actually they have been constructed by creating an edge path in a 3D mesh (we will address this topic in section 6.6.2). The positive direction of orientations of the parent vessel and right child vessel is “from father to child” (that is “bottom to top” in the figures); on the contrary, the orientation of the left child vessel is opposite to that of the right child vessel, to verify that the natural enforcement of internal boundary conditions of our scheme is independent of the chosen parametrization (actually this is a desirable feature, since we aim to apply the same scheme to complex networks in which the branches are automatically extracted from data, thus having orientations that cannot be predicted before the simulation). We applied the

	Radius [cm]	Length [cm]	c [cm ² kPa ⁻¹]	l [cm ⁻⁴ kPa s ²]	r [s ⁻¹]
vessel 1	0.4248	3.3	0.24083	$1.76 \cdot 10^{-4}$	1.551
vessel 2	0.2832	10.4	0.07136	$3.97 \cdot 10^{-5}$	3.491
vessel 3	0.3540	10.4	0.13937	$2.54 \cdot 10^{-5}$	2.234

Table 6.2: Numerical values used for our testing simulation of 1D blood flow in the branching geometry.

scheme (6.69) for $q_{\text{in}}(t)$ given by a half-sine wave with amplitude $10.7 \text{ cm}^3 \text{ s}^{-1}$ (mean flow rate 3.17). The initial pressure and flow rate were respectively 2 kPa and $0 \text{ cm}^3 \text{ s}^{-1}$. Both conductive loads and non-reflecting conditions have been considered at the end points of the tree.

Figures 6.13, 6.14 show the computed pressure and flow rate, propagating in the branching geometry, when non-reflecting boundary conditions are employed. We point out that the flow rate in the third vessel is negative, as expected due to its “inverse” orientation. In figure 6.15 the corresponding time courses at the middle points of each vessel are reported, comparing the two kinds of boundary conditions: notice the presence of reflected waves when conductive loads are considered.

The mass transport equations

The mass transport equation (6.13) is a reaction-diffusion problem of the same type than the $\frac{1}{2}$ D model of blood flow, plus an advection term. We consider a similar model equation on our branching geometry, that reads as follows:

$$A_0 \frac{\partial}{\partial t} u_i + \frac{\partial}{\partial s} \left(q_i u_i - A_0 D \frac{\partial}{\partial s} u_i \right) = 0, \quad (t, s) \in \mathbb{R}^+ \times (0, L_i), \quad i = 1, 2, 3,$$

where we denote by u_i the volume concentration in the i -th branch, and A_0 , D respectively the vessel (reference) cross-sectional area and the diffusion coefficient of the transported substance in blood. As in the previous subsections, we need suitable conditions at the extremal points of the branches; moreover, conditions at the branching point B have to respect the mass conservation principles. Here we assume that:

- (i) at node B_1 , the concentration is u_{in} ;
- (ii) at node B_i , $i = 2, 3$, the diffusive mass flux is neglected;
- (iii) at the branching node B the volume concentrations u_i have the same value, and the total mass flux entering in the node is zero.

It follows that the “external” boundary conditions (i-ii) in B_i are:

$$u_1(t, 0) = u_{\text{in}}, \quad \partial u_2(t, L_2)/\partial s = 0, \quad \partial u_3(t, L_3)/\partial s = 0, \quad (6.70)$$

and “internal” boundary conditions (iii) in B are⁵:

$$u_1(t, L_1) = u_2(t, 0) = u_3(t, 0), \quad (6.71)$$

and

$$-q_1 u_1(t, L_1) + A_0 D \frac{\partial u_1}{\partial s}(t, L_1) + \sum_{i=2,3} q_i u_i(t, 0) - A_0 D \frac{\partial u_i}{\partial s}(t, 0) = 0. \quad (6.72)$$

Observe that, since $q_1 = q_2 + q_3$ (conservation of the flow rate), and thanks to (6.71), the conservation of the advective fluxes holds; as a consequence, equation (6.72) is equivalent to the conservation of the diffusive fluxes only:

$$-A_0 D \frac{\partial u_1}{\partial s}(t, L_1) + \sum_{i=2,3} A_0 D \frac{\partial u_i}{\partial s}(t, 0) = 0,$$

that we already know how to enforce by a proper variational formulation. In particular, thanks to (6.71), we can look at $u_i(t, \cdot)$ as the restrictions $u|_{\Lambda_i}(t, \cdot)$ of a function $u(t, \cdot) \in \hat{V}$, and we can proceed as we did for the the $\frac{1}{2}D$ model. We denote $u^{(n)}$ an approximation of $u(t_n, \cdot)$, where $t_n = n\Delta t$, being $\Delta t > 0$ the time step; we consider the finite element space \hat{V}_h defined by eq. (6.53), together with the homogeneous subspace

$$\hat{V}_{0,h} = \left\{ u \in \hat{V}_h : u(B_1) = 0 \right\}.$$

The finite element / implicit Euler time advancing scheme reads: for $n \in \mathbb{N}$, find $u^{(n+1)} \in \hat{V}_h$ such that

$$\begin{aligned} \int_{\Lambda} A_0 u^{(n+1)} \psi \, ds - \Delta t \left(\int_{\Lambda} \frac{d}{ds} [qu^{(n+1)}] \psi \, ds + \int_{\Lambda} A_0 D \frac{d}{ds} u^{(n+1)} \frac{d}{ds} \psi \, ds \right) \\ = \int_{\Lambda} A_0 u^{(n)} \psi \, ds \quad \forall \psi \in \hat{V}_{0,h}, \quad (6.73) \end{aligned}$$

satisfying

$$u^{(n+1)}(B_1) = u_{\text{in}}(t_n).$$

Actually, this is often an *advection-dominated* problem, since coefficient $A_0 D/|\Lambda|$ is small compared to q . Therefore, proper stabilization techniques are in order to prevent oscillations to appear in the numerical solution: for instance, the *streamline upwind Petrov-Galerkin* stabilization method (SUPG), for which we refer the reader to [85].

An example of numerical simulation, with the same geometry of the previous 1D blood flow simulation, SUPG stabilization, in which at each time t_n the previously computed flow rate $q = q^{(n)}$ has been used, is shown in fig. 6.16 and 6.17. The input concentration is set to $u_{\text{in}}(t) = 1$, while the initial concentration is zero: $u^{(0)} = 0$; we considered a diffusion coefficient such that $A_0 D = 1.96 \cdot 10^{-5} \text{ cm}^4 \text{ s}^{-1}$ for all the vessels (this corresponds to the typical value of $D \simeq 2.5 \cdot 10^{-5} \text{ cm}^2 \text{ s}^{-1}$ of the diffusion constant for oxygen in blood). We see in fig. 6.16 how the chemical concentration is transported in the vessels, even with a bifurcating geometry. The time courses of u at the middle points of each vessel are reported in fig. 6.17 (four heart beats are necessary for the complete propagation of the input concentration).

⁵ We are imposing the conservation of both the volume concentration (assuming that the transported quantity splits proportionally to the blood volume) and the total mass flux at the bifurcation.

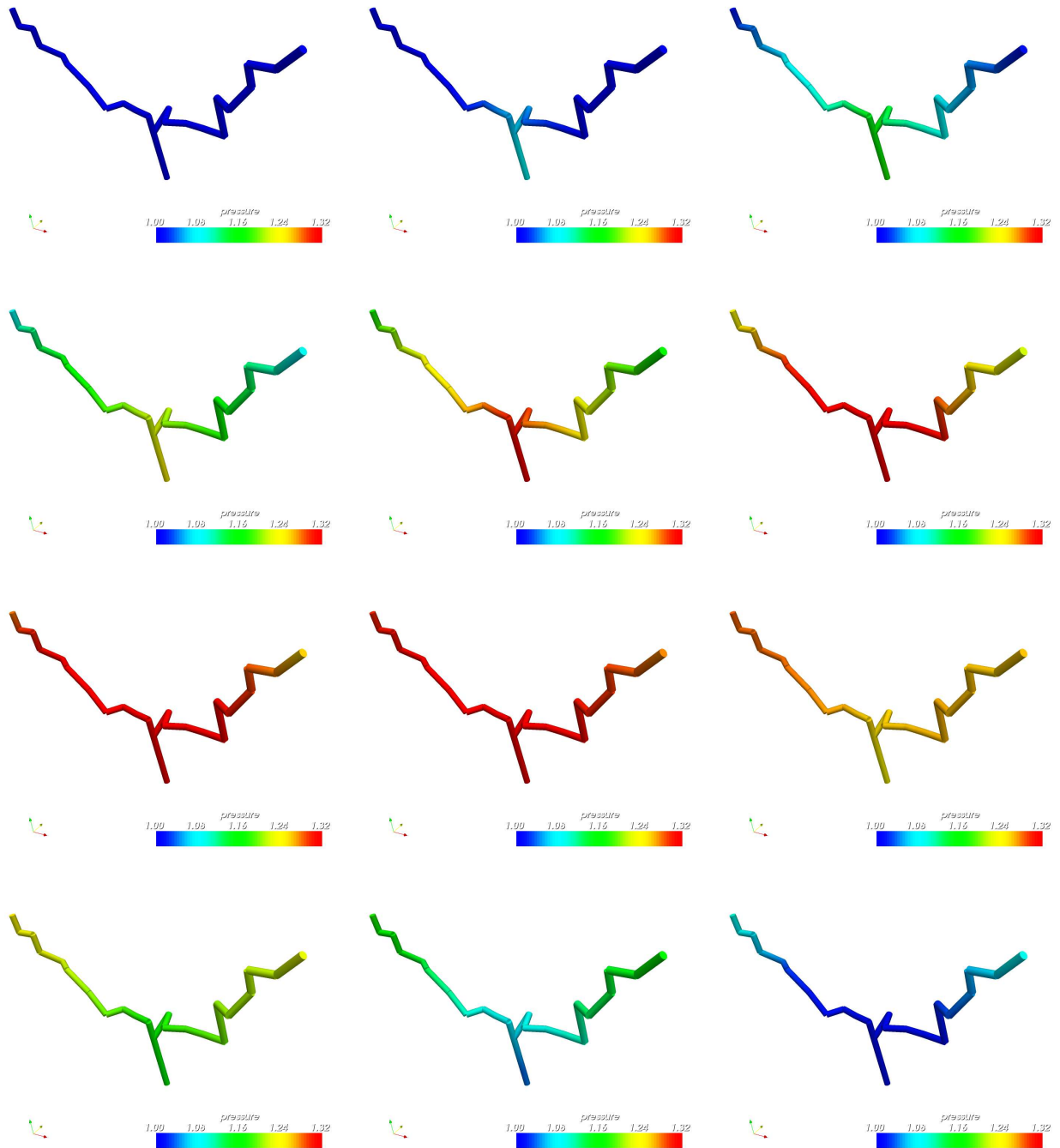


Figure 6.13: From left to right and from top to bottom: snapshots of the blood pressure [kPa] on the arterial tree at times $t_n = 0.05n$ sec, for $n = 0, 1, 2, \dots, 11$, showing the propagation of the pressure wave.

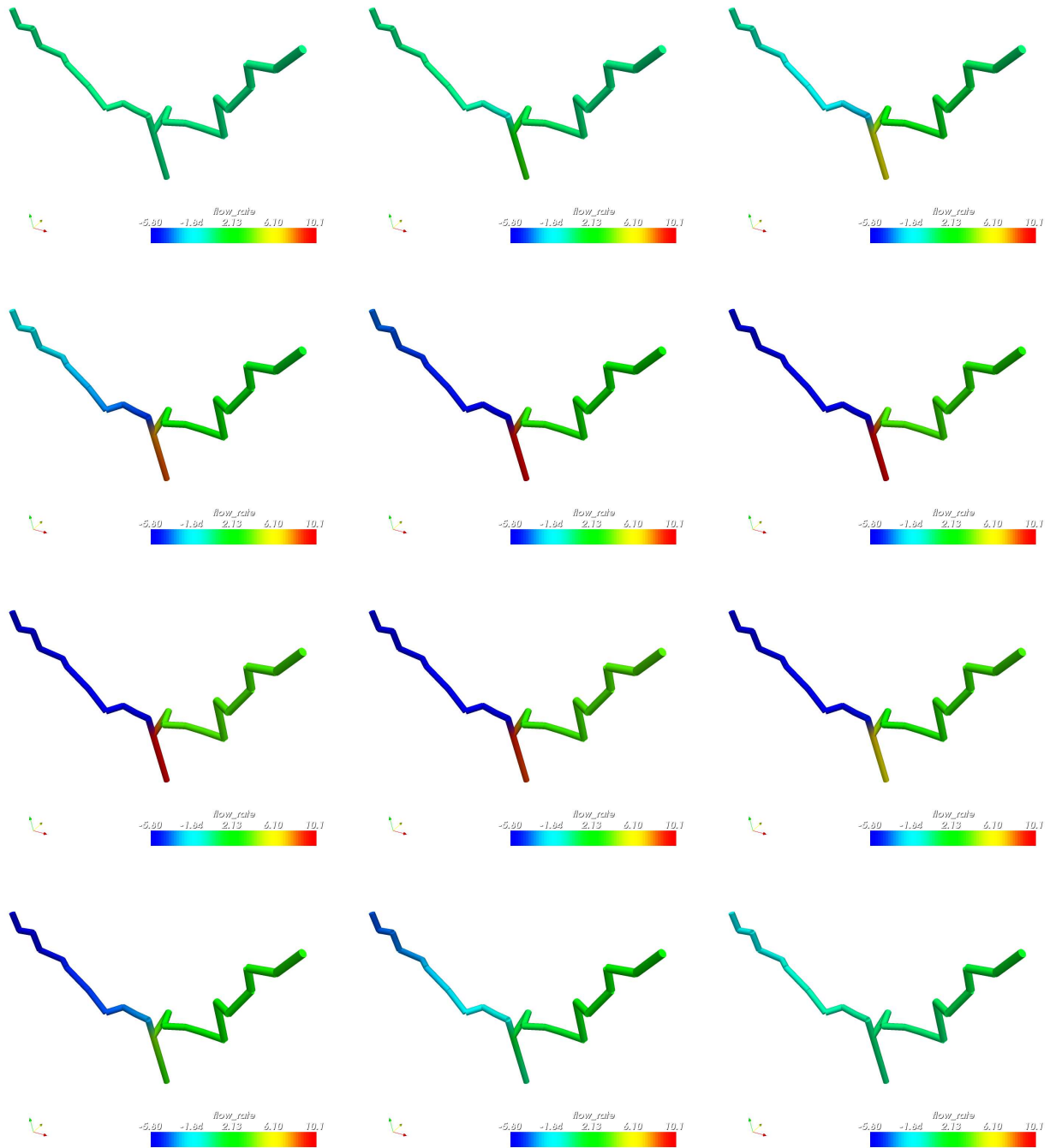


Figure 6.14: From left to right and from top to bottom: snapshots of the flow rate [cm s^{-1}] on the arterial tree at times $t_n = 0.05n$ sec, for $n = 0, 1, 2, \dots, 11$. Notice that due to the “inverse” orientation of the left branch, its flow rate has the opposite sign of the flow rate in the other branches.

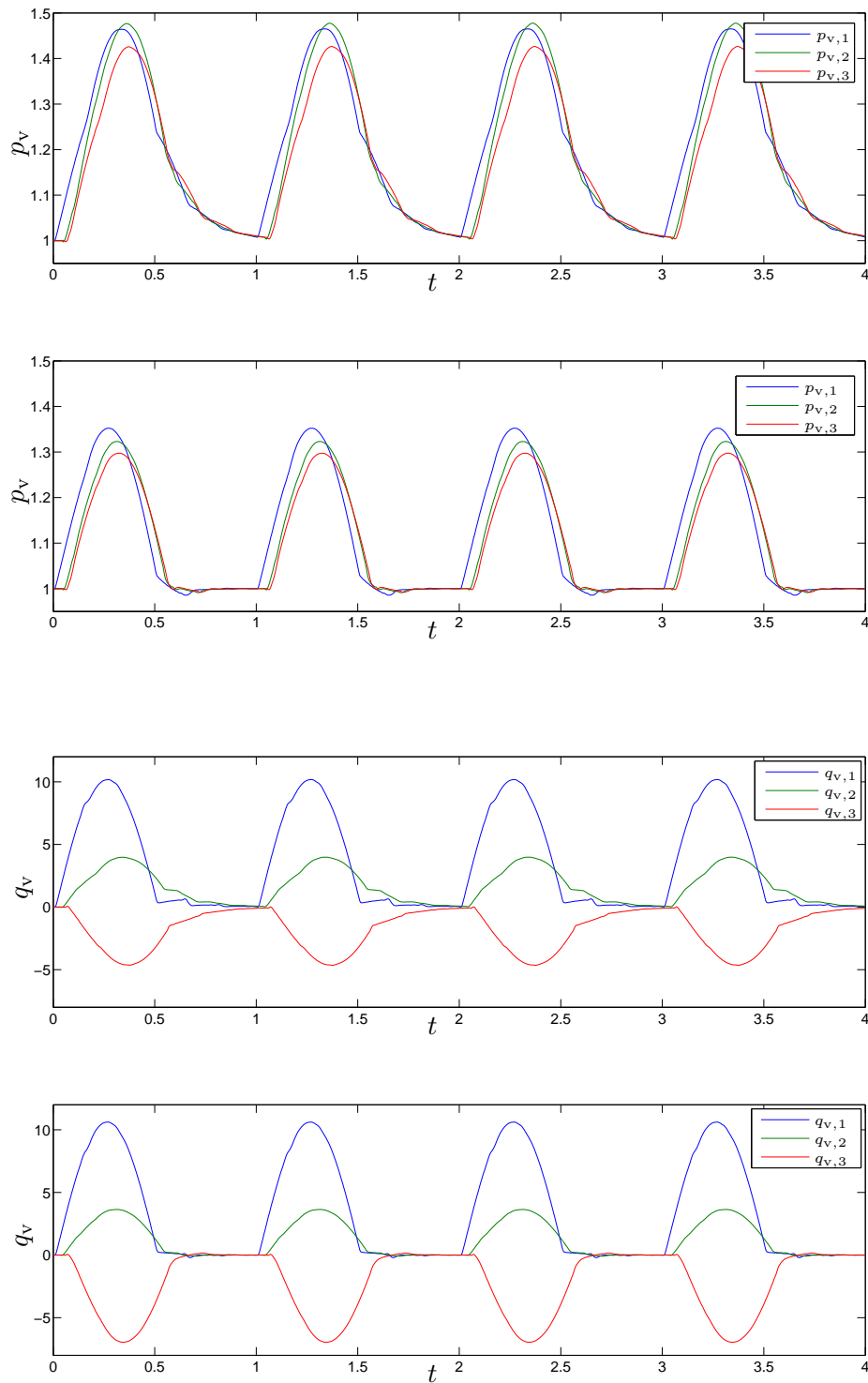


Figure 6.15: Time courses of pressure [kPa] and flow rate [cm s^{-1}] in the middle points of each branch. For each variable, simulation results are reported for both conducting loads (top; notice the presence of reflected waves) and non-reflecting boundary conditions (bottom) at end points B_2 , B_3 .

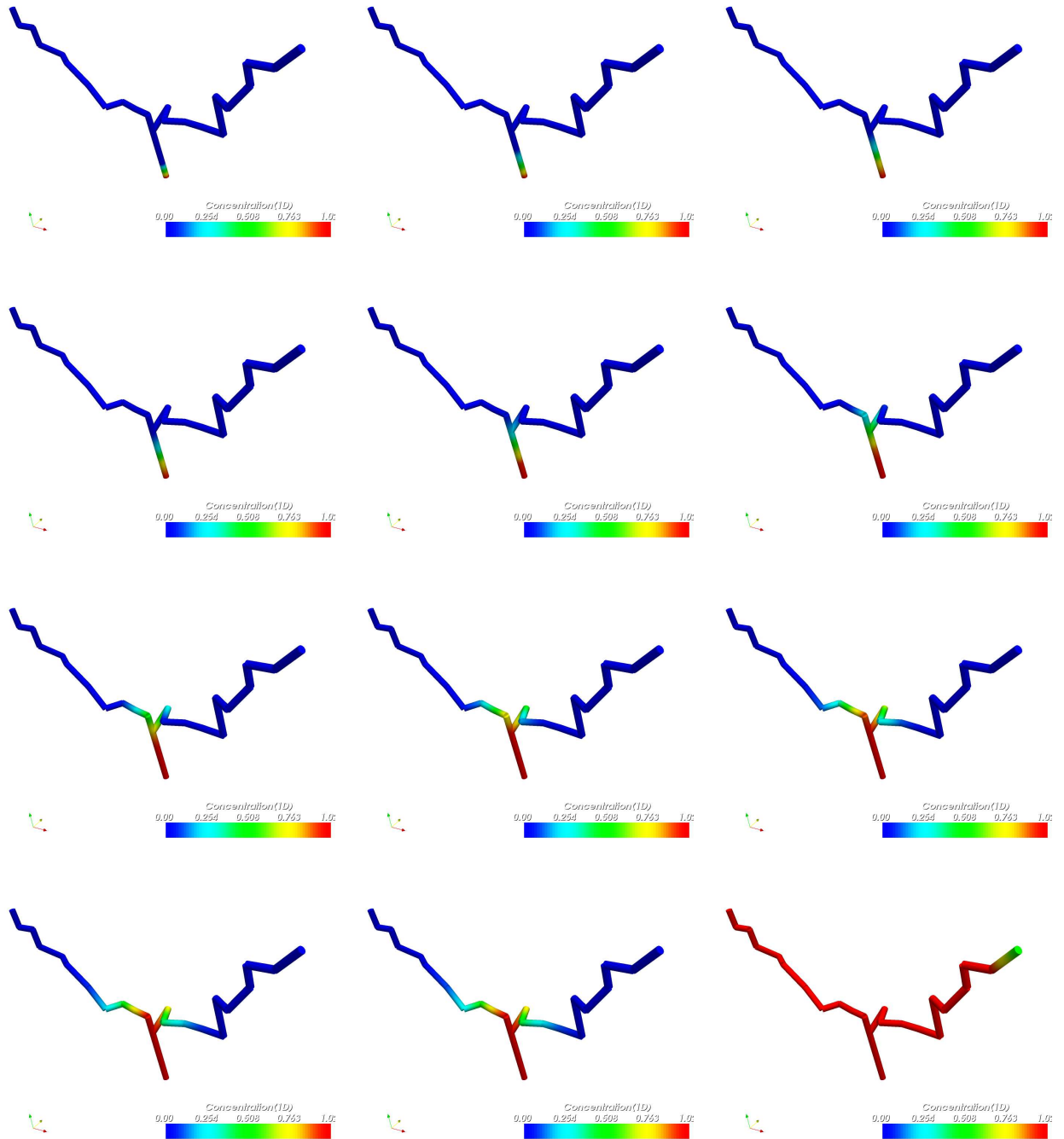


Figure 6.16: From left to right and from top to bottom: snapshots of the concentration at times $t = 0.05$ s, 0.10 s, 0.15 s, ..., 0.55 s, and at $t = 4$ s.

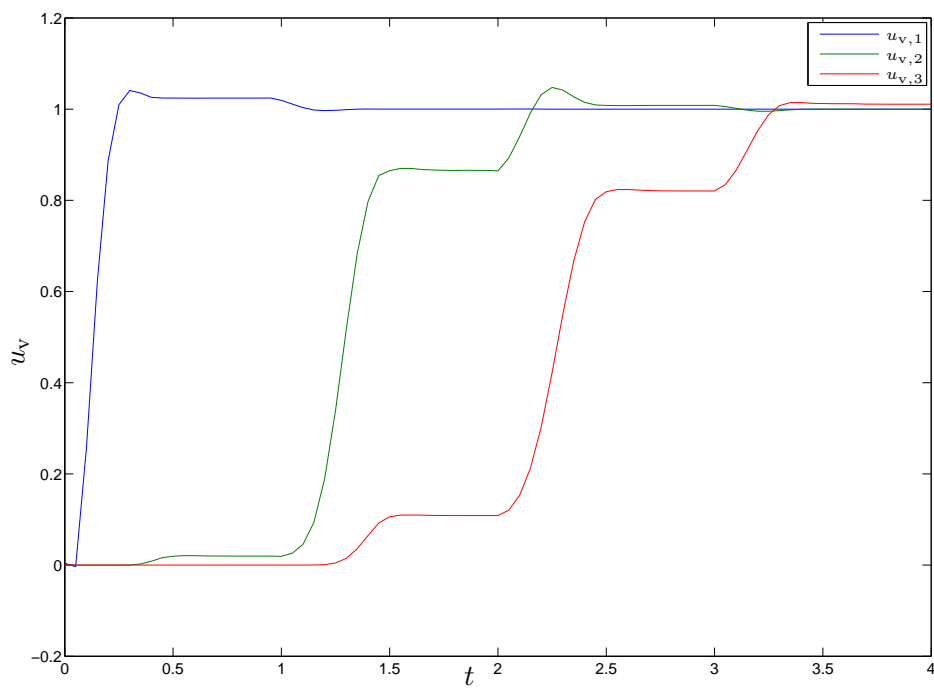


Figure 6.17: Time course of the concentration in the middle points of each branch: the “steps” are corresponding to the heart beats.

6.6.2 3D-1D simulations of blood flow and mass transport

In this section we discuss the simulation of multiscale 3D-1D problems introduced in section 6.5: we are thus considering a situation similar to that depicted in fig. 6.2. In particular, we will consider the simple case of the 1D vessel bifurcation of the previous sections, as an arterial tree embedded in a 3D cylindrical tissue region. We will describe how it is possible to build the 1D mesh as an *edge path* in the 3D one, using available data on the vessel geometry; further, we will perform simulations for the coupled problem and discuss the results.

Path extraction algorithms

The 3D tissue mesh is our starting point for medical applications of models presented in this chapter: the tissue geometry is usually simple, whereas the mesh of a complex 1D vascular network, even though one-dimensional, needs an automatic acquisition method. The geometrical data concerning this network are usually acquired by *imaging*, since it is relatively easy (see sec. 6.4.2, 6.4.3 for some examples) to analyze an image and get a *list of points* representing the skeleton of the vascular structures, with an arbitrary resolution (we have shown in the cited examples that in principle vessels may be described by *splines*). The question is whether this list of points can be employed to *automatically* build the 1D mesh approximating the skeleton of the vascular structures, as a *path of edges of the given 3D mesh*: if this is possible, then we can take advantage of the methods for the finite element approximation of coupled 3D-1D problems that we have described in chapter 5.

We have found that such a task can be done automatically. We are not aware of any standard algorithm to do that, so we have developed an “in house” method. To describe the algorithm, let us consider the case in which a single curve has to be fitted by a sequence of edges: the multi-vessel case is easily treated by iterating the same procedure.

Let $\mathcal{P} = \{\mathbf{p}_0, \mathbf{p}_1, \dots\}$ be a set of points $\mathbf{p}_i \in \mathbb{R}^3$ lying on the 1D curve we are considering, and represented by the blue line in fig. 6.18. As we said, we consider a set of points rather than an analytic parametrization because it is the simplest format of data that we can get from segmentation of images.

No assumption about the ordering of \mathcal{P} is made: we only require that \mathbf{p}_0 is one of the two end points, and that the direction from \mathbf{p}_0 to the other end point is assumed to be the positive orientation on the given curve. The goal is to find a sequence $\mathcal{X} = \{\mathbf{x}_0, \mathbf{x}_1, \dots, \mathbf{x}_N\}$ of neighboring nodes of a given 3D mesh, such that the piecewise linear curve given by the edge path associated to \mathcal{X} is “as close as possible” to the set of points \mathcal{P} . We denote by \mathcal{N} the set of the nodes of the 3D mesh, by \mathcal{E} the set of edges (edges are denoted by $[\mathbf{x}, \mathbf{y}]$, where $\mathbf{x}, \mathbf{y} \in \mathcal{N}$), and by σ a fixed number in $(0, 1)$. Our algorithm reads as follows.

1. The first node $\mathbf{x}_0 \in \mathcal{N}$ is chosen such that

$$\|\mathbf{x}_0 - \mathbf{p}_0\| = \min_{\mathbf{x} \in \mathcal{N}} \|\mathbf{x} - \mathbf{p}_0\|,$$

Set $n = 0$, $\mathcal{P}_0 = \mathcal{P}$, $\mathcal{U}_0 = \emptyset$.

2. Find the following subset \mathcal{U}_{n+1} of the nodes that share an edge with \mathbf{x}_n :

$$\mathcal{U}_{n+1} = \{\mathbf{y} \in \mathcal{N} : [\mathbf{y}, \mathbf{x}_n] \in \mathcal{E}\},$$

and define

$$h_{\max} = \max_{\mathbf{y} \in \mathcal{U}_{n+1}} \|\mathbf{y} - \mathbf{x}_n\|, \quad h_{\min} = \min_{\mathbf{y} \in \mathcal{U}_{n+1}} \|\mathbf{y} - \mathbf{x}_n\|,$$

$$\mathcal{D}_{n+1} = \{\mathbf{p} \in \mathcal{P}_n : \sigma h_{\min} < \|\mathbf{p} - \mathbf{x}_n\| < h_{\max}\}.$$

3. If $\mathcal{D}_{n+1} = \emptyset$, end. Otherwise, find the next node \mathbf{x}_{n+1} by solving

$$\text{dist}(\mathbf{x}_{n+1}, \mathcal{D}_{n+1}) = \min_{\mathbf{x} \in \mathcal{U}_{n+1} \setminus \mathcal{U}_n} \text{dist}(\mathbf{x}, \mathcal{D}_{n+1}).$$

4. Define

$$\mathcal{P}_{n+1} = \{\mathbf{p} \in \mathcal{P}_n : h_{\max} < \|\mathbf{p} - \mathbf{x}_n\|\},$$

then set $n \leftarrow (n + 1)$ and go back to step 2.

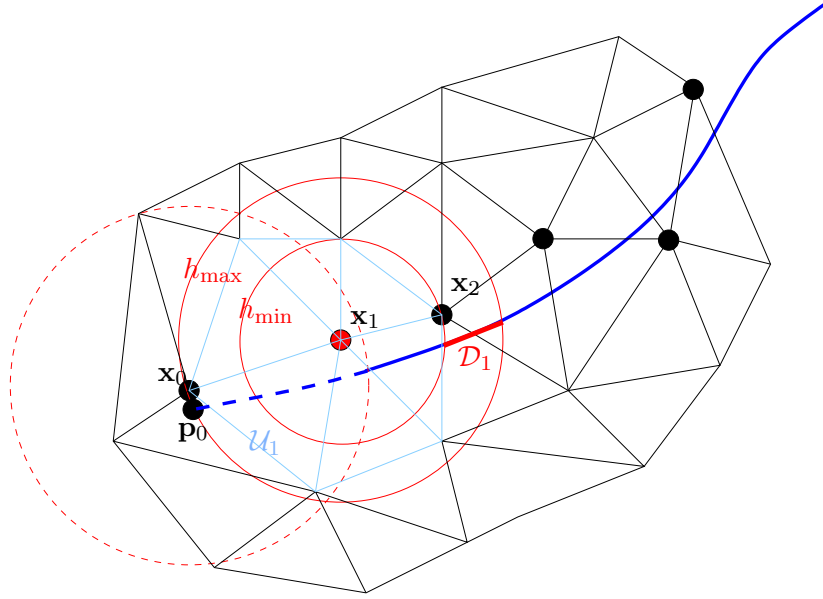


Figure 6.18: The path extraction algorithm at work.

We will call this algorithm the “rubber’s algorithm”: when a new node \mathbf{x}_n is extracted, the points inside a h_{\max} -neighborhood of that node are eliminated from the list (step n. 4). In practice, the set of points \mathcal{P}_n is shortening while n increases, as if a rubber (represented in fig. 6.18 by the dashed circle) was erasing points starting from a neighborhood of \mathbf{p}_0 , moving toward the other end point of the line every time n is incremented (the $n = 1$ iteration is represented; the erased points are depicted as the blue dashed part of \mathcal{P}). When all the points are erased, the algorithm ends. In this manner, the sequence of nodes moves starting from the closest node to \mathbf{p}_0 , according to the positive orientation of the line, keeping close to it (closer than the mesh size). We also point out that in step n. 3, we minimize the distance for $\mathbf{x} \in \mathcal{U}_{n+1}$, discarding the nodes in \mathcal{U}_n : with this choice, the edge path is such that two consecutive edges belong to different elements of the 3D mesh, which makes the path smoother.

We found that, if \mathcal{P} is a subset of the volume enclosed by the 3D mesh, then the proposed algorithm is able to correctly build a sequence \mathcal{X} such that the associated edge path is a “good” approximation of \mathcal{P} , the distance between the path and \mathcal{P} being less than the 3D mesh size h . The value of parameter σ we used in our codes was always 0.9. In fig. 6.19 the path extracted for a 3-vessels configuration is shown: the 1D mesh is extracted from a 3D cylindrical mesh enclosing the data points. This mesh is actually the one we used for the test cases of the previous sections. Further in this chapter we will consider other examples in which more complex arterial networks are successfully extracted by the same algorithm.

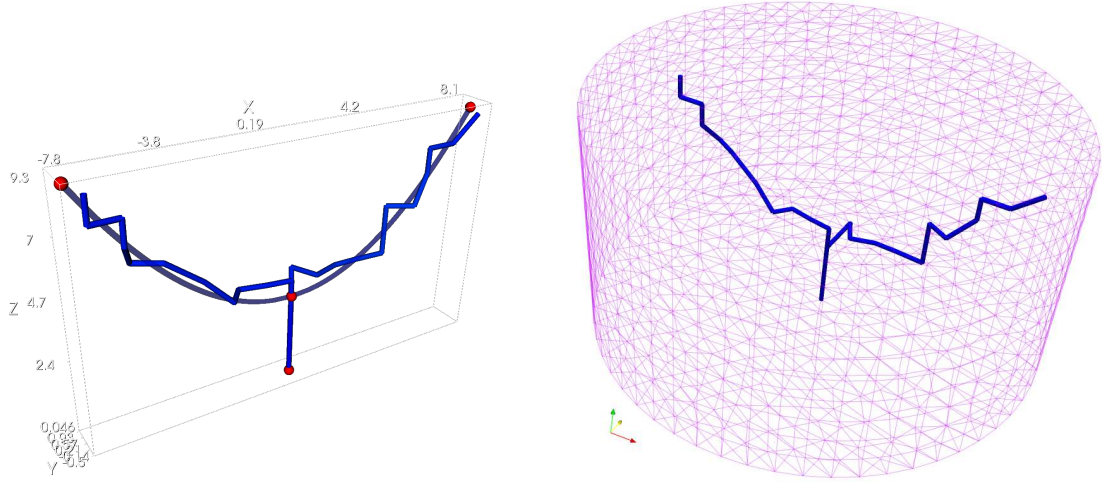


Figure 6.19: An example of extracted path for a branching vessel. On the left, the data points \mathcal{P} are given on the smooth semi-transparent curves (end points of each vessel have been marked in red); the edge paths are reported as well. On the right, the surface wireframe of the cylindrical 3D mesh used for the extraction is shown.

Numerical approximation

The numerical approximations of the 3D- $\frac{1}{2}$ D blood flow (BF) problem 6.5.1, 3D-1D BF problem 6.5.2, and 3D-1D mass transport (MT) problem 6.5.3, are achieved by applying a finite difference discretization in time (for example implicit/explicit Euler schemes) and a finite element discretization in space. To this end, we can take advantage of the previous studies on the finite element discretization of coupled 3D-1D problems (chapter 5); moreover, we will consider branching 1D geometries instead of a single vessel, thanks to the treatment of the 1D equations on trees we have discussed in this section.

In particular, we will assume all hypotheses of chapter 5, and consider the finite element space V_h defined by (5.1) for the tissue domain Ω , and the inherited space \hat{V}_h defined by (5.13) for the vessel domain Λ . We assume $\Lambda = \bigcup_{I_k \in \mathcal{I}_h} I_k$, where \mathcal{I}_h is a collection of edges of tetrahedra of the “triangulation” \mathcal{T}_h . They are both \mathbb{P}^1 spaces.

In order to fix the ideas, we shall consider simple boundary conditions; of course there are many other possible choices, for instance non-reflecting conditions for the 1D model; nevertheless this will help to make more clear our exposition. In this regard, as in section 6.6.1, we will assume that Λ is a tree with $M + 1$ end points, denoted by B_0, B_1, \dots, B_M . Branches of Λ will be denoted by Λ_i , and their length by L_i . Functions $f : \Lambda \rightarrow \mathbb{R}$ are parametrized on the i -th branch by the curvilinear abscissa $s \in [0, L_i]$. For the sake of simplicity, we also assume that a) for $i = 0, \dots, M$, the branch Λ_i is the one that contains B_i , and b) the positive direction on branch Λ_0 is the one *from* B_0 , while the positive direction on branch Λ_i , $i = 1, \dots, M$, is *toward* B_i . As we have seen, there are “internal” boundary conditions at the branching points as well, but we know how to naturally enforce them by the variational formulation; hence, the only conditions we have to impose explicitly are those at the end points B_i . We will consider the conditions reported in tab. 6.3.

In particular, for the 3D problems we impose that the flux across the boundary of the tissue domain is zero; for the 1D problems, we impose the value of flow rate/concentration at B_0 while using standard

	BF	MT
3D	homogeneous Neumann	homogeneous Neumann
1D	$q_v = q_{\text{in}}(t)$ at B_0 ; conductive loads G_i at $B_i, i > 0$: $q_v(B_i) = G_i(p_v(B_i) - p_{e,i})$	$u_v = u_{\text{in}}(t)$ at B_0 ; homogeneous Neumann at $B_i, i > 0$

Table 6.3: Boundary conditions considered for the configuration of a 1D arterial tree embedded in a 3D tissue.

Robin or Neumann conditions for the “outlets” $B_i, i > 0$. Depending on how many Dirichlet conditions we will have, besides spaces \hat{V}_h and \hat{W}_h defined respectively in (6.53) and (6.64), we will need to consider space

$$\hat{V}_{h,0} = \{f \in \hat{V}_h : f(B_0) = 0\},$$

as well as the “fully homogeneous spaces”

$$\hat{V}_{h,00} = \{f \in \hat{V}_h : f(B_i) = 0, i = 1, \dots, M\}, \quad \hat{W}_{h,00} = \{f \in \hat{W}_h : f(B_i) = 0, i = 1, \dots, M\}.$$

Let $\Delta t > 0$ be the time step; for $n \in \mathbb{N}$, set $t_n = n\Delta t$, and denote by $p_t^{(n)}, p_v^{(n)}, q_v^{(n)}$ respectively the approximation of the tissue blood pressure, vessel blood pressure and vessel flow rate at time t_n . Similarly, let $u_t^{(n)}, u_v^{(n)}$ be respectively the approximation of the tissue and the vessel concentration at time t_n . Symbols $(\cdot, \cdot)_\Omega$ and $(\cdot, \cdot)_\Lambda$ will denote respectively the L^2 scalar product on the tissue domain Ω and on the vessel domain Λ .

We will state the numerical approximation schemes distinguishing between three cases.

3D- $\frac{1}{2}$ D BF problem. Consider problem 6.5.1, with boundary conditions as in tab. 6.3. The fully discrete, backward Euler numerical approximation scheme reads:

Problem 6.6.1. Find $p_t^{(n)} \in V_h$ and $p_v^{(n)} \in \hat{V}_h, n \in \mathbb{N}$, such that

$$\begin{aligned} & \frac{1}{\Delta t} (C_t p_t^{(n+1)}, \psi)_\Omega + (K_t \nabla p_t^{(n+1)}, \nabla \psi)_\Omega + (\alpha p_t^{(n+1)}, \psi)_\Omega + (\beta_p \bar{p}_t^{(n+1)}, \psi)_\Lambda - (\beta_p p_v^{(n+1)}, \psi)_\Lambda \\ & = \frac{1}{\Delta t} (C_t p_t^{(n)}, \psi)_\Omega + (f_p, \psi)_\Omega \quad \forall \psi \in V_h, \\ & \frac{1}{\Delta t} (C_v p_v^{(n+1)}, \hat{\psi})_\Lambda + (K_v \frac{d}{ds} p_v^{(n+1)}, \frac{d}{ds} \hat{\psi})_\Lambda + (\beta_p p_v^{(n+1)}, \hat{\psi})_\Lambda - (\beta_p \bar{p}_t^{(n+1)}, \hat{\psi})_\Lambda + b_v(p_v^{(n+1)}, \hat{\psi}) \\ & = \frac{1}{\Delta t} (C_v p_v^{(n)}, \hat{\psi})_\Lambda + q_{\text{in}}(t_n) \hat{\psi}(B_0) + \sum_{i=1}^M G_i p_{e,i} \hat{\psi}(B_i) \quad \forall \hat{\psi} \in \hat{V}_h, \end{aligned}$$

where $\beta_p = 2\pi R L_p$, b_v is a bilinear form depending on boundary conditions at points B_i :

$$b_v(p_v^{(n)}, \hat{\psi}) = \sum_{i=1}^M G_i p_v^{(n)}(B_i) \hat{\psi}(B_i),$$

and where $p_t^{(0)}, p_v^{(0)}$, are given as initial conditions.

The backward Euler scheme is unconditionally stable, so there are no restrictions in the form of upper bounds on the choice of the time stepping. Notice that at each time step, problem 6.6.1 requires to solve a linear system that has the same block structure considered in chap. 5.

A forward Euler scheme is also a possible choice, that has the advantage of decoupling the tissue and the vessel subproblems. However, we point out that since the degrees of freedom of the 1D problem are usually much less than those of the 3D one, there is usually no significant difference in term of computational costs between solving the coupled problem or solving just the tissue one.

The drawback of the forward scheme is obviously the stability condition on the time step. In this regard, the fact that blood flow in the vessel matrix of the tissue is slow, has a numerical counterpart: the stability condition turns out to be not too restrictive. In practice, the use of the forward scheme is a valid alternative to the backward one.

3D-1D BF problem. Consider problem 6.5.2. In this case, the 1D problem is hyperbolic and characteristic extrapolation is used to provide the “missing” boundary conditions. When considering the situation of tab. 6.3, we can use the pressure extrapolation formula (6.65) at B_0

$$p_{\text{ex},0}(p^{(n)}, q^{(n)}) = p_0^{(n)} \left(\frac{\Delta t}{\sqrt{cl}} \right) + \sqrt{\frac{l}{c}} \left[(1 + 2r\Delta t)q_{\text{in}}(t + \Delta t) - q_0 \left(t, \frac{\Delta t}{\sqrt{cl}} \right) \right].$$

where the subscript i means the restriction to the i -th branch (for example, $p_i^{(n)} = p_{|\Lambda_i}^{(n)}$), so that the use of the curvilinear abscissa as argument is possible. Similarly, extrapolation formula (6.67) is employed at end points B_i , $i = 1, \dots, M$:

$$p_{\text{ex},i}(p_i^{(n)}, q_i^{(n)}) = \left[1 + \sqrt{\frac{l}{c}} G_i (1 + 2r\Delta t) \right]^{-1} \left[p_i^{(n)} \left(L_i - \frac{\Delta t}{\sqrt{cl}} \right) + \sqrt{\frac{l}{c}} \left(q_i^{(n)} \left(L_i - \frac{\Delta t}{\sqrt{cl}} \right) + (1 + 2r\Delta t) G_i p_{e,i} \right) \right].$$

We propose, for the 1D hyperbolic part, the scheme (6.69) introduced in section 6.6.1. Although this scheme is fully implicit and unconditionally stable, we are interested in capturing the wave propagation in the 1D domain: this will require a small time step. On the other hand, we could avoid to use such a fine time discretization for the tissue problem, that features slower dynamics. Therefore, we propose a *multirate* numerical approximation scheme. Multirate schemes have been introduced for dynamical systems in which a partitioning in “slow” and “fast” variables is possible, see for example [4], [32]. They have been applied first for the simulation of MOS circuits and other complex electronic systems; and similar *multiple time-stepping* methods have been used in molecular dynamics. In our case, for each (slow) step of the 3D problem, we consider m (fast) substeps of the 1D problem, with a steplength $\Delta t' = \Delta t/m$.

Problem 6.6.2. Let $m \in \mathbb{N}$, $m > 0$, and $\Delta t' = \frac{1}{m}\Delta t$. Denote by $[t]$, $t \in \mathbb{R}$, the greatest integer $\leq t$. Find $p_v^{(n')} \in \hat{V}_h$, $q_v^{(n')} \in \hat{W}_h$ and $p_t^{(n)} \in V_h$, $n', n \in \mathbb{N}$, such that

$$\begin{aligned} \frac{1}{\Delta t'} (cp_v^{(n'+1)}, \hat{\psi})_\Lambda - (q_v^{(n'+1)}, \frac{d}{ds} \hat{\psi})_\Lambda + (\beta_p p_v^{(n'+1)}, \hat{\psi})_\Lambda &= \frac{1}{\Delta t'} (cp_v^{(n')}, \hat{\psi})_\Lambda + (\beta_p \bar{p}_t^{([n'/m])}, \hat{\psi})_\Lambda \quad \forall \hat{\psi} \in \hat{V}_{h,00}, \\ \frac{1}{\Delta t'} (lq_v^{(n'+1)}, \hat{\varphi})_\Lambda + (\frac{d}{ds} p_v^{(n'+1)}, \hat{\varphi})_\Lambda + (rlq_v^{(n'+1)}, \hat{\varphi})_\Lambda &= \frac{1}{\Delta t'} (lq_v^{(n')}, \hat{\varphi})_\Lambda \quad \forall \hat{\varphi} \in \hat{W}_{h,00}, \\ \frac{1}{\Delta t} (C_t p_t^{(n+1)}, \psi)_\Omega + (K_t \nabla p_t^{(n+1)}, \nabla \psi)_\Omega + (\alpha p_t^{(n+1)}, \psi)_\Omega + (\beta_p \bar{p}_t^{(n+1)}, \psi)_\Lambda \\ &= \frac{1}{\Delta t} (C_t p_t^{(n)}, \psi)_\Omega + (\beta_p p_v^{((n+1)m)}, \psi)_\Lambda + (f_p, \psi)_\Omega \quad \forall \psi \in V_h, \end{aligned}$$

satisfying

$$\begin{aligned} p_v^{(n'+1)}(B_0) &= p_{\text{ex},0}(p_v^{(n')}, q_v^{(n')}), & q_v^{(n'+1)}(B_0) &= q_{\text{in}}(t_{(n'+1)/M}), \\ p_v^{(n'+1)}(B_i) &= p_{\text{ex},i}(p_v^{(n')}, q_v^{(n')}), & q_v^{(n'+1)}(B_i) &= G_i(p_v^{(n'+1)}(B_i) - p_{e,i}) \quad (i = 1, \dots, M), \end{aligned}$$

and where $p_t^{(0)}$, $p_v^{(0)}$ and $q_v^{(0)}$ are given as initial conditions.

This algorithm is decoupled into two implicit sub-schemes: first we advance by m micro-steps of the 1D problem, using the last computed 3D solution, then we advance by one macro-step of the 3D problem using the last computed 1D solution: in particular, a time splitting of the coupling term is considered. Of course we could have considered the explicit versions of both the sub-schemes. In this case Δt and $\Delta t'$ would have to fulfill stability conditions, the most restrictive one being on $\Delta t'$, in the form of a CFL condition $\Delta t' \lesssim Ch$, where h is the mesh size, and $0 < C \leq \sqrt{cl}$ (constant C is typically small, or, in other words, the pulse velocity in the 1D vessel is large). Nevertheless, this is not a critical point: since the 1D subproblem requires by far less computational resources than the 3D one, we can take advantage of a large ratio m between the two steplength to keep the CPU time within reasonable ranges.

3D-1D MT problem. Consider problem 6.5.3, with the vessel transport equation in the form (6.44). We are going to introduce a fully discrete, SUPG stabilized, backward Euler numerical approximation scheme. To this end, we define some parameters, obtained by solving the BF problem; first of all the tissue blood velocity, the tissue perfusion and the vessel blood flow rate at time t_n :

$$\mathbf{v}^{(n)} = -\frac{1}{n_b} K_t \nabla p_t^{(n)}, \quad \omega_t^{(n)} = \alpha p_t^{(n)} - f_p, \quad q^{(n)} = \begin{cases} -K_v \frac{d}{ds} p_v^{(n)} & \text{with the } \frac{1}{2}\text{D BF model,} \\ q_v^{(nm)} & \text{with the 1D BF model,} \end{cases} \quad (6.74)$$

then the exchange coefficient

$$\beta_u = 2\pi R L u, \quad (6.75)$$

and finally the SUPG bilinear forms (see [85, sec. 14.3.2]), that, when using \mathbb{P}^1 finite elements for the concentrations and test functions, and \mathbb{P}^0 elements for velocity and flow rate, read as follow:

$$\begin{aligned} a_{\text{stab},t}(u, \psi; \mathbf{v}) &= \delta_t \sum_{T \in \mathcal{T}_h} \left(\frac{1}{\Delta t} u + \mathbf{v} \cdot \nabla u + \omega_t u, \frac{h_T}{|\mathbf{v}|} \mathbf{v} \cdot \nabla \psi \right)_T, \\ b_{\text{stab},t}(u, \psi; \mathbf{v}) &= \delta_t \sum_{T \in \mathcal{T}_h} \left(\frac{1}{\Delta t} u + f_u, \frac{h_T}{|\mathbf{v}|} \mathbf{v} \cdot \nabla \psi \right)_T, \\ a_{\text{stab},v}(\hat{u}, \hat{\psi}; q) &= \delta_v \sum_{I \in \mathcal{I}_h} \left(\frac{1}{\Delta t} \hat{u} + q \frac{d}{ds} \hat{u}, \frac{h_I}{|q|} q \frac{d}{ds} \hat{\psi} \right)_I, \\ b_{\text{stab},t}(\hat{u}, \hat{\psi}; q) &= \delta_v \sum_{I \in \mathcal{I}_h} \left(\frac{1}{\Delta t} \hat{u} + f_u, \frac{h_I}{|q|} q \frac{d}{ds} \hat{\psi} \right)_I, \end{aligned} \quad (6.76)$$

where δ_t and δ_v are positive stabilization parameters, and h_T and h_K are the diameter of the tetrahedron T and the segment I , respectively. The stabilization parameters can be constant, or dynamically computed in an adaptive fashion [100].

The scheme we propose reads:

Problem 6.6.3. Find $u_t^{(n)} \in V_h$ and $u_v^{(n)} \in \hat{V}_h$, $n \in \mathbb{N}$, such that $u_v^{(n)}(B_0) = u_{\text{in}}(t_n)$, and

$$\begin{aligned} & \frac{1}{\Delta t} (u_t^{(n+1)}, \psi)_\Omega + (D_t \nabla u_t^{(n+1)}, \nabla \psi)_\Omega + (\mathbf{v}^{(n+1)} \cdot \nabla u_t^{(n+1)}, \psi)_\Omega + (\omega_t^{(n+1)} u_t^{(n+1)}, \psi)_\Omega \\ & \quad + (\beta_u \bar{u}_t^{(n+1)}, \psi)_\Lambda - (\beta_u u_v^{(n+1)}, \psi)_\Lambda + a_{\text{stab},t}(u_t^{(n+1)}, \psi; \mathbf{v}^{(n+1)}) \\ & = \frac{1}{\Delta t} (u_t^{(n)}, \psi)_\Omega + (f_u, \psi)_\Omega + b_{\text{stab},t}(u_t^{(n)}, \psi; \mathbf{v}^{(n+1)}) \quad \forall \psi \in V_h, \\ & \frac{1}{\Delta t} (A_0 u_v^{(n+1)}, \hat{\psi})_\Lambda + (D_v \frac{d}{ds} p_v^{(n+1)}, \frac{d}{ds} \hat{\psi})_\Lambda + (q^{(n+1)} \frac{d}{ds} u_t^{(n+1)}, \psi)_\Lambda + a_{\text{stab},v}(u_v^{(n+1)}, \hat{\psi}; q^{(n+1)}) \\ & = \frac{1}{\Delta t} (A_0 u_v^{(n)}, \hat{\psi})_\Lambda + b_{\text{stab},v}(u_v^{(n)}, \hat{\psi}; q^{(n+1)}) \quad \forall \hat{\psi} \in \hat{V}_{h,0}, \end{aligned}$$

where $u_t^{(0)}, u_v^{(0)}$, are given as initial conditions.

This is a fully implicit scheme: again, at each time step we have to solve a linear system with a block structure similar to (5.18).

6.6.3 An example of numerical simulation of BF and MT problems for a vessel tree - tissue configuration

In this section, a numerical simulation of blood flow (BF) and mass transport (MT) in a simple case of vessel-tissue system is presented. In particular, we address problem 6.6.2 for BF and problem 6.6.3 for MT.

We consider the geometry of fig. 6.19: here the tissue domain is a cylinder with a radius of 10 cm and a height of 10 cm, while the vessel domain is an arterial tree with one bifurcation (the parameters of the three branches are those of tab. 6.2). The volume of the tissue domain is $V = 3141$ ml.

We assume that the mean blood flow rate entering in the vessel is $2Q$, being $Q = 3.47$ ml s⁻¹ the flow rate provided to the tissue, while the other half of the blood leaves the system by the vessel outlets: the mean tissue perfusion is thus $1.2 \cdot 10^{-3}$ ml of blood per ml of tissue. Concerning the tissue domain, we consider a porosity $n_b = 1/50$ and a tissue permeability $K_t = 1$ cm² kPa⁻¹ s⁻¹, corresponding to flow in a matrix of vessels with diameters of about 0.3 mm (see the calculations in section 6.4.1). The compliance of the tissue is $C_t = 0.01$ kPa⁻¹ (which in the range of values of tab. 6.1). Assuming that the typical values for the vessel and the tissue blood pressure are respectively $p_{0,v} = 1$ kPa and $p_{t,0} = 0.5$ kPa, being the venous pressure set to the reference value $p_0 = 0$ kPa, we can state as a first estimation of the hydraulic conductance $\alpha \simeq Q/(V \cdot p_{t,0}) \simeq 2.2 \cdot 10^{-3}$ kPa⁻¹ s⁻¹. Moreover, we set $f_p = \alpha p_0 = 0$ s⁻¹; as a consequence, the tissue perfusion is $\omega_t = \alpha p_t$.

As regards the vessel-tissue interaction, the conductivity L_p can be estimated in the same manner: for example if $L = 23$ cm is the total length of the arterial tree and $R = 0.5$ cm is a reference radius, assuming

$$2\pi R L_p (p_{0,v} - p_{0,t}) \cdot L \simeq Q$$

then we have $L_p \simeq 96 \cdot 10^{-3}$ cm kPa⁻¹ s⁻¹.

We consider oxygen transport by the blood in the vessel and in the tissue. The blood is entering in the vessel with a oxygen concentration of $u_{v,0} = 8.75$ μmol ml⁻¹. The diffusion coefficient for oxygen is assumed to be $D_v = 5 \cdot 10^{-5}$ cm² s⁻¹ in blood, and $D_t = 1.7 \cdot 10^{-5}$ cm² s⁻¹ in the tissue [77] (tortuosity factor $\lambda^2 = 2.94$). The consumption rate of oxygen in the tissue is 0.06 μmol cm⁻³ s⁻¹; accordingly, we considered a Michealis-Menten law for the metabolic rate

$f_u(u_t) = -0.06 \mu\text{mol cm}^{-3} \text{s}^{-1} \frac{u_t}{u_{1/2} + u_t}$, with $u_{1/2} = \frac{1}{10}u_{t,0}$, being $u_{t,0} = 7.2 \mu\text{mol ml}^{-1}$ a reference value for the blood concentration of oxygen at the microscale (the tissue region). Correspondingly, we set $f_u = f_u(u_t^{(n+1)})$ in problem 6.6.3.

As we observed in section 6.5, the diffusive term L_u is actually a penalization term to enforce the condition $\bar{u}_t(s) = u_v(s)$. In our simulation we considered $L_u = 20 \text{ cm s}^{-1}$, that made this condition sufficiently satisfied.

As initial values for the unknowns, we take $p_{0,v}, p_{0,t}$ for the pressures, $u_{0,v}, u_{0,t}$ for the concentrations; and a zero initial value for blood flow rate in the vessel. Concerning boundary conditions, we will consider those of tab. 6.3, the time average of $q_{\text{in}}(t)$ being equal to $2Q$ (we take the waveform depicted as the dashed line with marks in fig. 6.21). We assume that the conductive loads G_2, G_3 are equal to $10 \text{ cm}^3 \text{ s}^{-1} \text{ kPa}^{-1}$, and that the reference pressures are $p_{e,2} = p_{e,3} = p_{0,v}$.

The simulation we present here spans a time interval of 10 s: the time step is $\Delta t = 0.05 \text{ s}$ for the 3D BF and 1D-3D MT problems, while for the hyperbolic 1D BF problem it is $\Delta t' = 0.001\Delta t$, corresponding to an oversampling factor $m = 1000$ in the multirate scheme 6.6.2. With this choice, both the fast flow in the 1D domain and the slow one in the 3D domain are accurately resolved: moreover, the CPU time of one 3D step and m 1D steps are in the same range. SUPG stabilization terms in eq. (6.76) were $\delta_t = 0.001, \delta_v = 0.4$. In fig. 6.20, the computed pressures from the BF

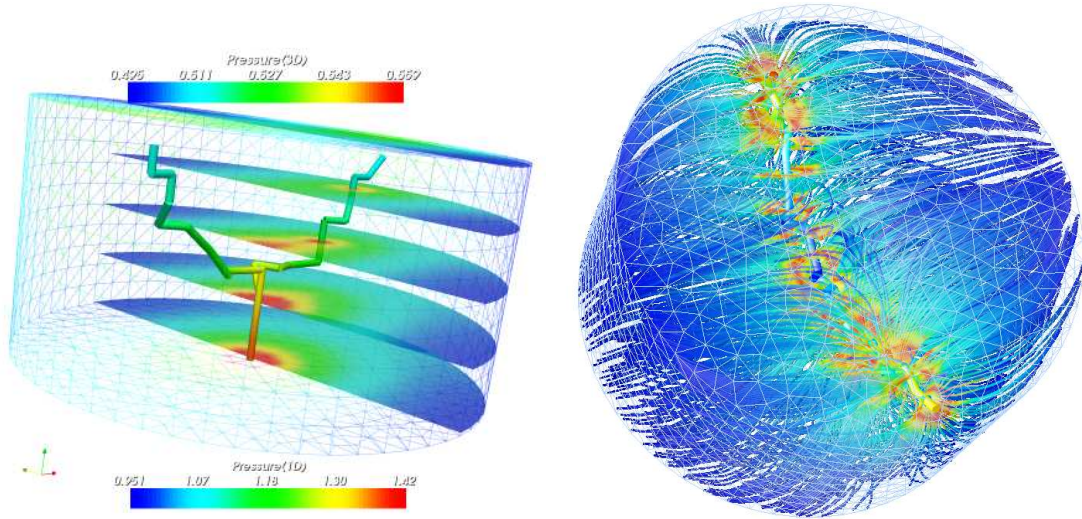


Figure 6.20: On the left: the pressure distribution in the vessel and on some slices of the tissue. On the right: streamlines of blood velocity in the tissue. The fact that streamlines originate from the vessel is due to the *hierarchical* flow from the 1D to the 3D domain.

problem are shown ($t = 5.3 \text{ s}$), as well as the streamlines of the blood velocity in the “capillary” matrix. We see how the geometry of the main vessels determines the flow pattern in the surrounding matrix of small vessels: the blood leakage from the vessel to the tissue causes in turn a pressure fall in the 1D domain. This leakage is emphasized in fig. 6.21, where the time courses of the flow rate at the middle points of each branch are reported, together with mean values. Fig. 6.22 shows the pressures at the same middle points, and the average of \bar{p}_t , that as we know has the meaning of the pressure of blood in the vessel matrix of the tissue “near” the vessel. The gap between the vessel and the tissue pressure, which is about 0.7 kPa on average, sustains the hierarchical flow from the 1D domain to the 3D one. Regarding the MT problem, the advection of the blood oxygen concentration is

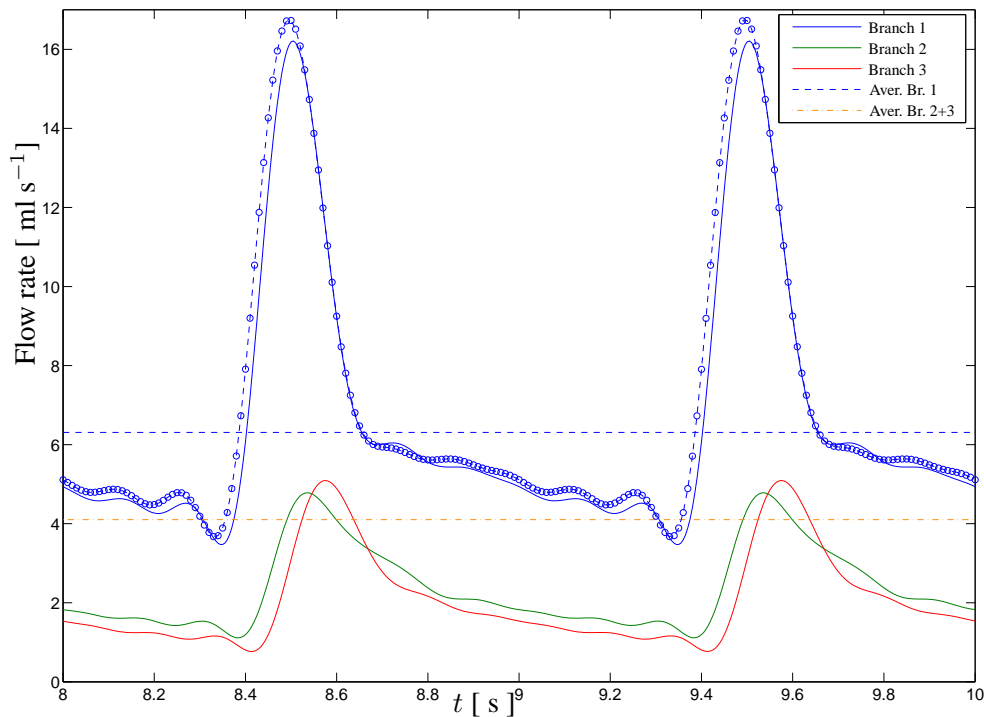


Figure 6.21: Comparison of the (absolute values of) flow rate q_v at the middle points of each branch; the input flow rate $q_{in}(t)$ is represented by the dashed line with marks. We observe that the average flow rate in the first branch is less than the average of the sum of the rates in the remaining branches (mean values are indicated by the dashed line). This gap is due to the transfer of blood from the vessel to the tissue.

shown in fig. 6.23, where an isosurface of u_t is tracked along its temporal evolution. In the figure the vessel concentration u_v is reported as well. Due to the mass transfer to the tissue, the initial and input values of u_v , that are both equal to $8.75 \mu\text{mol ml}^{-1}$, drop to $8.14 \mu\text{mol ml}^{-1}$: this is only partially compensated by the contribution of incoming blood, saturated by oxygen, so that a concentration gradient along the vessel is established after 10 seconds. On the other hand, as concerns the blood oxygen concentration in the tissue, the interplay between the metabolic consumption rate f_u and the supply by the blood coming from the vessel, results in a stationary value, slightly greater than the initial $7.2 \mu\text{mol ml}^{-1}$ concentration, which is about $7.43 \mu\text{mol ml}^{-1}$, as shown in fig. 6.24.

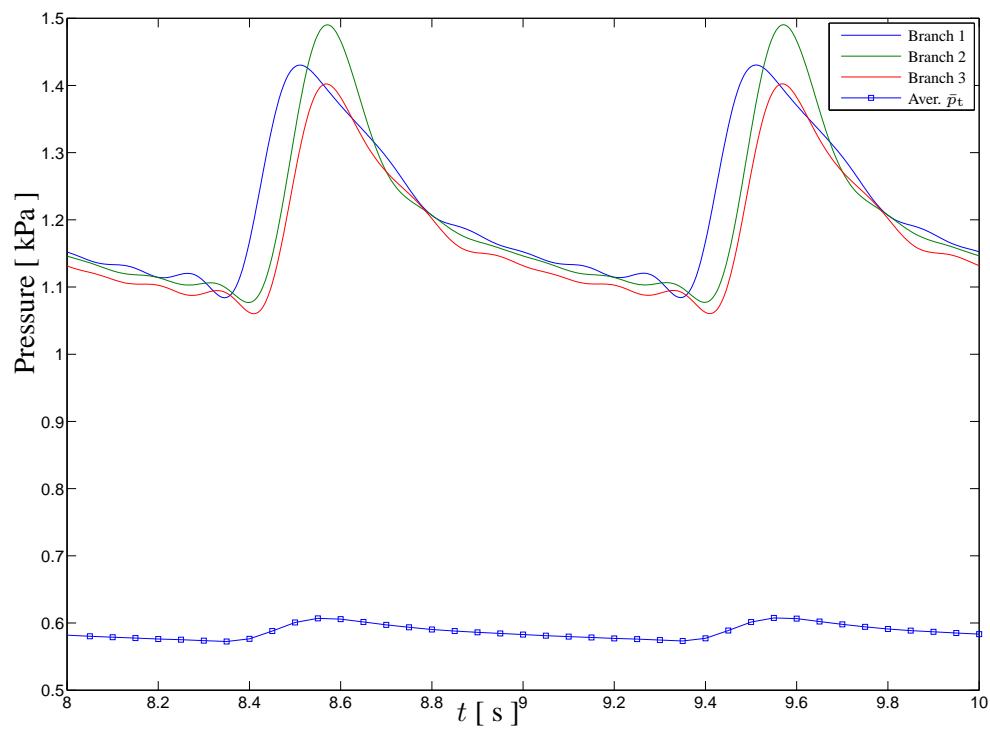


Figure 6.22: Blood pressures p_v at the middle points of each branch, and average value of \bar{p}_t on the vessel (solid line with marks; computed as $\frac{1}{|\Lambda|} \int_{\Lambda} \bar{p}_t(s) ds$). The time step used for the 1D problem is one thousandth of the one used for the 3D problem, so that pulse waves are resolved in the vessel (notice the high-frequency reflected waves).

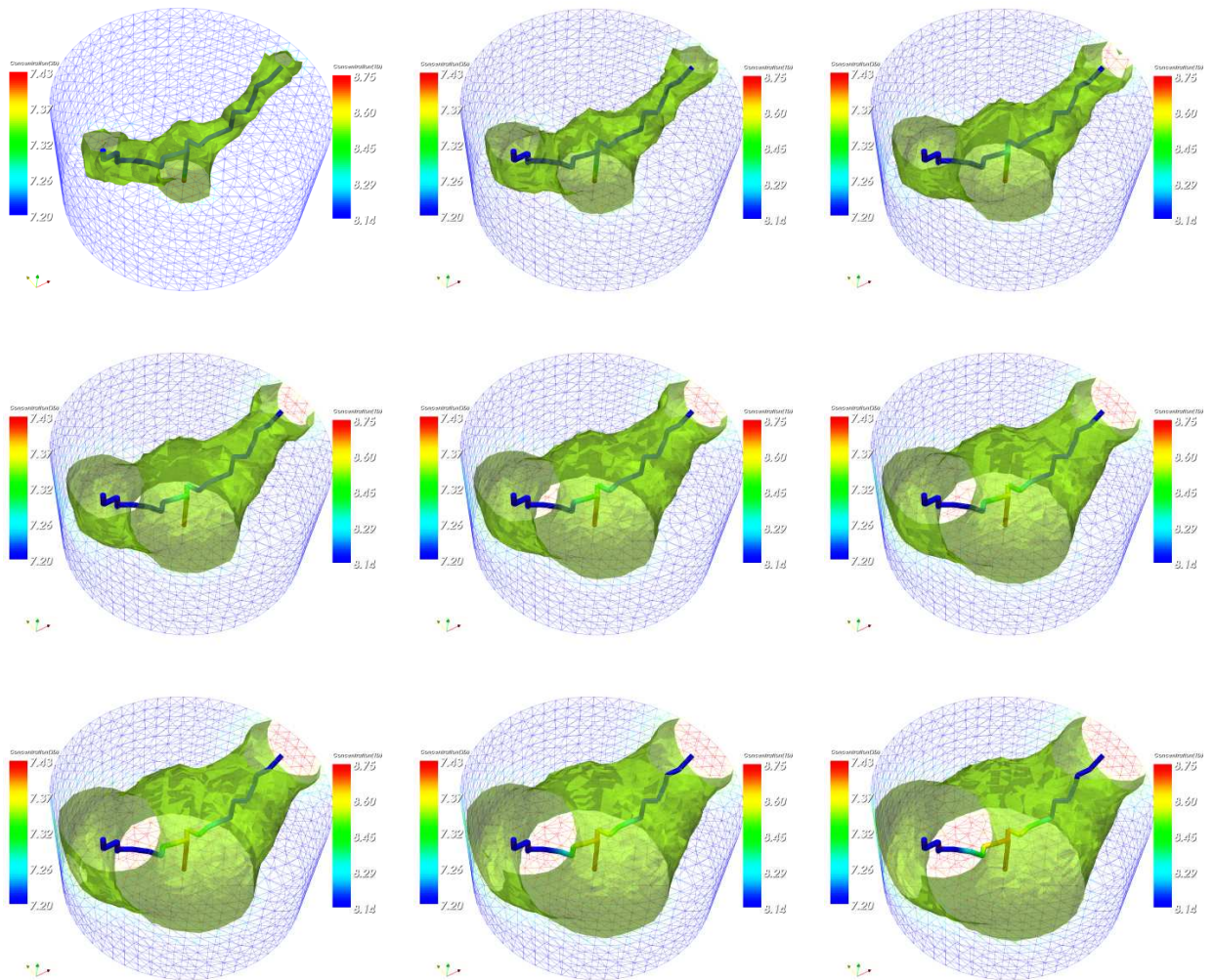


Figure 6.23: From left to right and from top to bottom: snapshots of the blood oxygen concentration in the 1D vessel, and of the $7.3 \mu\text{mol ml}^{-1}$ isosurface of the blood oxygen concentration in the tissue, at times $t = 1 \text{ s}, 2 \text{ s}, \dots, 9 \text{ s}$. The concentration is *transported* in the tissue along the streamlines in fig. 6.20.

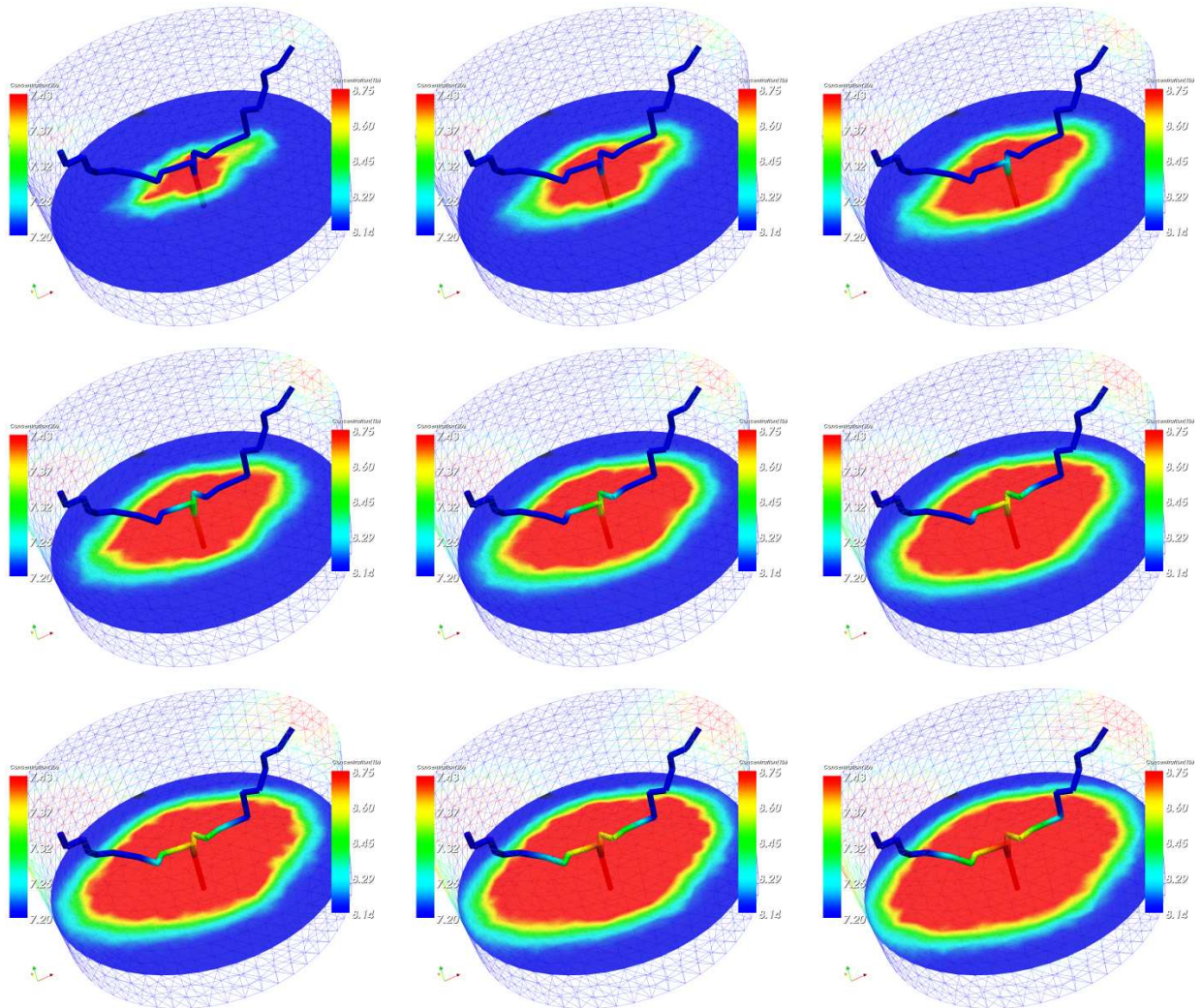


Figure 6.24: From left to right and from top to bottom: snapshots of the blood oxygen concentration in the 1D vessel, and on a slice of the tissue, at times $t = 1$ s, 2 s, \dots , 9 s.

6.6.4 An application to the study of brain perfusion: the Circle of Willis.

One of the most attractive features of a 3D-1D approach to model blood flow and mass transport in tissues, is the easiness of treating *networks* of vessels. The algorithm for “path extraction” described in sec. 6.6.2 allows the automatic generation of the 1D mesh as an edge path in the 3D mesh, also for networks of vessels. The needed geometrical data that have to be provided consist in a list of points describing with a certain resolution the axis of each vessel: this kind of data are easily and quickly acquired by medical images (since there is no need to extract *surfaces*, nor to compute spline *parametrizations*).

In this section, we describe an application to a “real” and physiologically interesting case of tissue perfusion: we consider the brain perfusion and the role played by Circle of Willis.

Circle of Willis (CoW) is a relevant example of a vessel network supplying a tissue: it is a net of blood vessels at the base of the brain, through which blood is distributed to the cerebral tissues. Blood enters the CoW by four medium arteries, namely the two internal carotid (ICA) and the two vertebral arteries (VA); they are connected by smaller communicating vessels in a ring structure, and six arteries originating from this circle provide the blood to the brain (see fig. 6.25)

Brain is one of the most oxygen consuming organs (at rest), and a failure in blood supply can rapidly lead to ischemia and eventual infarction. Thanks to its ring structure, the CoW provides alternative flow paths for the blood, should a vessel be occluded: it is a sort of “safety device” of the cerebral circulatory system.

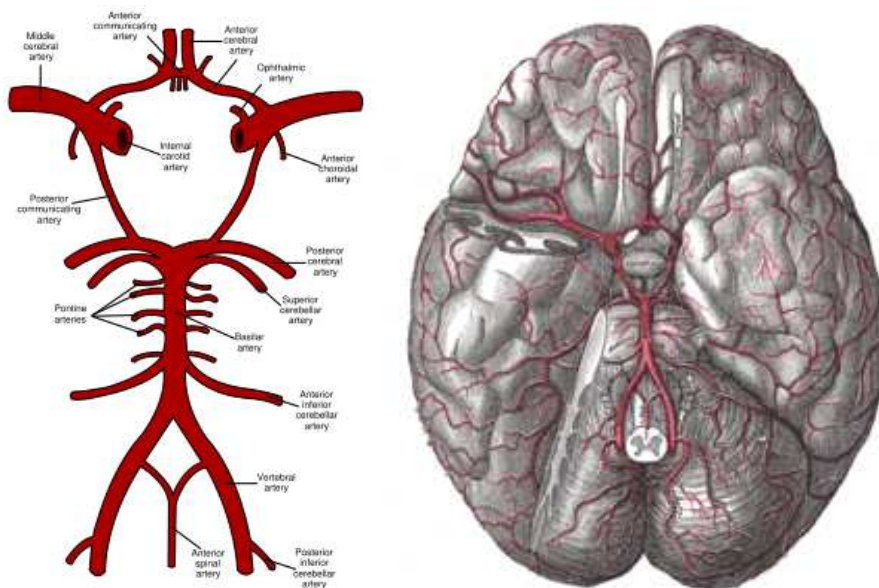


Figure 6.25: The Circle of Willis.

We already encountered the CoW in sec. 6.4.3 (see fig. 6.10), where we have shown that (at least in two dimensions) it is possible to extract the geometry of the major vessels of the Circle from medical images to perform simulations. Now we address the 3D case, and present a simulation of brain perfusion, resolving both the fast blood flow in the CoW and the slow flow in the cerebral tissue, using the techniques we introduced in this chapter. Oxygen transport in the brain will be considered as well.

The computational domains that we consider here are respectively the network of vessels and the “hemi-ellipsoid” in fig. 6.26. Although such an ellipsoid is only a rough approximation of the actual geometry of the cerebral tissues, it will suffice for our purposes. The 1D mesh has been extracted as an edge path in the 3D grid, using the algorithm presented in sec. 6.6.2, starting from available data on the geometry of the CoW. We will make use of the standard acronyms to denote the arteries of the CoW (see fig. 6.26): we will consider directly the basilar artery (BA) skipping the two vertebral artery.

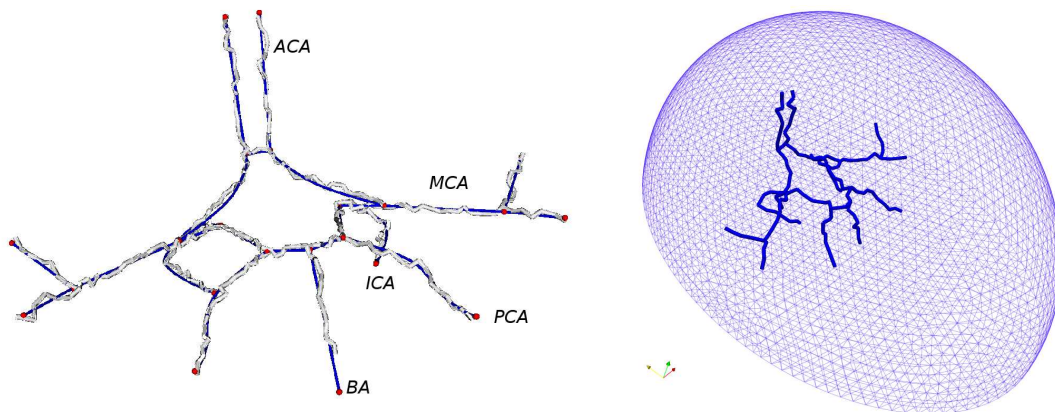


Figure 6.26: On the left: the set of points used for extracting the 1D mesh as an edge path in a 3D mesh is denoted by the blue line, while the extracted path is represented in white; the nodes of the network are indicated in red. Notice that the extracted path approximates the data with an error (distance) smaller than the 3D mesh size. The acronyms stand for: basilar artery (BA), internal carotid artery (ICA), anterior cerebral artery (ACA), middle cerebral artery (MCA), posterior cerebral artery (PCA). On the right: the 1D extracted mesh and the surface wireframe of the 3D mesh of the tissue domain, in which the path has been created.

The blood enters the CoW by the BA and the two ICA (left and right); it leaves the CoW by the ACA, the MCA, and the PCA. Then it is distributed to the cerebral tissues by smaller arteries, arterioles and capillaries originating from the former vessels.

A number of works has been devoted to the mathematical study of the hemodynamics of the CoW⁶. Several techniques for the simulation of blood flow in the CoW have been used in the literature. For instance, in [65] 1D and 3D models of the CoW are compared, and (mechanic) autoregulation⁷ is taken into account; in [17], the authors suggest that “fractal” 1D arterial trees (automatically generated by the computer) could provide more accurate boundary conditions for the 3D models.

At our knowledge, none of the existing works has addressed the presence of a continuous hierarchical flow from the CoW to the surrounding tissues. As we see in fig. 6.27, the vessels forming the CoW possess a large number of minor branches: these smaller arteries supply the tissues around the circle, so that a flow rate loss is expected from the entrance to the exit of the CoW. In fact, the average flow rates [ml s^{-1}] from data collected by references [27], [60] and [28], are: 4.6 for each ICA, 1.3 for each of the two vertebral arteries supplying the BA; and 1.1 for the ACA, 2.0 for the MCA, 0.8

⁶The motivation for such studies is that the CoW is one of the districts of the circulatory system of the brain with high incidence of aneurysms.

⁷The issue of the metabolic autoregulation in the CoW, driven by the oxygen dynamics, is discussed for example in [66].

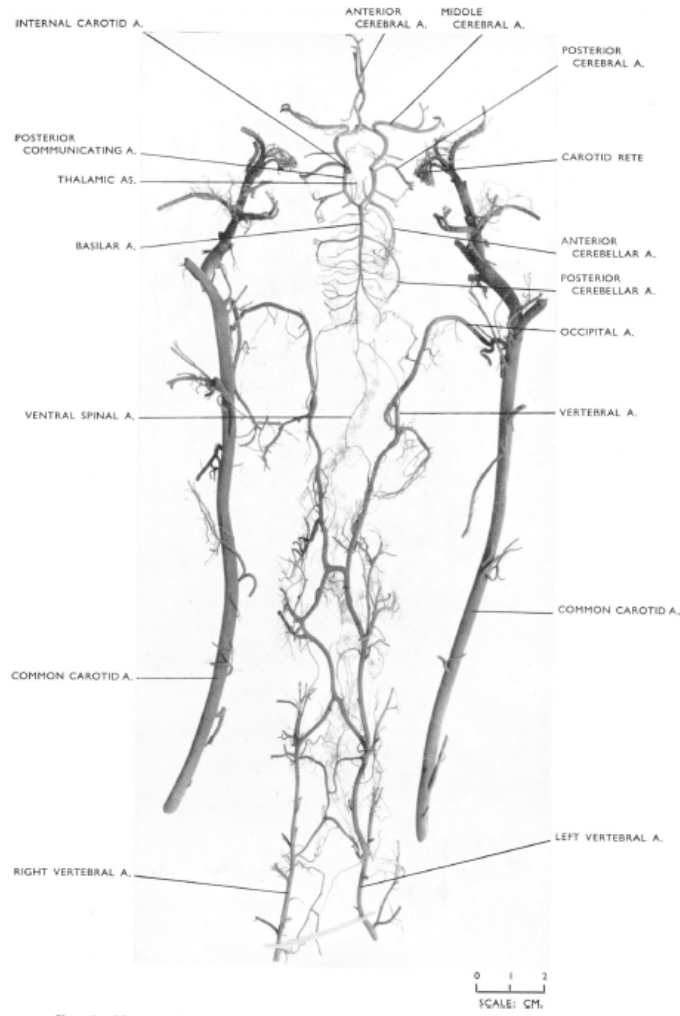


Figure 6.27: Cast of carotid arteries and CoW of a goat (from [3]): the large number of small arteries leaving the Circle indicates that a hierarchical flow takes place from the major vessels to the surrounding tissues.

for the PCA. Therefore, 11.8 ml s^{-1} is the total flow rate entering the circle, while only $q_{\text{out}} = 7.8 \text{ ml s}^{-1}$ of blood is leaving the CoW by major vessels: this means that 34% of the blood provided to the CoW goes into small branches that are usually not resolved by “standard” 3D geometries used in FEM simulations (this would be too complex due to their fractal structure). This kind of hierarchical flow can be modelled by our 3D-1D approach.

The volume of our tissue domain is $V = 1.56 \cdot 10^3 \text{ ml}$, the total length of our 1D mesh is $L = 54.3 \text{ cm}$. As we said, the mean blood flow rate entering in the CoW and then distributed to the brain is $Q = 11.8 \text{ ml s}^{-1}$: the mean tissue perfusion is thus $7.56 \cdot 10^{-3} \text{ ml}$ of blood per ml of tissue. We consider a porosity $n_b = 1/50$, a tissue permeability $K_t = 0.1 \text{ cm}^2 \text{ kPa}^{-1} \text{ s}^{-1}$ and a tissue compliance $C_t = 0.01 \text{ kPa}^{-1}$. Assuming that the typical value of the tissue blood pressure is $p_{t,0} = 8 \text{ kPa}$, we estimate the hydraulic conductance $\alpha \simeq Q/(V \cdot p_{t,0}) \simeq 9.4 \cdot 10^{-4} \text{ kPa}^{-1} \text{ s}^{-1}$; we are still assuming that the perfusion term $\omega_t = \alpha p_t$ corresponds to the blood flow rate per unit volume that

leaves the tissue and is collected by the venous bed.

As regards the vessel-tissue interaction, the conductivity L_p can be estimated as in the previous example. The typical vessel pressure is $p_{0,v} = 10$ kPa; assuming $R = 0.1$ cm as an average value for the radius, by

$$2\pi RL_p(p_{0,v} - p_{0,t}) \cdot L \simeq (Q - q_{\text{out}})$$

we have $L_p \simeq 0.114$ cm kPa⁻¹ s⁻¹ (one could consider similar estimations for each vessel separately).

Notice that the blood exiting the CoW is distributed to the cerebral tissues. Let $q_{\text{out}}^{(n)}$ be the total flow rate exiting the PCAs, MCAs and ACAs at time t_n ; in our scheme 6.6.2 we set

$$f_p = q_{\text{out}}^{(n)}/V$$

to take into account this contribution to brain perfusion.

Concerning oxygen transport, we consider the same data used for the previous simulation, with the exception of coefficient f_u . In fact, we have an additional mass flux term $f_{\text{out}}^{(n)}$, given by the oxygen transported by the blood exiting the CoW and perfusing the tissue; assuming that at the outlets B_i of the CoW (the end points of PCAs, MCAs, ACAs) the flow rate q_v is always positive (in other words blood is really exiting the CoW), this term reads

$$f_{\text{out}}^{(n)} = \frac{1}{V} \sum_i q_v^{(n)}(B_i) u_v^{(n)}(B_i).$$

Therefore, assuming a Michaelis-Menten metabolic rate, the f_u term we consider in problem 6.6.3 is

$$f_u = f_{\text{out}}^{(n)} - f_{O_2, \text{max}} \frac{u_t^{(n)}}{u_{1/2} + u_t^{(n)}},$$

where we take $f_{O_2, \text{max}} = 0.08$ μmol cm⁻³ s⁻¹. We choose $u_{1/2} = \frac{1}{10} u_{t,0}$, being $u_{t,0} = 7.2$ μmol ml⁻¹ the reference value for the blood oxygen concentration in the tissue.

Again, we consider the parameter L_u as a penalization term and set $L_u = 20$ cm kPa⁻¹ s⁻¹. The initial values are $p_{0,v}$, $p_{0,t}$ for the pressures, $u_{0,v}$, $u_{0,t}$ for the concentrations; the initial flow rate in the vessel is zero. We prescribe the flow rate at the BA and ICAs, using pulsatile waveforms having average values corresponding to the measurements we cited previously, and we assume conductive loads at the end points of all other vessels, equal to 2 cm³ s⁻¹ kPa⁻¹, with $p_{e,2} = p_{e,3} = p_{0,v}$.

In fig. 6.28, the blood pressures in the vessels of the CoW and in the surrounding tissues at $t = 2.1$ s are reported: again, the hierarchical flow from the vessels is responsible for the spatial pattern of the the blood pressure in the tissue.

The distribution of flow rates at the outlets of the vessels of the CoW is reported in fig. 6.29 (when a vessel is paired with a symmetric one, as for ICA, PCA etc., the values are referred to the left vessel). In the picture we also show the time course of the total flow rate q_{out} exiting the CoW: its mean value is less than the average input flow rate (11.8 cm³ s⁻¹), due to the presence of the hierarchical flow.

The blood pressures time courses at the same outlets are shown in fig. 6.30. Here we also emphasize the difference between the time step for the 3D (slow) and 1D (fast) problems: in our multirate scheme, the oversampling ratio between the two values was $m = 10^3$, allowing for a accurate resolution of wave propagation in the 1D domain. This propagation is visualized by the snapshots in fig. 6.31 as well: the pressure distribution on the vessels network results from the interplay of the geometry/topology of the network and the interaction with the tissue in which the network is embedded.

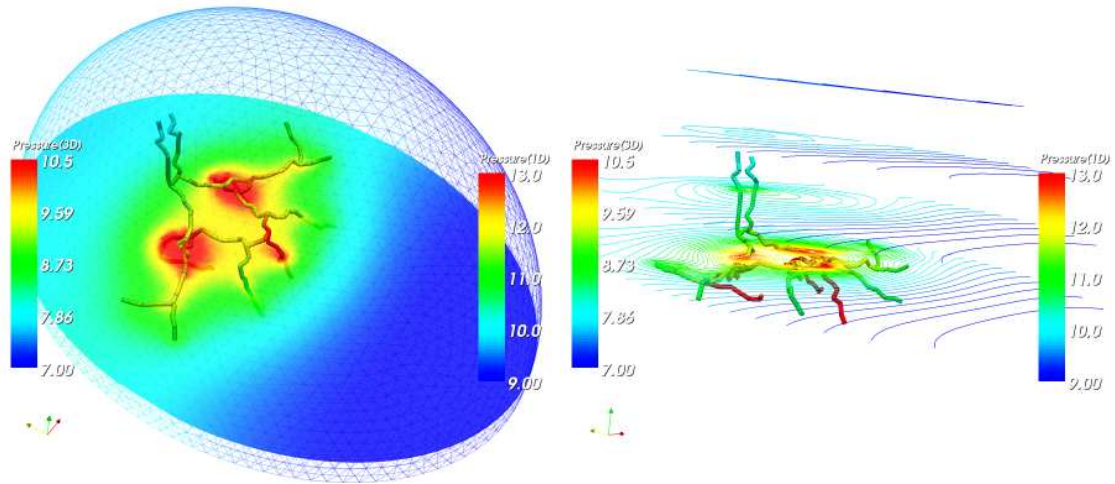


Figure 6.28: On the left: snapshot of the 1D blood pressure distribution in the Circle of Willis, and a slice of the 3D blood pressure. On the right some isolines of the 3D pressure are reported on parallel planes to show its spatial patterns.

Finally, we see in fig. 6.32 how a isosurface of the oxygen concentration ($7.93 \mu\text{mol ml}^{-1}$) is advected by the blood flow in the vessel matrix of the tissue: this result has been obtained using the mass transport scheme 6.6.3, using the values of tissue blood velocity and perfusion computed from the blood flow problem.

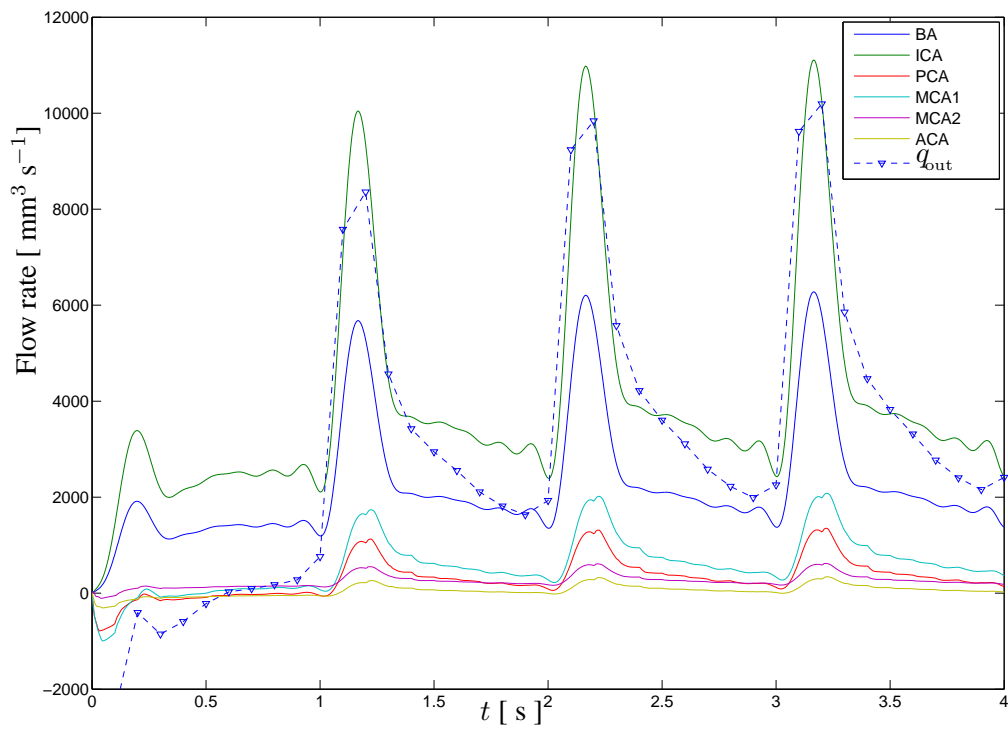


Figure 6.29: Comparison of the flow rates q_v computed at several districts of the CoW; the total flow rate q_{out} leaving the CoW by the outlets is indicated by the dashed line with marks, the rest of the input flow rate is transferred to the tissue due to hierarchical flow, depending on the parameter L_p .

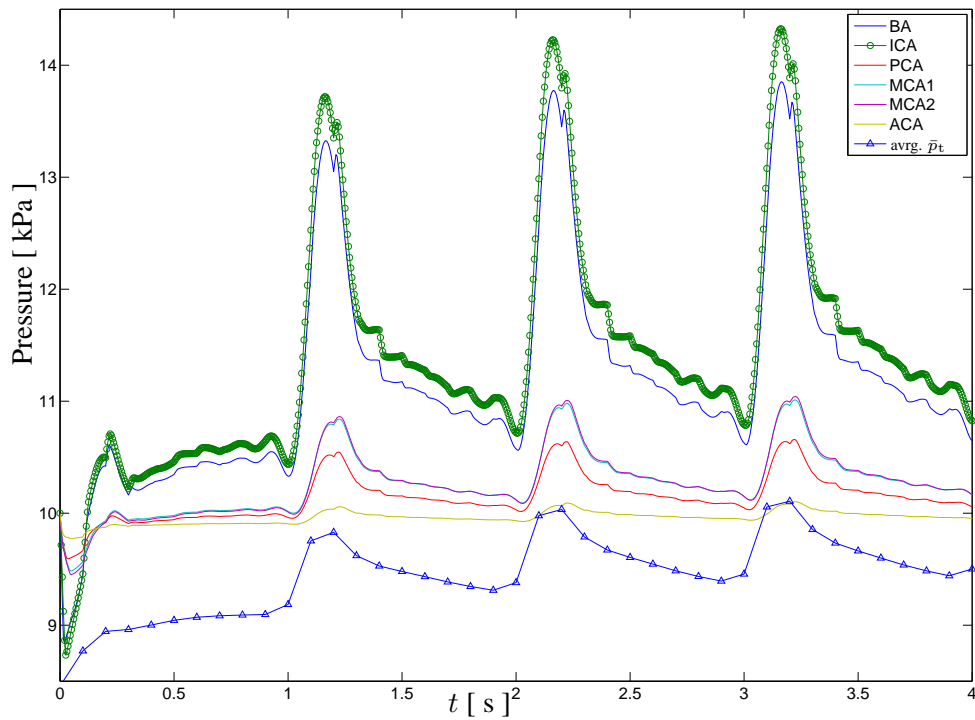


Figure 6.30: Blood pressures p_v computed at several districts of the CoW, and average value of \bar{p}_t on the vessel (computed as $\frac{1}{|\Lambda|} \int_{\Lambda} \bar{p}_t(s) ds$). The marks emphasize the difference in time steps due to our multirate advancing scheme (triangles correspond to a 3D time step, since \bar{p}_t is computed from the 3D pressure; each circle corresponds to 50 one-dimensional steps).

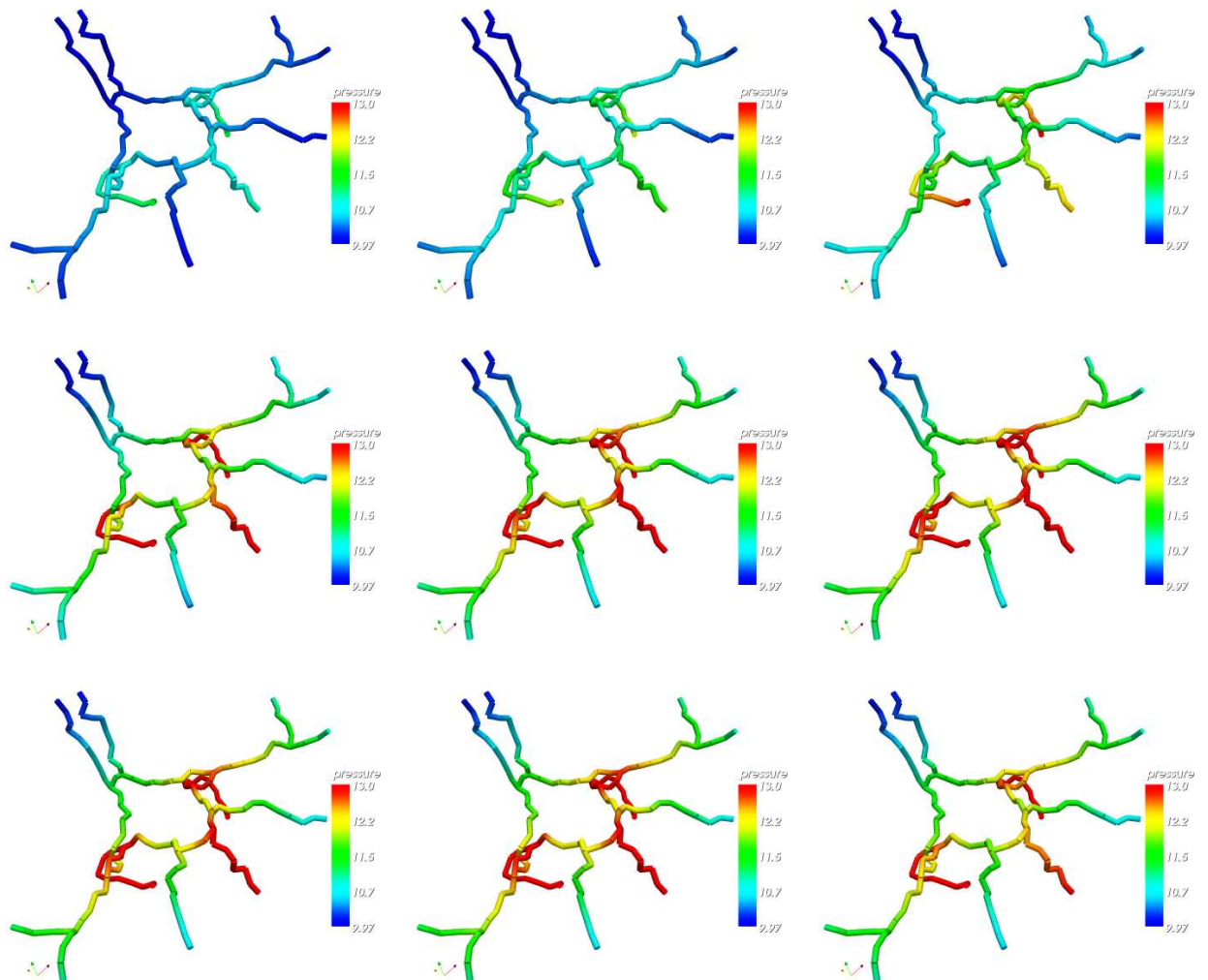


Figure 6.31: From left to right and from top to bottom: snapshots of the blood pressure at times $t = 1.000$ s, 1.025 s, 1.050 , \dots , 2.000 s.

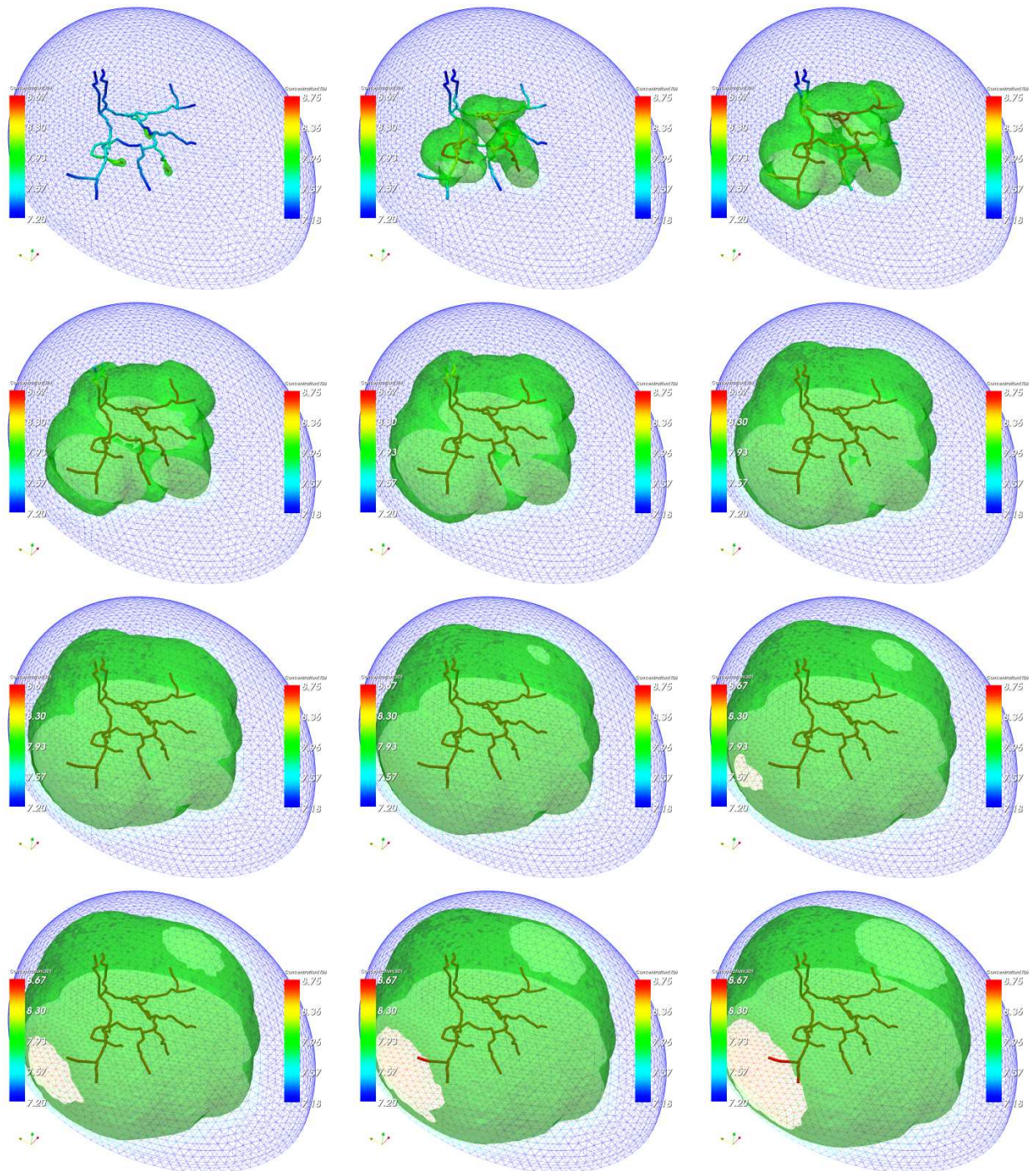


Figure 6.32: From left to right and from top to bottom: snapshots of a isosurface for the 3D oxygen concentration at times $t = 0.0$ s, 0.5 s, 1.0 , \dots , 5.5 s, showing the oxygen transport in the tissue.

Appendix A

Weighted Sobolev Spaces

In the sequel we denote by Ω a domain in \mathbb{R}^3 , and by $\Lambda \subset \Omega$ a 1D smooth manifold, described by eq. (3.1). We define Ω_v^R as the set of points that are closer than R to Λ , $R > 0$; under assumption (3.4), this subset is parametrized according to (3.2) by local coordinates (3.3).

We will denote by \hookrightarrow any continuous embedding between normed spaces; sometimes we will write $d(\mathbf{x})$ for the function $\text{dist}(\mathbf{x}, \Lambda)$.

A.1 Spaces $L_\alpha^2(\Omega)$

Definition A.1.1. Let $\alpha \in \mathbb{R}$; we denote by $L_\alpha^2(\Omega)$, the space of square integrable functions with respect to the measure μ_α defined by

$$d\mu_\alpha(\mathbf{x}) = \text{dist}(\mathbf{x}, \Lambda)^{2\alpha} d\mathbf{x}.$$

This means that $f \in L_\alpha^2(\Omega)$ if and only if $\text{dist}(\mathbf{x}, \Lambda)^\alpha f(\mathbf{x})$ is $L^2(\Omega)$. We have that $L_\alpha^2(\Omega)$ is a Hilbert space equipped with the scalar product

$$(u, v)_{L_\alpha^2(\Omega)} = \int_\Omega u(\mathbf{x})v(\mathbf{x}) d\mu_\alpha(\mathbf{x}).$$

Lemma A.1.1. We have:

a) $L_\alpha^2(\Omega)$ and $L^2(\Omega)$ are isometric via the map

$$f \in L_\alpha^2(\Omega) \mapsto d^\alpha f \in L^2(\Omega).$$

b) $L_\alpha^2(\Omega) \hookrightarrow L_\beta^2(\Omega)$ provided that $\alpha < \beta$.

c) If $\beta > -1 - \alpha$, then $d^\beta \in L_\alpha^2(\Omega)$.

Proof. Point a) follows directly from Definition A.1.1; point b) is a straightforward consequence of the boundedness of Ω ; point c) follows from point a) and from the fact that $\text{dist}(\cdot, \Lambda)^{2\beta+2\alpha} \in L^2(\Omega)$ iff $2\beta + 2\alpha > -2$. \square

A.2 Spaces $W^{1,p}(\Omega, \mu)$: fundamental properties

Most of the properties of standard Sobolev spaces are retained when considering weighted spaces, provided that the weight function satisfies certain basic properties: we refer to [38] for an overview of this topic and for the proofs of the results that we are going to introduce. In the general case of L^p -based spaces, the weight function must be p -admissible¹. A special class of p -admissible weight functions is the *Muckenhoupt class* A_p :

Definition A.2.1. Let $p > 1$: the Muckenhoupt class A_p is defined as the set of locally integrable functions w on \mathbb{R}^n such that

$$\sup_{\substack{B=B(\mathbf{x},r) \\ \mathbf{x} \in \mathbb{R}^n, r>0}} \left(\frac{1}{|B|} \int_B w(\mathbf{x}) \, d\mathbf{x} \right) \left(\frac{1}{|B|} \int_B w(\mathbf{x})^{-1/(p-1)} \, d\mathbf{x} \right)^{p-1} < +\infty$$

where $B(\mathbf{x}, r)$ is the ball centered in \mathbf{x} with radius r , and $|B|$ is its measure.

In the sequel, we always assume² that $w \in A_p$. In this case, the space defined by

$$W^{1,p}(\Omega; \mu) = \{f \in L^p(\Omega; \mu) : \nabla f \in L^p(\Omega; \mu)^3\}, \quad (\text{A.1})$$

where $d\mu(\mathbf{x}) = w(\mathbf{x}) \, d\mathbf{x}$, has the following density property:

Lemma A.2.1 (Density of smooth functions). $W^{1,p}(\Omega; \mu)$ is a reflexive Banach space; moreover it is the completion of $C^\infty(\Omega)$ with respect to the norm $\|\cdot\|_{W^{1,p}}$:

$$W^{1,p}(\Omega; \mu) = \overline{C^\infty(\Omega)}.$$

Definition A.2.2 (Space $W_0^{1,p}$). We define the space $W_0^{1,p}(\Omega; \mu) \subset W^{1,p}(\Omega; \mu)$ as the completion of $C_0^\infty(\Omega)$ with respect to the norm $\|\cdot\|_{W^{1,p}}$.

In this space the following inequality holds:

Theorem A.2.1 (Poincaré inequality in $W_0^{1,p}(\Omega; \mu)$). There exists a constant $C = C(\Omega, \mu) > 0$ such that:

$$\int_\Omega |u|^p \, d\mu \leq C \int_\Omega |\nabla u|^p \, d\mu \quad \forall u \in W_0^{1,p}(\Omega; \mu).$$

The next result gives a sufficient condition for continuous embeddings to hold between spaces having different weights:

Lemma A.2.2. If $\mu_2 \leq C\mu_1$, $C > 0$, then $W^{1,p}(\Omega; \mu_1) \hookrightarrow W^{1,p}(\Omega; \mu_2)$. In particular, if there are positive constants C_1, C_2 such that

$$C_1\mu_1^{-1} \leq \mu_2 \leq C_2\mu_1$$

then $W^{1,p}(\Omega; \mu_1)$ and $W^{1,p}(\Omega; \mu_2)$ are isomorphic:

$$W^{1,p}(\Omega; \mu_1) \simeq W^{1,p}(\Omega; \mu_2).$$

¹ See for instance [38, ch. 1], where the spaces $H^{1,p}(\Omega; \mu)$ are introduced; here we always consider $p = 2$. We point out that weight functions of the type $\text{dist}(\mathbf{x}, M)^\alpha$ are considered in [51], but only for $M \subset \partial\Omega$ with some special regularity assumptions on M .

² The main advantage of this assumption is that if $w \in A_p$ the space defined by (A.1) is the completion of $C^\infty(\Omega)$. If $w \notin A_p$, one usually defines $W^{1,p}(\Omega; \mu) = \overline{C^\infty(\Omega)}$, but this space does not coincide with (A.1) anymore.

Finally, one can show that for $p > 1$, $W^{1,p}(\Omega; \mu)$ is sequentially weakly compact. And for $p = 2$ a weighted Rellich-Kondrachov theorem holds (see [48], th. 8 with $p = q = 2$):

Theorem A.2.2. *Suppose that $\{u_i\}$ is a bounded sequence in $W^{1,2}(\Omega; \mu)$. Then there is a subsequence $\{u_{i_k}\}$ and a function $u \in W^{1,2}(\Omega; \mu)$ such that $u_{i_k} \rightarrow u$ strongly in $L^2(\Omega; \mu)$ and $\nabla u_{i_k} \rightarrow \nabla u$ weakly in $L^2(\Omega; \mu)$ ³. Moreover, if $\{u_i\} \subset W_0^{1,2}(\Omega; \mu)$ then $u \in W_0^{1,2}(\Omega; \mu)$.*

A.3 Spaces $H_\alpha^1(\Omega)$

In this work, spaces $W^{1,p}(\Omega; \mu)$ with $p = 2$ and measure $\mu = \mu_\alpha$ defined by $d\mu_\alpha = \text{dist}(\mathbf{x}, \Lambda)^{2\alpha} dx$ need a special attention. Below, we list some properties that are useful for our purposes. It is known that the function $|\mathbf{x}|^\gamma : \mathbb{R}^3 \rightarrow \mathbb{R}$ is an A_2 weight if $-3 < \gamma < 3$. The distance from a line is “less integrable” than the distance from a point, but one can easily show that $\text{dist}(\mathbf{x}, \Lambda)^{2\alpha}$ is a A_2 weight at least for $|\alpha| < 1$:

Property A.3.1. *If $-1 < \alpha < 1$, then the weight function $\text{dist}(\mathbf{x}, \Lambda)^{2\alpha}$ is A_2 .*

The corresponding weighted Sobolev space is a Hilbert space:

Definition A.3.1. *Let $|\alpha| < 1$; we define*

$$H_\alpha^1(\Omega) := W^{1,2}(\Omega; \mu_\alpha).$$

$H_\alpha^1(\Omega)$ is an Hilbert space endowed by the scalar product

$$(u, v)_{H_\alpha^1(\Omega)} = \int_\Omega u(\mathbf{x})v(\mathbf{x})d\mu_\alpha(\mathbf{x}) + \int_\Omega \nabla u(\mathbf{x}) \cdot \nabla v(\mathbf{x})d\mu_\alpha(\mathbf{x}).$$

Consider a subset $G \subset \Omega$ and suppose that $d_{\min} \leq \text{dist}(\mathbf{x}, \Lambda) \leq d_{\max} \forall \mathbf{x} \in G$, being d_{\max} , d_{\min} positive constants. Let $u \in H_\alpha^1(\Omega)$; since $u|_G \in W^{1,2}(G; \mu_\alpha)$ with $\|u\|_{W^{1,2}(G; \mu_\alpha)} \leq \|u\|_{H_\alpha^1(\Omega)}$, the restriction operator $|_G$ is continuous. Moreover, by property A.2.2 we have that $W^{1,2}(G; \mu_\alpha) \simeq H^1(G)$: therefore, $|_G$ is a continuous operator from $H_\alpha^1(\Omega)$ to $H^1(G)$. Let $\tilde{\gamma}$ be the standard trace operator (see for instance [57]) from $H^1(G)$ to $H^{1/2}(\partial G)$: the map defined by $\gamma u = \tilde{\gamma}u|_G$ is continuous from $H_\alpha^1(\Omega)$ to $H^{1/2}(\partial G)$, being the composition of the following continuous linear mappings:

$$H_\alpha^1(\Omega) \xrightarrow{|_G} W^{1,2}(G; \mu_\alpha) \xrightarrow{\simeq} H^1(G) \xrightarrow{\tilde{\gamma}} H^{1/2}(\partial G).$$

Moreover, γ satisfies $\gamma u = u|_{\partial G}$ for each $u \in C^\infty(\Omega)$, and it is unique due to the density of $C^\infty(\Omega)$ in $H_\alpha^1(\Omega)$.

If $\epsilon = \text{dist}(\partial\Omega, \Lambda) > 0$, these considerations hold with $G = \{\mathbf{x} \in \Omega : \text{dist}(\mathbf{x}, \partial\Omega) < \epsilon/2\}$ (as ∂G is Lipschitz). Since $\partial\Omega \subset \partial G$, we have a well-defined trace operator:

Property A.3.2 (Trace operator). *Let $|\alpha| < 1$, and $\text{dist}(\partial\Omega, \Lambda) > 0$. Then there exists a unique linear continuous map*

$$\gamma : H_\alpha^1(\Omega) \rightarrow H^{1/2}(\partial\Omega)$$

such that $\gamma u = u|_{\partial\Omega}$ for each smooth function $u \in C^\infty(\Omega)$.

An interesting property of spaces $H_\alpha^1(\Omega)$ is that for every $-1 < \alpha < 0$, a function in $H_\alpha^1(\Omega)$ admits a “trace on Λ ”, as stated by lemma 4.1.1. As a consequence, thanks to theorem A.2.2, we have the following Poincaré inequality in $H_\alpha^1(\Omega)$, $-1 < \alpha < 0$:

Property A.3.3. *Let $-1 < \alpha < 0$; then there exists a positive constant C such that*

$$\int_{\Omega} |u|^2 d\mu_{\alpha} \leq C \left(\int_{\Lambda} |u|^2 d\Lambda + \int_{\Omega} |\nabla u|^2 d\mu_{\alpha} \right) \quad \forall u \in H_{\alpha}^1(\Omega).$$

Proof. If not, we could find a sequence $\{u_n\} \subset H_{\alpha}^1(\Omega)$, $u_n \neq 0$, such that

$$\frac{1}{n} \int_{\Omega} |u_n|^2 d\mu_{\alpha} > \int_{\Lambda} |u_n|^2 d\Lambda + \int_{\Omega} |\nabla u_n|^2 d\mu_{\alpha} \quad \forall n \in \mathbb{N}.$$

Let $\tilde{u}_n := u_n / \|u_n\|_{L_{\alpha}^2(\Omega)}$; then

$$\frac{1}{n} > \int_{\Lambda} |\tilde{u}_n|^2 d\Lambda + \int_{\Omega} |\nabla \tilde{u}_n|^2 d\mu_{\alpha} \quad \forall n \in \mathbb{N}. \quad (\text{A.2})$$

The sequence $\{\tilde{u}_n\}$ is bounded in $L_{\alpha}^2(\Omega)$, hence in $H_{\alpha}^1(\Omega)$ thanks to (A.2). Therefore, by theorem A.2.2, there is a subsequence $\{u_{n_k}\}$ and a function $u \in H_{\alpha}^1(\Omega)$ such that $u_{n_k} \rightarrow u$ strongly in $L_{\alpha}^2(\Omega)$ and $\nabla u_{n_k} \rightarrow \nabla u$ weakly in $L_{\alpha}^2(\Omega)$ ³. In particular, $u_{n_k} \rightarrow u$ weakly in $H_{\alpha}^1(\Omega)$; since γ_{Λ} is a continuous linear operator, we have

$$\gamma_{\Lambda} u_{n_k} \rightarrow \gamma_{\Lambda} u \quad \text{weakly in } L^2(\Lambda). \quad (\text{A.3})$$

Thanks³ to (A.2), $\nabla u = \mathbf{0}$ so that u is a constant. Then, using (A.2, A.3) in the same way, we get $\int_{\Lambda} u^2 d\Lambda = 0$ so that $u = 0$. This is a contradiction, since $\|u\|_{L_{\alpha}^2(\Omega)} = \lim \|u_{n_k}\|_{L_{\alpha}^2(\Omega)} = 1$ (due to the L^2 convergence). \square

Finally, it is possible to prove the following imbedding theorem:

Lemma A.3.1. *Let $0 < \alpha < 1$; there exists a positive constant C , depending only on α , such that*

$$\|u\|_{L_{\alpha-1}^2(\Omega)} \leq C \|u\|_{H_{\alpha}^1(\Omega)} \quad \forall u \in H_{\alpha}^1(\Omega).$$

Moreover, $C = \mathcal{O}(\alpha^{-1})$ for $\alpha \rightarrow 0^+$.

Proof. We recall the following Hardy's inequality (see [36]), holding for every measurable positive function f , and $p > 1$:

$$\int_0^{\infty} \left(\frac{1}{r} \int_r^{\infty} f(t) dt \right)^p r^{\beta} dr \leq \left(\frac{p}{\beta + 1 - p} \right)^p \int_0^{\infty} f(r)^p r^{\beta} dr \quad \text{if } \beta > p - 1. \quad (\text{A.4})$$

We consider the three subdomains (3.2) separately. Let $\varphi \in C^{\infty}(\Omega)$, with $\text{supp}(\varphi) \subset \Omega_{v,0}^R$: using local cylindrical coordinates in $\Omega_{v,0}^R$ we have

$$r^{\alpha-1} \varphi(s, r, \theta) = r^{\alpha-1} \left(\varphi(s, R, \theta) - \int_r^R \frac{\partial \varphi}{\partial r}(s, t, \theta) dt \right) = r^{\alpha-1} \int_r^R \frac{\partial \varphi}{\partial r}(s, t, \theta) dt$$

³ The norm in a Hilbert space is weakly lower semicontinuous, so that

$$\|\nabla u\|_{L_{\alpha}^2(\Omega)}^2 \leq \liminf_k \|\nabla u_{n_k}\|_{L_{\alpha}^2(\Omega)}^2 \leq \liminf_k \frac{1}{n_k} = 0.$$

since $\varphi(s, R, \theta) = 0$. Squaring and integrating on $\Omega_{v,0}^R$ (where $\text{dist}(\mathbf{x}, \Lambda) = r$) we have

$$\int_{\Omega_{v,0}^R} \text{dist}(\mathbf{x}, \Lambda)^{2(\alpha-1)} \varphi(\mathbf{x})^2 r \, ds \, dr \leq \int_{\Omega_{v,0}^R} \left(\int_r^R \frac{\partial \varphi}{\partial r}(s, t, \theta) \, dt \right)^2 r^{2\alpha-1} \, ds \, dr \, d\theta. \quad (\text{A.5})$$

Choosing in (A.4) $f(t) = |\partial \varphi(s, t, \theta) / \partial r|$ for $t \in (0, R]$, $f(t) = 0$ for $t > R$, $p = 2$ and $\beta = 2\alpha + 1$, we get

$$\int_{\Omega_{v,0}^R} \left(\int_r^R \frac{\partial \varphi}{\partial r}(s, t, \theta) \, dt \right)^2 r^{2\alpha-1} \, ds \, dr \, d\theta \leq \frac{1}{\alpha^2} \int_{\Omega_{v,0}^R} \left(\frac{\partial \varphi}{\partial r}(s, t, \theta) \right)^2 r^{2\alpha} \, ds \, dr \, d\theta. \quad (\text{A.6})$$

From (A.5) and (A.6) we have

$$\|\varphi\|_{L_{\alpha-1}^2(\Omega_{v,0}^R)} \leq \frac{1}{\alpha} \|\nabla \varphi\|_{L_{\alpha}^2(\Omega)}. \quad (\text{A.7})$$

A similar proof gives, for smooth functions φ supported in $\Omega_{v,i}^R$, $i = 1, 2$.

Consider $\varphi \in C^\infty(\Omega)$, with $\text{supp}(\varphi) \subset \Omega_t^{R/2} = \Omega \setminus \overline{\Omega_v^{R/2}}$. Since

$$\text{dist}(\mathbf{x}, \Lambda) \geq \frac{R}{2} > 0 \quad \forall \mathbf{x} \in \Omega_t^{R/2}$$

we have

$$\|\varphi\|_{L_{\alpha-1}^2(\Omega_t^{R/2})} \leq \left(\frac{R}{2} \right)^{\alpha-1} \|\varphi\|_{L_{\alpha}^2(\Omega)}. \quad (\text{A.8})$$

Now consider $\varphi \in C^\infty(\Omega)$. Let $\{\psi_0, \dots, \psi_3\}$ be a partition of the unity associated to the covering $\Omega_{v,i}$, $i = 0, 1, 2$, and $\Omega_t^{R/2}$. Using (A.7) and (A.8) for $\psi_j \varphi$, we can prove the estimate

$$\|\varphi\|_{L_{\alpha-1}^2(\Omega)} \leq C \|\varphi\|_{H_{\alpha}^1(\Omega)}.$$

Since smooth functions are dense in $H_{\alpha}^1(\Omega)$, this estimate extends to $u \in H_{\alpha}^1(\Omega)$. Finally, from A.7 it follows that $C = (\alpha^{-1})$ for $\alpha \rightarrow 0^+$. \square

A.4 Nečas theorem

We recall the following theorems (see [67], [5], [85]):

Theorem A.4.1 (Nečas). *Let H_1 and H_2 be two Hilbert spaces, $F \in H_2'$ be a bounded linear functional on H_2 and $a(\cdot, \cdot)$ be a bilinear form on $H_1 \times H_2$ such that*

$$|a(u, v)| \leq C_1 \|u\|_{H_1} \|v\|_{H_2} \quad \forall (u, v) \in H_1 \times H_2, \quad (\text{A.9})$$

$$\sup_{u \in H_1} a(u, v) > 0 \quad \forall v \in H_2, v \neq 0, \quad (\text{A.10})$$

$$\sup_{\|v\|_{H_2} \leq 1} a(u, v) \geq C_2 \|u\|_{H_1} \quad \forall u \in H_1, \quad (\text{A.11})$$

where C_1 and C_2 are positive constants. Then there exists exactly one $u \in H_1$ such that

$$a(u, v) = F(v) \quad \forall v \in H_2,$$

which depends linearly and continuously on F :

$$\|u\|_{H_1} \leq \frac{1}{C_2} \|F\|_{H_2'}.$$

Theorem A.4.2. *Let the assumptions of theorem A.4.1 be fulfilled. Furthermore let $M_1 \subset H_1$, $M_2 \subset H_2$, both closed subspaces. Assume that*

$$\begin{aligned} \sup_{u \in M_1} a(u, v) &> 0 & \forall v \in M_2, \\ \sup_{\substack{v \in M_2 \\ \|v\|_{H_2} \leq 1}} a(u, v) &\geq \hat{C}_2 \|u\|_{H_1} & \forall u \in M_1, \end{aligned}$$

where $\hat{C}_2 = \hat{C}_2(M_1, M_2)$ is a positive constant. Consider $u \in H_1$, $\hat{u} \in M_1$ such that

$$a(u, v) = F(v) \quad \forall v \in H_2$$

and

$$a(\hat{u}, v) = F(v) \quad \forall v \in M_2.$$

Then

$$\|u - \hat{u}\| \leq \left(1 + \frac{C_1}{\hat{C}_2}\right) \inf_{\tilde{u} \in M_1} \|u - \tilde{u}\|. \quad (\text{A.12})$$

Bibliography

- [1] R. Al-Khoury, P. G. Bonnier, and R. B. J. Brinkgreve. Efficient finite element formulation for geothermal heating systems. Part I: steady state. *Int. J. Num. Meth. Eng.*, 63:988–1013, 2005.
- [2] D. Amadori, S. Ferrari, and L. Formaggia. Derivation and analysis of a fluid-dynamical model in thin and long elastic vessels. *Networks and heterogeneous media*, 2(1):99–125, 2007.
- [3] B. Andersson and P.A. Jewell. The distribution of carotid and vertebral blood in the brain and spinal cord of the goat. *Q. J. Exp. Physiol. Cogn. Med. Sci.*, 41:462–474, 1956.
- [4] J. F. Andrus. Numerical solution of systems of ordinary differential equations separated into subsystems. *SIAM J. Numer. Anal.*, 16(4):605–611, 1979.
- [5] I. Babuška. Error-bounds for finite element method. *Numer. Math.*, 16:322–333, 1971.
- [6] J. Bear and Y. Bachmat. *Introduction to Modeling of Transport Phenomena in Porous Media*. Kluwer Academic Publishers, 1990.
- [7] Z. Belhachmi, C. Bernardi, S. Deparis, and F. Hecht. A truncated Fourier/finite element discretization of the Stokes equations in an axisymmetric domain. *Math. Models Methods Appl. Sci.*, 16(2):233–263, 2006.
- [8] G. Bretti, R. Natalini, and B. Piccoli. Numerical approximations of a traffic flow model on networks. *Netw. Heterog. Media*, 1(1):57–84 (electronic), 2006.
- [9] H. Brezis and W. Strauss. Semilinear elliptic equations in L^1 . *J. Math. Soc. Japan*, 25:565–590, 1973.
- [10] G.A. Brooks, T.D. Fahey, and T.P. White. *Human Bioenergetics and Its Applications*. Mayfield Publishing Company, 1987.
- [11] M.E. Cabrera, G.M. Saidel, and S.C. Kalhan. Role of O_2 in regulation of lactate dynamics during hypoxia: Mathematical model and analysis. *Ann. of Biomed. Eng.*, 26:1–27, 1998.
- [12] M.E. Cabrera, G.M. Saidel, and S.C. Kalhan. Lactate metabolism during exercise: analysis by an integrative systems model. *Am. J. Physiol.*, 277:1522–1536, 1999.
- [13] S. Čanić and E.H. Kim. Mathematical analysis of quasilinear effects in a hyperbolic model blood flow through compliant axi-symmetric vessels. *Math. Meth. Appl. Sci.*, 26:1161–1186, 2003.

- [14] S. Čanić, D. Lamponi, A. Mikelić, and J. Tambača. Self-consistent effective equations modeling blood flow in medium-to-large compliant arteries. *Multiscale Model. Simul.*, 3(3):559–596 (electronic), 2005.
- [15] E. Carson and C. Cobelli. *Modelling Methodology for Physiology and Medicine*. Academic Press, 2001.
- [16] E. Carson, C. Cobelli, and L. Finklestein. *The mathematical modeling of metabolic and endocrine systems*. Wiley, 1983.
- [17] J.R. Cebra, M.A. Castro, O. Soto, R. Löhner, and N. Alperin. Blood-flow models of the circle of Willis from magnetic resonance data. *J. Eng. Math.*, 47(3-4):369–386, 2003.
- [18] Z. Chen and S. Molloy. Automatic 3D vascular tree construction in CT angiography. *Computerized Medical Imaging and Graphics*, 27:469–479, 2003.
- [19] T. Corno, V. Milišić, A. Quarteroni, and L.K. von Segesser. The non-circular shape of FloWatch-PAB prevents the need for pulmonary artery reconstruction after banding. Computational fluid dynamics and clinical correlations. *Eur. J. Cardiothorac. Surg.*, 29(1):93–99, 2006.
- [20] C. D’Angelo and V. Milišić. Reduced model for a coupling of axisymmetric Navier-Stokes equations with a reaction diffusion model for concentration. Internal report 02.2006, EPFL (École Polytechnique Fédérale de Lausanne), 2006.
- [21] C. D’Angelo and Y. Papelier. Mathematical modelling of the cardiovascular system and skeletal muscle interaction during exercise. *ESAIM:Proceedings*, 14:78–88, 2005.
- [22] L. Davis. *The Handbook of Genetic Algorithms*. Van Nostrand Reinhold, New York, 1991.
- [23] J. Donea, S. Giuliani, H. Laval, and L. Quartapelle. Time-accurate solutions of advection-diffusion problems by finite elements. *Comp. Meth. Appl. Mech. Engng.*, 45:123–145, 1984.
- [24] Donald A. Drew and Stephen L. Passman. *Theory of multicomponent fluids*, volume 135 of *Applied Mathematical Sciences*. Springer-Verlag, New York, 1999.
- [25] M.L. Ellsworth, A.S. Popel, and R.N. Pittman. Assessment and impact of heterogeneities of convective oxygen transport parameters in capillaries of striated muscle: Experimental and theoretical. *Microvasc. Res.*, 35(3):341–362, 1988.
- [26] M. Engelen, J. Porszasz, M. Riley, K. Wasserman, K. Maehara, and T.J. Barstow. Effects of hypoxic hypoxia on O_2 uptake and heart rate kinetics during heavy exercise. *J Appl Physiol.*, 81:2500–2508, 1996.
- [27] D.R. Enzmann, M.R. Ross, M.P. Marks, and N.J. Pelc. Blood flow in major cerebral arteries measured by phase-contrast cine MR. *AJNR Am. J. Neuroradiol.*, 15:123–129, 1994.
- [28] R. Fahrig, H. Nikolov, A.J. Fox, and D.W. Holdsworth. A three-dimensional cerebrovascular flow phantom. *Biorheology*, 26(8):1589–1599, 1999.
- [29] M. Fernández, V. Milišić, and A. Quarteroni. Analysis of a geometrical multiscale blood flow model based on the coupling of ODE’s and hyperbolic PDE’s. *SIAM J. on Multiscale Model. Simul.*, 4(1):215–236, 2005.

- [30] L. Formaggia, D. Lamponi, and A. Quarteroni. One dimensional models for blood flow in arteries. *Journal of Engineering Mathematics*, 47(3):251–276, Dec 2003.
- [31] L. Formaggia, F. Nobile, A. Quarteroni, and A. Veneziani. Multiscale modeling of the circulatory system: a preliminary analysis. *Computing and Visualisation in Science*, 2:75–83, 1999.
- [32] C. W. Gear and D. R. Wells. Multirate linear multistep methods. *BIT*, 24(4):484–502, 1984.
- [33] H.J. Green, R.L. Hughson, G.W. Orr, and D.A. Ranney. Anaerobic threshold, blood lactate, and muscle metabolites in progressive exercise. *J. Appl. Physiol.*, 54(5):1032–1038, 1983.
- [34] A.C. Guyton. *Textbook of Medical Physiology*. W.B. Saunders Company, Philadelphia, 1981.
- [35] J. Hansen, M. Sander, and G.D. Thomas. Metabolic modulation of sympathetic vasoconstriction in exercising skeletal muscle. *Acta Physiol. Scand.*, 168:489–503, 2000.
- [36] G. Hardy, J.E. Littlewood, and G. Polya. *Inequalities*. Cambridge University Press, 1966.
- [37] M. Hargreaves. Skeletal muscle metabolism during exercise in humans. *Clinical and Experimental Pharm. and Physiol.*, 27:225–228, 2000.
- [38] J. Heinonen, T. Kilpeläinen, and O. Martio. *Nonlinear potential theory of degenerate elliptic equations*. Oxford Science Publications, 1993.
- [39] R. Heinrich and S. Schuster. *The regulation of cellular systems*. Chapman & Hall, New York, 1996.
- [40] Goldbaum M. Hoover A, Kouznetsova V. Locating blood vessels in retinal images by piecewise threshold probing of a matched filter response. *IEEE Trans Med Imaging.*, 19(3), 2000.
- [41] H. Hoppeler and E.R. Weibel. Structural and functional limits for oxygen supply to muscle. *Acta Physiol. Scand.*, 168:445–456, 2000.
- [42] C. Houck and J. Joines. A Genetic Algorithm for Function Optimization: A Matlab Implementation. Technical paper NCSU-IE TR 95-09, NC State University, 1995.
- [43] J.M. Huyghe, C.W. Oomens, and K.H. Van Campen. Low Reynolds number steady state flow through a branching network of rigid vessels: II. A finite element mixture model. *Biorheology*, 26(1):73–84, 1989.
- [44] J.M. Huyghe, C.W. Oomens, K.H. Van Campen, and R.M. Heethaar. Low Reynolds number steady state flow through a branching network of rigid vessels: I. A mixture theory. *Biorheology*, 26(1):55–71, 1989.
- [45] J.M. Huyghe and D.H. Van Campen. Finite deformation theory of hierarchically arranged porous solids. 2. Constitutive behavior. *Int. J. Eng. Sci.*, 33:1873–1886, 1995.
- [46] J. Keener and J. Sneyd. *Mathematical Physiology*. Springer, New York, 1998.
- [47] A.-R.A. Khaled and R. Vafai. The role of porous media in modelling flow and heat transfer in biological tissues. *Int. J. of Mass and Heat Transfer*, 46:4989–5003, 2003.

- [48] T. Kilpeläinen. Smooth approximation in weighted Sobolev spaces. *Comment. Math. Univ. Carolinae*, 38(1):29–35, 1997.
- [49] B. Korzeniewski and J.A. Zoladz. A model of oxidative phosphorylation in mammalian skeletal muscle. *Biochem. Chem.*, 92:17–34, 2001.
- [50] P. Krstrup, R.A. Ferguson, M. Kjaer, and J. Bangsbo. ATP and heat production in human skeletal muscle during dynamic exercise: higher efficiency of anaerobic than aerobic ATP resynthesis. *J Physiol.*, 549(Pt. 1):1255–269, 2003.
- [51] A. Kufner. *Weighted Sobolev Spaces*. Wiley, 1985.
- [52] M.J. Kushmerick. Energy balance in muscle activity: Simulation of ATPase coupled to oxidative phosphorylation and to creatine kinase. *Comparative Biochem. and Physiol.*, 120:109–123, 1998.
- [53] M.J. Lambeth and M.J. Kushmerick. A computational model for glycogenolysis in skeletal muscle. *Ann Biomed Eng.*, 30:808–827, 2002.
- [54] J.S. Lee and T. Skalak, editors. *Microvascular Mechanics*. Springer-Verlag, 1990. Hemodynamics of systemic and pulmonary circulation.
- [55] C. Lenter, editor. *Geigy Scientific Tables*, volume 3. Medical Education Division, Ciba-Geigy, New Jersey, 1982.
- [56] T.-T. Li. *Global classical solution for quasilinear hyperbolic systems*. Research in Applied Mathematics. Wiley, New York, 1994.
- [57] J.L. Lions and E. Magenes. *Problèmes aux limites non homogènes et applications, 1*. Dunod, Paris, 1968.
- [58] K. Lu, J.W. Clark, J.R., F.H. Ghorbel, D.L. Ware, J.B. Zwischenberg, and A. Bidani. Whole-body gas exchange in human predicted by a cardiopulmonary model. *Cardiov. Eng.*, 3:1–19, 2002.
- [59] E. Magosso, A. Feliciani, and M. Ursino. A mathematical model of cardiovascular response to dynamic exercise. In *Proceedings of the 23rd Annual Conference of the IEEE Engineering in Medicine and Biology Society*, 2001.
- [60] P.J. Martin, D.H. Evans, and A.R. Naylor. Measurement of blood flow in the basal cerebral circulation: Advantages of transcranial color-coded sonography over conventional transcranial Doppler. *J. Clin. Ultrasound*, 23:21–26, 1995.
- [61] V.G. Maz'ja. *Sobolev Spaces*. Springer-Verlag, Heidelberg, 1986.
- [62] B. J. McGuire and T. W. Secomb. A theoretical model for oxygen transport in skeletal muscle under conditions of high oxygen demand. *J Appl Physiol*, 91(5):2255–2265, 2001.
- [63] F. Migliavacca, G. Pennati, G. Dubini, R. Fumero, R. Pietrabissa, G. Urcelay, E.L. Bove, T.Y. Hsia, and M.R. de Leval. Modeling of the norwood circulation: effects of shunt size, vascular resistances, and heart rate. *Am. J. Physiol. Heart Circ. Physiol.*, 280(5):H2076–H2086, May 2001.

- [64] V. Milišić and A. Quarteroni. Analysis of lumped parameter models for blood flow simulations and their relation with 1D models. *M2AN Math. Model. Numer. Anal.*, 38(4):613–632, 2004.
- [65] S. M. Moore, K. T. Moorhead, J. G. Chase, T. David, and J. Fink. One-dimensional and three-dimensional models of cerebrovascular flow. *Journal of Biomechanical Engineering*, 127(3):440–449, 2005.
- [66] K. T. Moorhead, J. G. Chase, T. David, and J. Arnold. Metabolic model of autoregulation in the circle of willis. *Journal of Biomechanical Engineering*, 128(3):462–466, 2006.
- [67] J. Nečas. Sur une méthode pour résoudre les équations aux dérivées partielles du type elliptique, voisine de la variationnelle. *Ann. Scuola Norm. Sup. Pisa*, 16:305–326, 1962.
- [68] C. Nicholson and J.M. Phillips. Ion diffusion modified by tortuosity and volume fraction in the extracellular microenvironment of the rat cerebellum. *J. Physiol.*, 321:225–257, 1981.
- [69] B. Nielsen. Arterial desaturation during exercise in man: implication for O_2 uptake and work capacity. *Scan. J. Med. Sci. Sports*, 13:339–358, 2003.
- [70] B. Opis and A. Kufner. *Hardy-type inequalities*. Pitman Res. Notes in Math. Longman Scientific & Technical, 1990.
- [71] Y. Papelier, P. Escourrou, J.P. Gauthier, and L.B. Rowell. Carotid baroreflex control of blood pressure and heart rate in men during dynamic exercise. *J. Appl. Physiol.*, 77:502–506, 1994.
- [72] Y. Papelier, P. Escourrou, F. Helloco, and L.B. Rowell. Muscle chemoreflex alters carotid sinus baroreflex response in humans. *J. Appl. Physiol.*, 82:577–583, 1997.
- [73] J. Peiro, S.J. Sherwin, K.H. Parker, L. Formaggia V. Franke, D. Lamponi, and A. Quarteroni. Numerical simulation of the arterial pulse propagation using one-dimensional models. In M. Atherton et Al. Eds., editor, *Wall-Fluid Interactions in Physiological Flows*, Advances in Computational Bioengineering Vol. 6. WIT press, 2004.
- [74] H.H. Pennes. Analysis of tissue and arterial blood temperature in the resting human forearm. *J. Appl. Physiol.*, 1:93–122, 1948.
- [75] F. Phythoud, N. Stergiopoulos, and J.-J. Meister. Forward and backward waves in the arterial system: nonlinear separation using riemann invariants. *Technology and Health Care*, 3:201–207, 1995.
- [76] R. Pietrabissa, A. Quarteroni, G. Dubini, A. Veneziani, F. Migliavacca, and S. Ragni. From the global cardiovascular hemodynamics down to the local blood motion: preliminary applications of a multiscale approach. In E. Onate et al., editor, *ECCOMAS 2000*, Barcelona, 2000.
- [77] A.S. Popel. Theory of oxygen transport to tissue. *Critical Reviews in Bioengineering*, 17(3):257–321, 1989.
- [78] A. R. Pries and T. W. Secomb. Rheology of the microcirculation. *Clin. Hemorheol. Microcirc.*, 29:143–8, 2003.
- [79] A.R. Pries, Secomb TW, and Gaehtgens P. Structural adaptation and stability of microvascular networks: theory and simulations. *Am. J. Physiol.*, 275:H349–H360, 1998.

- [80] A.R. Pries, Secomb TW, and Gaehtgens P. Structural autoregulation of terminal vascular beds. vascular adaptation and development of hypertension. *Hypertension*, 33:153–161, 1999.
- [81] D.N. Proctor, D.W. Koch, S.C. Newcomer, K.U. Le, and U.A. Leuenberger. Impaired leg vasodilation during dynamic exercise in healthy older women. *J. Appl. Physiol.*, 95(5):1963–1970, 2003.
- [82] M. Prosi, P. Zunino, K. Perktold, and A. Quarteroni. Mathematical and numerical models for transfer of low density lipoproteins through the arterial walls: a new methodology for the model set up with applications to the study of disturbed luminal flow. *J Biomech.*, 38(4):903–917, 2005.
- [83] L. Quartapelle. *Numerical solution of the incompressible Navier-Stokes equations*. Birkhäuser Verlag, Basel, 1993.
- [84] A. Quarteroni and L. Formaggia. Mathematical modelling and numerical simulation of the cardiovascular system. In P.G Ciarlet and J.L. Lions, editors, *Modelling of Living Systems*, Handbook of Numerical Analysis, Amsterdam, 2004.
- [85] A. Quarteroni and A. Valli. *Numerical Approximation of Partial Differential Equations*. Springer, New York, 1997.
- [86] A. Quarteroni and A. Veneziani. Analysis of a geometrical multiscale model based on the coupling of pde’s and ode’s for blood flow simulations. *SIAM J. on Multiscale Model. Simul.*, 1(2):173–195, 2003.
- [87] A. Quarteroni, A. Veneziani, and P. Zunino. Mathematical and numerical modelling of solute dynamics in blood flow and arterial walls. *SIAM J. Numer. Anal*, 39:1488–1511, 2001.
- [88] Alfio Quarteroni, Riccardo Sacco, and Fausto Saleri. *Numerical mathematics*, volume 37 of *Texts in Applied Mathematics*. Springer-Verlag, Berlin, second edition, 2007.
- [89] R. Reder. Metabolic Control Theory: A structural approach. *J Theor. Biol.*, 135(2):175–201, 1988.
- [90] R.S. Richardson, L.J. Haseler, A.T. Nygren, S. Bluml, and L.R. Frank. Local perfusion and metabolic demand during exercise: a noninvasive MRI method of assessment. *J. Appl. Physiol.*, 91(4):1845–1853, 2001.
- [91] G.M. Saidel, J.A. DiBella, and M.E. Cabrera. Metabolic system dynamics: lumped and distributed models. In Z.M. Arnez et al., editor, *Simulations in Biomedicine*, pages 100–110. WIT Press, 2003.
- [92] B. Saltin. Capacity of blood flow delivery to exercising skeletal muscle in humans. *Am. J. Card.*, 62:30E–35E, 1988.
- [93] G.W. Schmid-Schönbein, T.C. Skalak, and G. Firestone. The microvasculature in skeletal muscle (v). The arteriolar and venular arcades in normotensive and hypertensive rats. *Microvasc. Res.*, 34(3):385–393, 1987.
- [94] R. Scott. Finite element convergence for singular data. *Numer. Math.*, 21:317–327, 1973.

- [95] S.J. Sherwin, L. Formaggia, and J. Peiró. Computational modelling of 1d blood flow with variable mechanical properties. In *Proceedings of ECCOMAS CFD 2001*, ECCOMAS, September 2001. CD-ROM Edition.
- [96] T.C. Skalak and G.W. Schmid-Schönbein. The microvasculature in skeletal muscle (iv). A model of the capillary network. *Microvasc. Res.*, 32:333–347, 1986.
- [97] N. P. Smith, A. J. Pullan, and P. J. Hunter. An anatomically based model of transient coronary blood flow in the heart. *SIAM J. Appl. Math.*, 62(3):990–1018 (electronic), 2001.
- [98] G. Stampacchia. Le problème de Dirichlet pour les équations elliptiques du second ordre à coefficients discontinus. *Ann. Inst. Fourier*, 15:189–258, 1965.
- [99] N. Stergiopoulos, J.-J. Meister, and N. Westerhof. Evaluation of methods for estimation of total arterial compliance. *Am. J. Physiol. (Heart Circ. Physiol.)*, 268:H1540–H1548, 1995.
- [100] T. Tezduyar and S. Sathe. Stabilization parameters in SUPG and PSPG formulations. *JCAM*, 4(1):71–88, 2003.
- [101] M. Ursino. Interaction between carotid baroregulation and the pulsating heart: a mathematical model. *Am. J. Physiol. (Heart Circ. Physiol.)*, 275:H1733–H1747, 1998.
- [102] M. Ursino, E. Magosso, and G. Avanzolini. A mathematical model of CO_2 effect on cardiovascular regulation. *Am. J. Physiol. (Heart Circ. Physiol.)*, 281:H2036–H2052, 2001.
- [103] W.J. Vankan, J.M.R.J. Huyghe, J.D. Janssen, A. Huson, W. Hacking, and W. Schreiner. Finite element analysis of blood perfusion through biological tissue. *Int. J. Eng. Sci.*, 35:375–385, 1997.
- [104] A. Veneziani and C. Vergara. Flow rate defective boundary conditions in haemodynamics simulations. *Int. J. Num. Meth. Fluids*, 2004.
- [105] J. Voldřich. Neumann problem for elliptic equation in Sobolev power weighted spaces. *Math. Comp. in Sim.*, 61:199–207, 2003.
- [106] P.D. Wagner. Muscle O_2 transport and O_2 dependent control of metabolism. *Med. Sci. Sports. Exerc.*, 27:47–53, 1995.
- [107] H.G. Waistra. Modelonderzoek aan de baroreflex bloeddrukregelin. Internal report, TU Eindhoven, 1981.
- [108] J. Wermer. *Potential theory*. Springer-Verlag, Berlin, 1974. Lecture Notes in Mathematics, Vol. 408.

Curriculum Vitae

Carlo D'Angelo est né à Milan, le 23 décembre 1978. Il a effectué son école secondaire au Lycée A. Volta à Milan où il a obtenu en 1996 son Baccalauréat Scientifique. Ensuite, il a poursuivi ses études à l'Ecole Polytechnique de Milan pour obtenir en avril 2003 un diplôme d'ingénieur en électronique avec mention. Entre avril et novembre 2003, il collabore avec le laboratoire MOX de l'Ecole Polytechnique de Milan et l'entreprise Fincuoghi sur un projet concernant problèmes de forme optimale en thermodynamique. Depuis novembre 2003 il a été engagé comme assistant dans la chaire de modélisation et calcul scientifique du Professeur Alfio Quarteroni. Il a effectué son travail de recherche dans le cadre du projet transdisciplinaire de l'EPFL *Sport and Rehabilitation Engineering*. Il a participé à plusieurs conférences internationales et il est auteur des publications suivantes :

- C. D'Angelo, Y. Papelier, *Mathematical modelling of the cardiovascular system and skeletal muscle interaction during exercise*. ESAIM: Proc., September 2005, Vol. 14, pp. 72-88.
- C. D'Angelo, V. Milisic, *Reduced model for a coupling of axisymmetric Navier Stokes equations with a reaction diffusion model for concentration*, EPFL-IACS report 02.2006
- A. Abbà, F. Saleri, C. D'Angelo, *A 3D Shape Optimization Problem in Heat Transfer: Analysis and Approximation via BEM*, Math. Mod. Meth. Appl. Sci., Vol. 16, No. 8 (2006) 1243-1270